

Spring 5-17-2014

# Branching into RNAi: Synthesis, Characterization and Biology of Branch and Hyperbranch siRNAs

Anthony Muriithi Maina  
anthony.maina@student.shu.edu

Follow this and additional works at: <https://scholarship.shu.edu/dissertations>

 Part of the [Biochemistry Commons](#), [Biology Commons](#), [Cancer Biology Commons](#), and the [Medicinal-Pharmaceutical Chemistry Commons](#)

---

## Recommended Citation

Maina, Anthony Muriithi, "Branching into RNAi: Synthesis, Characterization and Biology of Branch and Hyperbranch siRNAs" (2014). *Seton Hall University Dissertations and Theses (ETDs)*. 1953.  
<https://scholarship.shu.edu/dissertations/1953>

**Branching into RNAi:**  
**Synthesis, Characterization and Biology of**  
**Branch and Hyperbranch siRNAs**

*A thesis submitted to the Department of Chemistry and Biochemistry at Seton Hall University in partial fulfillment of the requirements for the degree of Doctor of Philosophy*

By

**Anthony Muriithi Maina**

May 2014

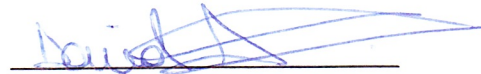
Department of Chemistry and Biochemistry  
Seton Hall University  
South Orange, New Jersey, USA

©Copyright by Anthony Muriithi Maina

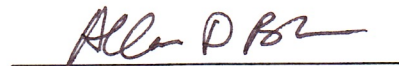
DISSERTATION COMMITTEE APPROVALS

We certify that we have read this thesis and that in our opinion it is sufficient in scientific scope and quality as a dissertation for the degree of Doctor in Philosophy

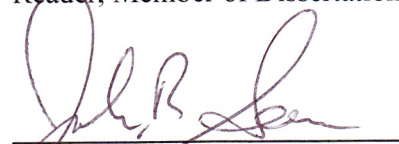
APPROVED BY:



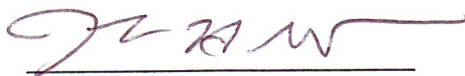
David Sabatino, Ph.D.  
Advisor, Seton Hall University



Allan D. Blake, Ph.D.  
Reader, Member of Dissertation Committee, Seton Hall University



John R. Sowa, Jr., Ph.D.  
Reader, Member of Dissertation Committee, Seton Hall University



Nicholas H. Snow, Ph.D.  
Chair, Department of Chemistry and Biochemistry, Seton Hall University

Dedicated to Goretti, Martin, Rita and my wife - Faith for their sacrifices during my studies and also Mr. James Pierson for his benevolence. My frequent absences juggling with studies and work, which they understood and bore lovingly made my life manageable.

## ABSTRACT

The cancer epidemic continues to afflict millions of humans world-wide each year and despite a renewed hope with the development of new and improved forms of therapy, a cure for cancer remains an elusive goal. This is partly related to the rise of resilient forms of tumors that have evolved with resistance towards conventional chemotherapy and radiation treatments. Moreover, these non-specific therapeutic regimens are highly toxic, leading to severe immunosuppressive effects which poisons the body and compromises the road towards remission. In an effort to mitigate these limitations, cancer-targeting approaches are currently experiencing a renaissance in the translation of new medicines from pre-clinical to bedside use. Notably, gene therapy has recently gained widespread traction in cancer research in the advent of the first RNA interference (RNAi) application in humans. RNAi solicits the use of a double-stranded RNA substrate, aptly named short-interfering RNA (siRNA), which binds to and triggers the degradation of a targeted complementary mRNA strand within the catalytic site of a protein complex named, the RNA-Induced Silencing Complex (RISC). In this manner, malignant mRNA expression is silenced, thereby inhibiting the translation of proteins that can lead to the production of pathological disorders such as cancer. In spite of their utility, several challenges still remain towards the development of a fruitful cancer-targeting gene therapy approach. For example, native siRNAs are plagued by poor pharmacokinetic properties which limit their therapeutic index and utility in clinical applications.

In this thesis, a new class of siRNA motifs is presented to increase substrate efficacy in the RNAi application. Our biological target is a member of the heat shock family of chaperone proteins, the Glucose Regulated Protein of 78 kilodaltons (GRP78) which signals tumor initiation, proliferation and resistance towards chemotherapy. Moreover, GRP78 is

overexpressed and cell surface localized on a wide range of resilient tumor types but not on healthy cells, making it a viable bio-marker for the development of the proposed cancer-targeting gene therapy approach.

Significantly, an efficient solid-phase synthesis method is described in Chapter 2 for the production of linear, V-shape, Y-branch and  $\times$  hyperbranch GRP78-silencing siRNAs. The novel V-shape, Y-branch and  $\times$  hyperbranch motifs were then studied by CD spectroscopy and thermal denaturation experiments (Chapter 3). CD spectroscopy was used to characterize the requisite A-type double-stranded RNA helix for RNAi application; whereas thermal denaturation experiments were used to validate siRNA hybrid stabilities. With stable siRNA hybrids in hand, their biological activity was next assessed in HepG2 hepatoblastoma cells, which constitutes a morbid form of pediatric liver cancer and a valid tumor model for studying our GRP78-targeting strategy. In Chapter 4 of this thesis, the GRP78 silencing activity of the putative branch and hyperbranch siRNAs is discussed and related to its underlying mechanisms for inducing apoptosis in cancer. Towards the development of an effective cancer-targeting gene therapy approach, Chapter 5 highlights preliminary results that showcase the utility of a cancer-targeting peptide (CTP) to condense and deliver siRNA within cancer cells for therapeutic treatment. The latter forms the basis of our cancer-targeting gene therapy approach. This thesis represents an important contribution towards this ultimate goal, in an effort to selectively eradicate some of the most lethal forms of cancer.

## ACKNOWLEDGEMENTS

I am greatly indebted to my mentor, Dr. Sabatino for his tireless efforts and guidance during my years of study at Seton Hall University. I appreciate the time he took to guide me and direct my efforts towards the completion of my doctoral degree.

I acknowledge the efforts of my committee members; Dr. Wei (Chair Person), Dr. Marzabadi, Dr. Blake and Dr. Sowa, who took time to review and judge my Matriculation Exam. Thanks to Dr. Sowa and Dr. Blake for reviewing my dissertation.

Special thanks to Dr. Blake and his research students, Brittany, Chris and Megan for their efforts and countless biology experiments that helped elucidate the biological activity of the RNA motifs detailed in this thesis. I am very grateful for the all the dedication to this project by Dr. Blake.

My heartfelt thanks is also extended to Stesha Joseph, the collaboration between her doctoral project and my project completed the overall picture of the study. Her dedication to her work and diligence played a great role toward the success of our projects.

Over my years of research I had the opportunity to work and train a few students. I am grateful to Maria Bender for all the simplicity and skills she brought on-board. I must admit, our first successful separation of the tritylated nucleoside was as a result of her actions. In addition, thanks to Eva Morzoko for pioneering the cell based assays and Mariana for helping with the CTP:siRNA biology. Also thanks to Mayur Patel, a doctoral student in our group that I had the chance to train and work with. Mayur has continued making the higher ordered siRNAs motifs discussed in this thesis and other new motifs. Thanks to Diana, Faith and Jon as well. I am also

grateful to all the other members of Dr. Sabatino's research group, present and those who graduated and moved on.

Thanks to my friends and family. I am deeply indebted to Mr. James Pierson, whom I consider my dad in America for his trust, unequalled sacrifice and support. The list of friends to thank is endless, so I will leave it unwritten here but always in my heart. I am grateful to my parents, and especially my mum who has for the last couple years spent a lot of time helping out in our home. I appreciate the sacrifice they made to send me abroad for further studies and the opportunities their selfless deed exposed me too. In addition, thanks to my wife and partner for her belief in me. I must admit her well spoken words kept the flame burning. In addition, I am grateful to our children, Goretti, Martin and Rita for the sacrifices they have made towards my studies. Goretti and Martin, I know I missed some of your important school events...but not anymore. Just know as you pursue your goals, you have all my support and understanding. Thanks to Goretti, for her help and many questions that made me realize the need to communicate at her level of understanding as well.

Finally, and most important of all, thanks be to God, because it is only through Him that all of this work has been possible.



## TABLE OF CONTENTS

DEDICATION	iii
ABSTRACT	iv
ACKNOWLEDGEMENTS	vi
TABLE OF CONTENTS	viii
ABBREVIATIONS AND SYMBOLS	xiii
LIST OF FIGURES	xix
LIST OF TABLES	xxiii
LIST OF SCHEMES	xxiii

### CHAPTER 1: DISCOVERY AND ANTI-CANCER APPLICATIONS

<b>OF SHORT- INTERFERING RNA (siRNA)</b>	1
1.1 DISCOVERY OF siRNA AND ITS ROLE IN THE RNA INTERFERENCE (RNAI) PATHWAY	1
1.2 RNAi IN CANCER	3
1.3 LIMITATIONS OF RNAi IN ONCOGENE THERAPY APPLICATIONS	7
1.4 CURRENT METHODS FOR RNAi APPLICATION IN ONCOLOGY	10
1.5 THESIS OBJECTIVES	17
1.6 REFERENCES	20

### CHAPTER 2: SYNTHESIS AND CHARACTERIZATION OF LINEAR,

<b>BRANCH AND HYPERBRANCH siRNAs</b>	29
2.1 ABSTRACT	29
2.2 INTRODUCTION	30
2.2.1 SOLID PHASE RNA SYNTHESIS	30
2.2.2 RNA PHOSPHORAMIDITES FOR SOLID PHASE RNA SYNTHESIS	31

2.2.3	AUTOMATED SOLID PHASE RNA SYNTHESIS	32
2.2.4	ANALYSIS AND PURIFICATION OF SYNTHETIC RNA BY HPLC	35
2.2.5	ANALYSIS AND PURIFICATION OF SYNTHETIC RNA BY PAGE	38
2.2.6	CHARACTERIZATION OF SYNTHETIC RNA BY MASS SPECTROMETRY	39
2.2.7	APPLICATIONS OF SYNTHETIC siRNAs AND ANALOGS	40
2.3	PROJECT OBJECTIVES	45
2.4	RESULTS AND DISCUSSION	47
2.4.1	SYNTHESIS AND CHARACTERIZATION OF BRANCHPOINT NUCLEOTIDES	47
2.4.2	SOLID PHASE SYNTHESIS OF BRANCH AND HYPERBRANCH siRNAs	54
2.4.3	ANALYSIS, PURIFICATION AND CHARACTERIZATION OF siRNAs	56
2.5	CONCLUSIONS	62
2.6	REFERENCES	63
2.7	EXPERIMENTAL SECTION	69
2.7.1	GENERAL METHODS	69
2.7.2	SYNTHESIS OF THE BRANCHPOINT PHOSPHoramidites, 2.16 AND 2.24	69
2.7.3	SOLID PHASE RNA SYNTHESIS	73
2.7.4	CLEAVAGE AND DEPROTECTION OF RNA	74
2.7.5	POLYACRYLAMIDE GEL ELECTROPHORESIS (PAGE)	75
2.7.6	ION PAIRING REVERSE PHASE HPLC (IP RP HPLC)	77
2.7.7	MASS SPECTROMETRY	77

<b>CHAPTER 3: STRUCTURE AND BIOPHYSICAL STUDIES OF siRNAs</b>	78
3.1 ABSTRACT	78
3.2 INTRODUCTION	79
3.2.1 CD SPECTROSCOPY OF RNA	79
3.2.2 UV-VIS SPECTROSCOPY OF RNA	83
3.3 CHAPTER OBJECTIVES	87
3.4 RESULTS AND DISCUSSION	87
3.4.1 CD SPECTROSCOPY OF siRNAs	87
3.4.2 UV-VIS SPECTROSCOPY OF siRNAs	89
3.5 CONCLUSIONS	91
3.6 REFERENCES	93
3.7 EXPERIMENTAL SECTION	96
3.7.1 UV-VIS SPECTROSCOPY	96
3.7.2 CD SPECTROSCOPY	96
<b>CHAPTER 4: RNAi ACTIVITY OF GRP78 TARGETING siRNAs</b>	98
4.1 ABSTRACT	98
4.2 INTRODUCTION	99
4.2.1 SELECTION OF GRP78 AS A MOLECULAR TARGET IN CANCER THERAPY	99
4.3 CHAPTER OBJECTIVES	107
4.4 RESULTS AND DISCUSSION	108
4.4.1 HepG2 CELL CULTURE	108
4.4.2 siRNA:LIPOFECTAMINE TRANSFECTIONS IN HepG2 CELLS	109
4.4.3 CELL SURFACE GRP78 EXPRESSION IN HepG2 CELLS	113
4.5 CONCLUSIONS	115
4.6 REFERENCES	117
4.7 EXPERIMENTAL SECTION	123
4.7.1 HepG2 CELL CULTURE	123
4.7.2 siRNA PREPARATION	123

4.7.3	siRNA TRANSFECTION IN HepG2 CELLS	123
4.7.4	SDS-PAGE AND WESTERN BLOTTING	124
4.7.5	CONFOCAL MICROSCOPY	125
4.7.6	CELL VIABILITY	125
<b>CHAPTER 5: PRELIMINARY STUDIES TOWARDS THE DEVELOPMENT OF A CANCER-TARGETING GENE THERAPY APPROACH</b>		127
5.1	ABSTRACT	127
5.2	INTRODUCTION	128
5.2.1	SELECTION OF PEP42 AS A GRP78-TARGETING PEPTIDE	128
5.2.2	POLY(ARGININE) PEPTIDES AS siRNA CELL DELIVERY AGENTS	132
5.3	CHAPTER OBJECTIVES	134
5.4	RESULTS AND DISCUSSION	136
5.4.1	PREPARATION AND CHARACTERIZATION OF CTP:siRNA COMPLEXES	136
5.4.2	BIOLOGICAL STUDIES OF THE CTP:siRNA COMPLEXES	141
5.5	CONCLUSIONS	143
5.6	REFERENCES	145
5.7	EXPERIMENTAL SECTION	147
5.7.1	CTP:siRNA COMPLEX FORMATION	147
5.7.2	CTP:siRNA STABILITY IN 10% FBS/DMEM	147
5.7.3	GEL SHIFT ASSAY	147
5.7.4	DYNAMIC LIGHT SCATTERING (DLS)	148
5.7.5	TRANSMISSION ELECTRON MICROSCOPY (TEM)	148
5.7.6	HepG2 CELL CULTURE	148
5.7.7	CTP:siRNA TRANSFECTION IN HepG2 CELLS	149
5.7.8	SDS-PAGE AND WESTERN BLOTTING	149
5.7.9	CELL VIABILITY	149

<b>CHAPTER 6: CONCLUSION AND CONTRIBUTIONS TO KNOWLEDGE</b>	151
6.1 CONCLUSIONS AND CONTRIBUTIONS TO KNOWLEDGE MADE IN THIS THESIS	151
6.1.1 SYNTHESIS AND CHARACTERIZATION OF BRANCH AND HYPERBRANCH siRNAs	151
6.1.2 GRP78 SILENCING AND CELL DEATH ACTIVITY OF BRANCH AND HYPERBRANCH siRNAs IN HepG2 CANCER CELLS	152
6.2 PUBLICATIONS, INVENTION DISCLOSURES AND CONFERENCE PRESENTATIONS	154
<b>APPENDIX</b>	157

## ABBREVIATIONS AND SYMBOLS

%H	% hyperchromicity
®	registered
µmol/g	micro mole per gram
°C	degree Celsius
A	adenosine
Å	Angstrom
A <sub>260</sub> or Abs	UV absorbance measured at 260nm
Ade	adenine
AE	anion exchange
Ago2,	agonaute 2 complex
AKI,	acute kidney injury;
AKT	protein kinase-B
AMD	age-related macular edema;
ANOVA	analysis of variance
Apo B	apolipoprotein B
Arg	arginine
asRNA	antisense RNA
AT1	angiotensin type 1;
ATF6	activating transcription factor 6
ATP	adenosine triphosphate
BIK	BCL2-interacting killer (apoptosis-inducing)
BLAST	Basic Local Assignment Search Tool
BuOH	butanol
©	copyright
C	cytosine
Ca <sup>2+</sup>	calcium ions
CD	circular dichroism
CEM	2'-cyanoethoxymethyl

CHL-1	neural cell adhesion molecule L1-like protein
CHOP	DNA-damage inducible transcript 3
c-Myc	myelocytomatosis viral oncogene
CNET	cyanoethyl
CO <sub>2</sub>	carbon dioxide gas
COSY	Correlation spectroscopy
COX-2	cyclooxygenase-2 inhibitor
CPG	controlled pore glass
CPPs	cell penetrating peptides
CPT-11	Camptosar, Irinotecan drug
CTPs	cancer targeting peptides
CXCR4	chemokine receptor
Cy3	cyanine 3 dye
Cy5	cyanine 5 dye
Cyt	cytosine
DABCO	1,4-diazabicyclo[2.2.2]octane
DAPI	4'-6-diamidino-2-phenylindole stain
DCA	dichloroacetic acid
DCM	dichloromethane
DGF	delayed graft function;
DLS	digital light scattering
DME	diabetic molecular edema;
DMEM	Dulbecco's modified eagle's medium
DMSO	dimethylsulfoxide
DMSO-d <sub>6</sub>	deuterated dimethylsulfoxide
DMT	dimethyltryptyl
DNA	deoxyribonucleic acid
DOTAP	N-[1-(2,3-dioleoyloxy)propyl]-N,N,N-trimethyl-ammonium methylsulfate;
dsRNA	double stranded RNA
e.g.	for example

EDTA	ethylenediaminetetracetic acid
EGCG	epigallocatechin gallate
EGFR	epidermal growth factor receptor;
EGR	epidermal growth receptor
eIF2 $\alpha$	eukaryotic initiation factor 2 alpha
ER	endoplasmic reticulum
ERK 1/2	mitogen-activated protein kinase
ESI-MS	electrospray ionization mass spectrometry
EtOH	ethanol
ETT	ethylthiotetrazole
FAK	focal adhesion kinase
FBS	fetal bovine serum
FDA	Federation of Drug Administration
FITC	fluorescein isothiocyanate
Fpmp	1-(2-fluorophenyl)-4-methoxypiperidin-4-yl
G	guanosine
GFP	green fluorescent protein
GM-CSF	granulocyte-macrophage colony-stimulating factor
GRP78	glucose regulated protein 78
Gua	guanine
HBV	hepatitis B virus
HCL	hydrochloric acid
HCV	hepatitis C virus
HDI	hydrodynamic tail vein injection
HepG2	human hepatocellular carcinoma cells
HER-2	human epidermal growth factor receptor 2
HFIP	hexafluoroisopropanol
HIF	hypoxia inducible factor
His	histine
HNK	honokiol
HPLC	high performance liquid chromatography



HSP70	heat shock protein 70
HSV	herpes simplex virus
hTERT	human telomerase reverse transcriptase
Huh-7	human hepatocarcinoma cells
ICV	intracerebroventricular
IM	intramuscular
INF	interferon
IP	intraperitoneal
iPr	isopropyl
IP-RP HPLC	ion-pairing reverse phase HPLC
IRE1	inositol requiring enzyme 1
IT	intratumor
IV	intravenous
IV	intravenous
IVT	intravitreal
KCl	potassium chloride
$K_D$	dissociation constant
KSP	kinesin spindle protein;
LC/MS	liquid chromatography mass spectrometry
LCAA	long chain alkyl amine
LIC-101	liposome complex made of 2- <i>O</i> -(2-diethylaminoethyl)-carbamoyl-1, 3- <i>O</i> -dioleoylglycerol and egg phosphatidylcholine
LiClO <sub>4</sub>	lithium perchlorate
LIMK1	LIM domain kinase 1
LNA	locked nucleic acid;
LODER	Local Drug EluteR polymer
Lv	levulinyl
Lys	lysine
m/z	mass per charge ratio
MALDI-TOF	matrix assisted laser desorption/ionization time of flight
MAPK	mitogen-activated protein kinase 1

MDR1	multidrug resistance gene
Me	2'-methyl
MeCN	acetonitrile
MgCl <sub>2</sub>	magnesium chloride
mHTT	mutant huntingtin
Min	minute
miRNA	microRNA
MMT-Cl	monomethoxytrityl chloride
MOE	2'-methoxyethyl
mRNA	messenger RNA
MS	mass spectrometry
msDNA	multicopy single-stranded DNA
Na <sub>2</sub> HPO <sub>4</sub>	sodium phosphate monobasic
<i>N</i> -Ac	N-Acetyl
NaCl	sodium chloride
NaClO <sub>4</sub>	sodium perchlorate
NaOAc	sodium acetate
<i>N</i> -Bz	N-Benzyl
NF-KB	nuclear factor of kappa light polypeptide
NH <sub>4</sub> OH	ammonium hydroxide
<i>N</i> - <i>i</i> Bu	N-isobutyl
NIH	ImageJ National Institute of Health ImageJ software
NMR	nuclear magnetic resonance
O.D.	optical density
O-Me	2'-O-methyl
OptiMEM	serum free medium
P.G	protecting group
Pac	phenoxyacetyl
PACT	protein Kinase RNA activator
PAGE	polyacrylamide gel electrophoresis
PAK-2	p-21 activated kinase-2

PAMAM	polyamidoamine dendrimers
PBS	phosphate buffer saline
PDT	photodynamic therapy
PEG	poly-ethyleneglycol
PEI	polyethyleneimine;
PERK	protein kinase like ER kinase
Ph	phenol
PI3K	phosphoinositide-3-kinase
PKN3	Protein Kinase 3;
PLK1	Polo-like Kinase;
pmol	pico mole
PVDF	polyvinylidifluoride
Raf	proto-oncogene serine/threonine kinase
Ras	retroviral associated sequence oncogene
RIPA	radio-immunoprecipitation assay buffer
RISC	ribosomal initiation silencing complex
RNA,	ribonucleic acid
RNase	ribonucleases
RONDEL	cyclodextrinpolymer platform;
RRM2	Ribonucleotide Reductase M2;
RSV	respiratory syncytial virus;
rU	ribouridine; branchpoint unit in the sequences
SC	subcutaneous;
SC	subcutaneously;
S-FAU	thioarabinouridine
shRNA	short hairpin RNA
siRNA	small interfering RNA
SNALP	stable nucleic acid lipid particle;
SOD1	superoxide dismutase;
ssRNA	sense strand RNA
TAT	trans-activator of transcription protein

tBDMS	2'-tert-butyldimethylsilane
TBE	tris borate EDTA buffer
TEA	triethylamine
TEAA	triethylammonium acetate
TEM	transmission electron microscopy
TGF- $\beta$	transforming growth factor- $\beta$
tiRNA	tripartite-interfering siRNA
TLC	thin layer chromatography
TLR	toll like receptors
T <sub>m</sub> ,	Thermal melts
TMB	3,3',5,5'-tetramethylbenzidine
TNF	tumor necrosis factor
TRBP	Transactivation response RNA binding protein
TREAT.3HF	triethylamine trihydrofluoride
TRIS	[tris(hydroxymethyl)aminomethane
TTR,	transthyretin;
™	trade mark
UPR	unfolded protein response
U	uridine
Ura	uracil
UV	ultraviolet
UV-VIS	Ultra Violet – Visible
VCD	Verrucosidin
VEGF,	vascular endothelial growth factor;
Vs.	versus
WM266-4	human melanoma cell line
ZEBOV	Polymerase (L) gene of the Zaire Species of Ebola Virus;
$\Delta G^\circ$	standard Gibbs free energy
$\Delta H^\circ$	standard enthalpy
$\Delta S^\circ$	standard entropy
$\mu$	micro

## LIST OF FIGURES

### CHAPTER 1

Figure 1.1	RNAi mechanism for silencing mRNA expression	2
Figure 1.2	RNA isomerization and cleavage steps during chemical and enzyme-catalyzed reactions	8
Figure 1.3	Methods of RNAi delivery <i>in vivo</i>	10
Figure 1.4	Design of effective siRNAs for clinical RNAi application	11
Figure 1.5	Chemically modified siRNAs and their bioconjugation with lipid moieties	13
Figure 1.6	siRNA transfection methods for triggering RNAi in mammalian cells	14

### CHAPTER 2

Figure 2.1	Attachment of a protected RNA monomer on a succinyl linked LCAA-CPG.	31
Figure 2.2	Structures of commercially available RNA phosphoramidites and their protecting groups	32
Figure 2.3	AE and IP RP HPLC analysis of RNA	37
Figure 2.4	IP RP HPLC analysis of a double stranded siRNA	38
Figure 2.5	Polyacrylamide gel electrophoresis	39
Figure 2.6	Live cell imaging with fluorescently labeled siRNAs	41
Figure 2.7	Single molecule FRET experiment for determining the mechanism of Ago action with a target mRNA substrate	43
Figure 2.8	Modified siRNAs for RNAi application	45
Figure 2.9	Structures of siRNAs designed, synthesized and characterized in this study	46

Figure 2.10	Branchpoint nucleotide phosphoramidites used in the preparation of branch, hyperbranch and lariat RNA	48
Figure 2.11	The $^1\text{H}$ - $^1\text{H}$ COSY NMR	51
Figure 2.12	$^{31}\text{P}$ NMR spectrum of the branchpoint phosphoramidite diastereomers, 2.16	53
Figure 2.13	IP RP LC/MS analysis of a pure V-shape siRNA, Seq. 4	57
Figure 2.14	IP RP LC/MS analysis of a pure hyperbranch siRNA, Seq. 7	58
Figure 2.15	Native and denaturing PAGE analyses of siRNAs synthesized in this study	59

### CHAPTER 3

Figure 3.1	CD spectroscopy method and sample analysis	80
Figure 3.2	CD Spectra of ApA dinucleotide vs. Adenosine and A-type double-stranded RNA helix	81
Figure 3.3	The global helical conformation of A-RNA and its preferred sugar conformation, structures and data	82
Figure 3.4	Schematic of UV-Vis absorption spectrophotometer	83
Figure 3.5	Typical melting curve displaying the phase transition from helix-coil at 260 nm with increasing temperatures	85
Figure 3.6	Structure and conformation of 2'-OMe RNA	86
Figure 3.7	CD spectroscopy of the siRNA sequences described in this study	89
Figure 3.8	Thermal denaturation curves of the siRNA sequences described in this study	91

### CHAPTER 4

Figure 4.1	The many roles of GRP78 in the UPR signaling pathway associated with ER stress	100
Figure 4.2	GRP78 cellular localizations and activities	101

Figure 4.3	Pluripotent cancer cell surface GRP78 signaling	102
Figure 4.4	Immunohistochemical staining of GRP78 in human glioma tissues and normal brain	104
Figure 4.5	Small molecule inhibitors of GRP78 activity	105
Figure 4.6	GRP78 gene-targeting method with hyperbranch siRNA:Lipofectamine complex	108
Figure 4.7	Lipofectamine™ 2000 toxicity in HepG2 cells	110
Figure 4.8	Western blot for the siRNA:Lipofectamine transfections	111
Figure 4.9	Linear, branch and hyperbranch siRNAs transfection results in HepG2 cells	113
Figure 4.10	Monitoring cell surface GRP78 expression with confocal laser microscopy	115

## CHAPTER 5

Figure 5.1	Binding assay of the Pep42 phage with recombinant proteins	129
Figure 5.2	Cell uptake and localization of Mut42	131
Figure 5.3	Tumor growth in xenograft mouse with (A) no treatment, (B) siRNA, (C) R15:mismatch HER-2 siRNA and (D) R15:HER-2 siRNA	134
Figure 5.4	Proposed cancer-targeting gene therapy strategy	135
Figure 5.5	Native PAGE gel shift assay	136
Figure 5.6	CD spectra of CTP:siRNA complexes	137
Figure 5.7	TEM image of CTP:siRNA complex	139
Figure 5.8	Thermal denaturation studies of the CTP:siRNA complex	141
Figure 5.9	Native PAGE gel of (A) siRNA (20 $\mu$ M) and (B) CTP:siRNA (20 $\mu$ M) in 10% FBS in DMEM	142
Figure 5.10	RNAi activity of CTP:siRNA complex. (A) Western blot and (B) data analysis by autoradiography of GRP78 expression (C) Cell viability data	143

## LIST OF TABLES

### CHAPTER 1

Table 1.1	RNAi in pre-clinical cancer therapy	5
Table 1.2	siRNA candidates in oncology clinical trial as of 2012	6
Table 1.3	siRNA delivery systems in RNAi oncogene therapy	16

### CHAPTER 2

Table 2.1	Characterization data for the siRNA sequences synthesized in this study	60
-----------	---	----

### CHAPTER 5

Table 5.1	DLS measurements of the effective diameters (nm) observed	138
-----------	---	-----

## LIST OF SCHEMES

### CHAPTER 2

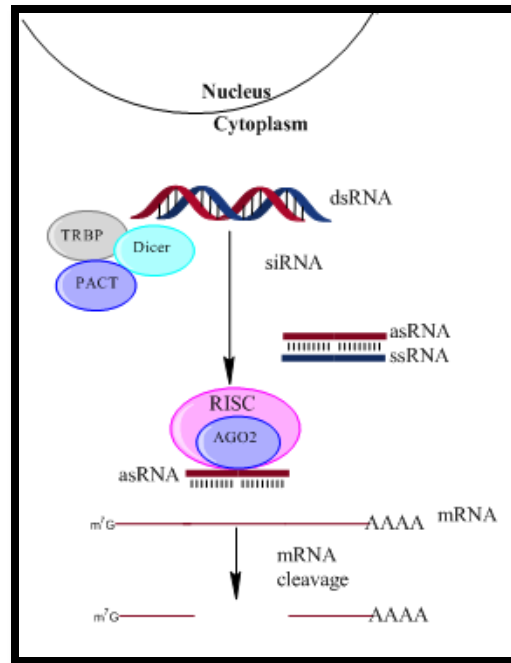
Scheme 2.1	Automated solid phase RNA synthesis cycle.	35
Scheme 2.2	Reaction and Conditions for branchpoint synthesis	49
Scheme 2.3	Solid phase branch RNA synthesis method	55



# CHAPTER 1. DISCOVERY AND ANTI-CANCER APPLICATIONS OF SHORT-INTERFERING RNA (siRNA)

## 1.1 DISCOVERY OF siRNA AND ITS ROLE IN THE RNA INTERFERENCE (RNAI) PATHWAY

RNA interference (RNAi) occurs naturally in animal and plant cells for regulating gene expression into functional proteins for normal cell structure and activity.<sup>1</sup> A crucial component to the RNAi application is the gene-silencing activity of short (18-21 base-pairs) double-stranded RNA (dsRNA) also known as short-interfering RNA (siRNA). siRNAs are produced naturally from the enzymatic processing of lengthy dsRNA sequences. Once formed, siRNAs are recruited into a protein complex referred to as the RNA-Induced Silencing Complex (RISC). A subunit of this protein complex (Ago2) catalyzes the hydrolytic degradation of a single siRNA strand, referred to as the sense-strand RNA (ssRNA). The remaining antisense-strand RNA (asRNA) functions as a template for targeting and binding to a complementary messenger RNA (mRNA) sequence for down-regulating its gene expression into protein form. In this mechanism, the asRNA:mRNA hybrid bound within the active site of RISC inhibits ribosome binding and the assembly of the translational machinery for protein synthesis. Moreover, RISC catalyzes the degradation of the mRNA strand facilitating the turnover of additional mRNA for potent gene silencing effects (**Figure 1.1**).



**Figure 1.1.** RNAi mechanism for silencing mRNA expression.<sup>1</sup>

The discovery of the RNAi mechanism was accidental, initially dating back to 1990 with the work of Jorgenson and co-workers in which they attempted to make a ‘super purple’ petunia.<sup>2</sup> Following insertion of an extra copy of a ‘purple’ gene targeting the production of chalcone synthase, the enzyme responsible for the production of the purple pigment anthocyanin in petunias, only white petunias were discovered. Albeit the mechanism responsible for down-regulating gene expression remained unclear, this discovery proved to be the first application of RNAi. It was not until 1998, when the seminal works of Fire and Mello produced a full understanding of the RNAi mechanism in the nematode *Caenorhabditis Elegans*.<sup>3</sup> For their contributions, Fire and Mello were awarded the Nobel Prize in physiology or medicine in 2006. Shortly after its discovery and characterization, RNAi research has evolved and demonstrated many fruitful applications of synthetic siRNAs for treating human diseases associated with the

expression of malignant genes (*e.g.* metabolic disorders, cancer, gene mutations and deletions etc.).<sup>1</sup>

## 1.2 RNAi IN CANCER

In relation to cancer, a number of siRNAs have demonstrated potent silencing of oncogene targets and anti-cancer effects in metastatic cell lines and in tumor-bearing animal models (**Table 1.1**).<sup>4</sup>

These include siRNAs targeting the oncogenesis pathways<sup>5-14</sup>, such as the Ras, Raf, c-Myc and HIF genes that are overexpressed in a variety of tumor tissues, including those associated with ovarian, melanoma and the pancreas. These oncogenes harbor cancer initiation, proliferation, and angiogenesis that led to the generation of metastatic forms of tumors that were found to be resilient to chemical and radiation treatments. In these cases, siRNA administration proved successful in halting the progression of these cancer types while resulting in significant tumor shrinkage.

The siRNAs targeting the anti-apoptotic factors aim to silence the causative genes in cancer that are responsible for evading the cell death pathways.<sup>15-18</sup> The anti-apoptotic oncogenes play a pivotal role in cancer cell replication without restriction, which is another hallmark of the disease.<sup>19</sup> siRNAs that may effectively silence the anti-apoptotic genes may lead to the activation of the cell death effectors (*e.g.* Caspase 3 and 7) which stimulate the signaling pathways that are associated with the cell death response (apoptosis).<sup>20</sup> For example, B-cell lymphoma 2 (Bcl-2) is an anti-apoptotic factor that is over expressed in many tumor tissues such as those belonging to the prostate and has been validated as a therapeutic target for pre-clinical RNAi application.<sup>15</sup> Other anti-apoptotic oncogene targets include: Survivin<sup>16,17</sup>, the Fas-associated death domain-like interleukin-1 $\beta$ -converting enzyme-like inhibitory protein (FLIP) and X-chromosome linked IA (XIAP)<sup>18</sup> have all demonstrated favorable responses to siRNA treatment in cancer cell lines

and tumor-bearing animal models. Moreover, down-regulation of Bcl-2 and XIAP with siRNA treatment sensitized drug-resistant breast cancer cells to Etoposide and Doxorubicin anti-cancer drugs, illustrating the potential for developing combination strategies involving oncogene and chemotherapeutics for more potent anti-cancer effects.<sup>18</sup>

The cell cycle regulators including the retinoblastoma tumor suppressor (Rb) and p53 pathways have been found to play a critical role in disrupting cellular senescence in cancer, the ability for cells to divide finite times before soliciting the cell death cascade.<sup>21</sup> Thus, siRNAs have been applied for silencing the expression of tumor suppressors and regaining cellular senescence. These effects have been demonstrated following siRNA treatment of Cyclin B1 and E6 tumor suppressor genes in cervical and prostate cancers, respectively.<sup>22-24</sup> Moreover, potent anti-cancer effects have also been demonstrated by silencing the human telomerase activity which has also been found to play a pivotal role in maintaining cellular senescence.<sup>25-26</sup>

The interaction between the developing cancer cell and the host environment (known as the tumor microenvironment) facilitates angiogenesis (formation of new blood cells) and tumor invasion (metastatic growth), another hallmark of cancer.<sup>19</sup> These tumor promoting oncogenes are associated with the vascular endothelial growth factor (VEGF) and chemokine receptor (CXCR4) among others, and have each been targeted with siRNAs for induction of leukemia, prostate and breast cancer cell death.<sup>27-31</sup>

Cancer drug resistance has limited the applications of chemotherapeutic agents in the treatment of cancer.<sup>32</sup> Cancer drug resistance has been partly associated with expression of the multidrug resistance gene (MDR1). For example, P-glycoprotein (P-gp) functions as a membrane bound efflux protein, which binds to intracellular drugs and pumps them out of the cell for limited to inconsequential therapeutic effect.<sup>33</sup> Targeting MDR1 with siRNA has sensitized

cancer cells to chemotherapeutics such as Doxorubicin and Taxol, by eliminating their drug resistance and inducing cancer cell death.<sup>34-35</sup>

**Table 1.1.** RNAi in pre-clinical cancer therapy<sup>4</sup>

Pathway	Oncogenes	Cancer types
Oncogenesis	Ras	Ovarian <sup>5</sup>
		Melanoma <sup>6</sup>
	Raf	Melanoma <sup>7</sup>
		Prostate <sup>8</sup>
		Breast <sup>9</sup>
	BCR-ABL	Chronic myelogenous leukemia (CML) <sup>10</sup>
	Beta catenin	Colon <sup>11</sup>
c-Myc	Breast carcinoma <sup>12</sup>	
Apoptosis	HIF-1	Cervical and colon <sup>13</sup>
		Breast and glioma <sup>14</sup>
	Bcl-2	Prostate <sup>15</sup>
	Survivin	Esophageal <sup>16</sup>
		Glioma <sup>17</sup>
Bcl-2 and XIAP	Breast <sup>18</sup>	
Cell cycle regulators	E2F4	Prostate <sup>22</sup>
	E6, E7	Cervical <sup>23</sup>
	Cyclin B1	Cervical <sup>24</sup>
Cell senescence	hTER	Colon and melanoma <sup>25</sup>
	hTERT	Bladder <sup>26</sup>
Tumor-host interactions	VEGF	Ewing's sarcoma <sup>27</sup>
		Leukemia <sup>28</sup>
	CD31	Prostate <sup>29</sup>
	RhoA/RhoC	Breast <sup>30</sup>
	CXCR4	Breast <sup>31</sup>
Chemotherapy resistance	MDR1	Pancreatic and gastric carcinoma <sup>34</sup>
		Uterine sarcoma <sup>35</sup>

In light of the flourishing pre-clinical data, a series of clinical trials have been issued (Table 1.2).<sup>36</sup> This has led to the first human clinical trials for the application of siRNAs in the treatment of liver cancers.<sup>37</sup> In spite of its unlimited potential, few siRNAs have effectively translated from the pre-clinical to clinical applications raising the unmet need to develop more potent and efficacious constructs.

**Table 1.2.** siRNA candidates in oncology clinical trial as of 2012 adapted from Uchino et al<sup>36</sup> and ClinicalTrials.gov.

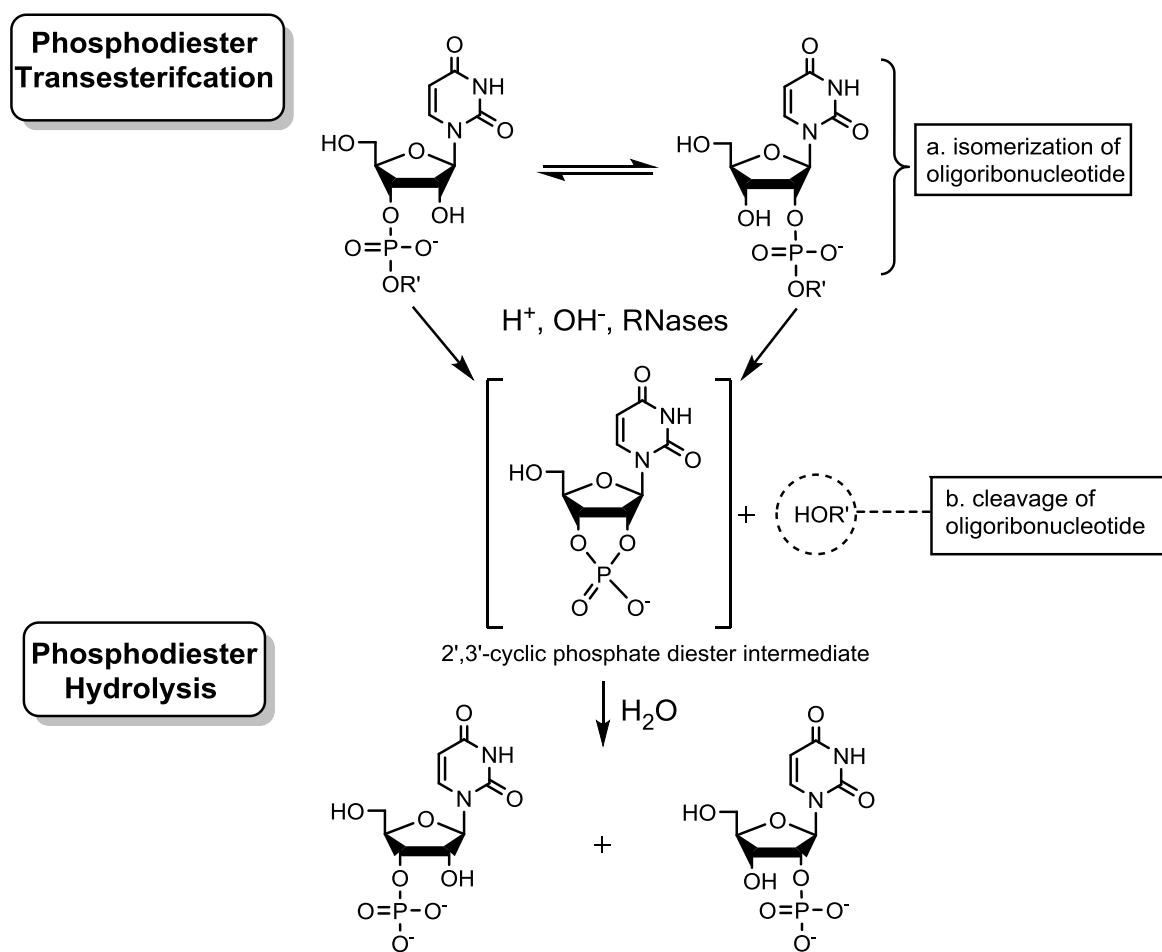
ClinicalTrials.gov identifier	Drug	Route	Delivery	Disease	Target	Phase	States	Company
NCT00499590	Bevasir anib	IVT	Naked siRNA	Wet AMD	VEGF	III	Terminated	Opko Health
NCT00363714, NCT00395057	AGN21 1745/ Sirna – 027	IVT	Naked siRNA	AMD	VEGF-R1	II	Terminated	Allergan/ Sirna
NCT01065935, NCT00658086	ALN-RSV01	Nebulization	Naked siRNA	RSV infection after lung transplantation	RSV Nucleocapsid	II	Completed	Alnylam
NCT00306904	Bevasir anib	IVT	Naked siRNA	DME	VEGF	II	Completed	Opko Health, Inc.
NCT01445899	PF-045236 55	IVT	Naked siRNA	DME	RTP801	II	Recruiting	Quark Pharma
NCT01200420	miraviren	SC	Naked LNA	HCV	miR-122	II	Completed	Santaris Pharma
NCT01551745 NCT01505166	FANG vaccine	Ex vivo, Intradermal	Electroporation	Ovarian cancer, colon cancer	Bi-shRNA-Furin and GM-CSF	II, II	Recruiting, Recruiting	Gradalis, Inc.
NCT00802347	I5NP	IV	Naked siRNA	DGF in kidney transplantation	P53	I/II	Recruiting	Quark Pharma
NCT01227291	SYL040 012	Ophthalmic drops	Naked siRNA in ophthalmic drops	Glaucoma and ocular hypertension	Adrenergic receptor beta-2 siRNA	I/II	Completed	Sylentis
NCT00725686, NCT00713518	PF-045236 55	IVT	Naked siRNA	Wet AMD	RTP801	I, II	Completed	Pfizer/Quark
NCT00716014	TD101	Intralesional	Naked siRNA	Pachyonychia congenita	Keratin 6a N171K mutant mRNA	Ib	Completed	TransDerm / IPCC
NCT00882180, NCT01158079	ALN-VSP02	IV	SNALP	Liver cancer, solid tumors	KSP and VEGF	I, I	Completed	Alnylam

NCT00554359, NCT00683553	I5NP	IV	Naked siRNA	AKI for major cardiovascular surgery	P53	I, I	Compl eted, termin ated	Quark Pharma
NCT01148953	ALN- TTR01	IV	SNALP	TTR-mediated amyloidosis	Transthyret in	I	Compl eted	Alnylam
NCT00689065	CALA A-01	IV	RONDEL	Solid cancer	RRM2	I	Active	Calando Pharma
NCT00466583	EZN- 2968	IV	Naked LNA	Advanced solid tumor, lymphoma	HIF-1a	I	Compl eted	Santaris Pharma
NCT01120288	EZN- 2968	IV	Naked LNA	Liver metastases	HIF-1a	I	Recrui ting	NCI
NCT00672542	siRNA in dendriti c cells	Ex vivo, Intrader mal	Electropor ation	Metastatic melanoma	Immunopro teasome subunits LMP2, LMP7, MECL1	I	Active	Duke University
NCT01061840	FANG vaccine	Ex vivo, Intrader mal	Electropor ation	Solid tumors	Bi-shRNA- Furin and GM-CSF	I	Recrui ting	Gradalis, Inc.
NCT01064505	QPI- 1007	IVT	Naked siRNA	Optic atrophy	Caspase-2	I	Active	Quark Pharma
NCT00938574	Atu027	IV	AtuPLEX	Advanced solid cancer	PKN3	I	Compl eted	Silence Therapeuti cs
NCT01188785	siG12D LODER	EUS biopsy needle	LODER polymer	Pancreatic ductal adenocarcinoma	KRASG12 D	I	Recrui ting	Silenseed Ltd
NCT01262235	TKM- 080301	IV	SNALP	Cancer	PLK1	I	Recrui ting	Tekmira
NCT00927459	PRO- 040201	IV	SNALP	Hypercholesterol emia	Apo B	I	Termi nated	Tekmira

### 1.3 LIMITATIONS OF RNAi IN ONCOGENE THERAPY APPLICATIONS

The application of RNAi in clinical oncology is faced with several challenges.<sup>4</sup> These include: poor delivery and cell permeability, immunostimulatory activity, non-selective (off-targeting) gene silencing effects, poor metabolic stability and acute toxicity.<sup>38</sup> For example, elevated immune responses following siRNA treatment were evaluated by the overexpression of inflammatory markers; interferon (INF) alpha and beta, cytokines such as interleukin-6 and tumor necrosis factor (TNF) alpha and chemokine induced by Toll-Like Receptors (TLR) agonists.<sup>39</sup> Sequence similarities between the first 11 nucleotides of the antisense siRNA strand

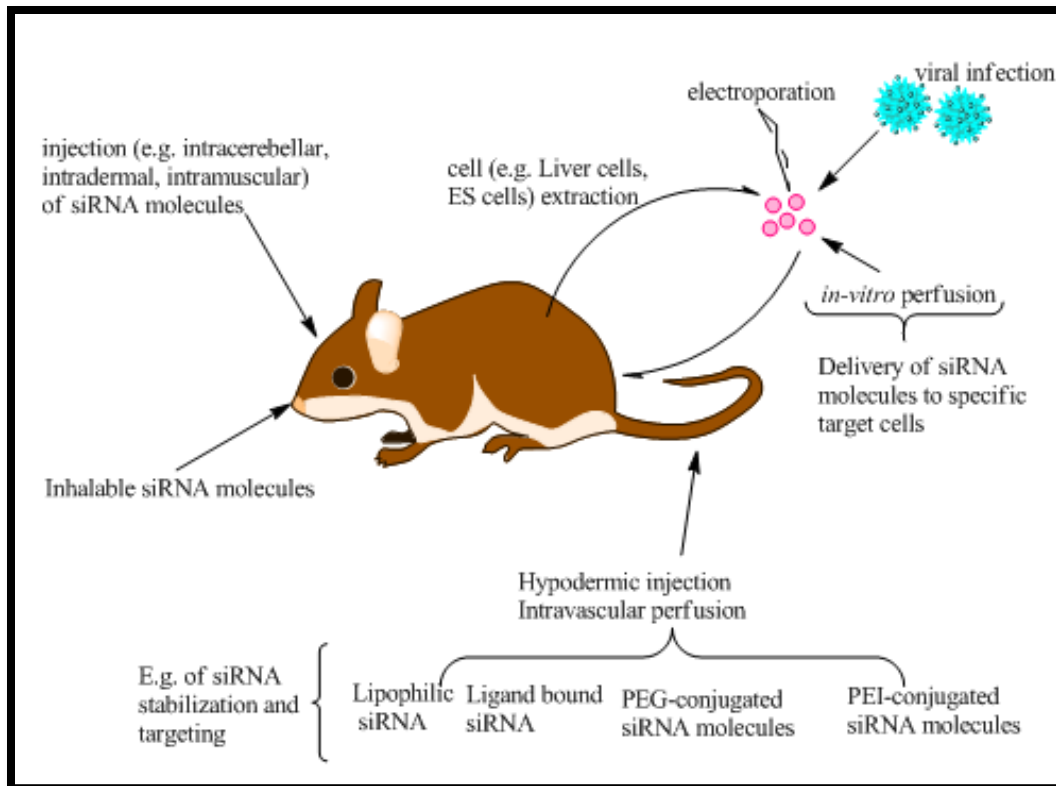
and other genes can bring about off-target silencing.<sup>40</sup> Moreover, the metabolic stability of the native siRNAs in biological media is poor, thereby minimizing its therapeutic index. This is especially the case in all types of RNA applications (*vs.* DNA) in biology and medicine. RNA contains a 2'-hydroxyl group which directs intramolecular transesterification and hydrolysis of the vicinal phosphodiester bond leading to RNA isomerization and degradation during acidic, alkaline and enzyme catalyzed conditions (**Figure 1.2**).<sup>41</sup> Direct cellular introduction of siRNAs results in transient gene silencing effects due to rapid degradation and renal clearance by endogenous serum ribonucleases (RNases) within 36-48 hours following siRNA transfection.<sup>42</sup>



**Figure 1.2.** RNA isomerization and cleavage steps during chemical and enzyme-catalyzed reactions.



Perhaps the most important obstacle to overcome for the clinical application of RNAi is the aspect of siRNA delivery. siRNAs are negatively charged as a result of their phosphate diester backbone. Moreover, they are bulky in size compared to small molecules, and consequently, siRNAs cannot penetrate the cell membrane by conventional diffusion. In order to facilitate siRNA cellular uptake, (transfection) vectors must have the ability to effectively condense (package) siRNA and penetrate the amphiphilic lipid bilayer for efficient intracellular penetration and cytosolic release of siRNA for RNAi action.<sup>43</sup> In order to fulfill these criteria, transfection vectors must: a) be non-toxic and bio-compatible, b) condense siRNA efficiently, c) prevent siRNA degradation during circulation, d) deliver siRNA to target sites and avoid off-target gene silencing, e) enhance uptake in cells and endosomal release once cell internalized, and f) facilitate the release of metabolically stable siRNAs to initiate potent RNAi effects. For example, in mouse studies, hydrodynamic injections of siRNA into the tail vein achieves the best RNAi responses (**Figure 1.3**).<sup>44</sup> However, these studies also indicated that the delivered siRNAs in mice spread to various tissues including the liver and kidneys, resulting in aberrant gene silencing effects and cytotoxicities.



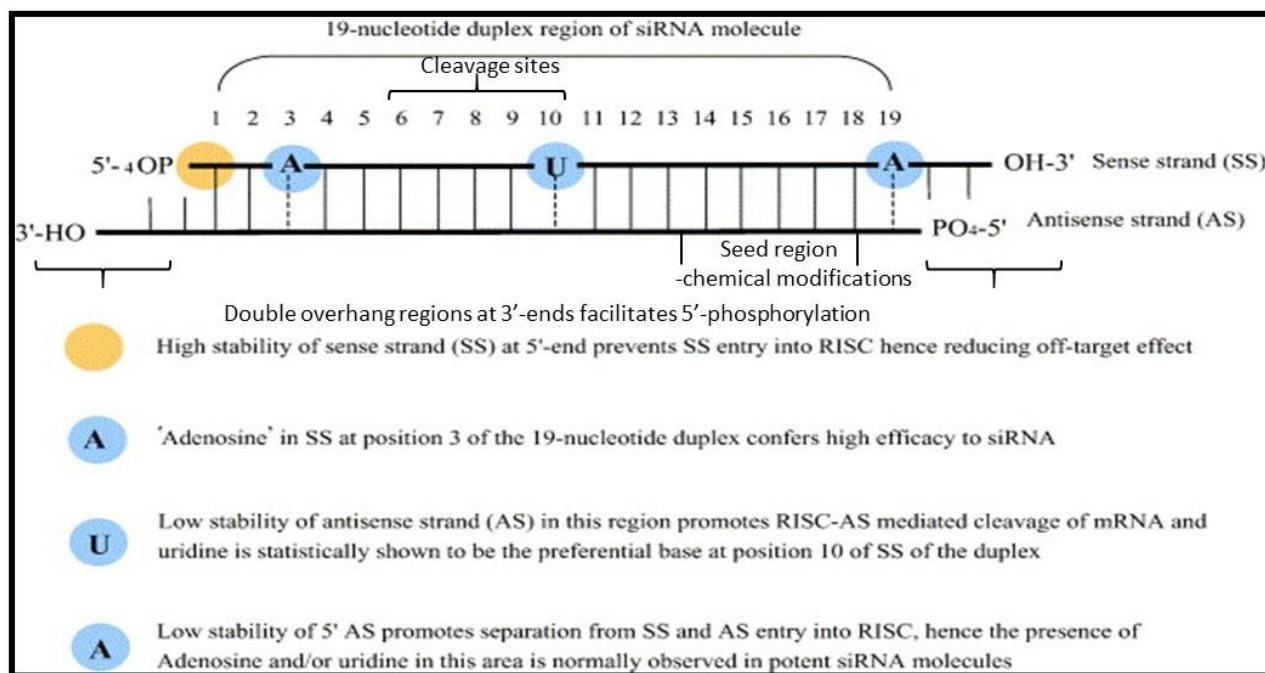
**Figure 1.3.** Methods of RNAi delivery *in vivo*.<sup>44</sup>

Therefore, for safe and effective RNAi applications in humans, several limitations must be addressed.

#### 1.4 CURRENT METHODS FOR RNAi APPLICATION IN ONCOLOGY

In an effort to address the drawbacks plaguing RNAi in the clinical settings, a series of improvements have been developed.<sup>45</sup> Firstly, the design of the siRNAs have evolved from the native siRNA sequences (short 18-21 base-pairs dsRNAs) to those which retain important features for enhanced siRNA stability and activity. These include the 3'-overhang regions which facilitate the incorporation of phosphate groups at the 5'-ends by intracellular kinases, activating the siRNAs for assembly into RISC. Moreover, the site specific incorporation of adenosine and uridine base-pairs facilitates siRNA strand separation within the active site of RISC for mRNA recruitment and processing activity. Moreover, the site-specific incorporation of modified RNA,

namely the 2'-OMe RNA, within the seed region of the antisense siRNA strand have been shown to improve siRNA metabolic stability while minimizing off-target gene silencing effects and immunostimulatory activity (**Figure 1.4**).

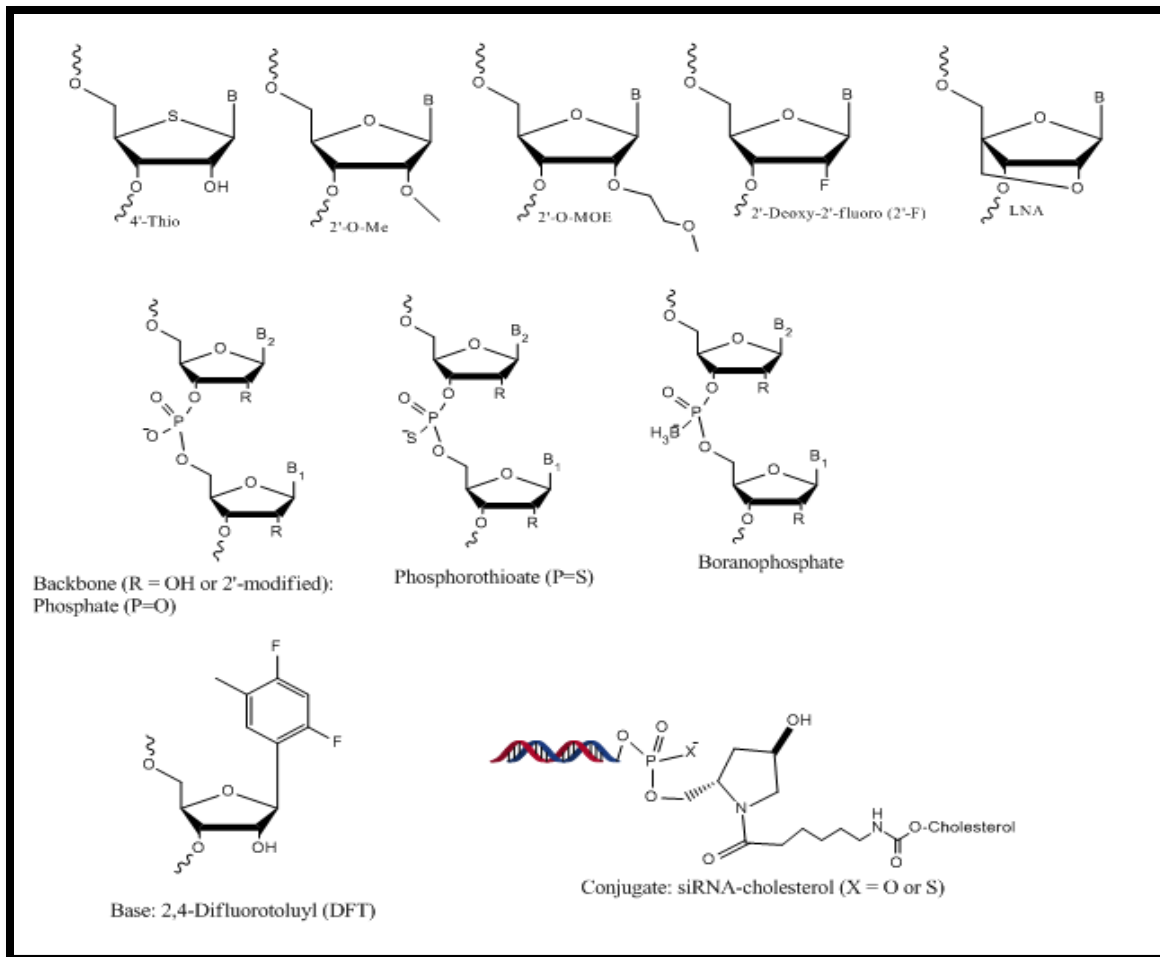


**Figure 1.4.** Design of effective siRNAs for clinical RNAi application<sup>43-45</sup>

The selected siRNAs are also screened against other gene targets to determine sequence homology that may lead to off-target gene silencing effects. For example, selected siRNAs (19-22 base pairs), are typically rich in guanosine-cytosine (GC) content, to stabilize siRNA duplex formation while minimizing RNA self-folding or binding to non-specific mRNA targets.<sup>46</sup> Computer algorithms such as, AsiDesigner, used in conjunction with BLAST and FASTA may help design the optimal siRNA candidates.<sup>47</sup>

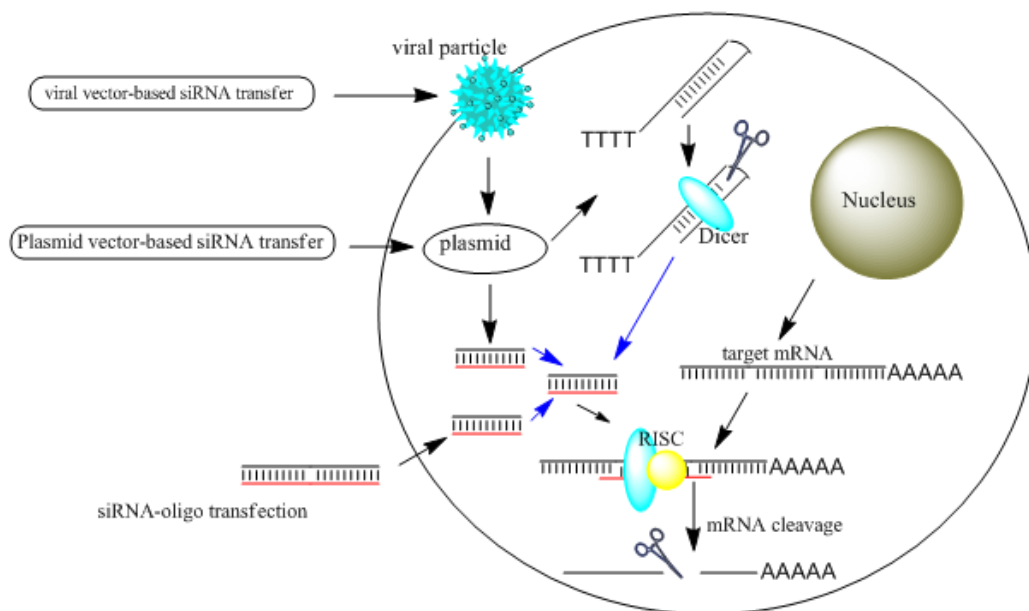
The rise and development of automated solid-phase RNA synthesis<sup>48</sup> has led to the rapid production of chemically derived siRNAs (**Figure 1.5**).<sup>49</sup> Chemical siRNA synthesis allows the incorporation of chemical modification without restriction to alleviate problems associated with

poor nuclease resistance, cell permeability, immunostimulatory activity and off-target gene silencing effects of the native siRNA sequences.<sup>38</sup> For example, bio-conjugation of siRNA with lipophilic molecules such as palmitic acid and cholesterol enables siRNA permeability in HeLa cells and potent anti-tumor effects *in-vivo*.<sup>50</sup> Chemical modification of the 2'-position of the ribose sugar has also been shown to enhance resistance against RNase degradation, while increasing the half-life of modified siRNA in the cytosol leading to a more effective therapeutic index.<sup>40</sup> Modification of the phosphodiester backbone to boranophosphate siRNA has also translated to beneficial RNAi effects, including gene silencing activity in HeLa cells for up to one week due to the enhanced metabolic stability of the backbone modified siRNAs.<sup>51</sup>



**Figure 1.5.** Chemically modified siRNAs and their bioconjugation with lipid moieties.<sup>38,40,49-51</sup>

To realize the full potential of synthetic siRNA in clinical applications of oncology, effective, bio-compatible and safe means of administration are necessary.<sup>4,36,38</sup> Currently, transfection methods for the tissue penetration and intracellular localization of siRNAs are divided into two categories; those belonging to the viral and non-viral delivery systems (**Figure 1.6**).



**Figure 1.6.** siRNA transfection methods for triggering RNAi in mammalian cells.<sup>4</sup>

Viral transduction methods for siRNA gene silencing applications are typically applied with inoculated viruses whose capsid is filled with the siRNA component for specific administration at the localized tumor tissue site.<sup>52</sup> The viral delivery systems (**Table 1.3**) are based on non-pathogenic strains of the Adenovirus, Lentivirus and Herpes Simplex Virus (HSV). In spite of their promising potential in oncologic gene therapy applications<sup>53</sup>, viral transduction methods are still hindered by some serious drawbacks, including those associated with a lack of tumor-target specificity, low siRNA transfer efficiency, and increased risk of cytotoxicity due to the infectious potential of the viral carrier.<sup>4,52</sup> Consequently, greater attention to non-viral siRNA transfection methods has gained widespread practice in cancer gene therapy applications.<sup>54</sup>

Non-viral transfection agents are typically synthetic poly(cationic) amphiphiles that have the dual bio-activity of condensing siRNA, due to favorable ionic interactions, and penetrating the cell surface plasma membrane through necessary amphipathic interactions.<sup>54</sup> Typically, the

siRNA:transfection agent internalizes within the cell by budding from the lipid bilayer through endosome formation and subsequent siRNA release occurs in the cytosol for RNAi activity.<sup>55</sup> Since these vectors are synthetic in nature, they have several advantages over viral transduction agents. These include: low cost and ease of production and quality control, bio-compatibility, non-immunogenic and non-cytotoxic, and high siRNA uptake and release at the target tissue site for effective RNAi application.<sup>54</sup> Fruitful examples of non-viral transfection agents in siRNA oncogene therapy include the use of cationic lipids, cell penetrating peptides, cationic polymers, dendrimers and the cancer-targeting peptides (**Table 1.3**). Polyethyleneimine, (PEI) is a cationic polymer that has been used to transfect siRNAs targeting the HER-2 receptor in breast cancer cells and in tumor-bearing mice with full bioactivity at completely nontoxic concentrations.<sup>56</sup> A poly(ethyleneglycol) PEG-grafted monolamellar liposome in complex with siRNA generates a stabilized nucleic acid lipid particle, SNALP™, that has been commercialized by Tekmira Pharmaceuticals for siRNA applications, albeit with limited success due to the poor cell permeability properties of PEG and accelerated blood clearance *in-vivo*.<sup>57</sup> Poly(cationic) hyperbranched molecules, dendrimers, such as those belonging to the poly(amidoamines) (PAMAM) and poly(lysines) have also been utilized as siRNA transfection agents.<sup>43</sup> Cell penetrating peptides (CPPs) containing basic amino acid residues such as His, Lys and Arg have also been employed as delivery vehicles for siRNA cell internalization in cancer cells types including HeLa and Neuro2A neuroblastoma cancer cells.<sup>58</sup>

The application of peptides in siRNA delivery is especially attractive due to the biological nature of the transfection reagent. These may provide enhanced bio-compatibility and reduced cytotoxicities relative to the synthetic polymers. Moreover, the rise of automated solid-phase peptide synthesis has provided a quick and efficient synthetic alternative for the

production of biologically active CPPs in bulk quantities (mg-g scales) for *in-vivo* siRNA application.<sup>59</sup> In spite of their promising potential, CPP and the synthetic poly(cationic) polymers remain devoid of cancer cell targeting capabilities, thereby dispersing in all tissues leading to aberrant gene knockdown effects and toxicity.<sup>60</sup> In order to overcome this limitation in oncogene therapy applications, cancer-targeting peptides, CTPs, have been identified through combinatorial solid-phase peptide synthesis and screening against cancer cell surface receptor targets<sup>61</sup>, or by phage display bio-panning methods that have facilitated the identification of short peptide ligands of tumor cell surface receptors.<sup>62</sup> Thus, CTPs have been employed to selectively deliver cytotoxic anti-cancer drugs and siRNAs for targeted anti-cancer applications.<sup>63</sup> Moreover, combination approaches employing anti-cancer drugs and siRNAs targeting cancer cell surface antigens have demonstrated the most success and promise in translating cancer therapy from pre-clinical to clinical settings.<sup>18,24,37</sup>

**Table 1.3.** siRNA delivery systems in RNAi oncogene therapy as modified from Uchino et al.<sup>36</sup>

Delivery	Tissue	Route	RNA
<b>Viral vector</b>			
Adenovirus	Brain	ICV	AT1a, AT1b shRNA <sup>64</sup>
Adenovirus	Muscles	IM	Anti-VEGF cluster <sup>65</sup> miRNA
Lentivirus	Brain	Intrastriatal	mHTT shRNA <sup>66</sup>
Lentivirus	Spinal cord	Intraspinal	SOD1 shRNA <sup>67</sup>
Herpes simplex virus	Dorsal root ganglia	Injection into the sciatic nerve	Trpv1 shRNA <sup>68</sup>
	Glioma	IT	EGFR shRNA <sup>69</sup>
<b>Non-viral vector</b>			
Oligofectamine	Colon cancer	IP/IV	B-catenin siRNA <sup>70</sup>
DOTAP	Liver, spleen	IV	GFP siRNA <sup>71</sup>
LIC-101	Liver metastasis	IV/SC	BCL-2 siRNA <sup>72</sup>



PEI	Ovarian cancer	IP/SC	HER-2 siRNA <sup>73</sup>
	Glioblastoma	IP/SC	PTN siRNA <sup>74</sup>
<b>Nanoparticle</b>			
SNALP	Ebola virus	IP/SC	ZEBOV siRNA <sup>75</sup>
	Lung cancer	IV	miR-34a/let-7 <sup>76</sup>
RONDEL	Melanoma	IV	RRM2 siRNA <sup>77</sup>
	Ewing's sarcoma	IV	EWS-FLI 1 siRNA <sup>78</sup>
AtuPLEX	Prostate/pancreatic	IV	PKN3 siRNA <sup>79</sup>
DOTAP, cholesterol and PEG	Melanoma	IV	c-Myc/MDM2/VEGF siRNA and miR-34a <sup>80</sup>
Atelocollagen	Testicular cancer	IT	HST-1/FGF-4 siRNA <sup>81</sup>
	Osteosarcoma	IV	miR-143 <sup>82</sup>
	Prostate cancer		miR-16 <sup>83</sup>
HDI	Liver	IV	HBV siRNA <sup>84</sup>
Carbon nanotube	Brain	Into the cerebral cortex	Caspase-3 <sup>85</sup>

## 1.5 THESIS OBJECTIVES

In spite of the growing number of siRNA applications in oncology, there remain few successful examples that have translated from the pre-clinical to clinical settings. Thus, there's still an unmet need to develop more potent siRNA constructs and efficacious delivery systems in oncogene therapy. In an attempt to improve the oncogene silencing efficacy of siRNAs, Chapter 2 describes the semi-automated solid-phase synthesis of linear, branch and hyperbranch siRNAs targeting Glucose Regulated Protein of 78 kiloDalton (GRP78) expression. GRP78 is a biological marker in tumors, typically found over-expressed and cell surface localized on a variety of cancer cell types. The branch siRNA motifs were designed to contain the sense and antisense strands embedded within the same molecular structure to favor duplex stability. While, the hyperbranch siRNAs contain multiple siRNA sequences, targeting single or multiple sites of

GRP78 mRNA for a synergistic gene silencing effect. The ability to silence multiple oncogene sites with hyperbranch siRNAs provides a method for rapidly screening oncogene sequences and enhancing the mRNA silencing effect in our gene therapy strategy. Their synthesis is reliant on the incorporation of a branch point nucleotide that may direct the chemical synthesis of the higher-order branch and hyperbranch siRNAs on solid-phase. Methods and characterization data for the branch point nucleotide and novel GRP78-targeting siRNA sequences are described in Chapter 2.

Following siRNA synthesis and characterization, Chapter 3 describes their bio-physical and structural properties. The fruitful application of siRNAs in the RNAi technology is dependent on the formation of stable siRNA hybrids in aqueous media that can adopt the prerequisite A-type helix for biological activity. Thermal denaturation and structural studies using UV-Vis and CD Spectroscopy, respectively, were used to identify the suitability of the siRNA constructs for the RNAi application. Interestingly, branch and hyperbranch siRNAs maintained the required hybrid stability and A-type helix for potential RNAi activity.

In collaboration with Brittany Blackman and Christopher Parronchi, MSc and BSc students researching in the lab of Dr. Allan D. Blake, the RNAi activity of the siRNA constructs was evaluated in HepG2 liver cancer cells. The siRNAs were found to elicit effective silencing of GRP78 expression (50-60%) while stimulating modest effects on cancer cell death (~15%). The biological assays and results are discussed in Chapter 4, which highlights the suitability of the novel branch and hyperbranch siRNAs in RNAi applications. Attempts to extrapolate their full anti-cancer potential are also discussed in Chapter 5, by combining the siRNAs with CTPs targeting cell surface GRP78 expression on HepG2 liver cancer cells. The CTPs described in this study were made and characterized by Stesha Joseph, a PhD student researching in the lab of Dr.

David Sabatino. The structural analyses of the CTP:siRNA complexes were partly contributed by Reeta Yadav, a PhD student researching in the lab of Dr. Uri Samuni, Queens College. Taken together, these preliminary results will highlight the first steps towards the development of a fruitful cancer-targeting gene therapy approach.

## 1.6 REFERENCES

1. Rossi, J.J.; Kim, D.H. Strategies for Silencing Human Diseases using RNA Interference (RNAi) *Nature* **2007**, *8*, 173-184.
2. Napoli, C.; Lemieux, C.; Jorgensen, R. Introduction of a Chimeric Chalcone Synthase Gene into Petunia Results in Reversible Co-Suppression of Homologous Genes in trans. *Plant Cell* **1990**, *2*, 279-289.
3. (a) Fire, A.; Xu, S.; Montgomery, M. K.; Kostas, S. A.; Driver, S. E.; Mello, C. C., Potent and specific genetic interference by double-stranded RNA in *Caenorhabditis elegans*. *Nature* **1998**, *391*, 806-811, (b) Mello, C. C.; Conte, D., Revealing the world of RNA interference. *Nature* **2004**, *431*, 338-342.
4. Masiero, M.; Nardo, G.; Indraccolo, S.; Favaro, E., RNA interference: Implications for cancer treatment. *Mol. Aspects Med.* **2007**, *28*, 143-166.
5. Brummelkamp, T. R.; Bernards, R.; Agami, R., Stable suppression of tumorigenicity by virus-mediated RNA interference. *Cancer cell* **2002**, *2* (3), 243-247. (b) Yang, G.; Thompson, J. A.; Fang, B.; Liu, J., Silencing of H-ras gene expression by retrovirus-mediated siRNA decreases transformation efficiency and tumorgrowth in a model of human ovarian cancer. *Oncogene* **2003**, *22*, 5694-5701.
6. Eskandarpour, M.; Kiaii, S.; Zhu, C.; Castro, J.; Sakko, A. J.; Hansson, J., Suppression of oncogenic NRAS by RNA interference induces apoptosis of human melanoma cells. *Int. J. Cancer* **2005**, *115*, 65-73.
7. Hingorani, S. R.; Jacobetz, M. A.; Robertson, G. P.; Herlyn, M.; Tuveson, D. A., Suppression of BRAFV599E in Human Melanoma Abrogates Transformation. *Cancer Res* **2003**, *63* (17), 5198-5202.
8. Pal, A.; Ahmad, A.; Khan S.; Sakabe, I.; Zhang, C.; Kasid, U.N. Ahmad, I. Systemic delivery of Raf siRNA using cationic cardiolipin liposomes silences Raf-1 expression and inhibits tumor growth in xenograft model of human prostate cancer. *Int. J. Oncol.* **2006**, *26*, 1087-1091.
9. Chien, P.-Y.; Wang, J.; Carbonaro, D.; Lei, S.; Miller, B.; Sheikh, S.; Ali, S. M.; Ahmad, M. U.; Ahmad, I., Novel cationic cardiolipin analogue-based liposome for efficient DNA and small interfering RNA delivery in vitro and in vivo. *Cancer Gene Ther* **2004**, *12* (3), 321-328.

10. Withey, J. M.; Marley, S. B.; Kaeda, J.; Harvey, A. J.; Crompton, M. R.; Gordon, M. Y., Targeting primary human leukaemia cells with RNA interference: Bcr-Abl targeting inhibits myeloid progenitor self-renewal in chronic myeloid leukaemia cells. *Br. J. Haematol.* **2005**, *129*, 377-380.
11. Verma, U. N.; Surabhi, R. M.; Schmaltieg, A.; Becerra, C.; Gaynor, R. B., Small Interfering RNAs Directed against  $\beta$ -Catenin Inhibit the in Vitro and in Vivo Growth of Colon Cancer Cells. *Clin. Cancer Res.* **2003**, *9*, 1291-1300.
12. Wang, Y.-h.; Liu, S.; Zhang, G.; Zhou, C.-q.; Zhu, H.-x.; Zhou, X.-b.; Quan, L.-p.; Bai, J.-f.; Xu, N.-z., Knockdown of c-Myc expression by RNAi inhibits MCF-7 breast tumor cells growth in vitro and in vivo. *Breast Cancer Res.* **2005**, *7*, R220 - R228.
13. Zhang, X.; Kon, T.; Wang, H.; Li, F.; Huang, Q.; Rabbani, Z. N.; Kirkpatrick, J. P.; Vujaskovic, Z.; Dewhirst, M. W.; Li, C.-Y., Enhancement of Hypoxia-Induced Tumor Cell Death In vitro and Radiation Therapy In vivo by Use of Small Interfering RNA Targeted to Hypoxia-Inducible Factor-1 $\alpha$ . *Cancer Res.* **2004**, *64*, 8139-8142.
14. Li, L.; Lin, X.; Staver, M.; Shoemaker, A.; Semizarov, D.; Fesik, S. W.; Shen, Y., Evaluating Hypoxia-Inducible Factor-1 $\alpha$  as a Cancer Therapeutic Target via Inducible RNA Interference In vivo. *Cancer Res.* **2005**, *65*, 7249-7258.
15. Yano, J.; Hirabayashi, K.; Nakagawa, S.-i.; Yamaguchi, T.; Nogawa, M.; Kashimori, I.; Naito, H.; Kitagawa, H.; Ishiyama, K.; Ohgi, T.; Irimura, T., Antitumor Activity of Small Interfering RNA/Cationic Liposome Complex in Mouse Models of Cancer. *Clin. Cancer Res.* **2004**, *10*, 7721-7726.
16. Wang, Y.; Zhu, H.; Quan, L.; Bai, J.; Zhang, G.; Zhan, Q.; Xu, N., Downregulation of survivin by RNAi inhibits the growth of esophageal carcinoma cells. *Cancer Biol. Ther.* **2005**, *4*, 974-978.
17. Uchida, H.; Tanaka, T.; Sasaki, K.; Kato, K.; Dehari, H.; Ito, Y.; Kobune, M.; Miyagishi, M.; Taira, K.; Tahara, H.; Hamada, H., Adenovirus-Mediated Transfer of siRNA against Survivin Induced Apoptosis and Attenuated Tumor Cell Growth in Vitro and in Vivo. *Mol Ther.* **2004**, *10*, 162-171.
18. Lima, R. T.; Martins, L. M.; Guimaraes, J. E.; Sambade, C.; Vasconcelos, M. H., Specific downregulation of bcl-2 and xIAP by RNAi enhances the effects of chemotherapeutic agents in MCF-7 human breast cancer cells. *Cancer Gene Ther.* **2004**, *11*, 309-316.

19. Hanahan, D.; Weinberg, R.A. Hallmarks of Cancer: The Next Generation. *Cell* **2011**, *144*, 646-20.
20. Kepp, O., Galluzzi, L., Lipinski, M., Yuan, J.; Kroemer, G. Cell death assays for drug discovery. *Nature Rev. Drug Discovery* **2011**, *10*, 221.
21. Campisi, J; d'Adda di Fagagna, F. Cellular senescence: when bad things happen to good cells. *Nat. Rev. Mol. Cell Biol.* **2007**, *8*, 729-740
22. DuPree, E. L.; Mazumder, S.; Almasan, A., Genotoxic Stress Induces Expression of E2F4, Leading to Its Association with p130 in Prostate Carcinoma Cells. *Cancer Res.* **2004**, *64*, 4390-4393.
23. Yamato, K.; Fen, J.; Kobuchi, H.; Nasu, Y.; Yamada, T.; Nishihara, T.; Ikeda, Y.; Kizaki, M.; Yoshinouchi, M., Induction of cell death in human papillomavirus 18-positive cervical cancer cells by E6 siRNA. *Cancer Gene Ther* **2005**, *13*, 234-241.
24. Yuan, J.; Kramer, A.; Matthess, Y.; Yan, R.; Spankuch, B.; Gatje, R.; Knecht, R.; Kaufmann, M.; Strebhardt, K., Stable gene silencing of cyclin B1 in tumor cells increases susceptibility to taxol and leads to growth arrest in vivo. *Oncogene* **2005**, *25*, 1753-1762.
25. Li, S.; Crothers, J.; Haqq, C. M.; Blackburn, E. H., Cellular and Gene Expression Responses Involved in the Rapid Growth Inhibition of Human Cancer Cells by RNA Interference-mediated Depletion of Telomerase RNA. *J. Biol. Chem.* **2005**, *280*, 23709-23717.
26. Zou, L.; Zhang, P.; Luo, C.; Tu, Z., shRNA-targeted hTERT suppress cell proliferation of bladder cancer by inhibiting telomerase activity. *Cancer Chemother. Pharmacol.* **2006**, *57*, 328-334.
27. Guan, H.; Zhou, Z.; Wang, H.; Jia, S.-F.; Liu, W.; Kleinerman, E. S., A Small Interfering RNA Targeting Vascular Endothelial Growth Factor Inhibits Ewing's Sarcoma Growth in a Xenograft Mouse Model. *Clin. Cancer Res.* **2005**, *11*, 2662-2669.
28. Shen, H.-L.; Xu, W.; Wu, Z.-Y.; Zhou, L.-L.; Qin, R.-J.; Tang, H.-R., Vector-based RNAi approach to isoform-specific downregulation of vascular endothelial growth factor (VEGF)<sub>165</sub> expression in human leukemia cells. *Leuk. Res.* **2007**, *31*, 515-521.
29. Santel, A.; Aleku, M.; Keil, O.; Endruschat, J.; Esche, V.; Durieux, B.; Loffler, K.; Fechtner, M.; Rohl, T.; Fisch, G.; Dames, S.; Arnold, W.; Giese, K.; Klippel, A.;

- Kaufmann, J., RNA interference in the mouse vascular endothelium by systemic administration of siRNA-lipoplexes for cancer therapy. *Gene Ther.* **2006**, *13*, 1360-1370.
30. Pille, J. Y.; Denoyelle, C.; Varet, J.; Bertrand, J. R.; Soria, J.; Opolon, P.; Lu, H.; Pritchard, L. L.; Vannier, J. P.; Malvy, C.; Soria, C.; Li, H., Anti-RhoA and Anti-RhoC siRNAs Inhibit the Proliferation and Invasiveness of MDA-MB-231 Breast Cancer Cells in Vitro and in Vivo. *Mol. Ther.* **2005**, *11*, 267-274.
31. Liang, Z.; Yoon, Y.; Votaw, J.; Goodman, M. M.; Williams, L.; Shim, H., Silencing of CXCR4 Blocks Breast Cancer Metastasis. *Cancer Res.* **2005**, *65*, 967-971.
32. Krishna, R.; Mayer, L.D. Multidrug resistance (MDR) in cancer. Mechanisms, reversal using modulators of MDR and the role of MDR modulators in influencing the pharmacokinetics of anticancer drugs. *Eur. J. Pharm. Sci.* **2000**, *11*, 265-283.
33. Lehne, G. P-glycoprotein as a drug target in the treatment of multi-drug resistant cancer. *Curr. Drug Targets* **2000**, *1*, 85-99.
34. Nieth, C.; Priebisch, A.; Stege, A.; Lage, H., Modulation of the classical multidrug resistance (MDR) phenotype by RNA interference (RNAi). *FEBS Lett.* **2003**, *545*, 144-150.
35. Hua, J.; Mutch, D. G.; Herzog, T. J., Stable suppression of MDR-1 gene using siRNA expression vector to reverse drug resistance in a human uterine sarcoma cell line. *Gynecol. Oncol.* **2005**, *98*, 31-38.
36. Uchino, K.; Ochiya, T.; Takeshita, F., RNAi Therapeutics and Applications of MicroRNAs in Cancer Treatment. *Jpn. J. Clin. Oncol.* **2013**, *43*, 596-607.
37. Taberero, J.; Shapiro, G.I.; LoRusso, P.M.; Cervantes, A.; Schwartz, G.K.; Weiss, G.J.; Paz-Ares, L.; Cho, D.C.; Infante, J.R.; Alsina, M.; Gounder, M.M.; Falzone, R.; Harrop, J.; White, A.C.; Toudjarska, I.; Bumcrot, D.; Meyers, R.E.; Hinkle, G.; Svrzikapa, N.; Hutabarat, R.M.; Clausen, V.A.; Cehelsky, J.; Nochur, S.V.; Gamba-Vitalo, C.; Vaishnav, A.K.; Sah, D.W.; Gollob, J.A.; Burris, H.A. 3rd First-in-humans trial of an RNA interference therapeutic targeting VEGF and KSP in cancer patients with liver involvement. *Cancer Discov.* **2013**, *3*, 406-417.
38. Bumcrot, D.; Manoharan, M.; Kotliansky, V.; Sah, D. W. Y., RNAi therapeutics: a potential new class of pharmaceutical drugs. *Nat Chem Biol* **2006**, *2*, 711-719.

39. Gantier, M.P. Strategies for designing and validating immunostimulatory siRNAs. *Meth. Mol. Biol.* **2013**, *942*, 179-191.
40. Jackson, A. L., Burchard, J., Leake, D., Reynolds, A., Schelter, J., Guo, J., Johnson, J.M., Lim, L., Karpilow, J., Nichols, K., Marshall, W., Khvorova, A., Linsley, P.S., , Position-specific chemical modification of siRNAs reduces “off-target” transcript silencing. *RNA* **2006**, *12*, 1197-1205.
41. Lonnberg, H. Cleavage of RNA phosphodiester bonds by small molecule entitites: a mechanistic insight. *Org. Biomol. Chem.* **2011**, *9*, 1687-1703.
42. Ryther, R. C. C.; Flynt, A. S.; Phillips, J. A.; Patton, J. G., siRNA therapeutics: big potential from small RNAs. *Gene Ther* **2004**, *12*, 5-11.
43. Wu, J.; Huang, W.; He, Z., Dendrimers as Carriers for siRNA Delivery and Gene Silencing: A Review. *The Scientific World Journal* **2013**, 1-17.
44. Leung, R. K. M.; Whittaker, P. A., RNA interference: From gene silencing to gene-specific therapeutics. *Pharmacol. Ther.* **2005**, *107*, 222-239.
45. Keaney, J.; Campbell, M.; Humphries, P. From RNA interference technology to effective therapy: how far have we come and how far to go? *Ther. Deliv.* **2011**, *2*, 1395-1406.
46. 47. Fellmann, C.; Lowe, S.W. Stable RNA interference rules for silencing. *Nat. Cell Biol.* **2013**, *16*, 10.
47. Park, Y-K.; Park, S-M.; Choi, Y-C.; Lee, D.; Won, M.; Kim, Y.J. Asi-Designer: exon based siRNA designer server considering alternative splicing. *Nucleic Acids Res.* **2008**, *36*, W97-W103.
48. Usman, N.; Pon, R.T.; Ogilvie, K.K. Preparation of ribonucleosides 3-O-phosphoramidites and their application to the automated solid-phase synthesis of oligonucleotides. *Tetrahedron Lett.* **1985**, *26*, 4567-4570.
49. Zlatev, I.; Lackey, J.G.; Zhang, L.; Dell, A.; McRae, K.; Shaikh, S.; Duncan, R.G.; Rajeev K.G.; Manoharan, M. Automated parallel synthesis of 5'-triphosphate oligonucleotides and preparation of chemically modified 5'-triphosphate small interfering RNA. *Bioorg. Med. Chem.* **2013**, *21*, 722-732.
50. 51. Prakash, T.P.; Lima, W.F.; Murray, H.M.; Elbashir, S.; Cantley, W.; Foster, D.; Jayaraman, M.; Chappell, A.E.; Manoharan, M.; Swayze, E.E.; Crooke, S.T.



- lipid Nanoparticles Improve Activity of Single-Stranded siRNA and Gapmer Antisense Oligonucleotides in Animals *ACS Chem. Biol.* **2013**, *8*, 1402-1406.
51. Hall, A.H.; Wan, J.; Spesock, A.; Sergueeva, Z.; Shaw, B.R.; Alexander, K.A. High potency silencing by single-stranded boranophosphate siRNA. *Nucleic Acids Res.* **2006**, *34*, 2773-2781.
52. Thomas, C. E.; Ehrhardt, A.; Kay, M. A., Progress and problems with the use of viral vectors for gene therapy. *Nat. Rev. Genet* **2003**, *4*, 346-358.
53. Park, M.Y.; Kim, D.R.; Eo, E.Y.; Lim, H.J.; Park, J.S.; Cho, Y.J.; Yoon, H.I.; Lee, J.H.; Lee, C.T. Genetic blockade of insulin-like growth factor-1 receptor via recombinant adenovirus in lung cancer can be enhanced by the histone deacetylase inhibitor, vorinostat. *J. Gene. Med.* **2013**, *15*, 115-122.
54. Jones, C.H.; Chen, C-K; Ravikirshnan, A.; Rane, S.; Pfeifer, B.A. Overcoming non-viral gene delivery barriers: perspective and future. *Mol. Pharmaceutics* **2013**, *10*, 4082-4098.
55. Juliano, R.L.; Ming, X.; Nakagawa, O. Cellular uptake and intracellular trafficking of antisense and siRNA oligonucleotides. *Bioconjug. Chem.* **2012**, *23*, 147-157.
56. Urban-Klein, B.; Werth, S.; Abuharbeid, S.; Czubayko, F.; Aigner, A., RNAi-mediated gene-targeting through systemic application of polyethylenimine (PEI)-complexed siRNA in vivo. *Gene Ther.* **2004**, *12*, 461-466.
57. Gomes-da-Silva, L. C.; Fonseca, N. A.; Moura, V.; Pedroso de Lima, M. C.; Simões, S.; Moreira, J. N., Lipid-Based Nanoparticles for siRNA Delivery in Cancer Therapy: Paradigms and Challenges. *Acc. Chem. Res.* **2012**, *45*, 1163-1171.
58. Chugh, A.; Eudes, F.; Shim, Y-S. Cell-Penetrating Peptides; Nanocarrier for Macromolecule Delivery in Living Cells. *Life* **2010**, *62*, 183-193.
59. Gooding, M.; Browne, L.P.; Quinteiro, F.M.; Selwood, D.L. siRNA delivery: from lipids to cell-penetrating peptides and their mimics. *Chem. Biol. Drug Des.* **2012**, *80*, 787-809.
60. Vives, E. Present and future of cell-penetrating peptide mediated delivery systems: "Is the Trojan horse too wild to go only to Troy" *J. Cont. Rel.* **2005**, *109*, 77.
61. Aina, O.H.; Liu, R.; Sutcliffe, J.L.; Marik, J.; Pan, C.X.; Lam, K.S. From combinatorial chemistry to cancer-targeting peptides. *Mol Pharm.* **2007**, *4*, 631-651.


62. Landon, L.A.; Deutscher, S.L. Combinatorial discovery of tumor targeting peptides using phage display. *J Cell Biochem.* **2003**, *90*, 509-517.
63. Kim, S-W.; Lee, S-H.; Tian, H.; Chen, X.; Park, T.G. Prostate Cancer-Cell Specific VEGF siRNA Delivery System using Cell-Targeting Peptide Conjugated Polyplexes. *J. Drug Target.* **2009**, *17*, 311-317.
64. Chen Y, C. H., Hoffmann A, , Adenovirus-mediated small-interference RNA for in vivo silencing of angiotensin AT1a receptors in mouse brain. *Hypertension* **2006**, *47*, 230-237.
65. Pihlmann, M.; Askou, A. L.; Aagaard, L.; Bruun, G. H.; Svalgaard, J. D.; Holm-Nielsen, M. H.; Dagnæs-Hansen, F.; Bek, T.; Mikkelsen, J. G.; Jensen, T. G.; Corydon, T. J., Adeno-associated virus-delivered polycistronic microRNA-clusters for knockdown of vascular endothelial growth factor in vivo. *J. Gene Med.* **2012**, *14*, 328-338.
66. Rodriguez-Lebron, E.; Denovan-Wright, E. M.; Nash, K.; Lewin, A. S.; Mandel, R. J., Intrastratial rAAV-mediated delivery of anti-huntingtin shRNAs induces partial reversal of disease progression in R6/1 Huntington's disease transgenic mice. *Mol. Ther.* **2005**, *12*, 618-633.
67. Raoul, C.; Abbas-Terki, T.; Bensadoun, J.-C.; Guillot, S.; Haase, G.; Szulc, J.; Henderson, C. E.; Aebischer, P., Lentiviral-mediated silencing of SOD1 through RNA interference retards disease onset and progression in a mouse model of ALS. *Nat. Med.* **2005**, *11*, 423-428.
68. Anesti, A.-M.; Peeters, P. J.; Royaux, I.; Coffin, R. S., Efficient delivery of RNA Interference to peripheral neurons in vivo using herpes simplex virus. *Nucleic Acids Res.* **2008**, *36*, e86.
69. Saydam, O.; Glauser, D. L.; Heid, I.; Turkeri, G.; Hilbe, M.; Jacobs, A. H.; Ackermann, M.; Fraefel, C., Herpes Simplex Virus 1 Amplicon Vector-Mediated siRNA Targeting Epidermal Growth Factor Receptor Inhibits Growth of Human Glioma Cells in Vivo. *Mol. Ther.* **2005**, *12*, 803-812.
70. Verma, U. N.; Surabhi, R. M.; Schmaltieg, A.; Becerra, C.; Gaynor, R. B., Small Interfering RNAs Directed against  $\beta$ -Catenin Inhibit the in Vitro and in Vivo Growth of Colon Cancer Cells. *Clin. Cancer Res.* **2003**, *9*, 1291-1300.
71. Sørensen, D. R.; Leirdal, M.; Sioud, M., Gene Silencing by Systemic Delivery of Synthetic siRNAs in Adult Mice. *J. Mol. Biol.* **2003**, *327*, 761-766.

72. Yano, J.; Hirabayashi, K.; Nakagawa, S.-i.; Yamaguchi, T.; Nogawa, M.; Kashimori, I.; Naito, H.; Kitagawa, H.; Ishiyama, K.; Ohgi, T.; Irimura, T., Antitumor Activity of Small Interfering RNA/Cationic Liposome Complex in Mouse Models of Cancer. *Clin. Cancer Res.* **2004**, *10*, 7721-7726.
73. Urban-Klein, B.; Werth, S.; Abuharbeid, S.; Czubayko, F.; Aigner, A., RNAi-mediated gene-targeting through systemic application of polyethylenimine (PEI)-complexed siRNA in vivo. *Gene Ther.* **2004**, *12*, 461-466.
74. Marius Grzelinski, B. U.-K., Tobias Martens, Katrin Lamszus, Udo Bakowsky, Sabrina Höbel, Frank Czubayko, Achim Aigner, RNA interference-mediated gene silencing of pleiotrophin through polyethylenimine-complexed smallinterferingRNAs in vivo exerts antitumoral effects in glioblastoma xenografts. *Human Gene Ther.* **2006**, *17*, 751-766.
75. Geisbert, T. W.; Hensley, L. E.; Kagan, E.; Yu, E. Z.; Geisbert, J. B.; Daddario-DiCaprio, K.; Fritz, E. A.; Jahrling, P. B.; McClintock, K.; Phelps, J. R.; Lee, A. C. H.; Judge, A.; Jeffs, L. B.; MacLachlan, I., Postexposure Protection of Guinea Pigs against a Lethal Ebola Virus Challenge Is Conferred by RNA Interference. *J. Infect. Dis.* **2006**, *193*, 1650-1657.
76. Trang, P.; Wiggins, J. F.; Daige, C. L.; Cho, C.; Omotola, M.; Brown, D.; Weidhaas, J. B.; Bader, A. G.; Slack, F. J., Systemic Delivery of Tumor Suppressor microRNA Mimics Using a Neutral Lipid Emulsion Inhibits Lung Tumors in Mice. *Mol. Ther.* **2011**, *19*, 1116-1122.
77. Davis, M. E.; Zuckerman, J. E.; Choi, C. H. J.; Seligson, D.; Tolcher, A.; Alabi, C. A.; Yen, Y.; Heidel, J. D.; Ribas, A., Evidence of RNAi in humans from systemically administered siRNA via targeted nanoparticles. *Nature* **2010**, *464*, 1067-1070.
78. Hu-Lieskovan, S.; Heidel, J. D.; Bartlett, D. W.; Davis, M. E.; Triche, T. J., Sequence-Specific Knockdown of EWS-FLI1 by Targeted, Nonviral Delivery of Small Interfering RNA Inhibits Tumor Growth in a Murine Model of Metastatic Ewing's Sarcoma. *Cancer Res.* **2005**, *65*, 8984-8992.
79. Aleku, M.; Schulz, P.; Keil, O.; Santel, A.; Schaeper, U.; Dieckhoff, B.; Janke, O.; Endruschat, J.; Durieux, B.; Röder, N.; Löffler, K.; Lange, C.; Fechtner, M.; Möpert, K.; Fisch, G.; Dames, S.; Arnold, W.; Jochims, K.; Giese, K.; Wiedenmann, B.; Scholz, A.;

- Kaufmann, J., Atu027, a Liposomal Small Interfering RNA Formulation Targeting Protein Kinase N3, Inhibits Cancer Progression. *Cancer Res.* **2008**, *68*, 9788-9798.
80. Chen, Y.; Zhu, X.; Zhang, X.; Liu, B.; Huang, L., Nanoparticles Modified With Tumor-targeting scFv Delivery of siRNA and miRNA for Cancer Therapy. *Mol. Ther.* **2010**, *18*, 1650-1656.
81. Minakuchi, Y.; Takeshita, F.; Kosaka, N.; Sasaki, H.; Yamamoto, Y.; Kouno, M.; Honma, K.; Nagahara, S.; Hanai, K.; Sano, A.; Kato, T.; Terada, M.; Ochiya, T., Atelocollagen-mediated synthetic small interfering RNA delivery for effective gene silencing in vitro and in vivo. *Nucleic Acids Res.* **2004**, *32*, e109.
82. Osaki, M.; Takeshita, F.; Sugimoto, Y.; Kosaka, N.; Yamamoto, Y.; Yoshioka, Y.; Kobayashi, E.; Yamada, T.; Kawai, A.; Inoue, T.; Ito, H.; Oshimura, M.; Ochiya, T., MicroRNA-143 Regulates Human Osteosarcoma Metastasis by Regulating Matrix Metalloprotease-13 Expression. *Mol. Ther.* **2011**, *19*, 1123-1130.
83. Takeshita, F.; Patrawala, L.; Osaki, M.; Takahashi, R.-u.; Yamamoto, Y.; Kosaka, N.; Kawamata, M.; Kelnar, K.; Bader, A. G.; Brown, D.; Ochiya, T., Systemic Delivery of Synthetic MicroRNA-16 Inhibits the Growth of Metastatic Prostate Tumors via Downregulation of Multiple Cell-cycle Genes. *Mol. Ther.* **2009**, *18*, 181-187.
84. Morrissey, D. V.; Blanchard, K.; Shaw, L.; Jensen, K.; Lockridge, J. A.; Dickinson, B.; McSwiggen, J. A.; Vargeese, C.; Bowman, K.; Shaffer, C. S.; Polisky, B. A.; Zinnen, S., Activity of stabilized short interfering RNA in a mouse model of hepatitis B virus replication. *Hepatology* **2005**, *41*, 1349-1356.
85. Al-Jamal, K. T.; Gherardini, L.; Bardi, G.; Nunes, A.; Guo, C.; Bussy, C.; Herrero, M. A.; Bianco, A.; Prato, M.; Kostarelos, K.; Pizzorusso, T., Functional motor recovery from brain ischemic insult by carbon nanotube-mediated siRNA silencing. *Proc. Nat. Acad. Sci.* **2011**, *108*, 10952-10957.

## CHAPTER 2. SYNTHESIS AND CHARACTERIZATION OF LINEAR, BRANCH AND HYPERBRANCH siRNAs.

### 2.1 ABSTRACT

A semi-automated solid phase synthesis method is described in this chapter for the rapid production of linear, branch and hyperbranch siRNAs. The branch and hyperbranch siRNAs are novel constructs disclosed for the first time in this thesis. These siRNAs were designed to improve gene silencing efficacy while expanding the scope of siRNA substrates that may trigger potent RNAi effects *in-vivo*. Significantly, the siRNAs were selected to target the Glucose Regulated Protein of 78 kilodalton (GRP78) mRNA for potent oncogene silencing effects in cancer cells. In this study, a solid phase synthesis method was developed using our Applied Biosystems™ (ABI) 3400 synthesizer (ABI) to yield a small library (17) of siRNAs. The siRNAs consisted of linear, V-shape, Y-branch and  hyperbranch motifs, the latter in which contained multiple siRNAs for synergistic GRP78 silencing effects in a representative tumor cell line. The various branch siRNAs were generated from either 5'-OLV 2'-or 3'-OMMT ribouridine phosphoramidite branchpoint nucleotides, to explore the influence of the branchpoint connectivities on siRNA structure and activity. Furthermore, the incorporation of 2'-OMe inserts within the siRNA sugar-phosphate backbone is proposed to improve efficacy while retaining metabolic stability in biological media. These siRNAs were synthesized in good yields (17-83%) and purities ( $\geq 90\%$ ) following ion pairing reverse-phase HPLC analysis and purification. Furthermore, the identities of the siRNAs were confirmed by molecular weight analyses using electrospray ionization mass spectrometry (ESI-MS, Novatia Inc, Newton PA). Denaturing and

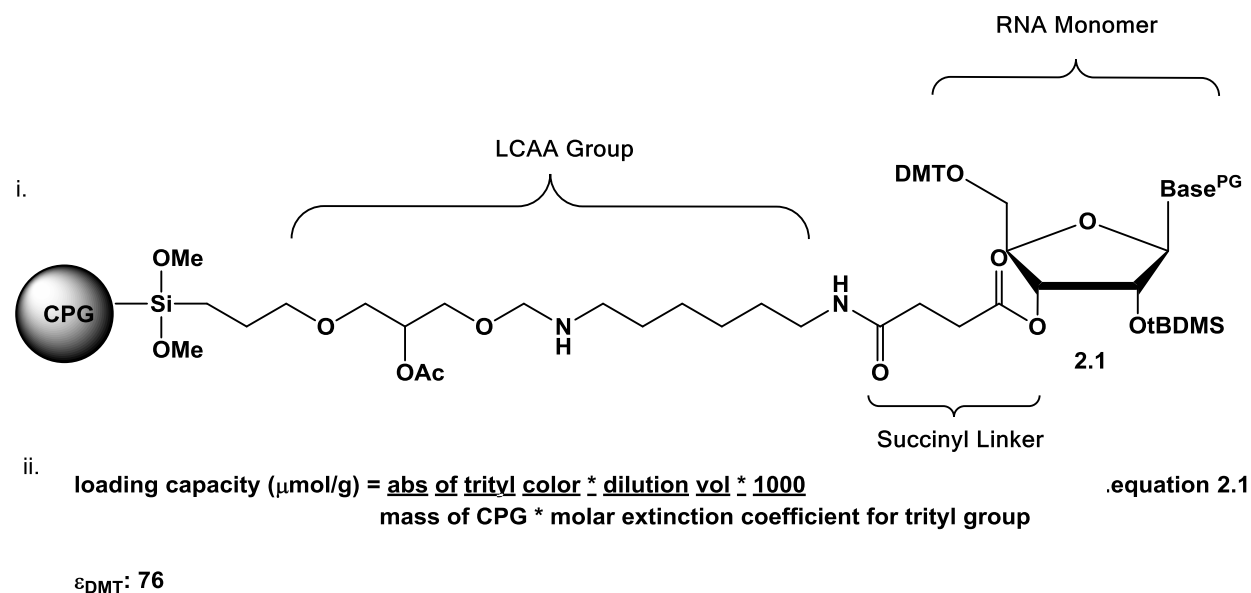
native PAGE were finally used to respectively ascertain sequence purity and hybridization for bio-physical, structural studies and RNAi application.

## 2.2 INTRODUCTION

### 2.2.1 SOLID PHASE RNA SYNTHESIS

The demand for synthetic siRNA has increased rapidly since the discovery of RNAi in order to satisfy applications in high-throughput gene screening and sequencing in addition to gene therapy.<sup>1</sup> Consequently, the rise of solid phase RNA synthesis has led to the rapid production of native and modified siRNAs. At the heart of this synthetic procedure is the use of an insoluble polymer support, initially composed of a divinylbenzene cross-linked polystyrene (DVB-PS).<sup>2</sup> This solid support was optimized<sup>3</sup> and is now composed of controlled pore glass (CPG) with pore sizes ranging from 500-3000 Å. The larger pore sizes facilitate the synthesis of lengthy and complex RNA sequences.<sup>4</sup> The CPG is typically derivatized with long chain alkyl amino (LCAA) groups that facilitate the incorporation of linkers for the attachment of the starting RNA monomer.<sup>3,5</sup> The CPG is typically composed of a 5'-dimethoxytrityl (5'-ODMT) 2'-*tert*-butyldimethylsilyl (2'-OtBDMS) RNA bound to the succinyl linker LCAA CPG solid support (**Figure 2.1, i**). The 5'-ODMT group is acid labile (3% dichloroacetic acid in dichloromethane) and can be deprotected to determine the loading of RNA on the solid support by UV-Vis spectrophotometry (**Figure 2.1, ii**). The loading capacity is also an important component in dictating synthesis yields and efficiencies, with higher loading supports (*i.e.* 80-100 µmol/g) producing more product at the cost of lower synthetic efficiencies.<sup>6</sup> The solid support is used to drive chemical reactions to completion by adding a large excess of reagents, while facilitating post reaction work-up procedures by simple filtrations and washing steps

leaving the RNA bound to the solid support. Thus, the solid support is necessary for generating full length RNA sequences in good crude yields and purities.

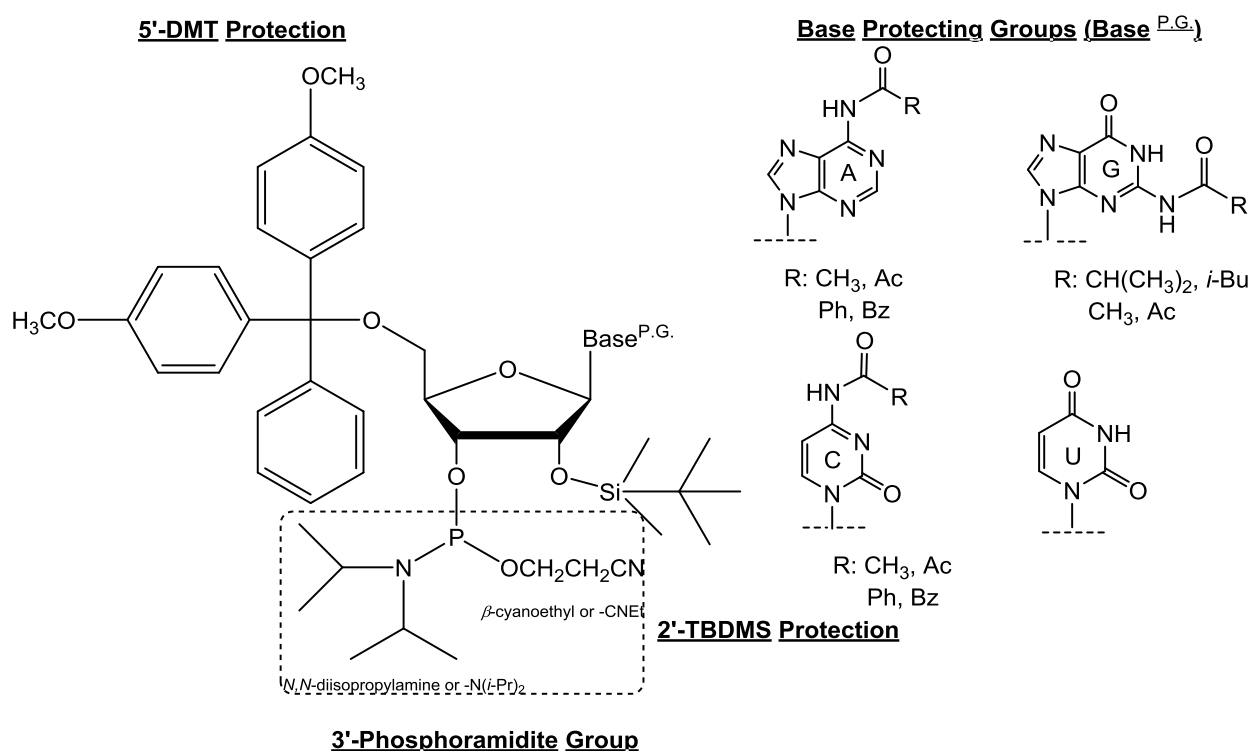


**Figure 2.1.** i. Attachment of a protected RNA monomer on a succinyl linked LCAA-CPG. ii. Equation for determining the loading capacity ( $\mu\text{mol/g}$ ) of RNA monomer attached to the solid support using UV-Vis spectrophotometry.

### 2.2.2 RNA PHOSPHoramidites FOR SOLID PHASE RNA SYNTHESIS

The conventional RNA building blocks for automated solid phase synthesis are composed of an acid labile 5'-ODMT group, base sensitive protecting groups masking the exocyclic amines (*e.g.* *N*-Bz, *N*-Ac, *N*-*t*Bu) on the nucleobases, a fluoride labile 2'-OtBDMS protecting group and a 3'-phosphoramidite which facilitates coupling reactions to the nascent support-bound RNA (**Figure 2.2**).<sup>7</sup> Although these building blocks are most commonly used in the production of siRNAs and their analogs (as exemplified in this study),<sup>31</sup> they remain limited in the production of lengthy, bio-active RNA (>80 nucleotides).<sup>8,9</sup> This limitation is primarily attributed to the chemical nature of the bulky 2'-OTBDMS groups, which sterically hinders the coupling of the 3'-phosphoramidites leading to the concomitant formation of short failure

sequences that diminishes yields and purities. For this reason, a variety of 2'-protecting groups have been developed for ameliorating the solid phase synthesis of lengthy and complex RNA.<sup>10</sup> As a best case example, a 110 nucleotide-long precursor mi-RNA has been produced with the use of the 2'-*O*-cyanoethoxymethyl (CEM) RNA phosphoramidite building blocks to provide 1.0 mg (5.5% yield) of pure RNA product.<sup>11</sup>



## 2.2

**Figure 2.2.** Structures of commercially available (Chemgenes Inc., Wilmington MA) RNA phosphoramidites and their protecting groups for automated solid phase RNA synthesis.

### 2.2.3 AUTOMATED SOLID PHASE RNA SYNTHESIS

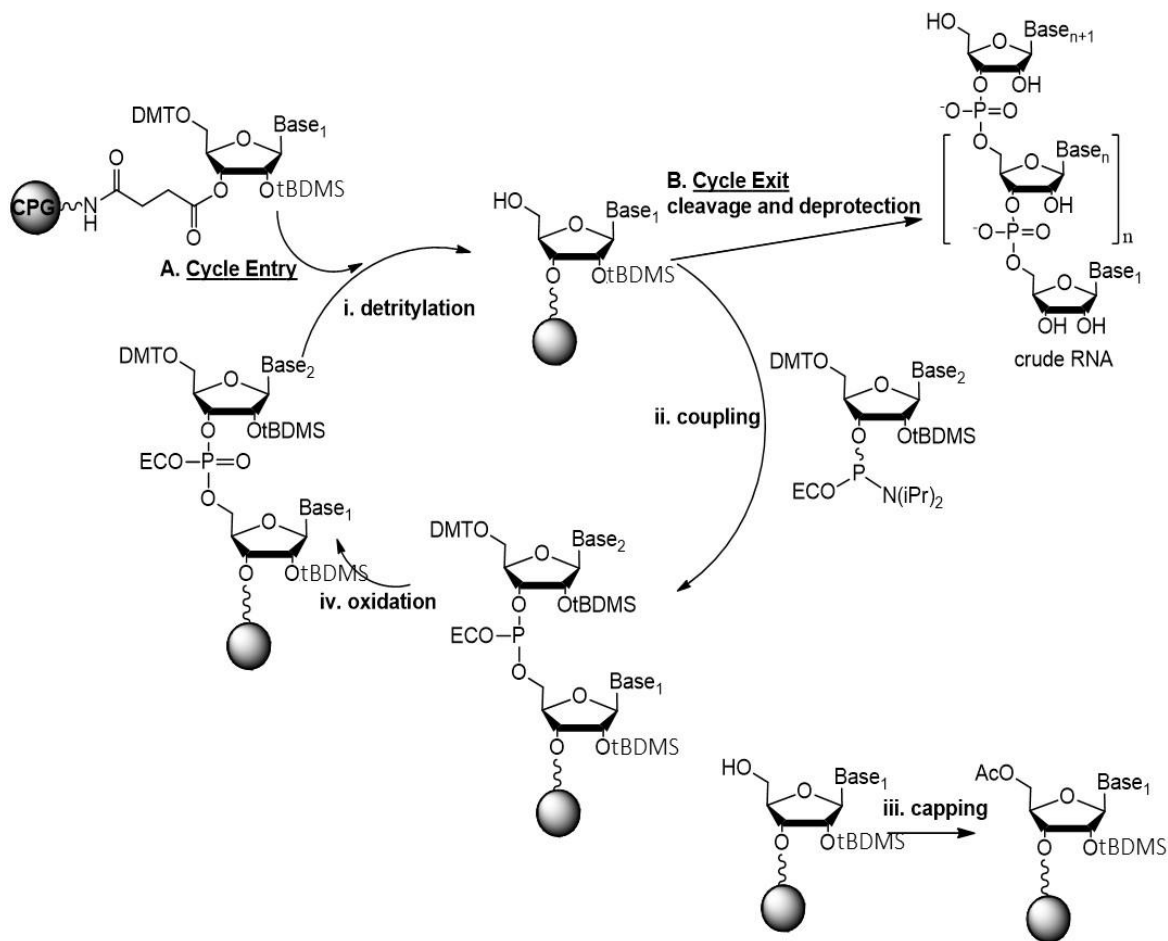
The phosphoramidite RNA building blocks were instrumental to the development of the first automated solid phase synthesis of RNA, founded by Ogilvie and co-workers at McGill University during the 1980s.<sup>12</sup> The introduction of the *gene machine* has ushered the rapid



production of small (microgram to milligram) and large (gram to kilogram) quantities of RNA for applications in biology and medicine.<sup>13</sup>

The automated solid phase RNA synthesis cycle (**Scheme 2.1**) begins with a detritylation step, for the removal of the 5'-DMT group from the RNA monomer linked to the CPG support (**Figure 2.1, i**). The detritylation step is performed with a 90 second delivery of 3% dichloroacetic acid in dichloromethane, 3% DCA: DCM, followed by a DCM wash cycle to remove any residual DCA prior to the coupling reaction. The RNA phosphoramidites (**Figure 2.2, 2.2**) are dissolved as 0.15 M solutions in anhydrous acetonitrile, MeCN, and mixed with a coupling reagent, 0.25 M 5-ethylthiotetrazole, ETT, in MeCN, for reaction with the support-bound RNA. Typically, the coupling reaction for RNA synthesis takes place in 10 minutes (15 minutes for riboguanosine due to the bulky protecting groups). The dinucleotide bound support is then washed with MeCN to remove the excess coupling reagent and phosphoramidite prior to the 'capping' step. The capping cycle is performed for 12 seconds with (Cap A: 1:1:8 v/v/v acetic anhydride:pyridine:tetrahydrofuran, Cap B: 16% *N*-methyl imidazole in tetrahydrofuran) to prevent side reactions with uncoupled RNA. During the course of the RNA synthesis procedure this step generates failure sequences; short RNA fragments that must be removed by RNA purification. Fortunately, each automated synthesis cycle for RNA is optimized to about 97-98% efficiency, such that the accumulation of failure sequences during synthesis is minimal. Following capping, an oxidation step for 14 seconds with a 0.02 M oxidant (I<sub>2</sub> in 75/20/5 v/v/v tetrahydrofuran/ pyridine/ water) converts the reactive phosphite triester to the more stable phosphate triester backbone. The support is then washed and dried with MeCN and argon prior to 5'-detritylation and continuation of the synthesis cycle until the desired sequence has been completed. Following synthesis, RNA is cleaved from the solid support and deprotected using

alkaline conditions, 1: 1 v/v ammonium hydroxide: methylamine (1: 1 AMA) for 10 minutes at 65 °C. RNA sequences that contain the more resilient protecting groups (*i.e.* Gua *N*-*i*Bu) require lengthier deprotection times, typically accomplished with 3 : 1 v/v ammonium hydroxide in ethanol (3 : 1 NH<sub>4</sub>OH:EtOH) for 16 hours at 55 °C. The alkaline solution is volatile and is evaporated on a Speedvac<sup>®</sup> concentrator. The crude RNA can be recovered from the CPG using autoclaved distilled water. The RNA is then concentrated and treated with a 1:1 v/v dimethylsulfoxide:triethylamine trihydrofluoride (1:1 DMSO:TREAT.3HF, 125 µL) to complete the 2'-desilylation reaction at 65 °C for 90 min. Following reaction, RNA is precipitated from the mixture using 3 M NaOAc (25 µL) in n-BuOH (1 mL), isolated by centrifugation and re-dissolved in autoclaved water for analyses and purification using anion exchange, AE, or reverse phase, RP, HPLC and with polyacrylamide gel electrophoresis, PAGE.



**Scheme 2.1.** Automated solid phase RNA synthesis cycle.

## 2.2.4 ANALYSIS AND PURIFICATION OF SYNTHETIC RNA BY HPLC

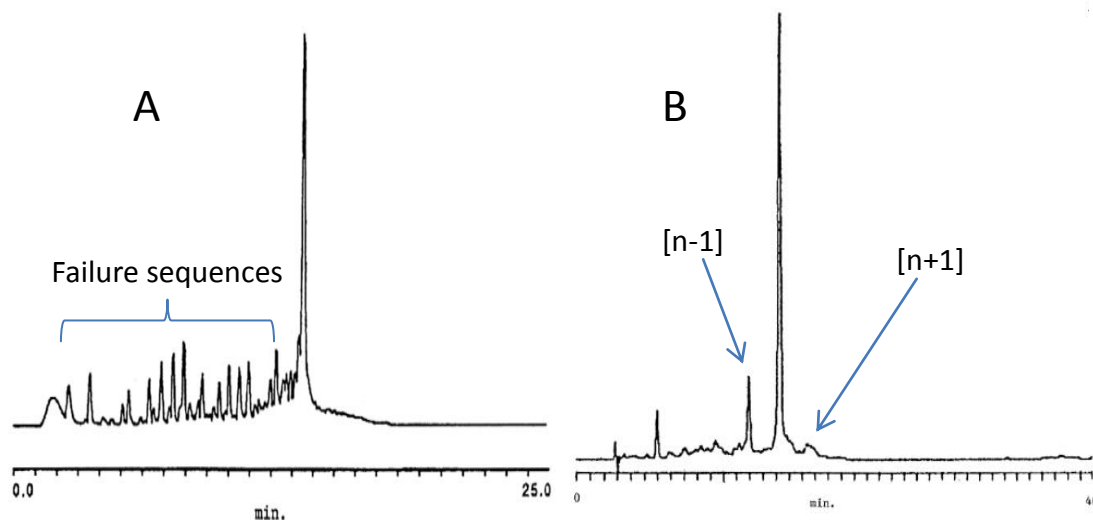
High Performance Liquid Chromatography (HPLC) is commonly implicated in RNA analysis and purification. This includes denaturing (single-strand RNA) and non-denaturing (double-strand siRNA) methods using anion exchange<sup>20</sup> (AE) and ion pairing reverse phase<sup>21</sup> (IP RP) HPLC.

AE HPLC relies on the separation of RNA based on favorable ionic interactions between the negatively charged phosphodiester backbone and the positively charged anion exchange resin. An eluent system, typically composed of aqueous perchlorate salts (*i.e.* 1 M NaClO<sub>4</sub> or 1 M LiClO<sub>4</sub>) is used to disrupt the ionic interactions between the RNA and resin, which gradually

begins to elute the RNA from the column. The lengthier RNA sequences are most retained on the stationary phase and elute with extended retention times, while the shorter ones with fewer phosphate groups elute faster on the column. In a typical AE HPLC chromatogram, (**Figure 2.3, a**), the shorter RNA sequences (labeled failure sequences) elute prior to the desired RNA product in crude purities ranging from 70-95%, which is dependent on the nature and length of the synthesized sequence. Following isolation of the desired RNA product, a desalting step (Sephadex G-25 size exclusion chromatography) is necessary to remove the salt contaminants from the purified RNA.

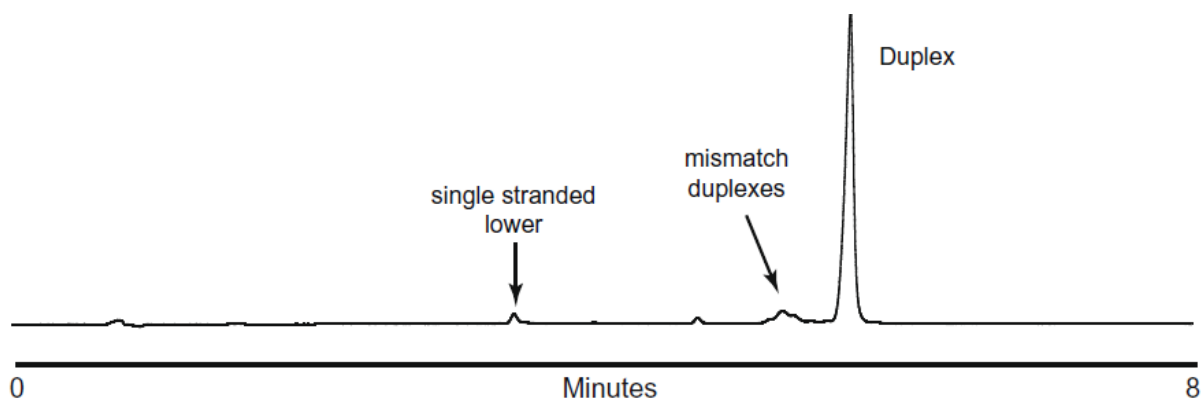
RP HPLC employs a column packed with a non-polar stationary phase (*e.g.* C18) which facilitates the separation of RNA based on favorable hydrophobic interactions. In order for this separation to occur, the anionic RNA phosphodiester backbone must be neutralized by the mobile phase, typically an ion-pairing agent composed of an organic alkylammonium salt (*e.g.* triethylammonium acetate, TEAA). This allows for the hydrophobic RNA nucleobases to interact with the stationary phase of the column. A combination of ion-pairing buffer in organic solvent (*e.g.* MeCN) allows for slow elution and separation of the RNA components in the crude reaction mixture. A typical IP RP HPLC chromatogram, (**Figure 2.3, b**), improves the separation of failure sequences, including the RNAs that have failed to incorporate the final phosphoramidite during solid phase RNA synthesis. These n-1 failure sequences are often challenging to remove from the desired product. Additionally, the incorporation of an extra phosphoramidite or incomplete deprotection may also result in the appearance of longer (n+1) sequences. In this case, IP RP HPLC may allow for better separation and purity of the targeted RNA sequence relative to AE HPLC (**Figure 2.3**). Furthermore, the eluent system in IP RP

HPLC is volatile, facilitating sample concentration and isolation of pure RNA for characterization.



**Figure 2.3.** AE and IP RP HPLC analysis of RNA. Representative chromatograms of (A) AE and (B) IP RP HPLC analysis of RNA showing the failure sequences eluting first followed by the desired RNA and  $n+1$  sequences resulting from incomplete deprotection or multiple couplings.<sup>20,21</sup>

The application of AE and IP RP HPLC in the analysis and purification of single strand RNA is accomplished at elevated temperatures ( $\sim 60$  °C). These conditions denature the H-bonding interactions that are responsible for RNA secondary structures. Interestingly, IP RP HPLC has been commonly applied for the analysis and purification of double-stranded siRNA.<sup>21</sup> In this case, IP RP HPLC conditions are performed at ambient temperatures ( $\sim 22$  °C) that maintain the integrity of the siRNA duplex structure (**Figure 2.4**). These methods are widely applicable for the analysis and purification of siRNA at a detection wavelength of 260 nm.

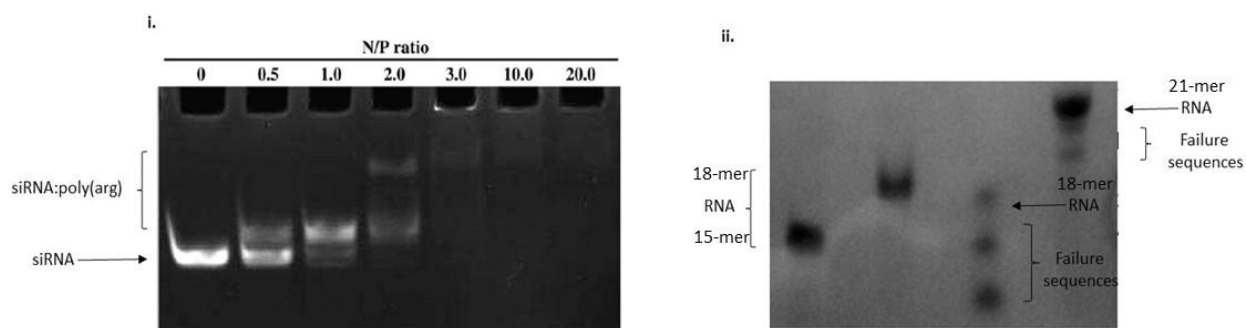


**Figure 2.4.** IP RP HPLC analysis of a double stranded siRNA eluted on a Waters C18 reverse phase column with eluent gradient from 35-85% B in 10 minutes, 0.2 mL/min, 20 °C. With solvent A: 100 mM TEAA pH 7 and B: 20% MeCN in 100 mM TEAA pH 7. Detection at 260 nm.<sup>21</sup>

### 2.2.5 ANALYSIS AND PURIFICATION OF SYNTHETIC RNA BY PAGE

Gel electrophoresis has been applied for the analysis and separation of medium length (5-25 nucleotides) to lengthy (>30 nucleotides) RNA.<sup>22</sup> In this technique, RNA samples (0.05 – 0.30 O.D. units for analytical and 5.0-15 O.D. units for preparative gel electrophoresis) are suspended in a gel loading buffer that either retains (sucrose) or denatures (formamide) RNA secondary structures. A 10-20% polyacrylamide gel is typically used in the analyses of lengthy RNA (> 80 nucleotides) whereas a 20-24% gel is most commonly used in the separation and purification of siRNA (18-21 nucleotides). A native polyacrylamide gel electrophoresis (PAGE) is used to track the formation of RNA structures (in this case double-stranded siRNAs) or the binding interaction between ligand and RNA.<sup>23</sup> For example, a poly(arginine) peptide sequence was added to siRNA and native PAGE was used to track the optimal stoichiometric ratios for complex formation (**Figure 2.5, i**).<sup>24</sup> Alternatively, a denaturing PAGE uses urea in the gel matrix to help denature non-covalent bonding interactions. This facilitates the migration of RNA across an electric field generated from an applied voltage and current. This result in efficient

separation of crude samples for analysis and purification.<sup>25</sup> The trend for RNA separation on PAGE is based on size, shape and charge, with the lengthier RNA sequences most retained and the shorter ones migrating at a faster rate (**Figure 2.5, ii**). Following electrophoresis, RNA may be visualized under UV shadowing (260 nm) or with the addition of an intercalating dye such as ethidium bromide, which makes a purple colored complex with RNA. For preparative PAGE, the desired RNA band is excised from the gel, transferred to a sterile tube and extracted in autoclaved water. Typical gel recoveries range from 40-60% and require an additional desalting step (Sephadex G-25 size exclusion chromatography) prior to mass spectrometry, structure analyses and biological studies.



**Figure 2.5.** Polyacrylamide gel electrophoresis of i. siRNA:poly(arginine) complexes under native conditions, 20% polyacrylamide gel with ethidium bromide staining and ii. Crude RNA analysis using denaturing conditions, 24% polyacrylamide gel using 7 M urea and RNA visualization at 260 nm.<sup>22-25</sup>

## 2.2.6 CHARACTERIZATION OF SYNTHETIC RNA BY MASS SPECTROMETRY

Mass spectroscopy (MS) is the most commonly used analytical technique for RNA characterization by providing mass to charge ratios ( $m/z$ ) of the observed ions and fragmentation

patterns. This characterization method is typically coupled with HPLC, providing the basis for LC/MS analysis and characterization of RNA samples in high-throughput sequences.<sup>26</sup> The most suitable types of MS analyses for RNA characterization provides mild sample ionization with little fragmentation. These include: electrospray ionization (ESI) and matrix assisted laser desorption/ionization time of flight (MALDI-TOF) mass spectrometry.<sup>27,28</sup> MALDI-TOF MS requires the RNA sample to be embedded within a suitable matrix, typically composed of azathiothymine/spermine and L-fucose, which is then subjected to a UV laser beam causing sample absorption, followed by desorption from the matrix and ionization.<sup>29</sup> The ions are then separated and detected by the TOF-MS producing a mass spectrum of the RNA sample in positive (protonated) or negative (deprotonated) mode. MALDI-TOF MS is a mild ionization method that is perfectly suitable for the target molecular weight detection of large RNA samples ( $\geq 300$  kDa) in the pico-femtomolar range.<sup>28,29</sup>

In ESI MS, RNA samples are dissolved in water ( $\mu\text{M}$  solutions) and turned into a fine spray of charged droplets by a high voltage produced by the ESI source. This desolves the samples and creates ions that are sorted by a quadrupole mass analyzer and detected by some type of electron multiplier detector. Typically, an eluent system that facilitate sample ionization and avoids ion quenching can be used. For example, buffers consisting of triethylamine and hexafluoroisopropanol (TEA:HFIP) are usually well suited for siRNA LC/MS applications.<sup>27</sup>

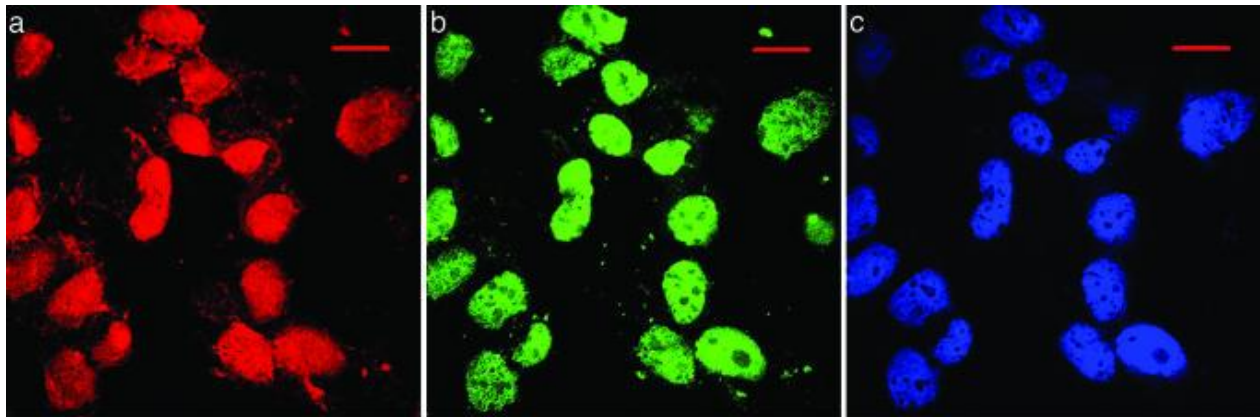
### **2.2.7 APPLICATIONS OF SYNTHETIC siRNAs AND ANALOGS**

The power of automated solid phase RNA synthesis has led to the rapid generation of siRNAs and analogs for high-throughput screening assays against gene targets and applications



in gene therapy for fighting human malignancies such as cancer.<sup>1</sup> Among the trove of examples represented in the literature, a few are discussed herein to highlight their significance in elucidating complex biological process and potentially treating some of the most debilitating disorders.

Fluorescent tags such as Alexa Fluor 488 and Cy5 have been conjugated to the 3'-ends of the sense and antisense strands, respectively, by solid phase RNA synthesis. The fluorescently labeled siRNAs were tracked in live Huh-7 cells with a laser confocal fluorescence microscope, which displayed real-time images of the siRNAs targeting nuclear 7SK, U6 and cytosolic NS3 mRNA.<sup>14</sup> These results demonstrated for the first time a responsive RNAi pathway in the nucleus of live cells (**Figure 2.6**).



**Figure 2.6.** Live cell imaging with fluorescently labeled siRNAs (a: Cy5 labeled siRNA, red > 635 nm b: Alexa Fluor labeled siRNA, green 495-520 nm) in the nucleus (c: DAPI blue dye stain) of Huh-7 human cells. Figure adapted from reference 14.

Similarly, a single molecule fluorescence resonance energy transfer (FRET) assay was recently developed to determine the mechanism of Argonaute (Ago) binding and cleavage activity of a single-stranded siRNA (antisense strand) in complex with a target mRNA strand.<sup>15</sup>

The Ago enzyme has been associated with mRNA processing, possessing the ability to selectively degrade the mRNA component during the RNAi pathway. Despite this knowledge, the mechanistic and kinetic aspects of Ago binding and cleavage activity of mRNA substrate remain unclear. In an effort to elucidate the mechanism of Ago activity, an antisense strand was conjugated with an acceptor Cy5 red (> 635 nm) fluorescent tag; whereas a target mRNA strand was conjugated with an acceptor Cy3 green (535-635 nm) fluorescent tag and a biotin label for binding to a streptavidin functionalized quartz slide. The antisense strand was mixed with Ago and incubated with the target mRNA bound to the solid support. Single molecule images at fixed time intervals were collected with a fluorescent microscope to determine the mRNA binding and cleavage activity of the Ago enzyme (**Figure 2.7**).



these fruitful examples, lipophilic siRNAs (**Figure 2.8, 2.3**) have been made by solid phase RNA synthesis and demonstrated effective cellular uptake and gene silencing effects *in vivo*.<sup>16</sup> Furthermore, elaborate combinatorial approaches have also been developed to improve the efficacy of siRNAs in the RNAi mechanism. A series of reports have demonstrated enhanced silencing effects of self-assembled RNA containing multiple siRNAs, thereby potently inhibiting gene expression in a synergistic manner. For example, a reducible disulfide siRNA dimer, linking an siRNA motif targeting the green fluorescent protein (GFP) and another targeting vascular endothelial growth factor (VEGF) expression demonstrated enhanced cellular uptake and gene silencing effects *in vitro* relative to the monomeric form (**Figure 2.8, 2.4**).<sup>17</sup> A tripartite-interfering RNA (tiRNA) (**Figure 2.8, 2.5**) displayed more potent and longer lasting activity compared to the linear control siRNAs.<sup>18</sup> Surprisingly, the self-assembled tiRNA targeting the Lamin, DBP and TIG3 genes did not require processing into its constituent siRNAs for gene silencing activity in mammalian cells. Lastly, branch siRNA nanostructures (**Figure 2.8, 2.6**) displaying multiple substrates for RNAi activity also retained the same trend, soliciting greater silencing effects relative to the linear siRNA controls.<sup>19</sup> These siRNAs effectively demonstrate that the RNAi mechanism is tolerant of modifications that may lead to more potent gene silencing effects *in vivo*.





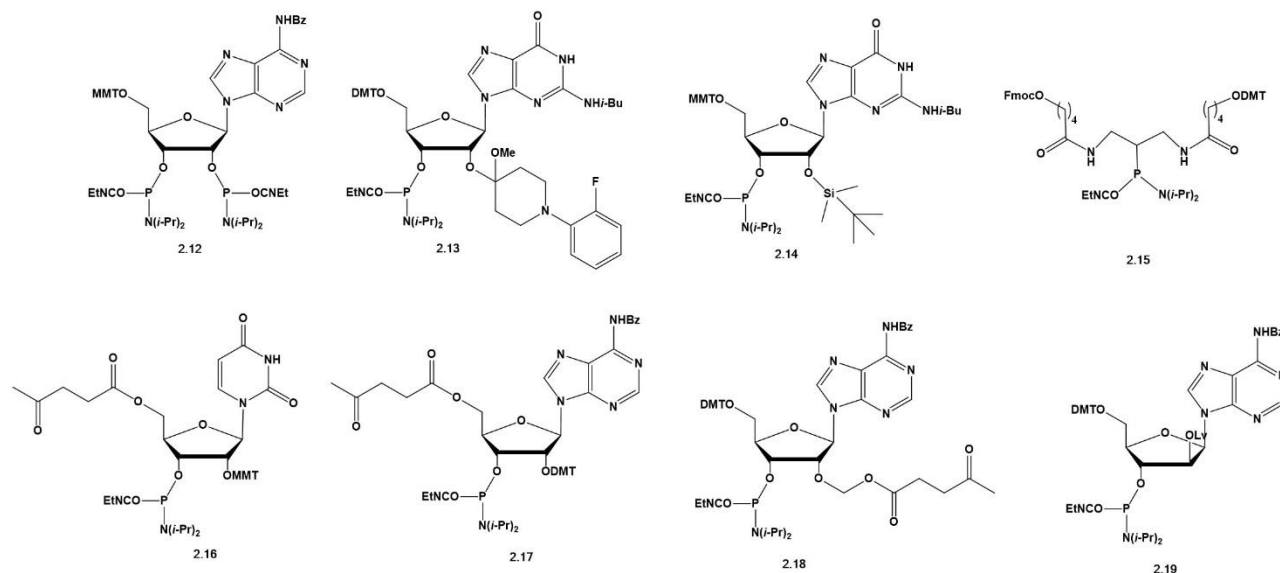
## 2.4 RESULTS AND DISCUSSION

### 2.4.1 SYNTHESIS AND CHARACTERIZATION OF BRANCHPOINT NUCLEOTIDES

Branchpoint nucleotides have been incorporated within RNA to generate higher-ordered and biologically relevant structures, such as those belonging to the branch, hyperbranch and lariat RNA.<sup>31,32</sup> These RNA motifs have been shown to have significant biological activity and serve as useful probes for exploring the influence of RNA structure on cell biology. For example, branch and lariat RNA have been synthesized and applied as inhibitors of mRNA splicing events for potential anti-cancer utility.<sup>33</sup> Moreover, we have recently demonstrated that branch and hyperbranch short-interfering RNA (siRNA) potently silence oncogenic Glucose Regulated Protein of 78 kilodalton (GRP78) expression leading to cell death activity in HepG2 liver cancer cells.<sup>31</sup>

A variety of branch point phosphoramidites have been synthesized in the literature and some are commercially available. For example, a branch point nucleoside composed of a 5'-OMMT *N*-Bz adenosine 2',3'-bisphosphoramidite has been made for the solution phase assembly of symmetrically branched RNA trinucleotides (**Figure 2.10, 2.12**).<sup>34</sup> The same branch point synthon has been applied for the solid-phase assembly of branch RNA structures, albeit composed of homopolymeric sequences.<sup>35</sup> Orthogonally protected branch point phosphoramidites have been developed for the preparation of asymmetric branch and hyperbranch RNA in addition to lariat structures on solid phase.<sup>19a,31,32,36</sup> For example, 5'-ODMT 2'-Fpmp, and 2'-OtBDMS branch point phosphoramidites (**Figure 2.10, 2.13, 2.14**) have been developed for the solid-phase synthesis of branch DNA/RNA chimeras, referred to as msDNA; a rare form of genetic material found in some bacteria.<sup>37</sup> Although these methods are suitable for the production of asymmetrically branched oligonucleotides, they lack in their ability to generate

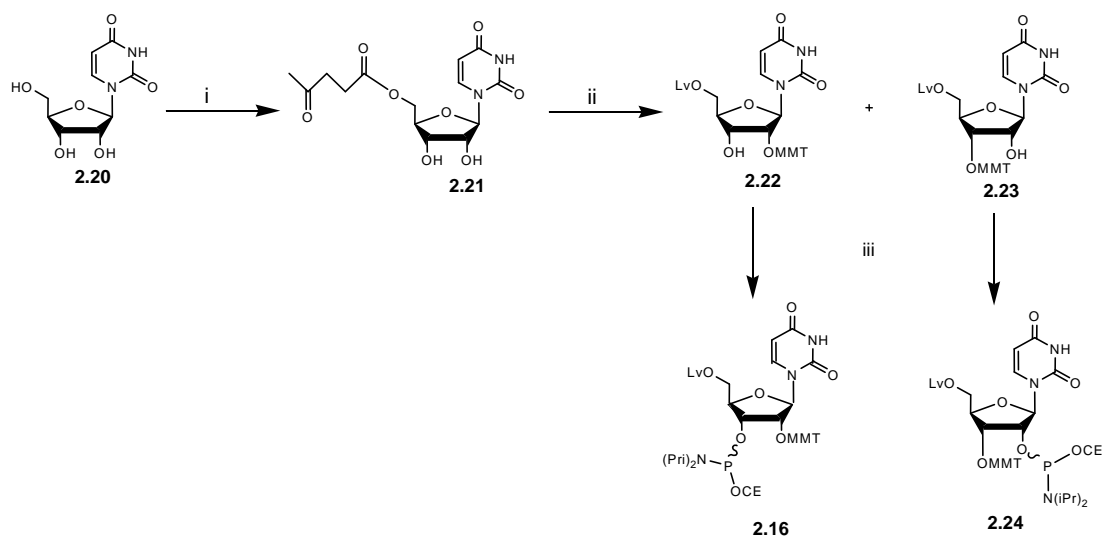
asymmetric RNA. Towards this goal, acyclic linkers containing orthogonal protecting groups (**Figure 2.10, 2.15**) have been marketed for the production of branch and self-assembled RNA.<sup>19a</sup> Most recently, the development of 5'-OLv 2'-OMMT ribouridine phosphoramidites<sup>31,36</sup> and related analogs<sup>32</sup> (**Figure 2.10, 2.16, 2.17-2.19**) have been employed for the asymmetric solid phase synthesis of biologically relevant branch, hyperbranch and lariat RNA species. The former is especially practical for generating lengthy (> 80 nucleotides) biologically active RNA nanostructures for applications in biology<sup>31-33</sup>, theranostics<sup>38</sup> and supramolecular<sup>19</sup> chemistry. Thus, the branchpoint phosphoramidites containing the 5'-OLv and 2'-OMMT orthogonal protecting groups are a focal point of the proposed research study (**Figure 2.10, 2.16**).



**Figure 2.10.** Branchpoint nucleotide phosphoramidites used in the preparation of branch, hyperbranch and lariat RNA.<sup>19a,31-36</sup>

The solution-phase synthesis of branchpoint amidites, **2.16** and **2.24**, 5'-*O*-levulinyl 2' and 3'-*O*- monomethoxytrityl ribouridine phosphoramidites (**Scheme 2.2**) was completed by a solution phase synthesis method based on literature precedence.<sup>36</sup>





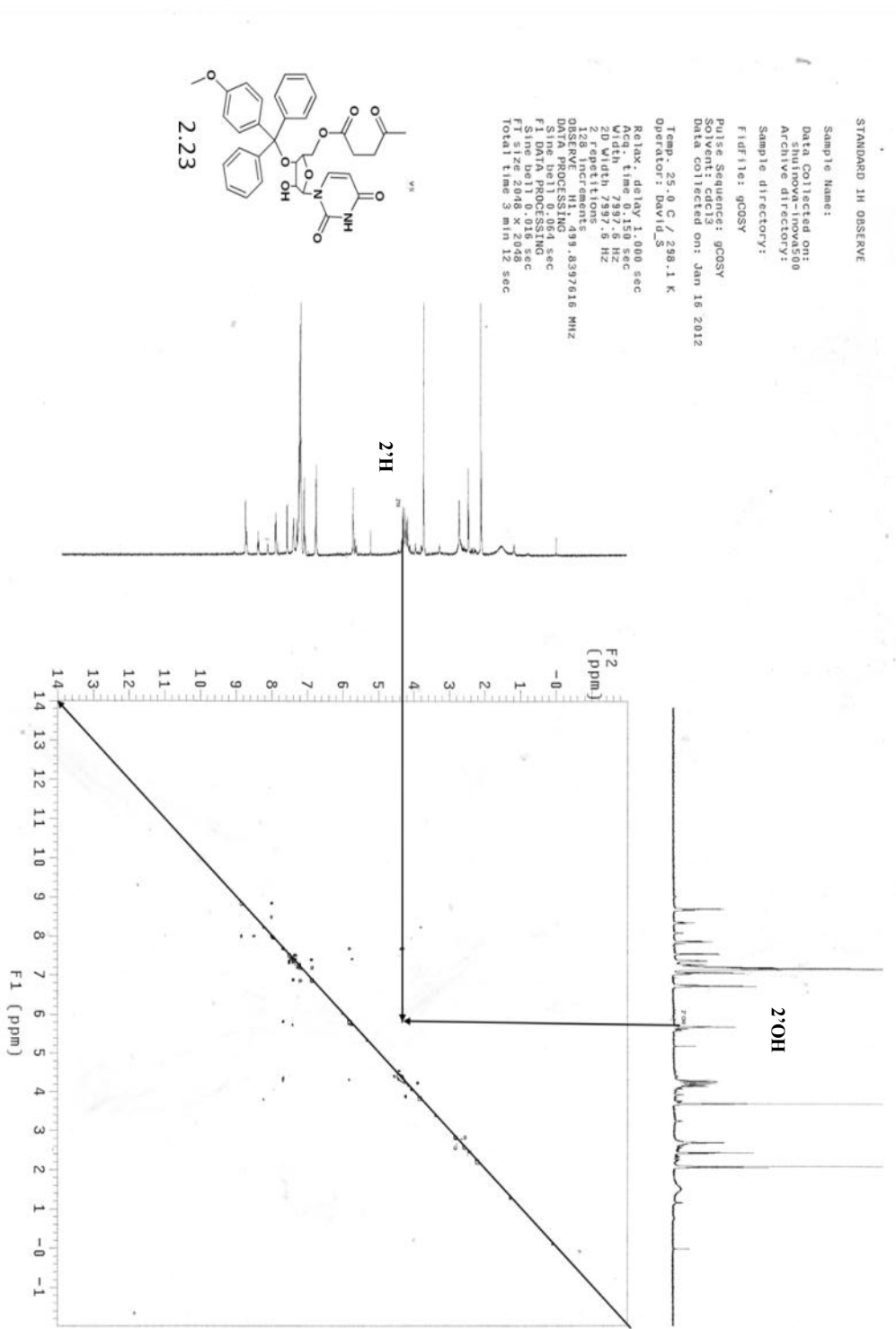
**Scheme 2.2.** Reaction and Conditions: (i).  $\text{Lv}_2\text{O}$ , Novozyme<sup>®</sup> 435, 1,4-dioxane, 22 °C, overnight, 80%. (ii). MMT-Cl,  $\text{AgNO}_3$ , THF, pyridine. 22 °C, 3 h, **2.22**: 40% and **2.23**: 20%, (iii).  $\text{Cl-P}(\text{OCE})\text{N}(\text{iPr})_2$ ,  $\text{Et-N}(\text{iPr})_2$ , THF, 22 °C, 3 h, **2.16**: 55% and **2.24**: 60%.

The solution phase synthesis of branchpoint phosphoramidites, **2.16** and **2.24**, was completed via a 3 step synthesis procedure featuring: (a) chemo-enzymatic 5'-levulination of ribouridine, (b) tritylation and (c) phosphitylation (**Scheme 2.2**). The first step entailed the regioselective chemo-enzymatic 5'-levulination of ribouridine using Novozyme<sup>®</sup> 435 immobilized on lipase.<sup>39</sup> This reaction is preferred over chemical levulination which produces multiple levulinated products upon treatment of ribouridine with levulinic anhydride and 1,4-diazabicyclo[2.2.2]octane (DABCO).<sup>40</sup> Instead, the chemo-enzymatic approach produced selectively the desired 5'-levulinyl ribouridine, **2.21**, in 80% yield. With pure product in hand, **2.21**, was tritylated using monomethoxytrityl chloride to give both the 2' and 3' tritylated regioisomers (**2.22** and **2.23**) respectively collected in purified yields of 40% and 20%. The reaction was found to favor the desired 2'-regioisomer due to the enhanced nucleophilicity of the 2'- over the 3'-hydroxyl.<sup>41</sup> The identity of the pure regioisomers was ascertained by NMR, in

which a COSY correlation cross-peak was used to explicitly assign the 2' and 3'-hydroxyl groups (**Figure 2.11**). The regioisomers, **2.22** and **2.23**, were phosphitylated separately to their branchpoint phosphoramidites in purified yields of 55% and 60%. In this case,  $^{31}\text{P}$  NMR was used to assess the purity of 5'-Lv 2'-OMMT and 5'-Lv 3'-OMMT ribouridine phosphoramidite diastereomers, **2.16** and **2.24**, respectively (**Figure 2.12**). These are perfectly suitable for solid phase RNA synthesis, in which the synthetic method removes the chirality at phosphorous. With pure branchpoint phosphoramidites in hand, opportunity now exists for developing a solid phase synthesis procedure for branch and hyperbranch siRNAs.



b)



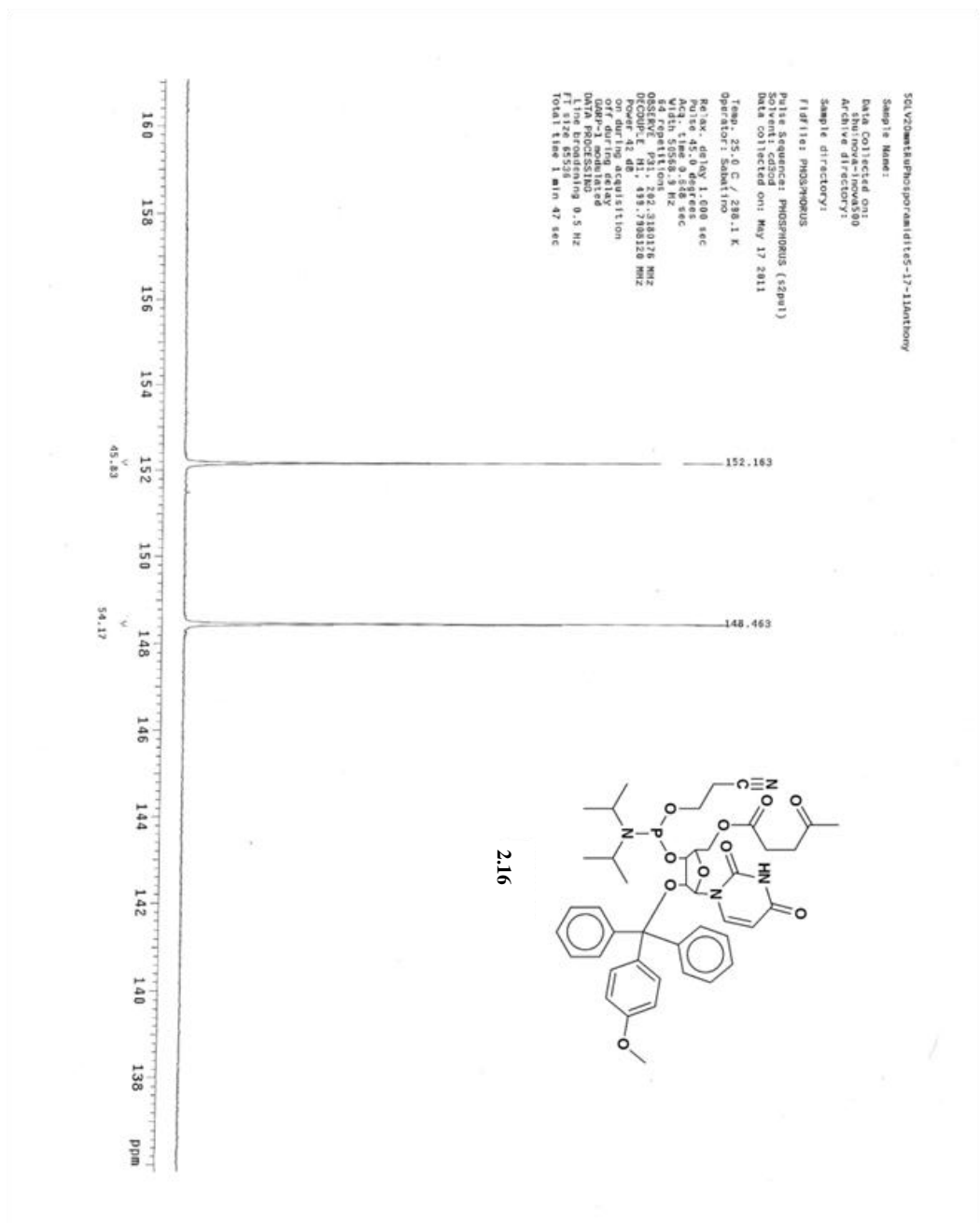
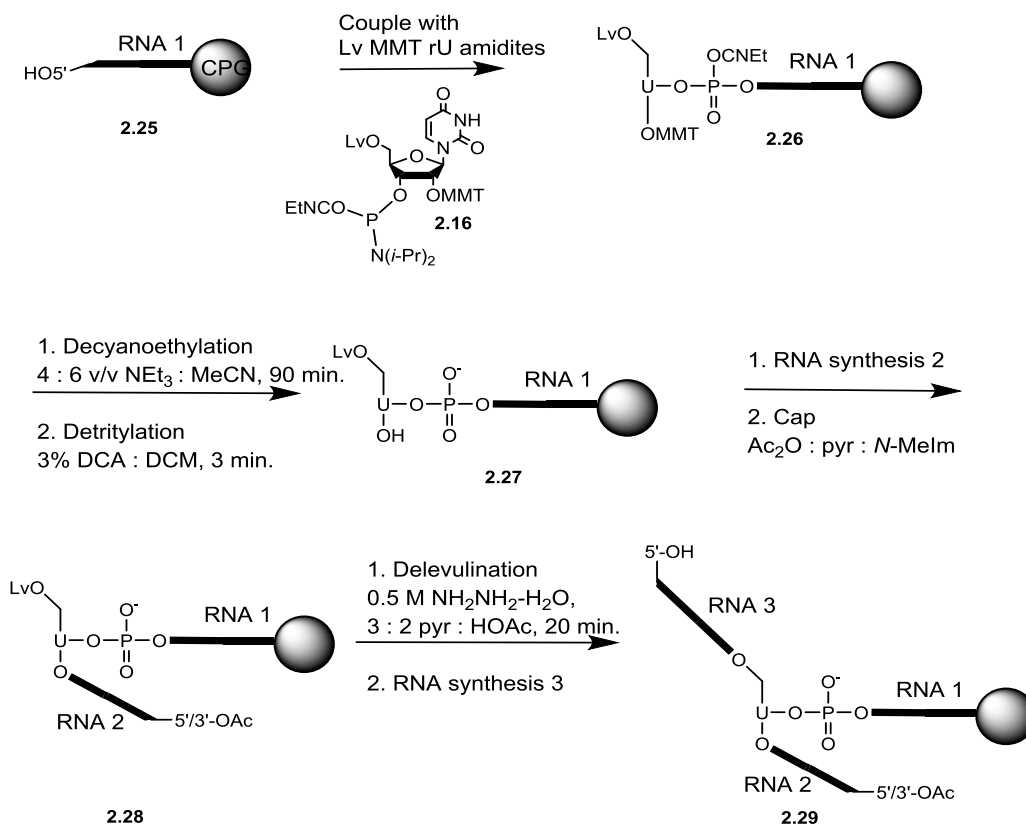


Figure 2.12.  $^{31}\text{P}$  NMR spectrum of the branchpoint phosphoramidite

#### 2.4.2 SOLID PHASE SYNTHESIS OF BRANCH AND HYPERBRANCH siRNAs.

The siRNA sequences synthesized in this study (**Table 2.1**) are based on the target nucleotides for down-regulating Glucose Regulated Protein 78 (GRP78) expression in human cancer cells.<sup>42</sup> An iterative protocol for the solid-phase synthesis of branch and hyperbranch siRNAs targeting GRP78 oncogenes is next described (**Scheme 2.3**). This solid phase synthesis approach entails linear RNA synthesis up to the branchpoint nucleotide **2.16**. The next reaction requires a decyanoethylation step, which liberates the phosphate protecting groups affording a more stable phosphate diester, **2.27**, relative to the triester, **2.26**, prior to acid detritylation and chain extension reactions.<sup>37</sup> An additional acetylation step caps the 3' or 5'-ends of the 'V-shaped' RNA molecule, **2.28**, and prevents additional coupling reactions by acetylating the terminal hydroxyl group. A manual delevulation procedure is used to liberate the branchpoint 5'-hydroxyl<sup>31,32,36</sup> and the branch siRNA, **2.29**, is completed by automated RNA synthesis. This cycle may be repeated for the generation of hyperbranch siRNA sequences (**Table 2.1, sequences 6, 7, 10, 11, 16, 17**). Additionally, this methodology lends itself to the incorporation of modified nucleic acids such as the 2'-OMe RNAs for improving siRNA pharmacokinetic properties (**Table 2.1, sequences 12-17**).<sup>42</sup> Moreover, branch and hyperbranch siRNAs consisting of the branchpoint nucleotide, **2.24**, were also synthesized to explore the influence of branchpoint connectivities on siRNA structure and RNAi activity (**Table 2.1, sequences 8-11**).



**Scheme 2.3.** Solid phase branch RNA synthesis method.

The synthesis of linear GRP78 siRNA sequences (**Table 2.1, sequences 1-3**) were accomplished on a 500 Å CPG support. These sequences were prepared as suitable controls, in order to validate their GRP78 silencing and cancer cell death activity.<sup>42</sup> The V-shape and Y-branch siRNAs (**Table 2.1, sequences 4-5**) necessitated the use of a 1000 Å CPG support, which led to the first successful isolation of the V-shape (**Figure 2.13**) and subsequently Y-branch siRNA. For the solid phase assembly of the hyperbranch siRNAs (**Table 2.1, sequences 6-7**), an optimized synthesis method was established with 2000 Å CPG. The synthesis method featured fast deprotecting RNA amidites (which replace the *N*-Bz/*N*-*i*Bu protecting groups for *N*-Ac, *N*-*i*Pr-Pac), milder oxidant (0.02 M iodine/water/pyridine/THF) and short, pulsating detritylation steps (60 and 30 sec) with 3% DCA:DCM (**Figure 2.14**). The anti-parallel orientations of the complementary siRNAs were maintained by introducing un-natural 2',3' and 3',3'-

phosphodiester linkages at the branchpoint nucleotides, and the use of reverse 5'-phosphoramidites.<sup>31,32,36,44</sup> Incredibly, these changes led to the successful synthesis of an 86-mer hyperbranch siRNAs (**Table 2.1, sequences 6-7**). Following this optimized procedure, the efficient solid phase synthesis of V-shape, Y-branch and  $\times$  hyperbranch siRNAs composed from the branchpoint nucleotide, **2.24**, was realized (**Table 2.1, sequences 8-11**). The 2'-OMe series proved to be a synthetic challenge due to the mixed sequence compositions. In spite of this challenge, the 2'-OMe siRNAs (**Table 2.1, sequences 12-17**) were synthesized in sufficient yields for structure and biological applications.

Following synthesis, RNA was cleaved from the solid support and deprotected using 1:1 v/v ammonium hydroxide / methylamine for 20 min at 65 °C. The crude samples were suspended in a mixture of 1:1 v/v dimethylsulfoxide/triethylamine trihydrofluoride for 2 h at 65 °C to complete the 2'-desilylation reaction. Following post-synthesis work-up conditions siRNAs, were analyzed and purified by IP RP HPLC and PAGE.

#### **2.4.3 ANALYSIS, PURIFICATION AND CHARACTERIZATION OF siRNAs.**

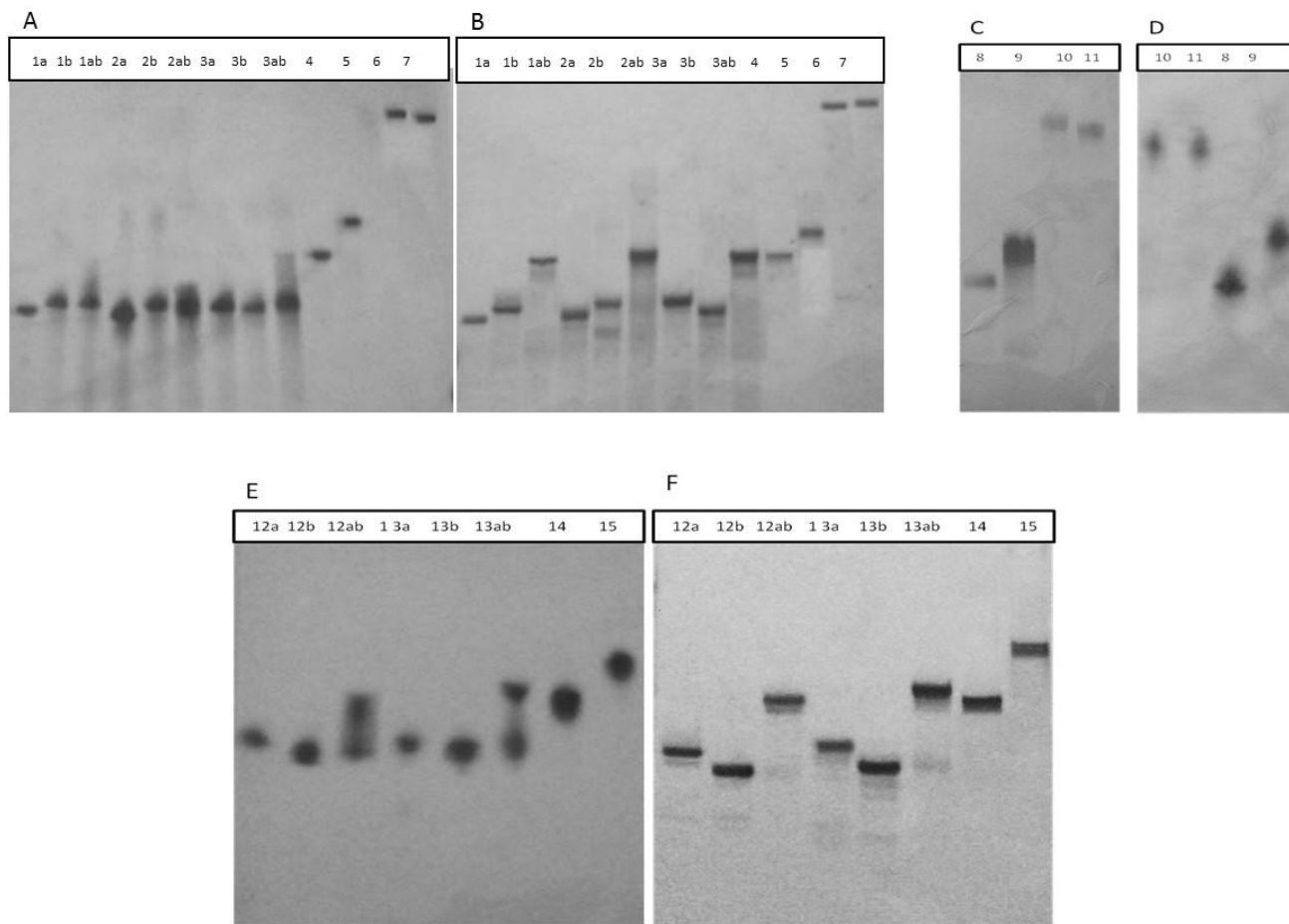
The analysis of crude siRNAs by IP RP HPLC generally demonstrated chromatograms containing lower molecular weight failure sequences with shorter retention times followed by the desired siRNAs. The failure sequences for linear siRNAs resulted from incomplete couplings that were typically held to a minimum (<10%) facilitating sample purification. In the case of the branch and hyperbranch siRNAs, the failure sequences predominantly consisted of incomplete couplings at the branchpoint nucleotides. This feature can be attributed to the chemically labile and sterically encumbered vicinal 2',3' or 3',3'-phosphodiester linkages at the branchpoint positions.<sup>36</sup> These branchpoint connectivities have been found to be especially sensitive to acid







entirely surprising, considering RNA hairpins possess thermodynamically more stable folded structures relative to their linear double-stranded sequences.<sup>43</sup>



**Figure 2.15.** Native and denaturing PAGE analyses of siRNAs synthesized in this study. A, C and E: denaturing (7 M urea) 18% PAGE; B, D and F: native (no urea) 18% PAGE of linear, branch and hyperbranch siRNAs (Table 2.1 sequences 1-15).

**Table 2.1.** Characterization data for the siRNA sequences synthesized in this study.

Seq. ID	Sequence <sup>a</sup>	size	Purity <sup>f</sup>			MW (g/mol) <sup>h</sup>	
			%Crude	%Yield <sup>e</sup>	%Purity <sup>f</sup>	Obs.	(Cal)
<b>1</b>	5'-A GUG UUG GAA GAU UCU GAU-3'	19	82	83	>99	6103.7	(6103.7)
	5'-A UCA GAA UCU UCC AAC ACTU -3'	19	100	77	>99	5949.4	(5947.4)
<b>2</b>	5'-G GAG CGC AUU GAU ACTU AGA-3'	19	95	78	>99	6124.7	(6124.8)
	5'-U CUA GUA UCA AUG CGC UCC-3'	19	73	78	>99	5958.6	(5955.3)
<b>3</b>	5'-AGU UCA ACG AGU AUC AGC A-3'	19	95	80	>99	6052.4	(6051.7)
	5'-UGC UGA UAC UCG UUG AAC U-3'	19	92	81	92	5998.8	(5999.6)
<b>4</b>	2' <sup>3</sup> : UCA CAA CCU UCU AAG ACU A-5'	39	58	47	>99	12420.5	(12421.5)
	5'-rU 3' <sup>5</sup> : AGU GUU GGA AGA UUG UGA U-3'						
<b>5</b>	2' <sup>3</sup> : UCA CAA CCU UCU AAG ACU A-5'	47	40	78	>99	14934.9	(14936.0)
	5'- UCA CAA CC - 3' <sup>5</sup> : -rU 3' <sup>5</sup> : AGU GUU GGA AGA UUG UGA U-3'						
<b>6</b>	3'-U AGU CUU AGA GGA UUG UGA-5' <sup>2'</sup>	47	40	78	>99	14934.9	(14936.0)
	5'-A UCA GAA UCU CCU AAC ACU-3' <sup>5'</sup>						
<b>7</b>	3'-A GAU CAU AGU UAC GCG AGG-5' <sup>2'</sup>	86	41	77	>99	27450.0	(27419.5)
	5'-U CUA GUA UCA AUG CGC UCC-3' <sup>5'</sup>						
<b>8</b>	2' <sup>5</sup> : AGU GUU GGA AGA UUG UGA U-3'	39	60	18	>90	12428.0	(12421.5)
	5'-rU 3' <sup>3</sup> : UCA CAA CCU UCU AAG ACU A-5'						

<b>9</b>	2 <sup>3'</sup> : AGU GGU GGA AGA UUG UGA U-3' 5 <sup>2'</sup> -UCA CAA CC - 3 <sup>5'</sup> -rU 3 <sup>3'</sup> : UCA CAA CCU UCU AAG ACU A-5'	47	78	17	>90	14941.6	(14936.0)
<b>10</b>	5 <sup>2'</sup> :A UCA GAA UCU CCU AAC ACU-3 <sup>3'</sup> 3 <sup>2'</sup> :U AGU CCU AGA GGA UUG UGA-5 <sup>5'</sup> rU2 <sup>5'</sup> -UCA CAA CC - 3 <sup>5'</sup> -rU 3 <sup>3'</sup> :UCA CAA CCU UCU AAG ACU A-5'	47	78	17	>90	14941.6	(14936.0)
<b>11</b>	5 <sup>2'</sup> :U CUA GUA UCA AUG CGC UCC-3 <sup>3'</sup> 3 <sup>2'</sup> :A GAU CAU AGU UAC GCG AGG-5 <sup>5'</sup> rU2 <sup>5'</sup> -UCA CAA CC - 3 <sup>5'</sup> -rU 3 <sup>3'</sup> :UCA CAA CCU UCU AAG ACU A-5'	86	67	23	>90	27485.2	(27449.5)
<b>12</b>	5 <sup>2'</sup> :A GUG UUG GAA GAA UCU GAU-3' 5 <sup>2'</sup> :A UCA GAA UCU UCC AAC ACU -3' 19	55	28	>99	6215.9	(6214.9)	
<b>13</b>	5 <sup>2'</sup> :G GAG CGC AUU GAU ACU AGA-3' 5 <sup>2'</sup> :U CUA GUA UCA AUU GCG UCC-3' 19	40	40	>99	6236.2	(6234.2)	
<b>14</b>	2 <sup>3'</sup> : UCA CAA CCU UCU AAG ACU A-5' 5 <sup>2'</sup> :rU 3 <sup>5'</sup> :A GUG UUG GAA GAU UCU GAU-3' 39	23	30	>90	12659.9	(12658.8)	
<b>15</b>	2 <sup>3'</sup> : UCA CAA CCU UCU AAG ACU A-5' 5 <sup>2'</sup> -UCA CAA CC - 3 <sup>5'</sup> -rU 3 <sup>5'</sup> :A GUG UUG GAA GAU UCU GAU-3' 47	16	28	>90	15230.5	(15229.5)	
<b>16</b>	3 <sup>2'</sup> :U AGU CCU AGA GGA UUG UGA-5 <sup>2'</sup> 5 <sup>2'</sup> :A UCA GAA UCU UCC AAC ACU-3 <sup>5'</sup> rU3 <sup>5'</sup> -UCA CAA CC - 3 <sup>5'</sup> -rU 3 <sup>5'</sup> :A GUG UUG GAA GAU UCU GAU-3' 86	15	23	>99	28141.9	(27840.2)	
<b>17</b>	3 <sup>2'</sup> :A GAU CAU AGU UAC GCG AGG-5 <sup>2'</sup> 5 <sup>2'</sup> :U CUA GUA UCA AUU GCG UCC-3 <sup>5'</sup> rU3 <sup>5'</sup> -UCA CAA CC - 3 <sup>5'</sup> -rU 3 <sup>5'</sup> :A GUG UUG GAA GAU UCU GAU-3' 86	43	26	>99	27766.3	(27870.2)	

<sup>a</sup>Sequences **1, 4, 5, 6, 8, 9, 10,** and **12** derived from nucleotides 1236-1254 containing the initiation codon for GRP78 mRNA<sup>42</sup>; <sup>b</sup>Sequences **2,** and **13** derived from nucleotides 1887-1906 of GRP78 mRNA<sup>42</sup>; <sup>c</sup>Sequence 3 is a non-specific control; <sup>d</sup>Sequences **7, 11, 17** contains sequence derived from **1** and **2**; <sup>e</sup>Sequences **4-7** and **14-17** are composed with branchpoint nucleotide **2.16**, sequences **8-11** are composed with branchpoint nucleotide **2.24**, and sequences **12-17** have 2'OMe inserts at the underlined positions; <sup>f</sup>Determined by IP RP HPLC using 80-20% 0.1 mM TEAA in MeCN pH: 7.2 (23 min); <sup>h</sup>Determined by UV-Vis spectroscopy; <sup>g</sup>Observed mass (calculated mass) determined by ESI-MS in negative mode (Dr. Mark Hail, Novatia LLC, Newtown, PA).

## 2.5 CONCLUSIONS

In conclusion, we have demonstrated the effective synthesis, purification and characterization of a novel class of siRNA molecules. In this study, branch and hyperbranch siRNAs were effectively prepared by solid phase RNA synthesis. These sequences were analyzed and purified by IP RP HPLC and by PAGE. The identities of the pure siRNA samples were confirmed by molecular weight analyses using ESI-MS (Dr. Mark Hail, Novatia LLC, Newtown, PA). Interestingly, the branch and hyperbranch siRNAs conferred stable single molecular hybrid structures as detected by native and denaturing PAGE analyses. These results effectively leads into the bio-physical and structural properties of the synthetic siRNAs, a focal point in Chapter 3 of this thesis.

## 2.6 REFERENCES

1. Paddison, P.J.; Hannon, G.J. RNA interference: the new somatic cell genetics? *Cancer Cell* **2002**, *2*, 17-23.
2. Letsinger, R. L.; Mahadevan, V. Oligonucleotide Synthesis on a Polymer Support. *J. Am. Chem. Soc.* **1965**, *87*, 3526-3527.
3. Pon, R.T.; Yu, S. Linker phosphoramidite reagents for the attachment of the first nucleoside to underivatized solid-phase supports. *Nucleic Acids Res.* **2004**, *32*, 623-631.
4. Goodwin, J.T.; Stanick, W.A.; Glick, G.D. Improved Solid-Phase Synthesis of Long Oligoribonucleotides: Application to tRNA<sup>phe</sup> and tRNA<sup>gly</sup>. *J. Org. Chem.* **1994**, *59*, 7941-7943.
5. (a) Pon, R.T.; Yu, S. and Sanghvi, Y.S. *Bioconj. Chem.* Rapid esterification of nucleosides to solid-phase supports for oligonucleotide synthesis using uronium and phosphonium coupling reagents. *Bioconj. Chem.* **1999**, *10*, 1051-1057, (b) Guzaev A.P.; Manoharan, M. A conformationally preorganized universal solid support for efficient oligonucleotide synthesis. *J. Am. Chem. Soc.* **2003**, *125*, 2380-2381, (c) Zhang, X.; Gaffney, B.L.; Jones, R.A. RNA synthesis using a universal, base-stable allyl linker. *Nucleic Acids Res.* **1997**, *25*, 3980-3983. (d) Johnsson, R.; Lackey, J.G.; Bogojeski, J.J.; Damha, M.J. New light labile linker for solid phase synthesis of 2'-O-acetalester oligonucleotides and applications to siRNA prodrug development. *Bioorg. Med. Chem. Lett.* **2011**, *21*, 3721-3725.
6. Patnaik, A.K.; Rao, N.S.; Kumar, P.; Sharma, A.K.; Garg, B.S.; Gupta, K.C. High-Loading Supports for oligonucleotide Synthesis, *Helv. Chim. Acta* **2000**, *83*, 322-327.
7. Damha, M.J. and Ogilvie, K.K. In *Methods in Molecular Biology: Protocols for Oligonucleotides and Analogs* **1993**, *20*, Humana Press Inc. Totowa, N.J.
8. Sproat, B.S. RNA synthesis using the 2'-O-(Tertbutyldimethylsilyl) Protection. In *Methods in Molecular Biology: Oligonucleotide Synthesis: Methods and Applications* **2005**, 288, Humana Press Inc. Totowa, N.J.
9. Wincott, F.; DiRenzo, A.; Shaffer, C.; Grimm, S.; Tracz, D.; Workman, C.; Sweedler, D.; Gonzalez, C.; Scaringe, S.; Usman, N.

- Synthesis, deprotection, analysis and purification of RNA and ribozymes. *Nucleic Acids Res.* **1995**, *23*, 2677-2684.
10. (a) Reese, C.B. In *Current Protocols in Nucleic Acid Chemistry* **2000**, 2.2.1-2.2.24, (b) Marshall, W.S.; Kaiser, R.J. Recent advances in the high-speed solid phase synthesis of RNA. *Curr. Opin. Chem. Biol.* **2004**, *8*, 222-229, (c) Beaucage, S. L.; Reese, C. B., Recent Advances in the Chemical Synthesis of RNA. *Current Protocols in Nucleic Acid Chemistry* 2009, *38*, 2.16.1 - 2.16.31
  11. (a) Shiba, Y.; Masuda, H.; Watanabe, N.; Ego, T.; Takagaki, K.; Ishiyama, K.; Ohgi, T.; Yano, J. Chemical synthesis of a very long oligoribonucleotide with 2-cyanoethoxymethyl (CEM) as the 2'-O-protecting group: structural identification and biological activity of a synthetic 110mer precursor-microRNA candidate. *Nucleic Acids Res.* **2007**, *35*, 3287-3296, (b) Masuda, H.; Shiba, Y.; Watanabe, N.; Takagaki, K.; Ishiyama, K.; Ohgi, T.; Yano J. Chemical synthesis of a very long RNA oligomer, a 110mer precursor-miRNA candidate, with 2-cyanoethoxymethyl (CEM) as the 2'-O-protecting group. *Nucleic Acids Symp. Ser. (Oxf)*, **2007**, *51*, 3-4.
  12. Usman, N.; Ogilvie, K.K.; Jiang, M.Y.; Cedergren, R.J. Automated Chemical Synthesis of Long Oligoribonucleotides Using 2'-O-Silylated Ribonucleoside 3'-O-Phosphoramidites on a Controlled Pore Glass Support: Synthesis of a 43-Nucleotide Sequence Similar to the 3'-Half Molecule of an Escherichia Coli Formylmethionine tRNA. *J. Am. Chem. Soc.* **1987**, *109*, 7845-7854.
  13. Ellington, A.D. What's so Great About RNA? *ACS Chem. Biol.* **2007**, *2*, 445-448.
  14. Berezina, S.Y.; Supekova, L.; Supek, F.; Schultz, P.G.; Deniz, A.A. siRNA in human cells selectively localizes to target RNA sites. *Proc. Natl. Acad. Sci. U S A.* **2006**, *103*, 7682-7687.
  15. Jung, S.R.; Kim, E.; Hwang, W.; Shin, S.; Song, J.J.; Hohng, S. Dynamic anchoring of the 3'-end of the guide strand controls the target dissociation of Argonaute-guide complex. *J. Am. Chem. Soc.* **2013**, *135*, 16865-16871.
  16. Wolfrum, C.; Shi, S.; Jayaprakash, K.N.; Jayaraman, M.; Wang, G.; Pandey, R.K.; Rajeev, K.G.; Nakayama, T.; Charrise, K.; Ndungo, E.M.; Zimmermann,



- T.; Koteliansky, V.; Manoharan, M.; Stoffel, M. Mechanisms and optimization of in vivo delivery of lipophilic siRNAs. *Nat. Biotechnol.* **2007**, *25*, 1149-1157.
17. Chung, H.J.; Hong, C.A.; Lee, S.H.; Jo, S.D.; Park, T.G. Reducible siRNA dimeric conjugates for efficient cellular uptake and gene silencing. *Bioconjug. Chem.* **2011**, *22*, 299-306.
18. Chang, C.I.; Lee, T.Y.; Kim, S.; Sun, X.; Hong, S.W.; Yoo, J.W.; Dua, P.; Kang, H.S.; Kim, S.; Li, C.J.; Lee, D.K., Enhanced intracellular delivery and multi-target gene silencing triggered by tripodal RNA structures. *J. Gene Med.* **2012**, *14*, 138-146.
19. (a) Avino, A.; Ocampo, S.M.; Perales, J. C.; Eritja, R., Branched RNA: A New Architecture for RNA Interference. *J. Nucleic Acids* 2011, *2011*, 7, (b) Nakashima Y, Abe H, Abe N, Aikawa K, Ito Y. Branched RNA nanostructures for RNA interference. *Chem. Commun. (Camb)*. **2011**, *47*, 8367-8369.
20. (a) Van Boom, J.H.; De Rooy, J.F.M. Sequence Analysis of Synthetic Oligonucleotides by High-Performance Liquid Anion-Exchange Chromatography. *J. Chrom.* **1977**, *131*, 169-177, (b) Cook, K.; Thayer, J. Advantages of ion-exchange chromatography for oligonucleotide analysis. *Bioanalysis*, **2011**, *3*, 1109-1120.
21. (a) McCarthy, S.M.; Gilar, M.; Gebler, J. Reversed-Phase Ion-Pair Liquid Chromatography Analysis and Purification of small interfering RNA. *Anal. Biochem.* **2009**, *390*, 181-188, (b) Noll, B.; Seiffert, S.; Vornlocher, H.-P.; Roehl, I., Characterization of small interfering RNA by non-denaturing ion-pair reversed-phase liquid chromatography. *J. Chromatogr. A* **2011**, *1218*, 5609-5617.
22. Rio, D.C.; Ares, M.; Hannon, G.J.; Nilsen, T.W. Polyacrylamide Gel Electrophoresis of RNA. *Cold Spring Harb. Protoc.* **2010**, *6*, 1-6.
23. Woodson, S.A.; Koculi, E. Analysis of RNA folding by native polyacrylamide gel electrophoresis. *Methods Enzymol.* **2009**, *469*, 189-208.
24. Kim, S.W.; Kim, N.Y.; Choi, Y.B.; Park, S.H.; Yang, J.M.; Shin, S. RNA interference in vitro and in vivo using an arginine peptide/siRNA complex system. *J. Control. Release.* **2010**, *143*, 335-343.

25. (a) Petrov, A.; Tsa, A.; Puglisi J.D. Analysis of RNA by analytical polyacrylamide gel electrophoresis. *Methods Enzymol.* **2013**, *530*, 301-313, (b) Petrov, A.; Wu, T.; Puglisi, E.V.; Puglisi, J.D. RNA purification by preparative polyacrylamide gel electrophoresis. *Methods Enzymol.* **2013**, *530*, 315-30.
26. Turner, J.J.; Hoos, J.S.; Vonhoff, S.; Klussmann, S. Methods for L-ribooligonucleotide sequence determination using LCMS. *Nucleic Acids Res.* **2011**, *39*, e147.
27. Beverly, M.; Hartsough, K.; Macheimer, L.; Pavco, P.; Lockridge, J., Liquid chromatography electrospray ionization mass spectrometry analysis of the ocular metabolites from a short interfering RNA duplex. *J. Chromatogr. B* **2006**, *835*, 62-70.
28. Kühn-Hölsken, E.; Lenz, C.; Sander, B.; Lührmann, R.; Urlaub, H. Complete MALDI-ToF MS analysis of cross-linked peptide-RNA oligonucleotides derived from nonlabeled UV-irradiated ribonucleoprotein particles. *RNA* **2005**, *11*, 1915-1930.
29. Distler, A.M.; Allison, J. Improved MALDI-MS Analysis of Oligonucleotides through the use of Fucose as a Matrix Additive. *Anal. Chem.* **2001**, *73*, 5000-5003.
30. Siolas, D.; Lerner, C.; Burchard, J.; Ge, W.; Linsley, P.S.; Paddison, P.J.; Hannon, G.J.; Cleary, M.A. Synthetic shRNAs as potent RNAi triggers. *Nat. Biotechnol.* **2005**, *23*, 227-231.
31. Maina, A.; Blackman, B.A.; Parronchi, C.J.; Morozko, E.; Bender, M.E.; Blake, A.D.; Sabatino D. Solid-phase synthesis, characterization and RNAi activity of branch and hyperbranch siRNAs. *Bioorg. Med. Chem. Lett.* **2013**, *23*, 5270-5274.
32. Katolik, A.; Johnsson, R.; Montemayor, E.; Lackey, J.G.; Hart, P.J.; Damha, M.J. Regiospecific Solid-Phase Synthesis of Branched Oligoribonucleotides That Mimic Intronic Lariat RNA Intermediates. *J. Org. Chem.* **2014**, [Epub ahead of print].
33. Carriero, S.; Damha, M.J. Inhibition of pre-mRNA splicing by synthetic branched nucleic acids. *Nucleic Acids Res.* **2003**, *31*, 6157-6167.
34. Damha, M.J.; Ogilvie, K.K. Synthesis and Stereospecific Analysis of Branched RNA Fragments: mRNA Splicing Intermediates. *J. Org. Chem.* **1988**, *53*, 3710-3722.
35. Damha, M.J.; Zabarylo, S. Automated Solid-Phase Synthesis of Branched Oligonucleotides. *Tetrahedron Lett.* **1989**, *30*, 6295-6298.

36. Sabatino, D. Expanding the size and shape of nucleic acids: studies on branched and heptose based nucleic acids. *Ph.D. Thesis* **2007**, McGill University, Montreal, Canada.
37. (a) Damha, M.J.; Braich, R.S. Synthesis of Branched DNA/RNA Chimera Similar to the mDNA Molecule of *Myxococcus xanthus*. *Tetrahedron Lett.* 1998, 39, 3907-3910, (b) Braich, R.S.; Damha, M.J. Regiospecific solid-phase synthesis of branched oligonucleotides. Effect of vicinal 2',5'- (or 2',3'-) and 3',5'-phosphodiester linkages on the formation of hairpin DNA. *Bioconjugate Chem.* **1997**, 8, 370-377.
38. (a) Shchepinov, M.S.; Udalova, I.A.; Bridgman, A.J. and Southern, E.M. Oligonucleotide dendrimers: synthesis and use as polylabelled DNA probes. *Nucleic Acids Res.* **1997**, 25, 4447-4454, (b) Mora, J.R. and Getts, R.C. Enzymatic microRNA detection in microtiter plates with DNA dendrimers. *BioTechniques* **2006**, 41, 420-424, (c) Capaldi, S.; Getts, R.C. and Sumedha, D.J. Signal amplification through nucleotide extension and excision on a dendritic DNA platform. *Nucleic Acids Res.* 2000, 28, e21.
39. Garcia, J.; Fernandez, S.; Ferrero, M.; Sanghvi, Y.S.; Gotor, V. Novel enzymatic synthesis of levulinyl protected nucleosides useful for solution phase synthesis of oligonucleotides. *Tetrahedron Asymm.* **2003**, 14, 3533-3540.
40. Iwai, S.; Sasaki, T.; Ohtsuka, E. Large scale synthesis of oligoribonucleotides on solid support: synthesis of a catalytic RNA duplex. *Tetrahedron* **1990**, 46, 6673-6688.
41. Wilkinson, K.A.; Merino, E.J.; Weeks, K.M. Selective 2'-hydroxyl acylation analyzed by primer extension (SHAPE): quantitative RNA structure analysis at single nucleotide resolution. *Nature* **2006**, 1, 1610-1616.
42. (a) Suzuki, T.; Lu, J.; Zahed, M.; Kita, K.; Suzuki, N. Reduction of GRP78 expression with siRNA activates unfolded protein response leading to apoptosis in HeLa cells. *Arch. Biochem. Biophys.* **2007**, 468, 1-14, (b) Tsutsumi, S.; Namba, T.; Tanaka, K.I.; Arai, Y.; Ishihara, T.; Aburaya, M.; Mima, S.; Hoshino, T.; Mizushima, T. Celecoxib upregulates endoplasmic reticulum chaperones that inhibit celecoxib-induced apoptosis in human gastric cells. *Oncogene* **2006**, 25, 1018-1029.
43. Khvorova, A.; Reynolds, A.; Jayasena, S.D. Functional siRNAs and miRNAs exhibit strand bias. *Cell* **2003**, 115, 209-216.

44. Srivastava, S.C.; Pandey, D.; Srivastava, N.P.; Bajpai, S.P. RNA Synthesis: phosphoramidites for RNA synthesis in the reverse direction. Highly efficient synthesis and application to convenient introduction of ligands, chromophores and modifications of synthetic RNA at the 3'-end. *Nucleic Acids Symp. Ser. (Oxf)*. **2008**, 52, 103-104.

## 2.7 EXPERIMENTAL SECTION

### 2.7.1 GENERAL METHODS

Chemical synthesis reagents and solvents were obtained from ChemGenes, Aldrich and VWR and used as received. Solid phase oligonucleotides synthesis reagents and materials were obtained from ChemGenes or Glen Research Inc. and also used without further purification. HPLC grade solvents for chromatography were purchased from EMI Biosciences. Analytical thin-layer chromatography (TLC) was performed on aluminum-backed silica gel plates (Merck 60 F254). TLCs were visualized under UV shadowing (260 nm) or staining (10% H<sub>2</sub>SO<sub>4</sub>/MeOH). Compound purification using silica gel chromatography was performed on 230-400 mesh silica (Sorbent Technologies). Molecular weights for **2.16**, **2.20-2.24** were measured as direct injections on a Hewlett Packard series 1100 MSD equipped with ESI as ion-source in positive mode using 50/50 v/v MeOH/H<sub>2</sub>O at a flow-rate of 1 mL/min. Nuclear magnetic resonance spectra (<sup>1</sup>H, <sup>13</sup>C, <sup>31</sup>P COSY, HMQC NMR) were recorded on an OXFORD NMR AS500 spectrophotometer. The NMR spectra were obtained at ambient temperature using either an indirect pulse-field gradient (ID-PFG) or a switchable pulse-field gradient (SW-PFG) probe. The obtained data was processed using VNMRJ software (version 2.2). The <sup>1</sup>H and <sup>13</sup>C assignments were based on gCOSY and gHMQC NMR correlation experiments.

### 2.7.2 SYNTHESIS OF THE BRANCHPOINT PHOSPHoramidites, **2.16** AND **2.24**

**5'-O-levulinyl ribouridine (2.21):** Levulinic acid (5.0 mL, 49 mmol) and 1 M *N,N*-dicyclohexylcarbodiimide (DCC) in dichloromethane (6.6 mL, 40 mmol) were stirred together in 260 mL of anhydrous diethyl ether to generate levulinic anhydride (Lv<sub>2</sub>O). The reaction was run at room temperature (22 °C) under N<sub>2</sub> atmosphere for 5 hours. The byproduct (DCU) was

removed by vacuum filtration and the filtrate was evaporated into viscous oil. In a second flask, ribouridine (2.15 g, 8.8 mmol) was vacuum dried for 5 hours and flushed with nitrogen before being suspended in 40 mL of anhydrous dioxane with resin-bound lipase enzyme, Novozyme<sup>®</sup> 435 (3 g). Crude Lv<sub>2</sub>O was dissolved in dioxane (160 mL) and added in 20 mL fractions over a period of one hour to the flask containing the ribouridine and enzyme in dioxane. The chemo-enzymatic reaction was run overnight (12-16 h) at 22 °C (room temperature) under N<sub>2</sub>. The reaction progress was monitored by TLC (10% MeOH in DCM) which confirmed 100 % conversion of starting material to product and the appearance of two non-polar product (R<sub>f</sub>: 0.48 and 0.35). The resin-bound lipase was filtered, washed (MeOH) and recycled for additional use. The filtrate was concentrated and purified by silica gel column chromatography (5-10 MeOH: DCM) to isolate the product in 80% yield.

<sup>1</sup>H NMR (**2.21**, 500 MHz, DMSO-d<sub>6</sub>): δ 11.32 (1H, bs, NH), 7.62 (1H, d, *J* = 8.5 Hz, H6), 5.66 (1H, d, *J* = 7.5 Hz, H5), 5.74 (1H, d, *J* = 5 Hz, H1'), 4.24 (1H, dd, *J* = 7.5 Hz, H5'), 4.14 (1H, dd, *J* = 12, 7.5 Hz, H5''), 4.06 (1H, t, *J* = 10 Hz, H2'), 3.95 (1H, bs, H3'), 3.32 (1H, s, H4'), 2.71 (2H, s, Lv CH<sub>2</sub>), 2.61 (2H, s, Lv CH<sub>2</sub>), 2.08 (3H, s, Lv CH<sub>3</sub>); <sup>13</sup>C NMR (**2.21**, 125 MHz, CDCl<sub>3</sub>-*d*<sub>1</sub>): δ 212.1 (CO), 177.4 (CO), 168.3 (CO), 155.8 (CO), 146.0 (C6), 107.2 (C5), 93.84 (C1'), 86.35 (C4'), 77.96 (C2'), 74.97 (C3'), 69.01 (C5'), 42.62 (CH<sub>2</sub>), 34.76 (CH<sub>2</sub>), 32.74 (CH<sub>3</sub>); ESI-MS [M+Na]<sup>+</sup>: Calcd. for C<sub>14</sub>H<sub>18</sub>N<sub>2</sub>O<sub>8</sub>Na : 364.3, found : 364.0.

**5'-*O*-levulinyl 2'-*O*-monomethoxytrityl ribouridine (2.22) and 5'-*O*-levulinyl 3'-*O*-monomethoxytrityl ribouridine (2.23):** A tritylation reaction was conducted using nucleoside **2.21** (2.0 g, 5.8 mmol), monomethoxytrityl chloride, MMT-Cl (2.4 g, 7.77 mmol) and silver nitrate (1.39 g, 4.50 mmol) which were dried under vacuum overnight before dissolving the

reagents in pyridine (6.0 mL) under nitrogen at room temperature (22 °C). The reaction was run for 3 h and tracked by TLC (95:5 CHCl<sub>3</sub>:MeOH) which confirmed the presence of the 2' and 3'-OMMT regioisomers, R<sub>f</sub>(**2.22**): 0.40 and R<sub>f</sub>(**2.23**): 0.28, respectively. The reaction mixture was then diluted with ethyl acetate (EtOAc) (60 mL) and washed twice with saturated sodium bicarbonate (NaHCO<sub>3</sub>) (60 mL). The organic layer was separated and dried using anhydrous sodium sulfate (Na<sub>2</sub>SO<sub>4</sub>). The solvent was evaporated and the crude product purified by silica gel column chromatography (96.5:2.5:1 chloroform:methanol:pyridine). The presences of pyridine in the elution buffer complicated the spotting on TLC, so a TLC plate pre-stained with 10% sulfuric acid in methanol was used to detect the product by detritylating the yellow colored MMT+ group. The 5'-*O*-levulinyl 2'-*O*-monomethoxytrityl ribouridine, **2.22**, eluted first and was dried as a white foam in yields of 40%. The 5'-*O*-levulinyl 3'-*O*-monomethoxytrityl ribouridine, **2.23**, eluted second and was dried to a white foam in yields of 20%. The identity of the 2' and 3'-OMMT regioisomers was confirmed by <sup>1</sup>H-<sup>1</sup>H COSY NMR which indicated a correlation cross-peak between the 3'H and 3'-OH in **2.22** and the 2'H and 2'-OH in **2.23**.

<sup>1</sup>H NMR (**2.22**, 500 MHz, DMSO-*d*<sub>6</sub>): δ 11.29 (1H, s, NH), 7.49-6.77 (14H, m, MMT), 7.12 (1H, d, *J* = 8.5 Hz, H6), 5.91 (1H, d, *J* = 7 Hz, H1'), 5.43 (1H, dd, *J* = 8 Hz, H5), 5.18 (1H, d, *J* = 6 Hz, 3'OH), 4.21 (1H, dd, *J* = 6.5 Hz, H2'), 4.0 (2H, m, H5'), 3.87 (1H, dd, *J* = 11.75 Hz, H4'), 3.71 (3H, s, OMe), 3.03 (1H, ddd, *J* = 1, 4.3, 7 Hz, H3'), 2.68 (2H, t, *J* = 6.3 Hz, Lv CH<sub>2</sub>), 2.37 (2H, ddd, *J* = 7.5 Hz, Lv CH<sub>2</sub>), 2.08 (3H, s, CH<sub>3</sub>); <sup>13</sup>C NMR (**2.22**, 125 MHz, DMSO-*d*<sub>6</sub>): δ 207.3 (Lv CO), 172.4 (Lv CO), 163.4 (C2, CO), 158.9 (C4, CO), 150.9-123.3 (MMT, 19C), 102.9 (C1'), 87.77 (C2'), 82.73 (C3'), 87.29 (C4'), 75.02 (C5'), 70.09 (OMe), 55.42 (CH<sub>2</sub>), 37.76 (CH<sub>2</sub>), 29.97 (CH<sub>3</sub>); ESI-MS [M+Na]<sup>+</sup>: Calcd. for C<sub>34</sub>H<sub>34</sub>N<sub>2</sub>O<sub>9</sub>Na : 635.6, found : 635.6.

$^1\text{H}$  NMR (**2.23**, 500 MHz, DMSO- $d_6$ ):  $\delta$  9.57 (1H, s, NH), 7.60-6.70 (14H, m, MMT), 6.85 (1H, d,  $J = 7.5$  Hz, H6), 5.86 (1H, s, H1'), 5.18 (1H, d,  $J = 7.5$  Hz, H5), 5.29 (1H, s, 2'OH), 4.30 (1H, s, H2'), 4.13 (2H, d,  $J = 12.5$  Hz, H5', 5''), 3.98 (1H, s, H4'), 3.78 (3H, s, OMe), 3.48 (1H, s, H3'), 2.70 (2H, m, CH<sub>2</sub>), 2.41 (2H, m, CH<sub>2</sub>), 2.15 (3H, s, CH<sub>3</sub>);  $^{13}\text{C}$  NMR (**2.23**, 125 MHz, CDCl<sub>3</sub>- $d_1$ ):  $\delta$  207.7 (CO), 172.4 (CO), 163.4 (CO), 159.0 (CO), 151.5-127.6 (MMT, 19C), 113.5 (C1'), 102.6 (C2'), 91.86 (C5), 88.21 (C3'), 80.89 (C4'), 74.23 (C5'), 72.39 (OMe), 55.31 (CH<sub>2</sub>), 37.79 (CH<sub>2</sub>), 29.70 (CH<sub>3</sub>); ESI-MS  $[\text{M}+\text{Na}]^+$ : Calcd. for C<sub>34</sub>H<sub>34</sub>N<sub>2</sub>O<sub>9</sub>Na : 635.6, found : 635.6.

**5'-O-levulinyl 2'-O-monomethoxytrityl 3'-O-phosphoramidous ribouridine (2.16) and 5'-O-levulinyl 3'-O-monomethoxytrityl 2'-O-phosphoramidous ribouridine (2.24)**: Each purified, tritylated nucleoside was reacted separately in a phosphitylation reaction by first drying the tritylated nucleoside (1.05 g, 1.70 mmol) overnight prior to reaction. Dry tetrahydrofuran (THF) (15 mL) was added to the nucleoside under a flow of nitrogen and *N,N*-diisopropylethylamine (DIPEA) (1.26 mL, 9.70 mmol) and the phosphitylating reagent, Cl-P(OCEt)N(*i*-Pr)<sub>2</sub> (700  $\mu\text{L}$ , 2.95 mmol) was to the flask. The reaction was stirred for 3 h at room temperature and monitored by TLC (2:1 Hexanes:Ethyl Acetate) until the formation of the phospharmadite diastereomers were observed,  $R_f$  (**2.16**): 0.50 and  $R_f$  (**2.24**) 0.50. A white precipitate, Cl<sup>+</sup>NE(Et)(*i*Pr)<sub>2</sub>, was also observed as an indication of reaction completion. Upon reaction completion, EtOAc (60 mL) was added to the reaction mixture prior to washing twice with saturated NaHCO<sub>3</sub> (30 mL). The organic phase was dried over Na<sub>2</sub>SO<sub>4</sub> and concentrated to a yellowish foam. The crude product was purified by silica gel chromatography (Hex:EtOAc, 2:1). Products **2.16** and **2.24** were collected, dried as a white foam in yields of 55% and 60%, respectively.



$^{31}\text{P}$  NMR (**2.16**, 80 MHz,  $\text{CD}_3\text{OD}-d_4$ ):  $\delta$  152.2 and 148.5; ESI-MS  $[\text{M}+\text{Na}]^+$ : Calcd. for  $\text{C}_{43}\text{H}_{51}\text{N}_4\text{O}_{10}\text{PNa}$  : 837.9, found : 837.4.

$^{31}\text{P}$  NMR (**2.24**, 80 MHz,  $\text{CD}_3\text{OD}-d_4$ ):  $\delta$  152.4 and 149.6; ESI-MS  $[\text{M}+\text{Na}]^+$ : Calcd. for  $\text{C}_{43}\text{H}_{51}\text{N}_4\text{O}_{10}\text{PNa}$  : 837.9, found : 837.4.

### 2.7.3 SOLID PHASE RNA SYNTHESIS

RNA was synthesized on an automated ABI 3400 synthesizer. Reagents for the synthesis cycle were as follows: *detritylation reagent* (3% solution of dichloroacetic acid in dichloromethane), *coupling reagent* (0.25 M ethylthiotetrazole in acetonitrile), *capping reagent* (Cap A: 1:1:8 v/v/v acetic anhydride:pyridine:tetrahydrofuran, Cap B: 16% *N*-methyl imidazole in tetrahydrofuran), *oxidation reagent* (0.02 M iodine in 75:20:5 v/v/v tetrahydrofuran:pyridine:water) and *acetonitrile wash* (Biotech grade purchased from EMI). Oligonucleotide syntheses were performed on a 1  $\mu\text{mol}$  scale using 500 - 2000 Å LCAA CPG. RNA phosphoramidites were prepared as 0.2 M solutions in anhydrous acetonitrile with coupling times of 3 min. For the synthesis of branch RNA, the branchpoint phosphoramidites (**2.16** or **2.24**) were also prepared as 0.2 M solutions in MeCN and coupled with an extended reaction time of 15 min.

RNA syntheses were performed using the following synthesis cycle: *Detritylation*: Dichloromethane wash (40 sec) followed by delivery of 3% dichloroacetic acid in dichloromethane (90 sec total) split into pulsed 60 sec, then 30 sec, *Coupling*: delivery of RNA phosphoramidites with activator (0.25 M ethylthiotetrazole in acetonitrile), *Capping*., delivery of Cap A and Cap B (12 sec) and *Oxidation*: delivery of oxidizing solution (0.02 M iodine in 75:20:5 v/v/v tetrahydrofuran:pyridine:water) for 14 sec followed by a wait period of 20 sec.

Single stranded RNA sequences were extended in the 3'→5' orientation on solid-phase until completion.

Branch and hyperbranch siRNA sequences (**4-7, 14-17**) and (**8-11**) were first grown in the 3'→5' position followed by coupling of the branchpoint phosphoramidite (**2.16**) and (**2.24**) respectively. The branchpoint phosphoramidite was coupled for 15 min, followed by a manual decyanoethylation step (2:3 v/v triethylamine:acetonitrile, 90 min) prior to the 2'-OMMT detritylation. The oligonucleotide bound CPG was washed with acetonitrile (30 mL) and replaced on the synthesizer to complete 3'→5' RNA synthesis of the antiparallel complimentary strand. The terminal 5'-OH was then capped with automated delivery of Cap A and Cap B (12 sec). Following siRNA synthesis, the 5'-levulinyl protecting group was removed by flushing the column with 0.5 M hydrazine hydrate buffered in 3:2 v/v pyridine:acetic acid (20 min). Following delevulination, the CPG-bound **4, 8, and 14** are cleaved and deprotected from the solid support for analysis and purification. For constructs (**5-7, 9-11, 15-17**) automated branch RNA synthesis was continued from the branchpoint 5'-OH. For hyperbranch sequences (**6, 7, 10, 11, 16 and 17**) an additional branch point phosphoramidite was coupled to the support-bound branch siRNA (**5**), and continued as previously described. In the case of hyperbranch siRNAs (**6, 7, 10, 11, 16 and 17**) reverse RNA phosphoramidites (Chemgenes Inc.) were incorporated to maintain the antiparallel duplex siRNA orientation.

#### **2.7.4 CLEAVAGE AND DEPROTECTION OF RNA**

Cleavage and deprotection of the synthesized RNA was performed after drying the synthesizer columns under Ar<sub>(g)</sub> for 10 min. CPG-bound RNA was then transferred into autoclaved screw-cap microtubes (1.5 mL) and treated with a 1 mL solution of 1:1 v/v

ammonium hydroxide/methylamine (AMA) (for UltraFast TBDMS RNA phosphoramidites, Glen Research Inc.) deprotection and heated at 65 °C for 10 min or standard RNA TBDMS phosphoramidites were treated with 3:1 v/v ammonium hydroxide in absolute ethanol at 55 °C for 16 to 20 hours. RNA samples were then evaporated *in-vacuo* and the CPG was washed twice with autoclaved distilled water (500 µL). Crude oligonucleotides were re-suspended in a mixture of 1:1 v/v dimethylsulfoxide:triethylamine trihydrofluoride (125 µL) to complete the 2'-desilylation reaction at 65 °C for 90 min. The crude RNA samples were subsequently precipitated from the reaction mixture with 3 M NaOAc (25 µL) in n-BuOH (1 mL). Precipitation was completed on dry ice for 1 h prior to centrifugation (12 000 rpm) leaving the crude oligonucleotides as a solid white pellet. For DMT-ON RNA purification, immediately after desilylation, samples were cooled to room temperature followed by addition of 1.75 mL of quenching buffer (Glen Research Inc). The quenched RNA samples were transferred to Glen-Pak RNA cartridges and purified according to the manufacturer's protocol. The collected RNA samples were dried in a Speedvac concentrator and re-suspended in autoclaved water (1 mL) for yield determination using UV absorbance measurements at 260 nm.

### **2.7.5 POLYACRYLAMIDE GEL ELECTROPHORESIS (PAGE)**

siRNA samples (**1-17**) were analyzed using denaturing PAGE. Analytical samples were prepared by drying 0.1 OD ( $A_{260}$ ) overnight and re-suspending the sample in a denaturing formamide solution (80% formamide in 10X TBE buffer) prior to loading on the gel. Samples were loaded (20 µL/well) along with dye solution (5 µL of 10 mL formamide mixed with trace amounts of bromophenol blue and xylene cyanol) to track gel migration. The gels were run at 500 V in 1X TBE running buffer on a 7 M urea (21 g), 18% polyacrylamide gel (acrylamide and

*N,N*-methylene bisacrylamide, 22.5 mL), prepared using 10x TBE buffer solution (5 mL) [tris(hydroxymethyl)aminomethane (TRIS) (54.5 g), boric acid (27.8 g) and ethylenediaminetetracetic acid (EDTA) (1.86 g) in autoclaved water (500 mL), pH 8] for 2 -3 hours. Gels were visualized under short range (265 nm) UV-shadowing and subsequently placed in a Stains-All<sup>®</sup> (Sigma) solution (25 mg Stains-All<sup>®</sup>, 50 mL isopropyl alcohol, 25 mL formamide, 125 mL water). After 2 h, the gel was removed from the stain solution and exposed to light for analyses.

For purification, branch and hyperbranch samples (**4-7**) were prepared using >6.0 OD ( $A_{260}$ ). Samples were loaded with formamide (150  $\mu$ L) and run at 500 V in 1X TBE running buffer until completion (2 -3 h). Desired product bands were excised from gel and incubated in 1 mL of autoclaved water overnight at 22 °C to complete the extraction of RNA from the gel. RNA was desalted using NAP-10 Sephadex G-25 (Illustra<sup>™</sup>) according to the manufacture's protocol and quantified using UV-Vis spectroscopy at 260 nm.

Pure siRNAs (**1-17**) were analyzed by native PAGE. Samples were prepared by hybridizing stoichiometric quantities (0.5 nmol) of complimentary single strands in 20  $\mu$ L of 1X TAE buffer (40 mM Tris, 20 mM acetic acid, and 1 mM EDTA pH 8.0) and 5  $\mu$ L of 30% sucrose solution in 1X TAE buffer. Branch and hyperbranch oligonucleotide (0.1 – 0.2  $\mu$ M) were directly dissolved in 30% sucrose loading buffer (30% sucrose in 5X TAE buffer). All samples were heated at 95 °C for 5 min cooled to room temperature over 1 h and stored at 4 °C overnight. A 18% native PAGE was prepared using 5 mL of 10X TBE buffer, 22.5 mL (acrylamide and *N,N*-methylene bisacrylamide) and 22.5 mL of autoclaved water. Gel was run at 500 V for 2.5 h and visualized under UV shadowing at 260 nm.

### **2.7.6 ION PAIRING REVERSE PHASE HPLC (IP RP HPLC)**

All samples (**1-17**) were analyzed by IP RP HPLC to determine purity. HPLC was performed on a Waters<sup>®</sup> 2695 Alliance Separations Module. Crude samples were dissolved in autoclaved water (0.1 OD for analytical) and injected into a Waters Symmetry C-18 reverse phase column (4.6 x 150 mm, 5 µm particle size, 120 Å) using a gradient of 10-95% (20% acetonitrile in 0.1 M triethylammonium acetate) at 60 °C with a flow rate of 1 mL/min over 23 min at 260 nm. Peak areas were calculated to determine percent purity of samples. IP RP HPLC was used to confirm siRNA purities >90% following purification.

### **2.7.7 MASS SPECTROMETRY**

siRNA samples (0.1-0.4 µM) were dissolved in autoclaved water and analyzed by mass spectrometry. Samples were analyzed by Dr. Mark Hail at Novatia LLC, Newton, PA, utilizing Oligo HTCS equipped ESI/MS in negative mode. The data was obtained and deconvoluted using ProMass software. Theoretical molecular weights were calculated by entering each sequence on IDT website OligoAnalyzer 3.1 or on Mongo and analyzing the sequence; <http://www.idtdna.com/analyzer/Applications/OligoAnalyzer>, or <http://rna-mdb.cas.albany.edu/RNAmods/rnamass.htm> respectively.

## CHAPTER 3. STRUCTURE AND BIOPHYSICAL STUDIES OF siRNAs

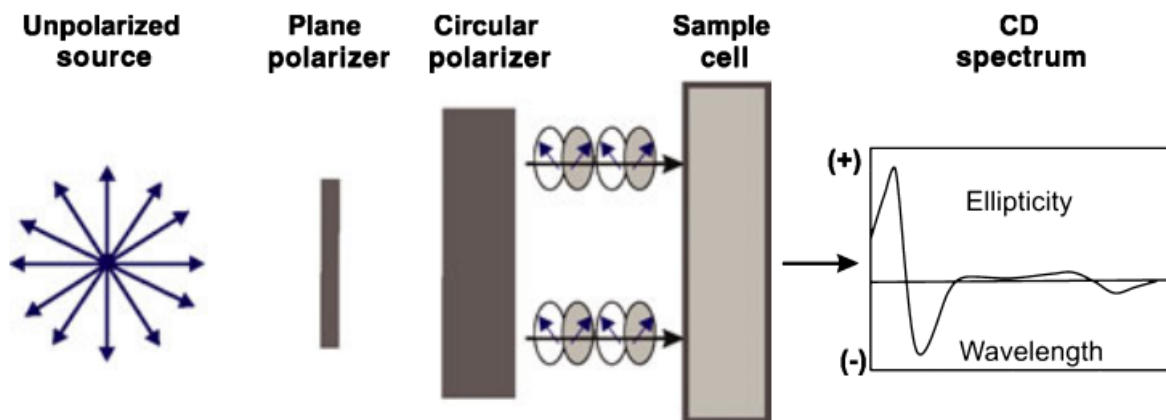
### 3.1 ABSTRACT

Methods for characterizing siRNA structure and biophysical properties are highlighted in this chapter. Specifically, Circular Dichroism (CD) spectroscopy was used to investigate siRNA secondary structure in physiological conditions. Linear, branch and hyperbranch siRNAs were all found to exhibit the putative A-type helix, which is the trademark RNA structure associated with double-stranded RNA sequences. Moreover, thermal denaturation experiments using UV-Vis spectrophotometry were used to evaluate hybrid stability at 260 nm (% hyperchromicity) with changes in temperatures (5-90 °C). The melting temperatures at which 50% of the hybrids dissociates to single-strands ( $T_m$ ) were used to evaluate the thermal stabilities of the siRNAs. Branch and hyperbranch siRNAs displayed stable hybrid structures ( $T_m$ : 68 - >90 °C) relative to the linear controls ( $T_m$ : 67 - 76 °C), and in some cases were found to contain multiple hybrid-to-single-strand transitions. These results were found to be consistent with stable unimolecular RNA hybrids, such as those associated with RNA hairpins and with more complex RNA structures which contain multiple complementary sequences that can denature at elevated temperatures. Moreover, the 2'-OMe siRNAs were found to display well defined A-type helical structures and stable thermal denaturation curves ( $T_m$ : >90 °C) relative to the native sequences. Thus, linear, branch and hyperbranch siRNAs were found to exhibit the pre-requisite hybrid structures and stabilities for triggering the RNAi response.

## 3.2 INTRODUCTION

### 3.2.1 CD SPECTROSCOPY OF RNA

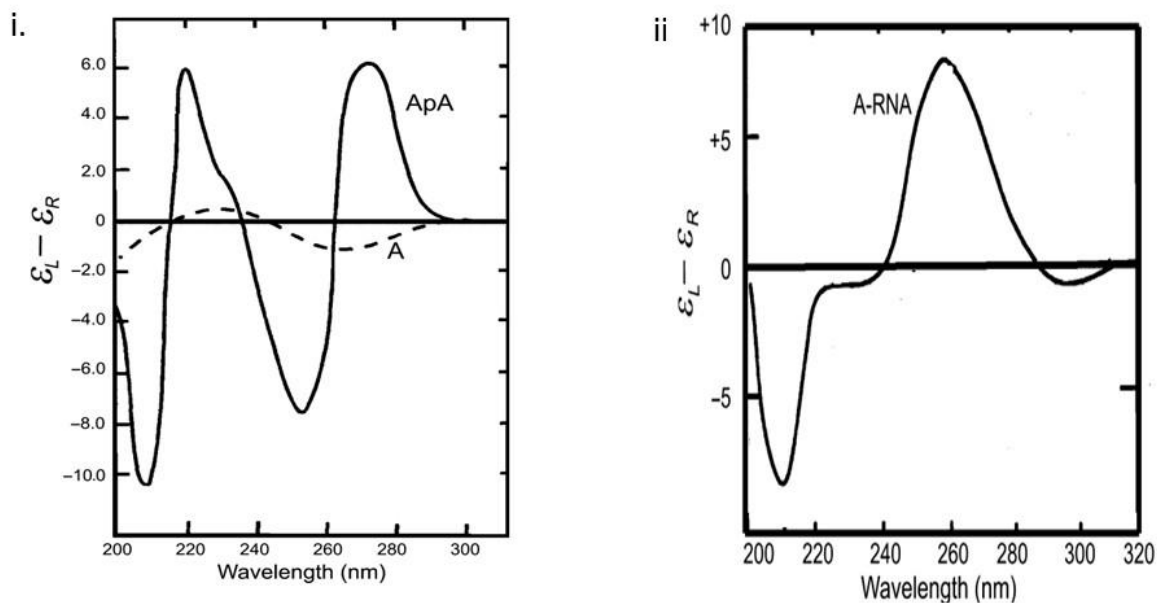
Circular Dichroism (CD) spectroscopy determines the effects of circularly polarized light on an asymmetric molecule.<sup>1</sup> In this application, unpolarized light from a suitable source (*e.g.* Xenon arc lamp) is filtered by a monochromator which selects the wavelengths of interest, typically in the far UV-region (190 - 310 nm) for biomacromolecules, while minimizing stray light. The beam is then deflected by mirrors and prisms into a plane polarizer which focuses the light in the same direction before it passes through a photoelastic modulator. This circular polarizer produces left and right-handed circularly polarized light. The circularly polarized light then passes through the sample compartment where it interacts with the analyte and produces a CD signal (ellipticity) as a function wavelength (**Figure 3.1**). The interaction between chromophoric chiral molecules and circularly polarized light has been shown to provide important structural information of simple asymmetric molecules and more challenging macromolecules.<sup>2</sup> Thus, any conformational change in an asymmetric molecule that can absorb light can be studied by CD spectroscopy. This technique is especially advantageous for the rapid structure determination of complex biomacromolecules such as proteins, DNA and RNA.<sup>3</sup> This technique produces very sensitive and well resolved structural characteristics of biological molecules in dilute solutions (low  $\mu\text{M}$  concentrations) which mimic physiological conditions, and thereby providing insight on its biologically active structure. Moreover, a CD analysis is a relative experiment, in which a CD spectrum of an unknown sample is typically compared with suitable controls to determine structural differences and similarities between samples. Therefore, CD spectroscopy is an ideal method for producing quick structural analyses of complex, biologically active molecules.



**Figure 3.1.** CD spectroscopy method and sample analysis.<sup>2</sup>

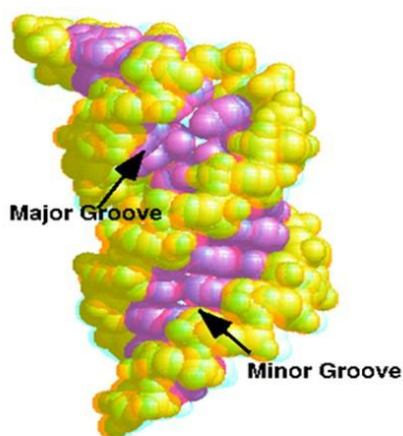
Nucleic acids own the ability to absorb circularly polarized light and emit a CD spectrum contingent on their conformations. This is due to the chiral sugar component and the aromatic nucleobases that absorb light strongly in the UV region ( $\epsilon_{260 \text{ nm}}$ : Ade = 15, 340, Cyt = 7,600, Gua = 12, 160, Ura = 10, 210) resulting in  $\pi \rightarrow \pi^*$  transitions.<sup>4</sup> In the case of single-stranded RNA, the CD spectrum depends on the chirality of the sugar-phosphate backbone and the absorption of the nucleobases, relating their stacking arrangement in solution. For example, the CD spectrum of the dinucleotide ApA, originates from the chiral adenine-adenine interaction which projects a CD signature that contains a combination of positive and negative extrema at 260 nm, referred to as exciton bands (**Figure 3.2, i**).<sup>2,5</sup> In comparison, the CD spectrum for double-stranded RNA is strikingly distinct, featuring a maximum band near 260 nm, a minimum one near 210 nm and less intense exciton bands in between 290 – 310 nm (**Figure 3.2, ii**).<sup>2,6</sup> This CD signature corresponds to A-type RNA, which is the canonical double-stranded RNA structural motif characterized as an anti-parallel, complementary, right-handed, helical duplex structure.<sup>7</sup>



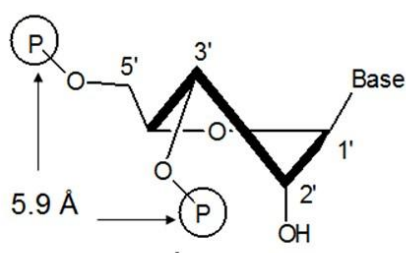


**Figure 3.2.** CD Spectra of i. ApA dinucleotide vs. Adenosine and ii. A-type double-stranded RNA helix.<sup>2</sup>

The A-type RNA double-stranded helix is pre-organized by a nucleotide sugar pucker conformation which adopts a *Northern* or *C3'-endo* geometry.<sup>8</sup> In this conformation, the C3' and C5' carbons lie above the median plane defined by C1'-O4'-C4' such that the C5'-C3'-phosphate diester bond distance is reduced to 5.9 Å. This conformational restraint results in a more compact duplex conformation with 11 base pairs per helical turn and distances between base-pairs along the helix axis of 2.6 Å. Furthermore, the bases are displaced by 4.5 Å from the parallel helix axis creating a deep but narrow *major groove* and shallow but broad *minor groove*. This conformation is also stabilized by the O4'-O2' *anomeric effect* and the *gauche effects* of the O2'-C2'-C1'-O4' torsion angles.<sup>8</sup> These characteristics generate the geometric parameters found in A-RNA duplexes (**Figure 3.3**).<sup>9</sup>



**A-form RNA**



**C3'-endo**

**A-Form RNA**

i.	Helical Sense:	Right
ii.	Sugar Conformation:	C3'-endo
iii.	Helix Diameter:	25.5 Å
iv.	Residues/Turn:	11
v.	Base-pair distance	
	from axis center:	4.5 Å
vi.	Major Groove	
	width:	2.7 Å
	depth:	13.5 Å
	Minor Groove	
	width:	11 Å
	depth:	2.8 Å

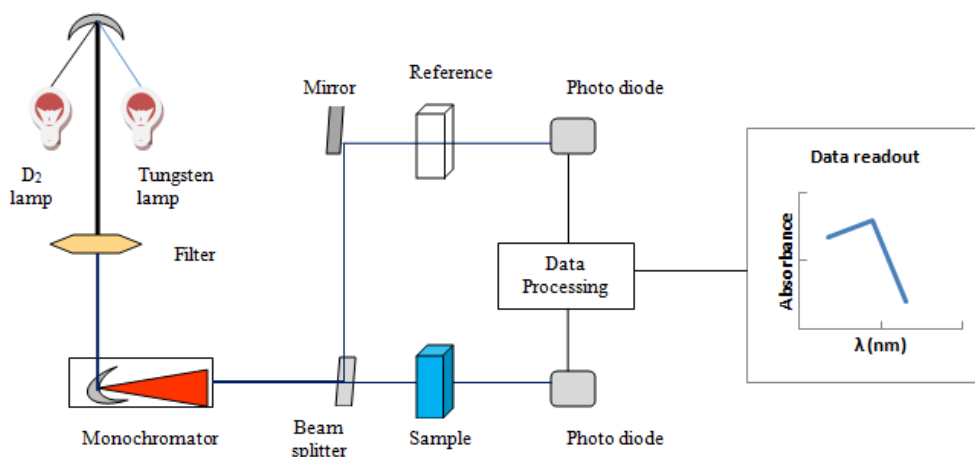
**Figure 3.3.** The global helical conformation of A-RNA and its preferred sugar conformation. Structures and data adapted from reference 9.

Considering siRNA encompass a class of short (18-21 nucleotides) double-stranded RNA, CD spectroscopy is perfectly suitable for studying the structures of native and modified sequences. The A-form RNA geometry is a pre-requisite for siRNA binding to RISC and for stimulating RNAi activity. Moreover, the incorporation of modified nucleic acids have been shown to improve the pharmacokinetic properties of the siRNAs, while instilling more potent gene silencing effects. For example, the selective incorporation of 2'-OMe RNA was found to reduce toxic 'off-target' gene silencing effects.<sup>10</sup> Meanwhile, the incorporation of 2'-deoxy-2'-fluoro-4'-thioarabouridine (4'-S-FAU) within siRNA was shown to maintain A-type RNA structure while triggering RNAi activity targeting the firefly luciferase gene.<sup>11</sup>

### 3.2.2 UV-VIS SPECTROSCOPY OF RNA

UV-Vis (absorption) spectroscopy measures the interaction of light in the near UV (190 – 400 nm) to visible region (400 – 800 nm) with a suitable chromophore.<sup>12</sup> The chromophore is typically a conjugated molecule (*e.g.* aromatic) owning the ability to absorb light and inducing an electronic transition from a ground to excited state (*e.g.*  $\pi \rightarrow \pi^*$ ). The absorption of light by the sample at a given wavelength produces an absorption spectrum.

UV-Vis spectrophotometers<sup>12</sup> are equipped with two light sources, typically a deuterium lamp for the UV region and a tungsten-halogen lamp for the visible region. The light source passes through a monochromator which focuses the beam of light onto the sample. Based on the molar absorptivity of the sample, concentration of the solution and path length of the cell, light is absorbed (while some is transmitted) and detected by a photomultiplier or a photodiode detector. The UV-Vis (absorption) spectrum correlates the absorbance of the solute in a transparent solvent (*e.g.* buffer) at a given wavelength (**Figure 3.4**).



**Figure 3.4.** Schematic of UV-Vis absorption spectrophotometer.

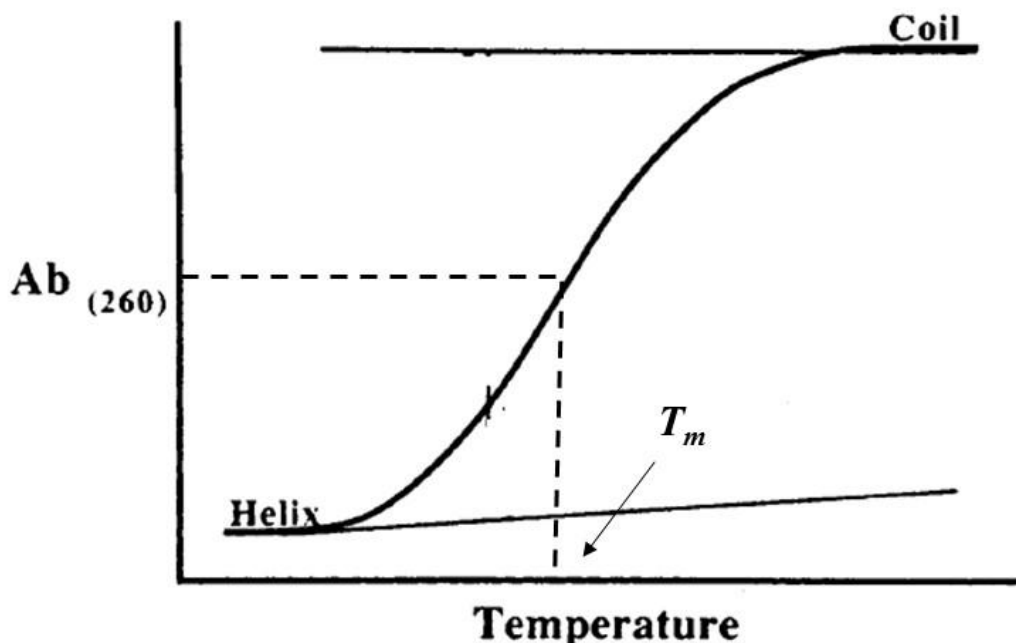
UV-Vis (absorption) spectroscopy can correlate the concentration of the sample in solution for quantitative measurements. Moreover, this method can also provide information on ligand-binding interactions, conformational transitions and thermodynamic properties of complex biomacromolecules.<sup>12</sup>

Absorption spectroscopy is particularly well suited for RNA analyses. This is due to the favorable absorptivities of the nucleobases in the far-UV (210-310 nm) region ( $\epsilon_{260\text{ nm}}$ : Ade = 15, 340, Cyt = 7,600, Gua = 12, 160, Ura = 10, 210).<sup>4</sup> This property facilitates the quantitative determination of RNA in solution.<sup>12</sup> For example, the optical density (O.D.) measures the absorption of RNA at 260 nm ( $A_{260\text{ nm}}$ ) in 1 mL of buffer and analyzed in a 1 cm path length cuvette. Stoichiometric measurements can be calculated using the Beer-Lambert law (**equation 3.1**), which correlates the absorption of the RNA sample at 260 nm ( $A_{260\text{ nm}}$ ) with its concentration ( $c$ , mol/L) in solution, the molar absorptivity of the RNA sequence ( $\epsilon$ ,  $\text{Lmol}^{-1}\text{cm}^{-1}$ ) and the path length of the cuvette ( $\ell$ , cm).

$$A_{260\text{ nm}} = \epsilon c \ell \quad \text{equation 3.1}$$

Changes in RNA secondary structures can also be monitored by absorption spectroscopy.<sup>13-14</sup> For example, increases in UV absorptivities typically accompanies transitions from ordered RNA duplexes to random single-stranded forms. This change in hyperchromicity is associated with the ability for the RNA nucleobases to absorb light strongly as ‘open’ single-strands vs. ‘closed’ hybrids. Denaturing agents such as formamide, urea and heat have all been applied to disrupt the Watson-Crick hydrogen bonding interactions between the complementary strands. The ability to resist hybrid denaturation provides a measurement of hybrid stability.

This is the case with thermal denaturation experiments, which monitors the % changes in hyperchromicities at 260 nm with increasing temperatures.<sup>13</sup> The melting curve describes a phase transition for the melting of a duplex to single-stranded form (**Figure 3.5**). The midpoint of this curve provides the melting temperature ( $T_m$ , °C) at which 50% of the RNA duplex has denatured to single-stranded form (helix-coil transition). Basically, the higher the melting temperature the more stable the hybrid structure.

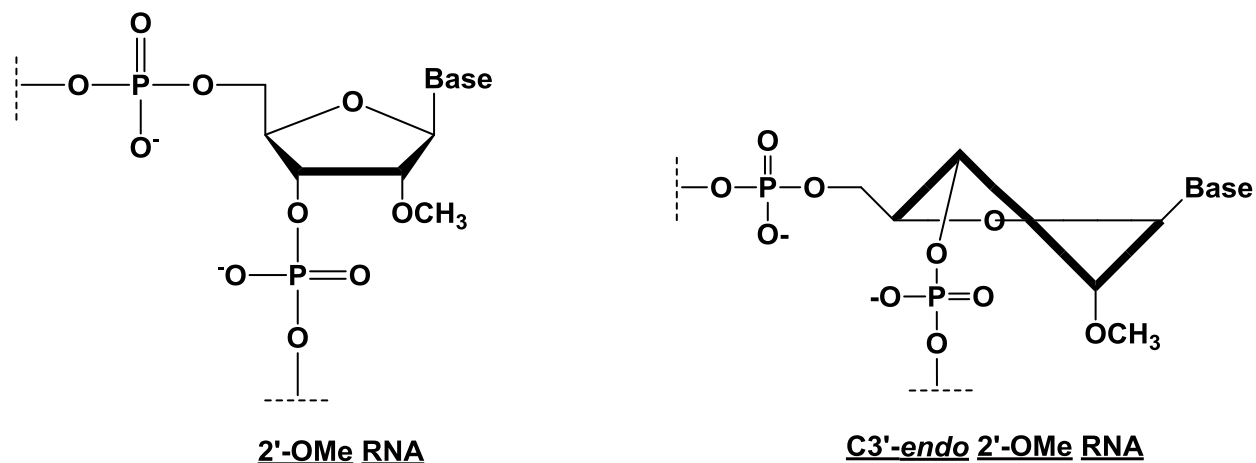


**Figure 3.5.** Typical melting curve displaying the phase transition from helix-coil at 260 nm with increasing temperatures.<sup>14</sup>

Since RNA hybrid thermal stability can be determined from the melting curves, this experiment may also lead to a thorough thermodynamic analysis of the folded RNA structure.<sup>14</sup> RNA thermal denaturation thus provides the basis for calculating thermodynamic data associated with this energy driven process. These include: standard free energy changes in hybrid stability ( $\Delta G^\circ$ ), enthalpy measuring the heat changes during the temperature dependent thermal melt

( $\Delta H^\circ$ ) and the entropy gain ( $\Delta S^\circ$ ) during the helix-to-coil transition. These calculations are thoroughly reviewed elsewhere<sup>14</sup>, and will not be further discussed in this study.

Stable siRNA hybrids and related analogs have been shown to trigger potent gene silencing effects. This is especially the case with the site specific incorporations of 2'-OMe RNA within bio-active siRNA sequences. 2'-OMe RNA stabilizes the requisite C3'-endo sugar pucker in an A-type helical arrangement due to favorable *anomeric* and *gauche* interactions (**Figure 3.6**).<sup>8,15</sup> This effect has been shown to produce effective GRP78 silencing siRNA in HeLa cells.<sup>16</sup> Moreover, the 2'-OMe RNA modifications were also found to increase siRNA metabolic stability leading to extended RNAi activity, while minimizing the silencing of unintended gene targets which diminishes toxicity.<sup>10,16</sup> The latter is a focal point of our study, which aims to develop potent GRP78 siRNAs for applications in cancer-targeting gene therapy (Chapter 4).



**Figure 3.6.** Structure and conformation of 2'-OMe RNA

### 3.3 CHAPTER OBJECTIVES

The bio-physical and structural studies of linear, branch and hyperbranch siRNAs will be reported in this chapter. These studies are essential in determining the pre-requisite siRNA structure for biological activity. In the RNAi pathway, the RNA-Induced Silencing Complex (RISC) recognizes and binds to an A-type double-stranded RNA helix. This structure has been found to be the bio-active conformation for high affinity and selective RNA substrate binding to the active site of RISC.<sup>17</sup> Moreover, this protein complex also contains enzymatic activity associated with RNA hydrolysis.<sup>18</sup> Thus, A-form siRNA structure and duplex stability are necessary requirements for RISC recognition and mRNA cleavage activity in order to stimulate potent gene silencing effects *in vivo*. In this chapter a variety of siRNA sequences and motifs targeting GRP78 mRNA will be studied using CD spectroscopy (structure analyses) and UV-Vis thermal denaturation (hybrid stability) in order to elucidate their suitability for RNAi application (Chapter 4).

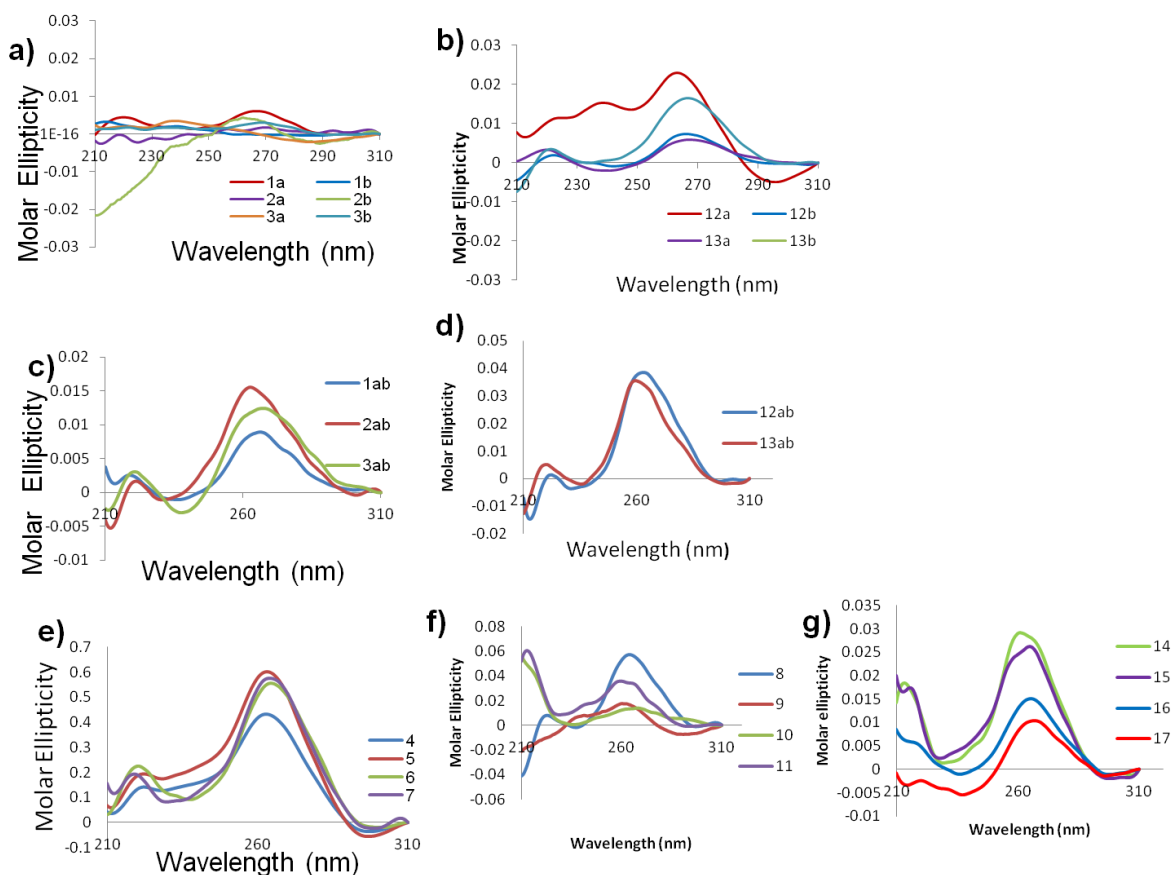
### 3.4 RESULTS AND DISCUSSION

#### 3.4.1 CD SPECTROSCOPY OF siRNAs

In order to assess whether the siRNAs described in Chapter 2 of this thesis (**Table 2.1, sequences 1-17**) adopt the pre-requisite A-type duplex for RNAi activity, CD spectroscopy<sup>1-6</sup> was used to determine their secondary structures relative to single strand controls (**Figure 3.7**). Briefly, siRNA samples were prepared by annealing complementary sequences in a physiologically relevant phosphate buffer (50  $\mu$ M, 140 mM KCl, 1.0 mM MgCl<sub>2</sub>, 5.0 mM Na<sub>2</sub>HPO<sub>4</sub>, pH 7.2) prior to structural analyses by CD spectroscopy. Linear GRP78 siRNA<sup>16</sup> demonstrated typical CD profiles for A-form helices, displaying small minimum bands at 210

and 240 nm in addition to a broad maximum between 255-290 nm (**Figure 3.7, c, d**).<sup>6</sup> These characteristic signatures in the CD spectrum were distinct from the single-strand controls (**Figure 3.7, a, b**), which were found to display random coils with weak exciton bands at around 260 nm corresponding to the absorptivities of the nucleobases.<sup>2</sup> In the case of the branch and hyperbranch sequences (**Figure 3.7, e-g**), the A-type broad maximum and minimum bands were also observed between 255-290 nm and at 210, 240 nm, respectively, albeit with a decrease in the amplitudes of molar ellipticities at these characteristic wavelengths. This suggests some of the branch hybrids may contain varying proportions of random coil. This is not entirely surprising, considering the branchpoint nucleotide has been found to slightly distort duplex structure by restricting the complementary strands within a single molecular structure.<sup>9</sup> Nevertheless, branch oligonucleotides were found to maintain their putative geometry for triggering biological activity.<sup>9,19</sup> In this case, the branch siRNAs composed of the un-natural 2',5'- and vicinal 3',3'-phosphodiester linkages were found to be particularly un-stable, leading the hydrolysis of the branchpoint linkages and release of the single strands (**Figure 3.7, f**).<sup>9</sup> In spite of this change, branch and hyperbranch sequences generally maintained CD signatures that were consistent with the canonical A-like helical structures. Thermal denaturation experiments were next conducted to determine the thermal stabilities of the duplex structures.





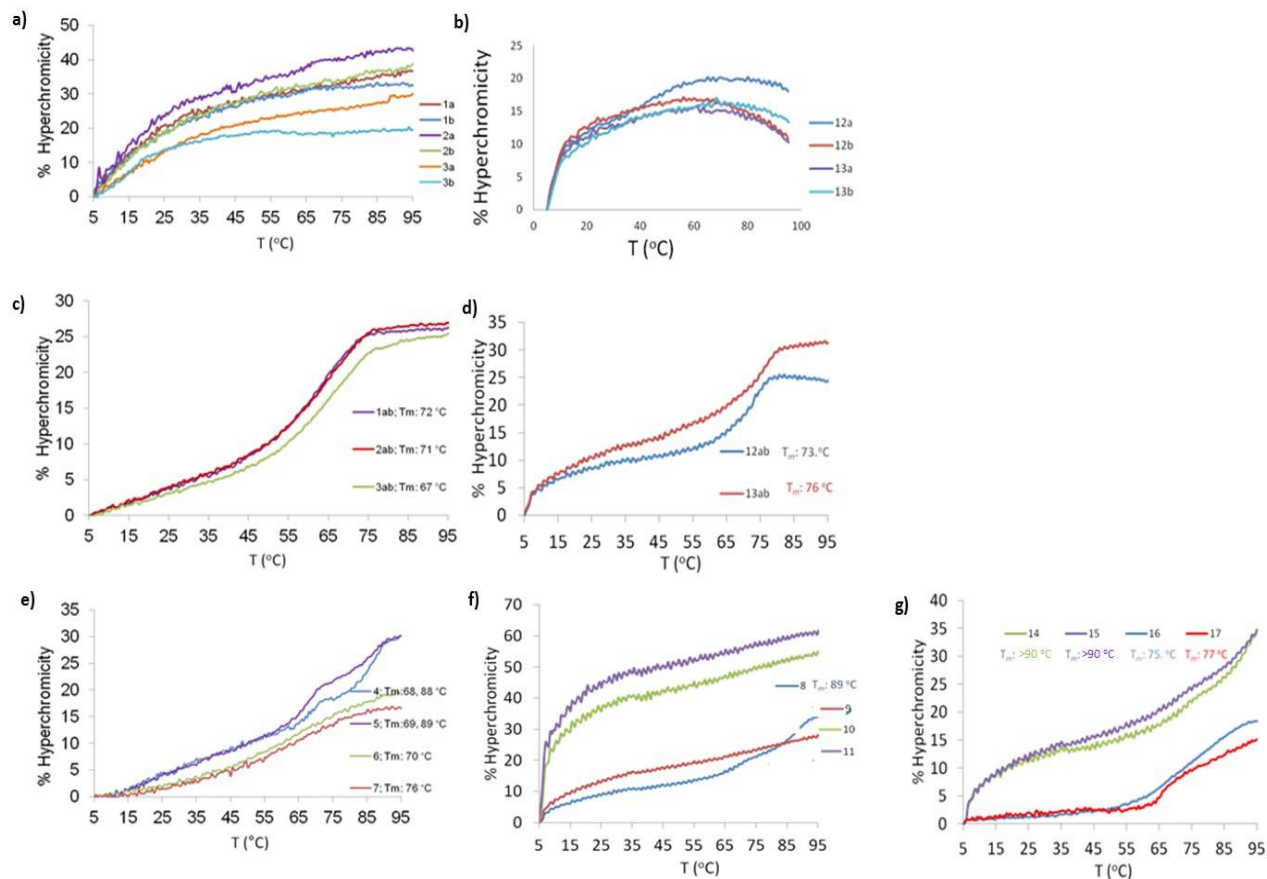
**Figure 3.7.** CD spectroscopy of the siRNA sequences described in this study (**Table 2.1**).

### 3.4.2 UV-VIS SPECTROSCOPY OF siRNAs

In order to assess the duplex stabilities of the branch and hyperbranch siRNAs relative to their linear controls, thermal denaturation experiments were conducted. The siRNAs (**Table 2.1, sequences 1-17**, 0.10 - 0.40  $\mu\text{M}$ ) were prepared as previously described for the CD studies, by annealing samples in physiological phosphate buffer (140 mM KCl, 1 mM  $\text{MgCl}_2$ , 5 mM  $\text{Na}_2\text{HPO}_4$ , pH 7.2) followed by the bio-physical studies using UV-Vis spectroscopy<sup>12-14</sup> (**Figure 3.8**). Linear single stranded RNAs had little or no hyperchromic shifts in the  $T_m$  studies (**Figure 3.8, a, b**). However, once annealed, linear siRNA sequences **1-3**, gave characteristic thermal denaturation curves that were consistent with a helix-to-coil transitions, ( $T_m$ : 67 – 72  $^\circ\text{C}$ , **Figure**

**3.8, c**). Site specific incorporation of 2'-OMe RNA within the native siRNA sequences **1** and **2**, produced more stable hybrids ( $\Delta T_m$ : +1 and +5 °C, for **12** and **13**, respectively) with consistent changes in hyperchromicities ( $\Delta H$ : 25-30%) during thermal denaturation (**Figure 3.8, c and d**). Branch and hyperbranch sequences, **4-7**, exhibited broad thermal denaturation curves suggesting multiple helix-to-coil transitions (**Figure 3.8, e**). These results are consistent with those associated with more complex RNA motifs, from which each helix-to-coil transition may be measured at a distinct  $T_m$  value.<sup>20</sup> Moreover, the branch and hyperbranch siRNAs, **4-7**, displayed greater thermal stabilities ( $T_m$ : 68 – 89 °C) and enhanced hyperchromicities (%H: 5-35 %) relative to their linear controls ( $T_m$ : 67 - 72 °C and %H: 5-25%). Considering that structurally related RNA hairpins possess thermodynamically more stable folded structures relative to their linear double-stranded sequences, the enhanced hybrid stabilities observed for the branch siRNAs was not unexpected.<sup>21</sup> Consistent with the CD data, the branch siRNAs composed of the un-natural 2',5'- and vicinal 3',3'-phosphodiester linkages were found to be particularly unstable, leading to broad  $T_m$  curves that were reminiscent of the linear single strand controls (**Figure 3.8, a and f**). Whereas the branch siRNAs composed of the 2'-OMe RNA inserts, **14-17**, ( $T_m$ : 75 – 77 and >90 °C, **Figure 3.8, g**) were found to produce more stable hybrids when compared to the native branch sequences, **4-7**, ( $T_m$ : 69 – 89 °C, **Figure 3.8, e**). This was found to correlate with literature precedence, which reports that 2'-OMe RNA stabilizes the requisite C3'-endo sugar pucker in an A-type helical arrangement due to favorable *anomeric* and *gauche* interactions (**Figure 3.6**).<sup>8,15</sup> These results are also in agreement with the native polyacrylamide gel electrophoresis (**Figure 2.15**) and CD spectroscopy (**Figure 3.7**) data which displayed stable, higher ordered A-type helical structures for the branch and hyperbranch sequences in comparison

to the linear double stranded siRNA controls. In light of their enhanced duplex stabilities and A-type helices, branch and hyperbranch siRNAs were next evaluated for RNAi activity (Chapter 4).



**Figure 3.8.** Thermal denaturation curves of the siRNA sequences described in this study (Table 2.1).

### 3.5 CONCLUSIONS

In this chapter, siRNA structure and biophysical properties have been validated. CD spectroscopy was used to confirm the A-type helical geometry for the siRNAs in physiological buffer. Moreover, thermal denaturation experiments using UV-Vis spectrophotometry revealed the melting temperatures ( $T_m$ ) of the siRNAs at 260 nm. In general, branch and hyperbranch

siRNAs displayed stable hybrid structures ( $T_m$ : 68 - >90 °C) relative to the linear controls ( $T_m$ : 67 - 76 °C). These results were found to be consistent with those associated with RNA hairpins that can form stable hybrids from a single molecular structure. Interestingly, short hairpin RNA (shRNA) have also been implicated in the RNAi response leading to potent gene silencing effects.<sup>22</sup> Moreover, the 2'-OMe siRNAs were found to display well defined A-type helical structures and stable thermal denaturation curves ( $T_m$ : >90 °C) relative to the native sequences. This highlights their potential utility in stabilizing the canonical siRNA structure for RNAi activity.<sup>10, 16</sup> Exceptionally, the branch siRNAs encompassing the labile 2',5'- and 3',3'-phosphodiester bonds at the branchpoint positions were found to produce unstable hybrids according to the CD and thermal denaturation data. Thus, linear, branch and hyperbranch siRNAs were found to generally display the pre-requisite hybrid structures and stabilities for triggering the RNAi response. The biological activity of the siRNAs synthesized in this study (**Table 2.1, sequences 1-17**) will be highlighted in Chapter 4.

### 3.6 REFERENCES

1. Abu-Shumays, A.; Duffield, J.J. Circular Dichroism Theory and Instrumentation. *Anal. Chem.* **1966**, *38*, 29A-58A.
2. Ranjbar, B.; Gill, P. Circular Dichroism Techniques: Biomolecular and Nanostructural Analyses- A Review. *Chem. Biol. Drug Des.* **2009**, *74*, 101-120.
3. (a) Hammes, G.G. Spectroscopy for the Biological Sciences. 2005, New York USA, John Wiley & Sons, Inc., (b) Berova, N.; Nakanishi, K.; Woody, R.W. Circular Dichroism: Principles and Applications, 2000, 2<sup>nd</sup> ed. New York, USA, Wiley-VCH., (c) Fasman, G.D. Circular Dichroism and the Conformational Analysis of Biomolecules. New York, USA, Plenum Publishing Corp.
4. Gray, D.M.; Hung, S.H.; Johnson, K.H., Absorption and circular dichroism spectroscopy of nucleic acid duplexes and triplexes. In *Methods in Enzymology*, **1995**, *246*, 19-34.
5. (a) Warshaw, M.M.; Cantor, C.R. Oligonucleotide interactions. IV. Conformational Differences between deoxy and ribodinucleoside phosphates. *Biopolymers* 1970, *9*, 1079-1103., (b) Bloomfield, V.A.; Crothers, D.M.; Tinoco, I. Jr. Nucleic Acids: Structures, Properties and Functions. **2000**, Sausalito, California USA: University Science Books.
6. Gray, D.M.; Liu, J.J.; Ratliff, R.L.; Allen, F.S. Sequence dependence of the circular dichroism of synthetic double-stranded RNAs. *Biopolymers* **1981**, *20*, 1337-1382.
7. (a) Tanaka, Y.; Fujii, S.; Hiroaki, H.; Sakata, T.; Tanaka, T.; Uesugi, S.; Tomita, K.; Kyogoku, Y. A-form RNA double helix in a single crystal structure of r(UGAGCUUCGGCUC). *Nucleic Acids Res.* **1999**, *27*, 949-959, (b) Arnott S, Hukins DW, Dover SD. Optimized parameters for RNA double helices. *Biochem. Biophys. Res. Commun.* **1972**, *48*, 1392-1399.
8. (a) Thibaudeau, C.; Plavec, J.; Watanabe, K.A. and Chattopadhyaya, J. How do the aglycones drive the pseudorotational equilibrium of the pentofuranose moiety in C-nucleosides? *J. Chem. Soc. Chem. Comm.* **1994**, 537-540, (b) Thibaudeau, C.; Plavec, J.; Garg, N.; Papchikhin, A. and Chattopadhyaya, J. How Does the Electronegativity of the Substituent Dictate the Strength of the Gauche Effect? *J. Am. Chem. Soc.* **1994**, *116*, 4038-4043. (c) Ruben, E.A.; Plumely, J.A.; Chapman, M.S.; Evanseck, J.D. Anomeric Effect in 'High Energy' Phosphate Bonds. Selective Destabilization of the Scissile Bond and Modulation of the Exothermicity of Hydrolysis. *J. Am. Chem. Soc.* **2008**, *130*, 3349-

- 3358, (d) Li, L.; Szostak, J.W. The Free-Energy Landscape of Pseudorotation in 3'-5' and 2'-5' Linked Nucleic Acids. *J. Am. Chem. Soc.* **2014**, *136*, 2858-2865.
9. Sabatino, D. Expanding the Size and Shape of Nucleic Acids: Studies on branched and heptose based nucleic acids. *Ph.D. Thesis*, **2007**, McGill University, Montreal Canada.
10. Jackson, A.L.; Burchard, J.; Leake, D.; Reynolds, A.; Schelter, J.; Guo, J.; Johnson, J.M.; Lim, L.; Karpilow, J.; Nichols, K.; Marshall, W.; Khvorova, A.; Linsley, P.S. Position-specific chemical modification of siRNAs reduces "off-target" transcript silencing. *RNA* **2006**, *12*, 1197-1205.
11. Watts, J.K.; Choubdar, N.; Sadalpure, K.; Robert, F.; Wahba, A.S.; Pelletier, J.; Pinto, B.M.; Damha, M.J. 2'-Fluoro-4'-thioarabino modified oligonucleotides: conformational switches linked to siRNA activity. *Nucleic Acids Res.* **2007**, 1-11.
12. Schmid, F.X. Biological Macromolecules: UV-visible Spectrophotometry. *Encyclopedia Life Sci.* **2001**, 1-4.
13. (a) Lacroix, J.-L. M. L., Analysis of Thermal Melting Curves. *Oligonucleotides* **2003**, *13*, 515-537, (b) Owczarzy, R., Melting temperatures of nucleic acids: Discrepancies in analysis. *Biophys. Chem.* **2005**, *117*, 207-215.
14. (a) Nikolova, E.N.; Al-Hashimi, H.M. Thermodynamics of RNA Melting. *RNA* **2010**, *16*, 1687-1691, (b) Marky, L.A.; Breslauer, K.J. Calculating Thermodynamic Data for Transitions of any Molecularity from Equilibrium Melting Curves. *Biopolymers* **1987**, *26*, 1601-1620, (c) Puglisi, J.D.; Tinoco Jr., I.; Absorbance Melting Curves of RNA. *Meth. Enzym.* **1989**, *180*, 304-325.
15. Blommers MJ, Piele U, De Mesmaeker A. An approach to the structure determination of nucleic acid analogues hybridized to RNA. NMR studies of a duplex between 2'-OMe RNA and an oligonucleotide containing a single amide backbone modification. *Nucleic Acids Res.* **1994**, *22*, 4187-4194.
16. Suzuki, T.; Lu, J.; Zahed, M.; Kita, K.; Suzuki, N. Reduction of GRP78 expression with siRNA activates unfolded protein response leading to apoptosis in HeLa cells. *Arch. Biochem. Biophys.* **2007**, *468*, 1-14.

17. Rana, T. Illuminating the Silence: Understanding the Structure and Function of small RNAs *Nature* **2007**, *8*, 23-36.
18. Liu, J.; Carmell, M.A.; Rivas, F.V.; Marsden, C.G.; Thomson, J.M.; Song, J.J.; Hammond S.M.; Joshua-Tor L.; Hannon, G.J. Argonaute2 is the catalytic engine of mammalian RNAi. *Science*. **2004**, *305*, 1437-1441.
19. Katolik, A.; Johnsson, R.; Montemayor, E.; Lackey, J.G.; Hart, P.J.; Damha, M.J. Regiospecific Solid-Phase Synthesis of Branched Oligoribonucleotides That Mimic Intronic LariatRNA Intermediates. *J. Org. Chem.* **2014**, *79*, 963-975.
20. Ballin, J.D.; Bharill, S.; Fialcowitz-White, E.J.; Gryczynski, I.; Gryczynski, Z.; Wilson, G.M. Site-specific variations in RNA folding thermodynamics visualized by 2-aminopurine fluorescence. *Biochemistry* **2007**, *46*, 13948-13960.
21. Khvorova, A.; Reynolds, A.; Jayasena, S. D., Functional siRNAs and miRNAs Exhibit Strand Bias. *Cell* **2003**, *115*, 209-216.
22. Dallas, A.; Johnston, B.H. Design and chemical modification of synthetic short shRNAs as potent RNAi triggers. *Methods Mol. Biol.* **2013**, *942*, 279-290.

## 3.7 EXPERIMENTAL SECTION

### 3.7.1 UV-VIS SPECTROSCOPY

siRNAs (0.1 - 0.5  $\mu\text{M}$ , **Table 2.1 sequences 1-17**) were annealed in physiological phosphate buffer (1.0 mL, 140 mM KCl, 1.0 mM  $\text{MgCl}_2$ , 5.0 mM  $\text{Na}_2\text{HPO}_4$ , pH 7.2) and heated at 95  $^\circ\text{C}$  for 5 min and allowed to cool to room temperature for 1 h and stored at 4  $^\circ\text{C}$  overnight prior to thermal denaturation experiments. Complementary siRNA strands were measured on a CARY 3E, UV-Vis spectrophotometer equipped with a temperature controller monitoring the changes in hyperchromicities at 260 nm with increasing temperatures (5-95  $^\circ\text{C}$  at 0.5  $^\circ\text{C}/\text{min}$ ). Nitrogen was used to prevent condensation at lower temperatures (<20  $^\circ\text{C}$ ). The melting temperature ( $T_m$ ) was calculated from the first derivative plots of the melting curves, representing the temperature at which 50% of the duplex has denatured to the corresponding single strands. This data was exported into an Excel<sup>TM</sup> spreadsheet for plotting the  $T_m$  curves.

### 3.7.2 CD SPECTROSCOPY

Samples were prepared in similar fashion to the  $T_m$  experiments, briefly, siRNAs (0.10 - 0.50  $\mu\text{M}$ , **Table 2.1 sequences 1-17**) in physiological phosphate buffer, 140 mM KCl, 1.0 mM  $\text{MgCl}_2$ , 5.0 mM  $\text{Na}_2\text{HPO}_4$  pH 7.2. Annealed siRNAs were transferred to fused quartz cells with a 1 cm path length and maintained within the cell holder at 10  $^\circ\text{C}$  under  $\text{N}_2$  for 10 minutes prior to spectral acquisition. Spectra were collected using a Laurier AVIV 62A DS CD spectrophotometer as an average of 3 scans with a 1.0 nm band width interval and a 0.5 nm step interval. Spectra were analyzed between 210 and 310 nm and raw data was processed using J-700 Windows<sup>®</sup> software (version 1.00) and correcting by subtracting the buffer followed by smoothing the data points. The data was then exported into Windows Excel<sup>TM</sup> spreadsheet



software for plotting the CD spectra as changes in molar ellipticities with increasing wavelengths.

## CHAPTER 4. RNAi ACTIVITY OF GRP78 TARGETING siRNAs

### 4.1 ABSTRACT

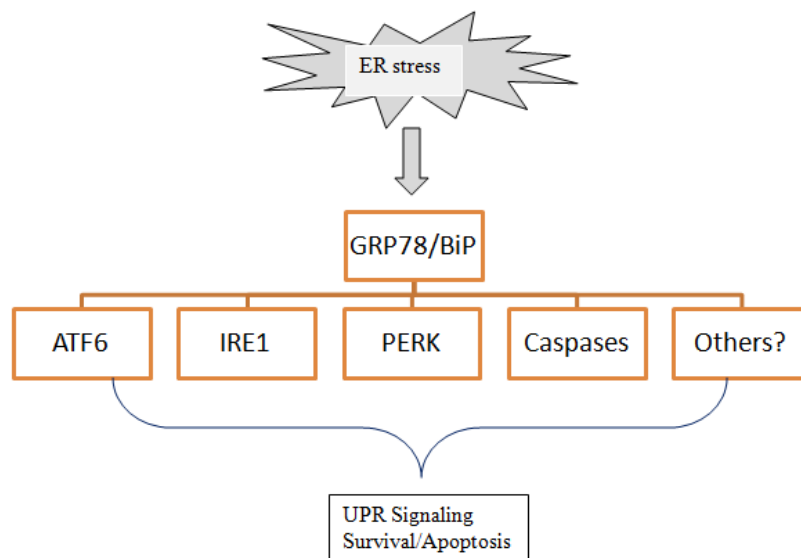
Following successful synthesis, structural and biophysical characterization, the biological activity of linear, branch and hyperbranch siRNAs is described in this chapter. More specifically, GRP78 targeting siRNAs were applied for silencing GRP78 mRNA and triggering cancer cell death within HepG2 hepatoblastoma cells. GRP78 has been classified as a valid molecular target in cancer therapy due to its implications in cancer initiation, proliferation, metastatic spread and resistance towards chemotherapeutics. Thus, inhibiting GRP78 function in resilient cancer cell lines (*e.g.* HepG2 cancer cells) may serve as an ideal method for overcoming tumor resistance, thereby providing a breakthrough in the development of more effective anti-cancer treatment methods. Towards this goal, Lipofectamine™ 2000 was used as the benchmark siRNA cell delivery (*i.e.* transfection) reagent in quantities ( $< 7 \mu\text{g}$ ) that did not compromise HepG2 cell viability. In complex with siRNAs (40 - 80 pmol), potent GRP78 silencing (50 - 70%) was observed by confocal laser scanning microscopy and western blotting. The branch and hyperbranch siRNAs (**Table 2.1, sequences 4-7**) were found to trigger significant GRP78 knockdown (50 - 70%), illustrating their potential as new substrates for silencing oncogene expression. In spite of their potent GRP78 silencing effects in HepG2 hepatoblastomas, only modest cancer cell deaths ( $< 20\%$ ) were observed following siRNA treatment (20-80 pmol, 48-96 h). These results confirm the suitability of the novel branch and hyperbranch siRNAs in the RNAi application, but also highlights the resiliency of the HepG2 cells towards GRP78 knockdown. This discovery is not only important to the development of new gene therapy applications, but also for screening new gene targets that may be implicated in cancer resistance.

## 4.2 INTRODUCTION

### 4.2.1 SELECTION OF GRP78 AS A MOLECULAR TARGET IN CANCER THERAPY

The Glucose Regulated Protein 78 (GRP78) was originally identified from tissue culture grown in the absence of glucose and resulting in the overexpression of a 78 kilodalton protein.<sup>1</sup> GRP78 is also referred to as Bip, due to its ability to bind to the immunoglobulin heavy chains on pre-B cells.<sup>2</sup> GRP78 has since then been characterized as a member of the heat shock family of chaperone proteins (HSP70), primarily assisting in protein folding events in the lumen of the endoplasmic reticulum (ER).<sup>3</sup> GRP78 activity is stimulated in the presence of physiological ER stress signaling, typically associated with cell aging, intracellular  $\text{Ca}^{2+}$  efflux, glucose deprivation, hypoxia and the accumulation of misfolded proteins. These signaling pathways have been extensively reviewed elsewhere<sup>4,8</sup>, and only a cursory review of GRP78 activity associated with physiological ER stress signaling will be described herein. In the case of protein misfolding, the unfolded protein response (UPR) is activated, inhibiting the biosynthesis of additional proteins and stimulating the activity of chaperone proteins such as GRP78 to assist in protein folding events.<sup>4</sup> In this mechanism, ER stress signaling stimulates the release of free form GRP78 from protein kinase like ER kinase (PERK), inositol requiring enzyme 1 (IRE1) and activating transcription factor 6 (ATF6) to unleash the UPR signaling pathway (**Figure 4.1**).<sup>4</sup> This results in PERK-catalyzed phosphorylation of the eukaryotic initiation factor 2 alpha (eIF2 $\alpha$ ), preventing the translocation of additional proteins in the ER.<sup>5</sup> Dimerization of IRE1 stimulates its endoribonuclease activity which splices XBP1 mRNA leading to the expression of a basic leucine zipper family of transcription factors that assist in the production of chaperone proteins.<sup>5</sup> Similarly, ATF6 is transported to the Golgi where it is cleaved and activated to a functional transcription factor that aids in the expression of chaperone genes that assists in protein folding events as part of the UPR signaling pathway.<sup>6</sup> In this manner, the UPR functions

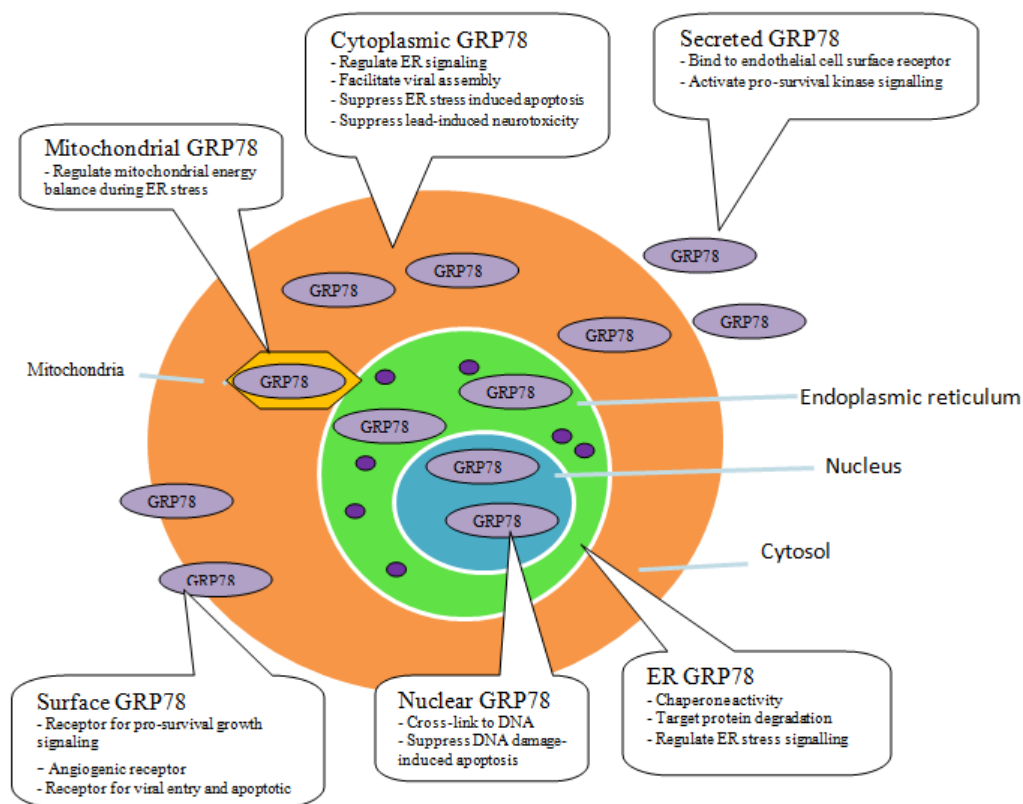
to elevate GRP78 expression levels and activity to release the ER biosynthetic burden in stressed cells, while allowing them to maintain their functionality for cell survival. Thus, GRP78 functions to inhibit cell apoptosis by rescuing the accumulation of unfolded proteins that may compromise cell activity, suppress the formation of reactive oxygen species during hypoxia, and by interfering with caspase activation and caspase mediated cell death.<sup>7</sup>



**Figure 4.1.** The many roles of GRP78 in the UPR signaling pathway associated with ER stress. Figure redrawn from reference 4c.

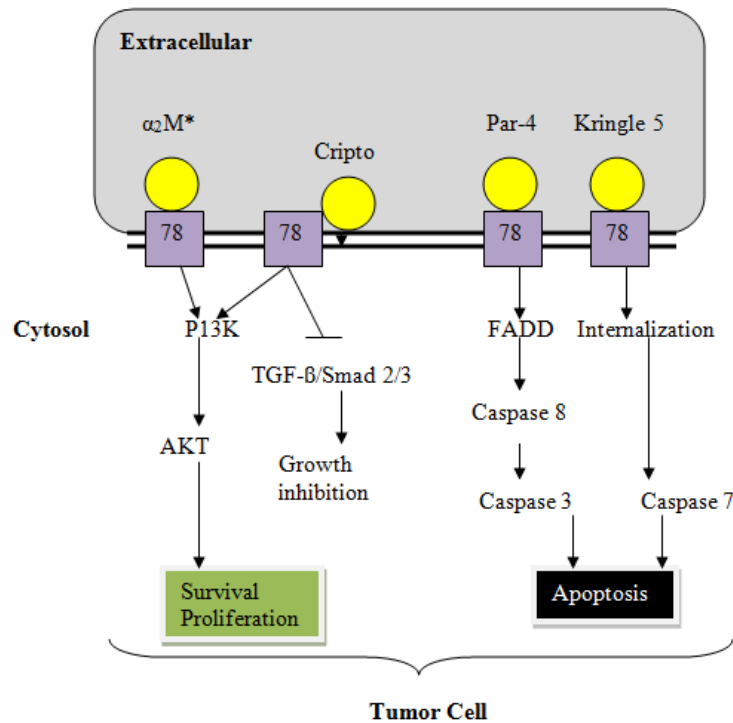
Moreover, electron microscopy has demonstrated that GRP78 is secreted from the ER to a variety of intracellular organelles for widespread biological activity (**Figure 4.2**).<sup>8</sup> For example, GRP78 activity in the perinuclear portion of the ER is also associated with preserving intracellular  $\text{Ca}^{2+}$  homeostasis. In this manner, GRP78 regulates  $\text{Ca}^{2+}$  efflux from the ER to the mitochondria where it functions to stimulate oxidative metabolism for cellular bioenergetics and survival.<sup>9</sup> GRP78 expression and activity have also been observed in the nucleus of the cell, where it is speculated to play a pivotal role against DNA-damage induced apoptosis.<sup>10</sup> Cytosolic

GRP78 functions to regulate UPR signaling associated with the protein misfolding response, viral protein assembly and minimizing lead neurotoxicity.<sup>11</sup> Interestingly, under ER stress or pathological conditions, GRP78 is translocated from the ER to the plasma membrane. As such, cell surface GRP78 has been characterized on rapidly proliferating endothelial, monocytic cells and tumors, where it behaves as a signaling receptor for cell survival.<sup>12</sup> A certain fraction of cell surface GRP78 may also be secreted extracellularly, where anti-GRP78 antibodies are produced and can be isolated from the serum.<sup>13</sup> The antibodies which bind to the *N*-terminal domain of GRP78 have been shown to stimulate cell proliferation and protection against apoptotic events. Conversely, the selection of *C*-terminal GRP78 antibodies has been shown to trigger apoptosis.



**Figure 4.2.** GRP78 cellular localizations and activities. Redrawn from reference 8.

The cell surface localization of GRP78 in selected cell types associate's with physiological stress conditions such as with hypoxia or glucose deprivation and pathological disorders such as in cancer and metabolic diseases makes GRP78 a potential molecular target for therapeutic applications. In cancer, cell surface GRP78 signals initiation, proliferation, metastasis, resistance towards chemotherapy and radiation treatments (**Figure 4.3**).<sup>4,8,14</sup>



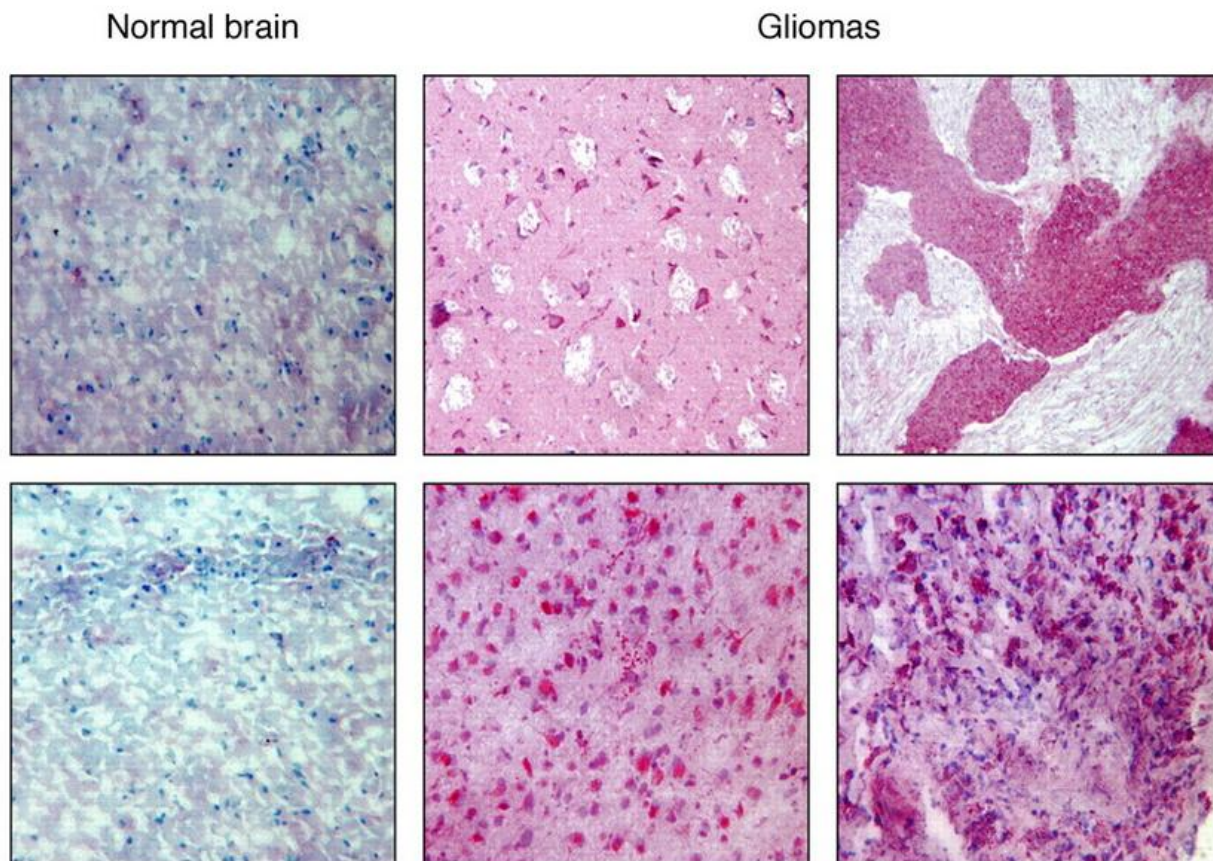
**Figure 4.3.** Pluripotent cancer cell surface GRP78 signaling. Redrawn from reference 8.

Although these signaling pathways are extensively described elsewhere<sup>4,8,14</sup>, a cursory review is provided in this section to highlight the relevance of GRP78 signaling on tumorigenesis. In 1-LN prostate cancer cells, GRP78 has been found to act as a receptor for activated  $\alpha_2$ -macroglobulin binding which signals the activation of p-21 activated kinase-2 (PAK-2), LIM domain kinase 1 (LIMK1) and cofilin phosphorylation that subsequently

promotes tumor metastatic spread.<sup>15</sup> Moreover, the GRP78- $\alpha$ 2-macroglobulin binding interaction also triggers cell survival and proliferation in solid tumors via the AKT and NF- $\kappa$ B signaling cascade which is activated by phosphorylation with intracellular kinases (*e.g.* ERK 1/2, MAPK, Akt, PI3K).<sup>16</sup> Cripto, a multifunctional cell surface protein also binds to cell surface GRP78, enhancing tumor growth by inhibiting transforming growth factor- $\beta$  (TGF- $\beta$ ) signaling activity.<sup>17</sup> Moreover, Kringle 5 and Par-4 have also been identified as GRP78 cell surface binding partners that increase intracellular apoptotic events. The ability for GRP78 to block apoptosis includes its binding and inactivation of CHOP, BIK and caspase 7, cell death effector proteins.<sup>18</sup> Additionally, GRP78 chemoresistance has been hypothesized by the synergistic effects of the pro-survival UPR mechanism and cell proliferative effects of the AKT/PI3K signaling pathway.<sup>19</sup> Thus, GRP78 signaling pluripotency enables tumor cell survival and progression by evading the cell death response or depending on protein partner, increases apoptosis.

Cell surface GRP78 signaling activity and overexpression have been correlated with a variety of solid tumors of the urinary, lymphatic, digestive, mammary, cerebral and respiratory systems, but not in normal tissues (**Figure 4.4**).<sup>4,8,14</sup> For example, the GRP78 immunohistochemical reactivity was found to be significantly higher in prostate cancer and lymph node metastasis specimens when compared to corresponding benign tissue controls.<sup>20</sup> GRP78 levels were also found to be markedly higher in human renal carcinoma<sup>21</sup> and in gastric cancer<sup>22</sup> specimens relative to the adjacent non-tumor tissues. Overexpression of GRP78 in hepatocellular carcinoma promoted tumor invasion *in vitro* and *in vivo* due to the activation and activity of a focal adhesion kinase (FAK) which negatively regulated Rock kinase activity by promoting the phosphorylation of p190RhoGAP.<sup>23</sup> In breast cancer, GRP78 has been found to

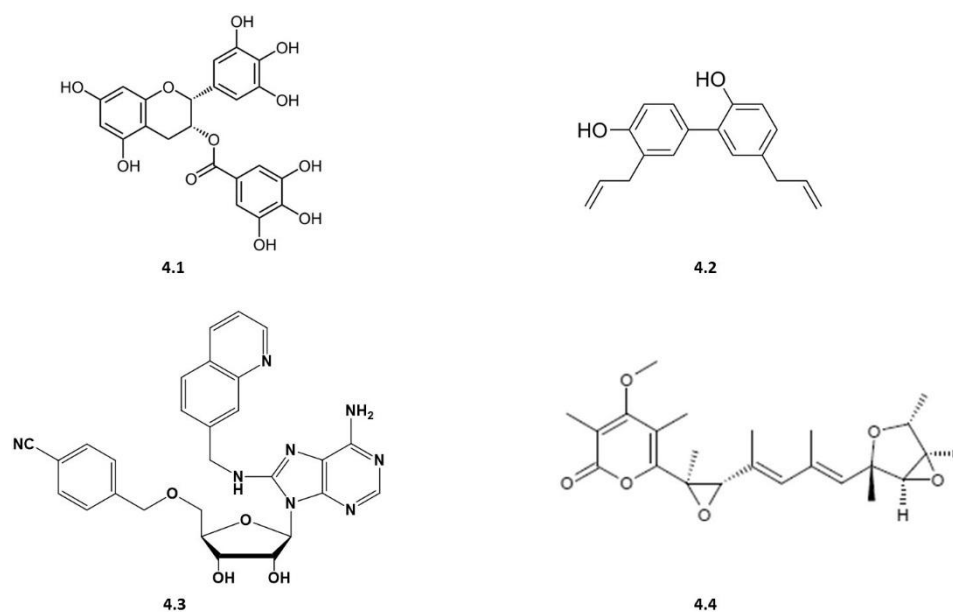
correlate with metastatic spread and resistance towards chemotherapeutic treatments such as adriamycin, etoposide, taxol and vinblastine.<sup>24</sup> The overexpression of GRP78 has also been found in brain tumors associated with malignant glioma tissues (**Figure 4.4**). In these cases, GRP78 activity has been correlated with resistance to chemotherapy and  $\gamma$ -radiation, induction of tumor proliferation and a low median survival rate for the patients.<sup>25</sup> The same trend has also been observed in lung<sup>26</sup> and melanoma<sup>27</sup> tumors, making GRP78 a ubiquitous tumor biomarker for the development of targeted anti-cancer approaches.



**Figure 4.4.** Immunohistochemical staining of GRP78 in human glioma tissues and normal brain. The two cross-sections of peritumoral brain tissues were stained with anti-GRP78 antibody (red) and blue hematoxylin as background stain.<sup>25</sup>



Inhibitors of GRP78 activity have been shown to trigger apoptosis in cancer cells (**Figure 4.5**). For example, epigallocatechin gallate, (**4.1**, EGCG), a flavonoid natural product found in green tea leaves and honokiol, (**4.2**, HNK), a magnolia grandiflora derivative have been shown to bind to the GRP78 ATPase domain, induce ER stress leading to potent cell death effects in melanoma, glioblastoma and neuroblastoma cell lines with and without ER stress inducers fenretinide or bortezomib.<sup>28</sup> In a structure-design based approach, a library of synthetic adenosine-based inhibitors, targeting the GRP78 ATP binding domain were developed for structure-activity relationship studies.<sup>29</sup> The lead analog, **4.3**, retained potent ( $K_D$ : 60 nM) and selective GRP78 binding affinity when screened against homologous heat shock proteins. Verrucosidin (**4.4**, VCD) a fungal metabolite with putative GRP78 inhibitory activity, was found to exhibit potent cytotoxic effects in breast cancer cell lines by inhibiting the mitochondrial energy production.<sup>30</sup> This finding has fueled speculation that other supposed GRP78 inhibitors (e.g. arctigenin, deoxyverrucosidin, efrageptin, piericidin, pyrvinium, rottlerin, valinomycin) might also act in a GRP78-independent fashion.<sup>30</sup>




**Figure 4.5.** Small molecule inhibitors of GRP78 activity.<sup>28-30</sup>

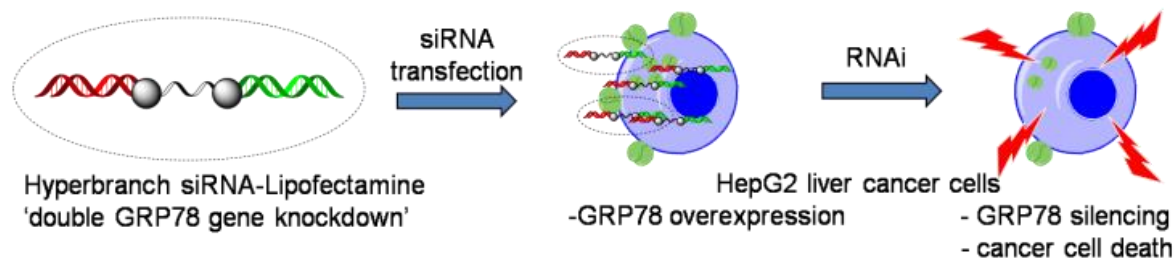
Leading into biopolymer modulators of GRP78 activity, the serine protease subtilase cytotoxin was used to selectively cleave GRP78, thereby sensitizing apoptosis-resistant cancer cells to Photofrin-mediated photodynamic therapy (PDT).<sup>31</sup> The discovery of a peptide ligand derived from the cochaperone Bag-1 has been shown to bind to and inhibit the refolding activity of GRP78 causing apoptosis in *in vivo* xenograft tumor models.<sup>32</sup> Moreover, peptide ligands and circulating GRP78 antibodies have been identified to selectively bind cell surface GRP78 on tumor cells, forming the basis for GRP78 tumor-targeting approaches,<sup>33</sup> as highlighted in Chapter 5.

Knockdown of GRP78 has also been shown to sensitize cancer cells to chemotherapy or radiation treatments resulting in cancer cell death. For example, siRNA-mediated silencing of GRP78 expression enhanced the cytotoxic effects of fenretinide or bortezomid in CHL-1 and WM266-4 melanoma cells by two- to three-fold relative to the untransfected controls.<sup>27</sup> siRNA transfection in primary cultures of human brain endothelial cells, derived from the blood vessels of malignant glioma tissues (TuBEC) reversed chemoresistance to a wide range of anti-cancer drugs including CPT-11, etoposide and temozolomide.<sup>19b</sup> Similarly, GRP78 knockdown enhanced apoptosis in colon cancer DLD-1 cells following treatment with epirubicin. In this case, GRP78 silencing sensitized the cells to the cytotoxic drug treatment by decreasing intracellular levels of ROS and survival signaling of the Akt pathway.<sup>34</sup> In a similar combination approach against human urothelial carcinoma cells, GRP78 knockdown potentiated the cytotoxic effects of celecoxib, a selective cyclooxygenase-2 inhibitor (COX-2).<sup>35</sup> It is also worthwhile to note that while siRNA-mediated knockdown of GRP78 was found to reverse chemoresistance and enhance the cytotoxic effects of the anti-cancer drugs, silencing of GRP78 is in itself insufficient to stimulate apoptosis. These results confirm the synergy associated with GRP78

activity and cell survival, but also underscores the importance of targeting GRP78 in combination approaches that abolishes resistance in highly resilient and recurring tumors.

### 4.3 CHAPTER OBJECTIVES

A novel GRP78 gene-targeting approach is described in this chapter with the use of linear, V-shape, Y-branch and  hyperbranch siRNAs (**Figure 2.9**).<sup>42</sup> In this study conducted by Brittany Blackman<sup>40</sup> and Christopher Parronchi in collaboration with Dr. Allan Blake (Department of Biological Sciences, Seton Hall University), siRNAs (**Table 2.1, sequence no. 1-7**) were treated with Lipofectamine™ 2000 (Invitrogen, CA), and transfected in HepG2 liver hepatoblastoma cells to explore their biological activity (**Figure 4.6**). In order to confirm their suitability for the RNAi application, cell lysates are used to determine the total GRP78 content with and without siRNA treatment. In this case, western blotting with an anti-GRP78 antibody and a suitable secondary antibody for detection will be used to determine GRP78 expression levels in HepG2 cells. Moreover, laser scanning confocal microscopy will be used to monitor cell surface GRP78 expression levels with and without siRNA treatment. In order to investigate the anti-cancer activity of the siRNAs, a Trypan blue cell viability assay will be conducted. In this manner, the novel siRNAs synthesized (Chapter 2) and characterized (Chapter 3) will be evaluated for anti-cancer application.



**Figure 4.6.** GRP78 gene-targeting method with  $\lambda$  hyperbranch siRNA:Lipofectamine complex<sup>42</sup>

## 4.4 RESULTS AND DISCUSSION

### 4.4.1 HepG2 CELL CULTURE

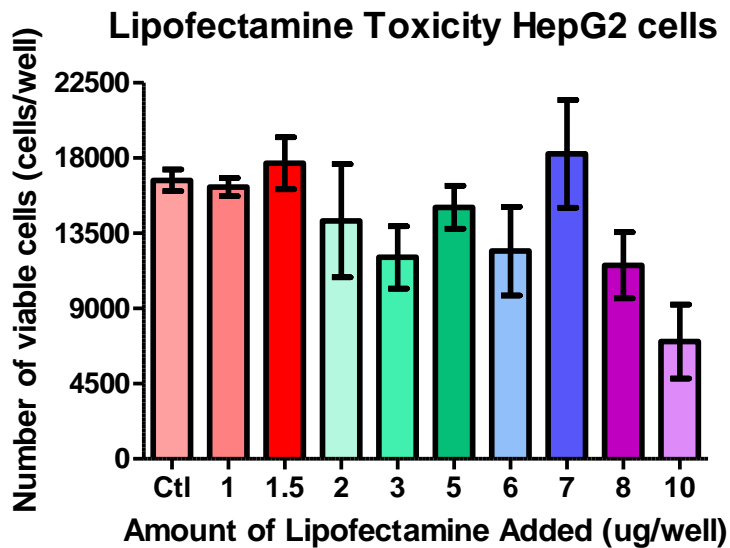
Hepatoblastoma (HB) is an embryonal form of liver cancer often found in the early stages of childhood.<sup>35</sup> HepG2 hepatoblastomas are a relevant tumor cell line model for the pre-clinical study of pediatric liver diseases.<sup>36</sup> The HepG2 cell line (ATCC, CA) is credited to Dr. Barbara Knowles and colleagues (Wistar Institute, PA) who extracted them from the liver tissue of a 15 year old white male who had developed a well differentiated hepatocellular hepatoblastoma back in 1979.<sup>36,37</sup> Moreover, cell surface GRP78 expression has been correlated with tumor invasion in HepG2 cells making it a clinically relevant tumor model for validating our GRP78-targeting strategy.<sup>38</sup>

Based on literature precedence for the HepG2 cell culture<sup>37,38</sup>, HepG2 liver cancer cells ( $\sim 5 \times 10^4$  cells) were plated in 24-well culture plates and grown in DMEM with 10% fetal bovine serum for 48 h in a humidified incubator at 37 °C with 5% CO<sub>2</sub>. Following a 24 h incubation period, the HepG2 cells were passaged and treated with a basal, serum free medium (OptiMEM) and incubated for an additional 24 h prior to analyses. Cell counting to discern viability was performed with a Countess automated cell counter using a Trypan blue exclusion assay. A rich population of HepG2 cells (50,000 cells/well), were maintained for siRNA transfections.

#### 4.4.2 siRNA:LIPOFECTAMINE TRANSFECTIONS IN HepG2 CELLS

In order to facilitate cell penetration of the GRP78 targeting siRNAs, a suitable transfection reagent functions to bind siRNA and mask the negatively charged phosphodiester bonds for efficient translocation across the negatively charged amphiphilic plasma membrane. For example, Lipofectamine™ 2000, a cationic amphiphile forms an ionic complex with siRNA and ushers its delivery across the lipid bilayer for RNAi application. This reagent is the benchmark transfection agent for delivery of oligonucleotides inside cells.<sup>39</sup>

Prior to siRNA transfection, the toxicity of Lipofectamine™ 2000 was evaluated within HepG2 cells to determine a range in which this reagent can be used without triggering cell cytotoxicities.<sup>40</sup> In this toxicity experiment, Lipofectamine™ 2000 (1 µg/well to 10 µg/well) was administered to the HepG2 cells in a 96-well plate (9 wells/treatment) and incubated for 48 h at 37 °C with 5% CO<sub>2</sub>. Following incubation, a Calcein AM cell viability assay<sup>41</sup> was performed to determine cell viability with and without Lipofectamine treatment (**Figure 4.7**). In this assay, only cells treated with higher quantities of Lipofectamine (10 µg) exhibited a significant drop in cell viability (>50%). Thus, an effective range of Lipofectamine™ 2000 (1-7 µg) can be used for optimizing the siRNA transfection protocol.

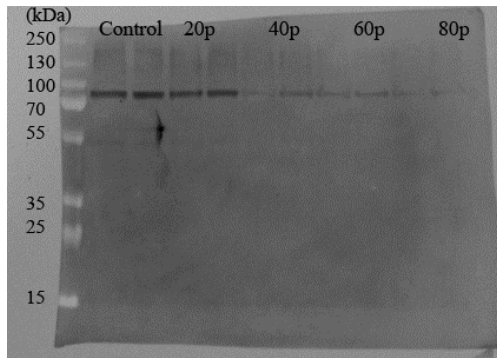


**Figure 4.7.** Lipofectamine™ 2000 toxicity on HepG2 cells. HepG2 cells were plated 50,000 cells/well in 96 well plate with 9 wells per treatment with Lipofectamine™ 2000 (0 – 10 µg/well). The number of viable cells/well after Calcein AM treatment is shown (n=1).<sup>40,41</sup>

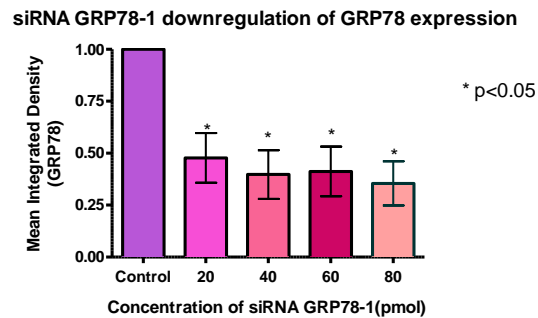
In order to test the optimal stoichiometric ratios for the Lipofectamine:siRNA complex to be used in the transfection experiments, increasing amounts of a linear control GRP78-targeting siRNA (20 - 80 pmol, Table 2.1, sequence no. 1) were tested with a nominal quantity of Lipofectamine (1 µg).<sup>40</sup> Following transfection, Western blot<sup>44</sup> and Trypan blue exclusion<sup>45</sup> assays were used to determine the extent of total GRP78 knockdown and HepG2 cell death, respectively. The Western blot studies (**Figure 4.8**) revealed a dose-response relationship between the siRNA treatment (20 - 80 pmol) and GRP78 silencing (50-60%), illustrating the effectiveness of the siRNA:Lipofectamine complex in the RNAi application. In spite of these encouraging results, minimal HepG2 cell death (< 5%) was observed even at the highest siRNA doses (80 pmol) and extended incubation times (4 days). These results are not surprising,

considering GRP78 knockdown has been shown to be in itself insufficient for stimulating cell death,<sup>42,43</sup> but however sensitizes cells to chemotherapeutic agents which can trigger apoptosis.<sup>19b,27,34,35,38</sup>

**A.**




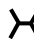
**B.**



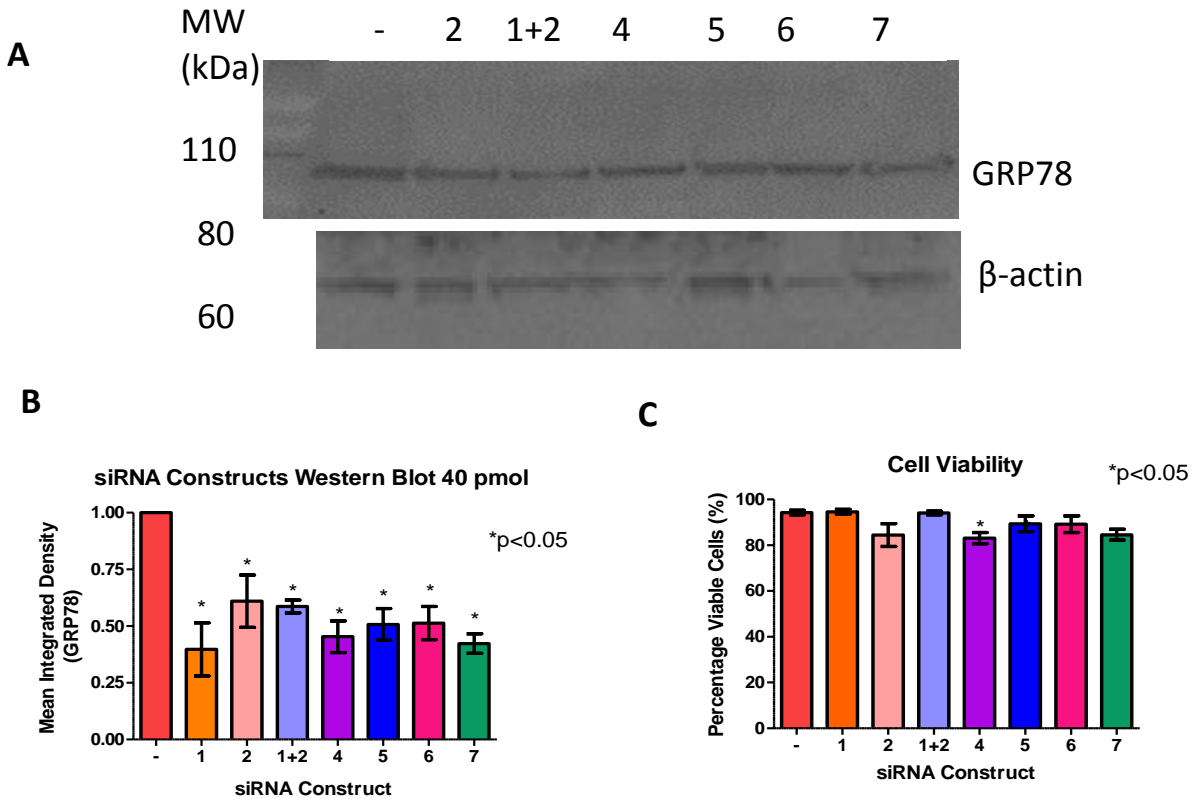
**Figure 4.8.** Western blot for the siRNA:Lipofectamine transfections. **A.** Representative western blot (n=5) with varying concentrations of GRP78-targeting siRNA (20 - 80 pmol, Table 2.1, sequence no. 1); **B.** GRP78 protein expression levels quantified using NIH Image J (n=5); statistical significance was determined by ANOVA ( $p < 0.05$ ).<sup>40,42</sup>

From this preliminary study (**Figure 4.8**), optimized methods for the Lipofectamine:siRNA transfection experiments were developed in HepG2 cells in order to deduce the influence of the GRP78-targeting siRNA constructs (**Table 2.1, sequence no. 1-7**) on RNAi activity.<sup>40,42</sup> Briefly, siRNA samples (40 pmol) were transfected with Lipofectamine™ 2000 (1 µg) in HepG2 cells (50,000 cells/well), and incubated in OPTIMEM at 37°C with 5% CO<sub>2</sub>. Following transfection (48 h), cell lysates were prepared (RIPA lysis buffer, Invitrogen) and resolved by SDS PAGE for immunoblotting with an anti-GRP78 primary antibody and a secondary antibody conjugated to horseradish peroxidase (HRP). In this assay, total HepG2 cells' GRP78 expression levels were determined by the redox activity of the 3,3',5,5'-

tetramethylbenzidine (TMB) substrate.<sup>44,46</sup> The gel (**Figure 4.9 A**) was analyzed by autoradiography and demonstrated effective silencing (40-60%) of GRP78 expression by linear (~40-60%, **Table 2.1 sequence no. 1 and 2**), V-shape (~50%, **Table 2.1 sequence no. 4**), Y-branch (~55%, **Table 2.1 sequence no. 5**) and hyperbranch (~50-60%, **sequence no. 6 and 7**) siRNAs (**Figure 4.9 B**). These results confirm the GRP78-targeting and silencing effects of the linear siRNA controls (**Table 2.1 sequence no. 1 and 2**), but also underscores the unprecedented RNAi activity of the V-shape, Y-branch and  hyperbranch siRNAs.

Cell viability data was also collected following a Trypan blue cell staining assay<sup>45</sup>, to establish the extent of HepG2 cell death following GRP78 knockdown. In this assay, GRP78-targeting siRNAs (**Table 2.1 sequence no. 1-7**) stimulated 10-20% HepG2 cell death. The observed cell death percentages for linear siRNA controls were consistent with those observed in the literature<sup>43</sup>, with approximately 5% (**1**), compared to about 15% with V-shape siRNA (**4**), about 10% with Y-branch siRNA (**5**) and ~15% with  hyperbranch siRNAs (**7**) (**Figure 4.9 C**). Interestingly, hyperbranch siRNA (**Table 2.1 sequence no. 7**), targeting double sites of GRP78 mRNA exhibited more potent GRP78 knockdown (60% vs. 40%) and cell death (15% vs. 5%) relative to the linear controls (**Table 2.1 sequence no. 1 and 2**), highlighting its synergistic effects in the RNAi application.



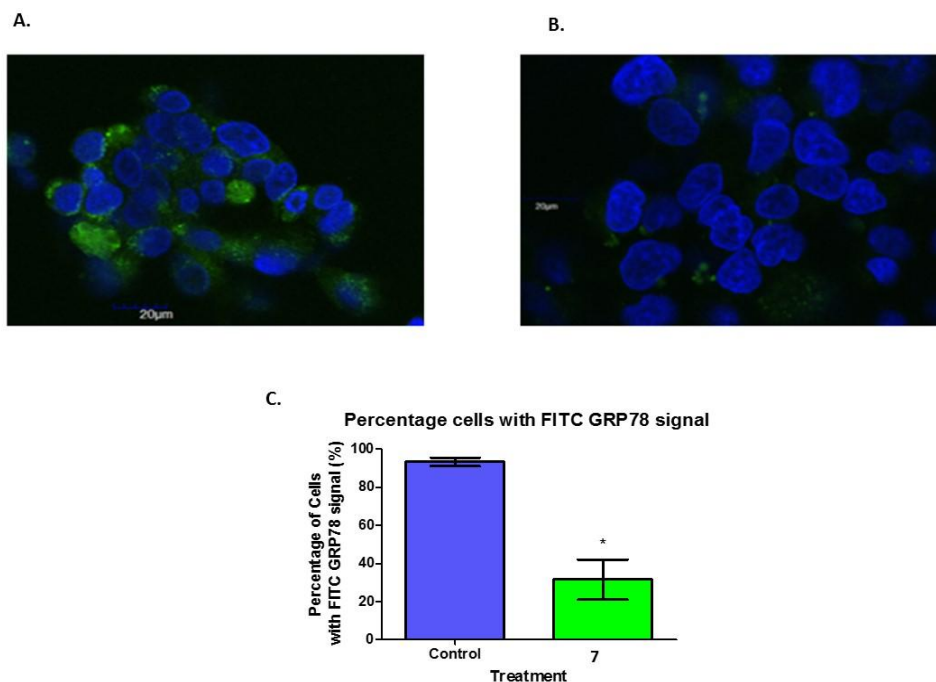


**Figure 4.9.** Linear, branch and hyperbranch siRNAs transfection results in HepG2 cells. A: Western blot of HepG2 cells lysates showing GRP78 expression following transfection with linear (2) and (1+2) siRNA controls and with V-shape (4), branch (5) and hyperbranch siRNAs (6,7), B: GRP78 expression levels were detected by autoradiography and quantified using NIH ImageJ, C: Cell viability data determined by Trypan blue exclusion. The data shown are the mean  $\pm$  SEM for 3 or more experiments, each performed in duplicate and analyzed with GraphPad Prism 4.0 and statistical significance was determined by ANOVA ( $p < 0.05$ ).<sup>40,42</sup>

#### 4.4.3 CELL SURFACE GRP78 EXPRESSION IN HepG2 CELLS

Confocal laser scanning microscopy was used to confirm the presence of cell surface GRP78 on HepG2 cells with an anti-GRP78 primary and a secondary antibody conjugated to fluorescein isothiocyanate (FITC).<sup>40,42</sup> HepG2 cell images (**Figure 4.10**) were captured with a

40X oil objective lens, from which FITC labeled GRP78 stained green and DAPI-stained cell DNA shone blue (**Figure 4.10, A**). Cell surface GRP78 knockdown was subsequently assessed by transfecting the HepG2 cells with Lipofectamine:hyperbranch siRNA (40 pmol, **Table 2.1 sequence no. 7**) followed by incubation at 37 °C for 48 hours. Following transfection, cells were plated on glass slides and treated with the same anti-GRP78 primary and FITC-labeled secondary antibodies to examine GRP78 expression levels (**Figure 4.10, B**). In this assay, hyperbranch siRNA **7** potently silenced GRP78 expression (~70% knockdown) as shown by the minimal ‘yellow’ FITC-signaling relative to the control untransfected cells (**Figures 4.10, A - C**). Moreover, these results also suggest that HepG2 cell GRP78 may be further exploited for the tumor-targeted delivery of siRNAs (Chapter 5).



**Figure 4.10.** Monitoring cell surface GRP78 expression with confocal laser microscopy of A. paraformaldehyde fixed HepG2 cells with an anti-GRP78 antibody (FITC; green) and DAPI (blue) nuclear stain. Cells were viewed using a 40X oil objective lens, and the cells are representative of separate viewing fields from two independent experiments.; B. HepG2 cells transfected and incubated (48 h) with hyperbranch siRNA (**Table 2.1 sequence no. 7**), fixed with 2 % paraformaldehyde and stained with DAPI (blue), and FITC conjugated to GRP78 protein expression (green).; C. Percentage of the HepG2 cells with FITC-GRP78 signal for both the control and transfected sample. Statistical significance determined with student's t-test and p value < 0.05.<sup>40,42</sup>

## 4.5 CONCLUSIONS

In this chapter the putative RNAi activity of the GRP78-targeting siRNAs (**Table 2.1, sequence no. 1-7**) has been validated in HepG2 hepatoblastomas. The novel V-shape, Y-branch, and  $\times$  hyperbranch siRNA motifs (**Table 2.1, sequence no. 4-7**) were found to solicit potent GRP78 silencing (50% – 60%). Significantly, hyperbranch siRNA, **7**, targeting double sites of

GRP78 mRNA expression was found to trigger more potent GRP78 knockdown (60% vs. 40%) and HepG2 cell death (15% vs. 5%) highlighting its synergistic effects relative to the linear control siRNAs, **1** and **2**. This finding is important for the development of new siRNA constructs that may target multiple genes in a combination approach for improving RNAi efficacy and also for screening new oncogene targets. Moreover, confocal laser scanning microscopy also confirmed potent cell surface GRP78 knockdown (~70%) with hyperbranch siRNA, **7**. Interestingly, FITC-labeling of GRP78 on the cell surface of HepG2 cells suggests the possibility of developing a tumor-targeting approach for the selective delivery of siRNAs in cancer cells. The latter is a focal point of the final thesis chapter (Chapter 5), which highlights the preliminary studies towards the development of a cancer-targeting gene therapy approach.

## 4.6 REFERENCES

1. Shiu, R.P.; Pouyssegur, J.; Pastan, I. Glucose depletion accounts for the induction of two transformation-sensitive membrane proteins in Rous sarcoma virus-transformed chick embryo fibroblasts. *Proc. Natl. Acad. Sci. USA* **1977**, *74*, 3840-3844.
2. Haass, I.G.; Wabl, M. Immunoglobulin heavy chain binding protein. *Nature* **1983**, *306*, 387-389.
3. (a) Lee, A.S.; Bell, J.; Ting, J. Biochemical Characterization of the 94- and 78-kilodalton glucose regulated proteins in hamster fibroblasts. *J. Biol. Chem.* **1984**, *259*, 4616-4621, (b) Lee, A.S. Coordinated Regulation of a Set of Genes by Glucose and Calcium Ionophore. *Trends Biochem. Sci.* **1987**, *12*, 20-23.
4. Kaufman, R.J. Stress Signaling from the Lumen of the Endoplasmic Reticulum: coordination of gene transcriptional and translational controls. *Genes Dev.* **1999**, *13*, 1211-1233, (b) Rutkowski, D.T.; Kaufman, R.J. A trip to the ER: coping with stress. *Trends Cell. Biol.* **2004**, *14*, 20-28, (c) Lee, A.S. The ER Chaperone and Signaling Regulator GRP78/Bip as a Monitor of endoplasmic reticulum stress. *Methods* **2005**, *35*, 373-381, (d) Zhang, L.H.; Zhang, X. Roles of GRP78 in Physiology and Cancer. *J. Cell. Biochem.* **2010**, *110*, 1299-1305.
5. Bertolotti, A.; Zhang, Y.; Hendershot, L.M.; Harding, H.P.; Ron, D. Dynamic interaction of BiP and ER stress transducers in the unfolded-protein response. *Nat. Cell. Biol.* **2000**, *2*, 326-332.
6. Hong, M.; Luo, S.; Baumeister, P.; Huang, J.M.; Gogia, R.K.; Li, M.; Lee, A.S. Underglycosylation of ATF6 as a novel sensing mechanism for activation of the unfolded protein response. *J. Biol. Chem.* **2004**, *279*, 11354-11363.
7. Rao, R.V.; Peel, A.; Logvinova, A.; del Rio, G.; Hermel, E.; Yokota, T.; Goldsmith, P.C.; Ellerby, L.M.; Ellerby, H.M.; Bredesen, D.E. Coupling endoplasmic reticulum stress to the cell death program: role of the ER chaperone GRP78. *FEBS Lett.* **2002**, *514*, 122-128.
8. Ni, M.; Zhang, Y.; Lee, A.S. Beyond the endoplasmic reticulum: atypical GRP78 in cell viability, signaling and therapeutic targeting. *Biochem. J.* **2011**, *434*, 181-188.

9. Ouyang, Y.B.; Xu, L.J.; Emery, J.F.; Lee, A.S.; Giffard, R.G. Overexpressing GRP78 influences Ca<sup>2+</sup> handling and function of mitochondria in astrocytes after ischemia-like stress. *Mitochondrion* **2011**, *11*, 279–286.
10. (a) Matsumoto, A.; Hanawalt, P.C. Histone H3 and heat shock protein GRP78 are selectively cross-linked to DNA by photoactivated gilvocarin V in human fibroblasts. *Cancer Res.* **2000**, *60*, 3921-3926, (b) Barker, S.; Weinfeld, M.; Zheng, J.; Li, L.; Murray, D. Identification of cross-linked mammalian proteins cross-linked to DNA by ionizing radiation. *J. Biol. Chem.* **2005**, *280*, 33826-33838, (c) Huang, S.P.; Chen, J.C.; Wu, C.C.; Chen, C.T.; Tang, N.Y.; Ho, Y.T.; Lo, C.; Lin, J.P.; Chung, J.G.; Lin, J.G. Capsaicin-induced apoptosis in human hepatoma HepG2 cells. *Anticancer Res.* **2009**, *29*, 165-174.
11. (a) Rutkowski, D.T.; Kang, S.W.; Goodman, A.G.; Garrison, J.L.; Taunton, J.; Katze, M.G.; Kaufman, R.J.; Hedge, R.S. The role of p58IPK in protecting the stressed endoplasmic reticulum. *Mol. Biol. Cell* **2007**, *18*, 3681-3691, (b) Buchkovich, N.J.; Maguire, T.G.; Yu, Y.; Paton, A.W.; Paton, J.C.; Alwine, J.C. Human cytomegalovirus specifically controls the levels of endoplasmic reticulum chaperone Bip/GRP78, which is required for viron assembly. *J. Virol.* **2008**, *82*, 31-39, (c) Qian, Y.; Harris, E.D.; Zheng, Y.; Tiffany-Castiglioni, E. Lead targets GRP78, a molecular chaperone in C6 rat glioma cells. *Toxicol. Appl. Pharmacol.* **2000**, *163*, 260-266.
12. Philipova, M.; Ivanova, D.; Joshi, M.B.; Kyriakakis, E.; Rupp, K.; Afonyushkin, T.; Bochkov, V.; Erne, P.; Resink, T.J.; Identification of proteins associating with glycosylphosphatidylinositol-anchored T-cadherin on the surface of vascular endothelial cells: Role of GRP78/Bip in T-cadherin dependent cell survival. *Mol. Cell. Biol.* **2008**, *28*, 4004-4017.
13. Misra, U.K.; Gonzalez-Gronow, M.; Gawdi, G.; Pizzo, S.V. Ligation of Cancer Cell Surface GRP78 with antibodies directed against its COOH-terminal domain up-regulates p53 activity and promotes apoptosis. *Mol. Cancer Ther.* **2009**, *8*, 1350-1362.
14. (a) Biquon Luo, B.S.; Lee, A.S. The critical roles of the endoplasmic reticulum chaperones and unfolded protein response in tumorigenesis and anti-cancer therapies. *Oncogene* **2013**, *32*, 805-818, (b) Lee, A.S. GRP78 Induction in Cancer: Therapeutic and Prognostic Implications. *Cancer Res.* **2007**, *67*, 3496-3499, (c) Sato, M.; Yao, V.J.; Arap,

- W.; Pasqualini, R. GRP78 Signaling Hub: A receptor for targeted tumor therapy. *Adv. Gen.* **2010**, *69*, 97-114.
15. Misra, U.K.; Deedwania, R.; Pizzo, S.V. Binding of activated  $\alpha$ 2-macroglobulin to its cell surface receptor GRP78 in 1-LN prostate cancer cells regulates PAK-2 dependent activation of LIMK. *J. Biol. Chem.* **2005**, *280*, 26278-26286.
16. Misra, U.K.; Deedwania, R.; Pizzo, S.V. Activation and cross-talk between Akt, NF-KB, and the unfolded response signaling in 1-LN prostate cancer cells consequent to ligation of cell surface-associated GRP78. *J. Biol. Chem.* **2006**, *281*, 13694-13707.
17. Shani, G.; Fischer, W.H.; Justice, N.J.; Kelber, J.A.; Vale, W.; Gray, P.C. GRP78 and Cripto form a complex at the cell surface and collaborate to inhibit transforming growth factor b signaling and enhance cell growth. *Mol. Cell. Biol.* **2008**, *28*, 666-677.
18. (a) Reddy, R.K.; Mao, C.; Baumeister, P.; Austin, R.C.; Kaufman, R.J.; Lee, A.S. Endoplasmic reticulum chaperone protein GRP78 protects cells from apoptosis induced by topoisomerase inhibitors: role of ATP binding site in suppression of caspase-7 activation. *J. Biol. Chem.* **2003**, *278*, 20915–20924, (b) Fu, Y.; Li, J.; Lee, A.S. GRP78/BiP inhibits endoplasmic reticulum BIK and protects human breast cancer cells against estrogen-starvation induced apoptosis. *Cancer Res.* **2007**, *67*, 3734–3740.
19. (a) Roller, C.; Maddalo, D. The molecular chaperone GRP78/Bip in the development of chemoresistance: mechanism and possible treatment. *Fron. Pharm.* **2013**, *4*, 1-5, (b) Virrey, J.J.; Dong, D.; Stiles, C.; Patterson, J.B.; Pen, L.; Ni, M.; Schonthal, A.H.; Chen, T.C.; Hofman, F.M.; Lee, A.S. Stress chaperone CRP78/Bip confers chemoresistance to tumor associated endothelial cells. *Mol. Cancer Res.* **2008**, *6*, 1268-1275.
20. Daneshmand, S.; Quek, M.L.; Lin, E.; Lee, C.; Cote, R.J.; Hawes, D.; Cai, J.; Groshen, S.; Lieskovsky, G.; Skinner, D.G.; Lee, A.S.; Pinski, J. Glucose-Regulated Protein 78 is up-regulated in prostate cancer and correlates with recurrence and survival. *Hum. Path.* **2007**, *38*, 1547-1552.
21. Fu, W.; Wu, X.; Li, J.; Mo, Z.; Yang, Z.; Huang, W.; Dinq, Q. Upregulation of GRP78 in renal carcinoma and its significance. *Urology* **2010**, *75*, 603-607.
22. Azatian, A.; Yu, H.; Dai, W.; Schneiders, F.I.; Botelho, N.K.; Lord, R.V. Effectiveness of HSV-tk suicide gene therapy driven by the Grp78 stress-inducible promoter in

- esophagogastric junction and gastric adenocarcinomas. *J. Gastrointest. Surg.* **2009**, *13*, 1044-1051.
23. Su, R.; Li, Z.; Li, H.; Song, H.; Bao, C.; Wei, J.; Cheng L. Grp78 promotes the invasion of hepatocellular carcinoma. *BMC Cancer* **2010**, *10*, 20-32.
24. Lee, E.; Nichols, P.; Spicer, D.; Groshen, S.; Yu, M.C.; Lee, A.S. GRP78 as a novel predictor of responsiveness to chemotherapy in breast cancer. *Cancer Res.* **2006**, *66*, 7849-7853.
25. Pyrko, P.; Schonthal, A.H.; Hofman, F.M.; Chen, T.C.; Lee, A.S. The unfolded protein response regulator GRP78/Bip as a novel target for increasing chemosensitivity in malignant gliomas. *Cancer Res.* **2007**, *67*, 9809-9816.
26. Tsai, H.Y.; Yang, Y.F.; Wu, A.T.; Yang, C.J.; Liu, Y.P.; Jan, Y.H.; Lee, C.H.; Hsiao, Y.W.; Yeh, C.T.; Shen, C.N.; Lu, P.J.; Huang, M.S.; Hsiao, M. Endoplasmic reticulum ribosome-binding protein 1 (RRBP1) overexpression is frequently found in lung cancer patients and alleviates intracellular stress-induced apoptosis through the enhancement of GRP78. *Oncogene* **2013**, *32*, 4921-4931.
27. Martin, S.; Hill, D.S.; Paton, J.C.; Paton, A.W.; Birch-Machin, M.A.; Lovat, P.E.; Redfern, C.P.F. Targeting GRP78 to enhance melanoma cell death. *Pigment Cell Melanoma Res.* **2010**, *23*, 675-682.
28. Martin, S.; Lamb, H.K.; Brady, C.; Lefkove, B.; Bonner, M.Y.; Thompson, P.; Lovat, P.E.; Arbiser, J.L.; Hawkins, A.R.; Redfern, C.P. Inducing apoptosis of cancer cells using small-molecule plant compounds that bind to GRP78. *Br. J. Cancer* **2013**, *109*, 433-443.
29. Macias, A.T.; Williamson, D.S.; Allen, N.; Borgognoni, J.; Clay, A.; Daniels, Z.; Dokurno, P.; Drysdale, M.J.; Francis, G.L.; Graham, C.J.; Howes, R.; Matassova, N.; Murray, J.B.; Parsons, R.; Shaw, T.; Surgenor, A.E.; Terry, L.; Wang, Y.; Wood, M.; Massey, A.J. Adenosine-derived inhibitors of 78 kDa glucose regulated protein (Grp78) ATPase: insights into isoform selectivity. *J. Med. Chem.* **2011**, *54*, 4034-4041.
30. Thomas, S.; Sharma, N.; Gonzalez, R.; Pao, P.W.; Hofman, F.M.; Chen, T.C.; Louie S.G.; Pirrung, M.C.; Schönthal, A.H. Repositioning of Verrucosidin, a purported inhibitor of chaperone protein GRP78, as an inhibitor of mitochondrial electron transport chain complex I. *PLoS One* **2013**, *8*, e65695.



31. Firczuk, M.; Gabrysiak, M.; Barankiewicz, J.; Domagala, A.; Nowis, D.; Kujawa, M.; Jankowska-Steifer, E.; Wachowska, M.; Glodkowska-Mrowka, E.; Korsak, B.; Winiarska, M.; Golab, J. GRP78-targeting subtilase cytotoxin sensitizes cancer cells to photodynamic therapy. *Cell Death Dis.* 2013, 4, e741.
32. Maddalo, D.; Neeb, A.; Jehle, K.; Schmitz, K.; Muhle-Goll, C.; Shatkina, L.; Walther, T.V.; Bruchmann, A.; Gopal, S.M.; Wenzel, W.; Ulrich, A.S.; Cato, A.C. A peptidic unconjugated GRP78/BiP ligand modulates the unfolded protein response and induces prostate cancer cell death. *PLoS One* **2012**, 7, e45690.
33. Arap, M.A.; Lahdenranta, J.; Mintz, P.J.; Hjitou, A.; Sarkis, A.S.; Arap, W.; Pasqualini, R. Cell surface expression of the stress response chaperone GRP78 enables tumor targeting by circulating ligands. *Cancer Cell* **2004**, 6, 275-284.
34. Chang, Y.J.; Huang, Y.P.; Li, Z.L.; Chen, C.H. GRP78 knockdown enhances apoptosis via the down-regulation of oxidative stress and Akt pathway after epirubicin treatment in colon cancer DLD-1 cells. *PLoS One*, 2012, 7, e35123.
35. Finegold, M.J. Hepatic tumors in childhood. Pathology of pediatric gastrointestinal and liver disease, Springer-Verlag, New York (2004), p. 300.
36. Lopez-Terrada, D.; Cheung, S.W.; Finegold, M.J.; Knowles, B.B. HepG2 is a hepatoblastoma-derived cell line. *Human Pathol.* **2009**, 40, 1512-1515.
37. Aden, D.P.; Fogel, A.; Plotkin, S.; Damjanov, I.; Knowles, B.B. Controlled synthesis of HbsAg in a differentiated human liver carcinoma-derived cell line *Nature* **1979**, 282, 615-616.
38. Wu, L.F.; Guo, Y.T.; Zhang, Q.H.; Xiang, M.Q.; Deng, W.; Ye, Y.Q.; Pu, Z.J.; Feng, J.L.; Huang, G.Y. Enhanced antitumor effects of adenoviral-mediated siRNA against GRP78 gene on adenosine-induced apoptosis in human hepatoma HepG2 cells. *Int J. Mol. Sci.* 2014, 15, 525-544.
39. Dalby, B.; Cates, S.; Harris, A.; Ohki, E.C.; Tilkins, M.L.; Price, P.J.; Ciccarone, V.C. Advanced transfection with Lipofectamine 2000 reagent: primary neurons, siRNA, and high-throughput applications. *Methods* **2004**, 33, 95-103.

40. Blackman, B.A. Glucose-Regulated-Protein 78 Cell Surface Signaling for Apoptosis of HepG2 Hepatoblastoma Cancer Cells. *MSc. Thesis* **2013**, Seton Hall University, 37pp.
41. Neri, S.; Mariani, E.; Meneghetti, A.; Cattini, L.; Facchini, A. Calcein-Acetoxymethyl Cytotoxicity Assay: Standardization of a Method Allowing Additional Analyses on Recovered Effector Cells and Supernatants. *Clin. Diagn. Lab Immunol.* **2001**, *8*, 1131–1135.
42. Maina, A.; Bender, M.; Morozko, E.; Blackman, B.A.; Parronchi, C.J.; Blake, A.D.; Sabatino, D. Solid-phase synthesis, characterization and RNAi activity of branch and hyperbranch siRNAs. *Bioorg. Med. Chem.* **2013**, *23*, 5270-5274.
43. Suzuki, T.; Lu, J.; Zahed, M.; Kita, K.; Suzuki, N. Reduction of GRP78 expression with siRNA activates the unfolded protein response leading to apoptosis in HeLa cells. *Arch. Biochem. Biophys.* *2007*, *468*, 1-14.
44. Mahmood, T.; Yang, P.C. Western blot: technique, theory and trouble-shooting. *N. Am. J. Med. Sci.* *2012*, *4*, 429–434.
45. Lees, G.J. Trypan blue in vivo stains nigral dopaminergic neurons killed by 6-hydroxydopamine. *Histochemistry* *1989*, *91*, 357-359.
46. Badway, A.C.; West, F.M.; Tente, S.M.; Blake, A.D. Somatostatin regulates intracellular signaling in human carotid endothelial cells. *Biochem. Biophys. Res. Commun.* **2004**, *319*, 1222-1227.

## **4.7 EXPERIMENTAL SECTION**

### **4.7.1 HepG2 CELL CULTURE**

The human hepatoblastoma, HepG2 cells (American Type Culture Collection, Manhasset, VA) were cultured in T25 cm<sup>2</sup> and T75 cm<sup>2</sup> flasks (Grenier Bio-one Cell star, FL) in Dulbecco's Modified Eagle Medium (DMEM) with GlutaMAX and heat-inactivated 10% Fetal Bovine Serum (Gibco, CA), containing 1% penicillin/streptomycin (Gibco, CA), in an incubator set at 37 °C with a humidified atmosphere of 5% CO<sub>2</sub>. Cells were routinely passaged at 75% confluence using Dulbecco's PBS (Gibco, CA) and 0.05% Trypsin-EDTA (1X), Phenol Red (Gibco, CA) and then split into a 1:10 dish ratio. Cells used in the transfection experiments were cultured in 6- 96-well culture plates and allowed to recover for 24 hours before treatment.

### **4.7.2 siRNA PREPARATION**

A solution of each single strand siRNA (50 μM) was prepared by taking an aliquot from the crude stock and adding millipore water to give the required concentration. From these stock solutions (50 μM), siRNAs (30 μL) were combined in a microcentrifuge tube and treated with annealing buffer (15 μL of 5X Annealing Buffer: 50 mM Tris-HCl, pH 8.0, 100 mM NaCl, 5.0 mM EDTA) to give a final volume, 75 μL (20 μM). The solution was then heated at 95 °C (1 min) to denature higher-order structure, centrifuged and allowed to slow cool at room temperature (1 h) before being placed in the fridge overnight for hybrid formation. The resulting duplexes were frozen at – 20 °C until use.

### **4.7.3 siRNA TRANSFECTION IN HepG2 CELLS**

HepG2 cells were transfected with the appropriate siRNA, **1-7**, (40 pmol) and Lipofectamine™ 2000 (1 μL) according to the manufacturer's instructions. Briefly, 5 x 10<sup>4</sup> cells

were plated in 24-well culture plates containing DMEM (10% fetal bovine serum) and maintained for 48 h in a humidified incubator at 37 °C with 5% CO<sub>2</sub>. Twenty four hours prior to transfection the cells were switched to a basal, serum free medium (OptiMEM). Transfections were performed with Lipofectamine™ 2000 (1 µL) and the appropriate siRNA, **1-7**, (40 pmol siRNA in 50 µL of OPTIMEM). The siRNA-Lipofectamine complexes were incubated at room temperature for 20 min, added to the cell monolayers and the plates were incubated at 37 °C with 5% CO<sub>2</sub>. After 24 h, the serum free basal medium was removed and replaced with growth medium. Transfected cells were harvested 48 h after transfection for analysis.

#### **4.7.4 SDS-PAGE and WESTERN BLOTTING**

Parallel cultures of HepG2 cells were prepared with serum-free basal medium (OptiMEM) for 24 h and then incubated in the presence or absence of varying concentrations of siRNAs (**1-7**) for 48 hours at 37 °C. Cell lysates were prepared with RIPA lysis buffer, heated to 70 °C for 10 min., resolved on NuPAGE 10% Bis-Tris gels and electroblotted onto polyvinylidene difluoride (PVDF) membranes. Membranes were treated for 90 min in a blocking buffer containing 5% (w/v) of non-fat dehydrated milk to minimize non-specific binding. Total HepG2 cells' GRP78 expression was immunodetected with a 1:200 final dilution of anti-GRP78 N-20 antibodies. The membrane associated immunoreactivity was then detected using a 1:5000 dilution of a horseradish peroxidase-conjugated anti-goat secondary antibody and detected using ECL Plus chemiluminescence. The resulting autoradiograph was scanned, quantified with NIH ImageJ and expressed as integrated pixel density.

#### **4.7.5 CONFOCAL MICROSCOPY**

HepG2 cells were plated at a cell density of 15,000 cells/well on 4 well chamber glass slides. Cells were transfected and incubated for an additional 48 hours prior to confocal microscopy. Cells were then rinsed with Serum free DMEM, and fixed on the glass slides with 2% paraformaldehyde in PBS (Gibco, CA) for 10 minutes. The samples were then blocked in 10% rabbit serum for 30 minutes, incubated in goat-anti human GRP78 N-20 antibody (Santa Cruz Biotechnology, CA) 1:75 dilution in 2.5% rabbit serum in PBS for 2 hours at room temperature. After PBS washing the slides were incubated in goat anti-rabbit conjugated with Fluorescein isothiocyanate (FITC) antibody in 2.5% rabbit serum in PBS for 50 minutes and Vectorshield (Vector Laboratories, CA) covered to protect from photobleaching. Slides were counterstained with 4',6-diamino-2-phenylindole (DAPI) in 0.50  $\mu\text{g}/\text{mL}$  in PBS for 3 minutes and then a mounting medium with fluorescence was added with coverslips. Slides were viewed on a Confocal Laser Scanning Microscope (Olympus, MA) with a 40X oil objective lens in conjunction with the Olympusview program.

#### **4.7.6 CELL VIABILITY**

Cell viability was determined in 24-well plates with HepG2 cells cultured in serum-free basal medium for 24 h and then incubated in the presence or absence of varying concentrations of Lipofectamine 2000 (1-10  $\mu\text{g}$ ) and siRNAs (20-80 pmol, **1-7**) for 48 h at 37 °C. The samples were removed with Enzyme Free Dissociation Buffer (Invitrogen, CA) for 3 minutes at 37 °C. Samples were pelleted and re-suspended in Dulbecco's PBS (1 mL) and Trypan blue 0.4% stain (100  $\mu\text{L}$ ) was added. Samples were quantified using a Countess automated cell counter

(Invitrogen, CA). The resulting data was analyzed with GraphPad Prism 4.0 and statistical significance was determined by ANOVA ( $p < 0.05$ ).


## CHAPTER 5. PRELIMINARY STUDIES TOWARDS THE DEVELOPMENT OF A CANCER-TARGETING GENE THERAPY APPROACH

### 5.1 ABSTRACT

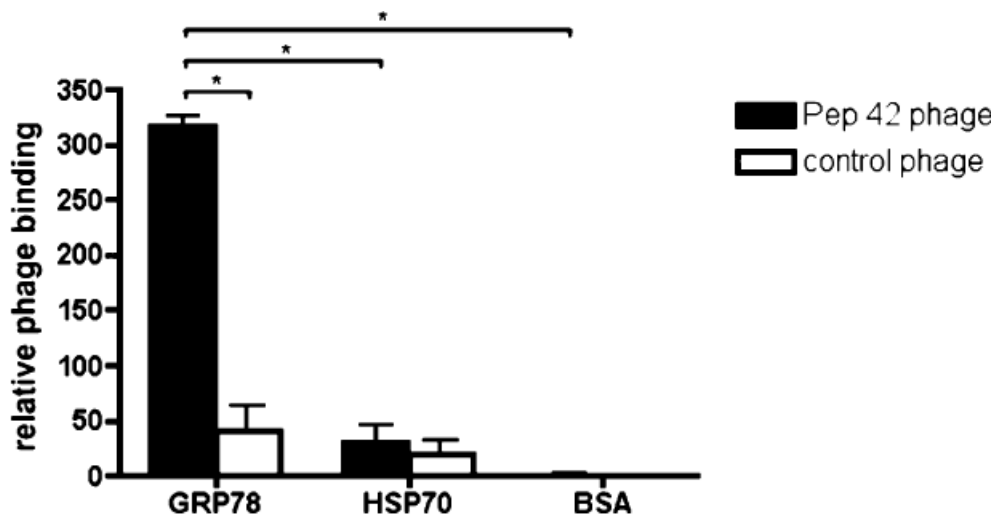
Linear, branch and hyperbranch GRP78 siRNAs proved to be valuable substrates for silencing GRP78 expression (50-70%) and triggering cell death (5-15%) in a HepG2 hepatoblastoma cancer cell line (Chapter 4). In this chapter, preliminary results which showcase the combination of GRP78-targeting siRNAs and peptides (*i.e.* cancer-targeting peptides, CTPs) are described towards the development of a cancer-targeting gene therapy approach. In this method, linear, branch and hyperbranch GRP78-silencing siRNAs are complexed with poly(arginine) derived GRP78-targeting peptides that may usher the selective delivery of siRNAs into GRP78 harboring tumor cells for RNAi and cell death activity. The complexes formed between the CTPs:siRNAs were effectively characterized by native PAGE, CD spectroscopy, thermal denaturation, DLS and TEM experiments which demonstrated the formation of stable, higher-ordered complexes. Moreover, the direct transfection of a linear GRP78 silencing siRNA (**Table 2.1, sequence no. 1**) with a CTP derived from the Pep42-R9 sequence demonstrated significant GRP78 silencing (50-60%) and modest cell death (5-15%) in HepG2 cells which mirrored the results obtained from the benchmark Lipofectamine:siRNA transfection studies (Chapter 4). These results suggests that the Pep42-R9 sequence and related CTPs may function as useful GRP78-targeting transfection agents in a wide range of cancer cell types that display cell surface overexpression of GRP78. This discovery is important for the development of an effective cancer-targeting gene therapy approach, which aims to kill cancer cells selectively, while leaving the healthy ones unscathed.

## 5.2 INTRODUCTION

### 5.2.1 SELECTION OF PEP42 AS A GRP78-TARGETING PEPTIDE

The selection of Pep42, a cyclic peptide composed of  CTVALPGGYVRVC was discovered from a library of short cyclic peptide sequences expressed on the surface of M13 filamentous phage.<sup>1</sup> In a process referred to as whole cell phage display biopanning<sup>2</sup>, the peptides coated on the phage surface were screened against highly metastatic melanoma cells (Me6652/4) and a low metastatic clone as control (Me6652/56) for cell binding affinity and specificity. Following multiple rounds of evolution and selection, phages which strongly adsorbed on the surface of highly metastatic melanoma cells but not on the low metastatic clone were isolated and analyzed to determine the identity of the peptide and receptor involved in the binding interaction. The corresponding peptide sequence, Pep42, was found to exhibit high affinity and selective binding to GRP78, even relative to the homologous heat shock protein, Hsp70, chaperone and the ubiquitous bovine serum albumin, BSA, a surrogate for serum proteins **(Figure 5.1).**<sup>3</sup>



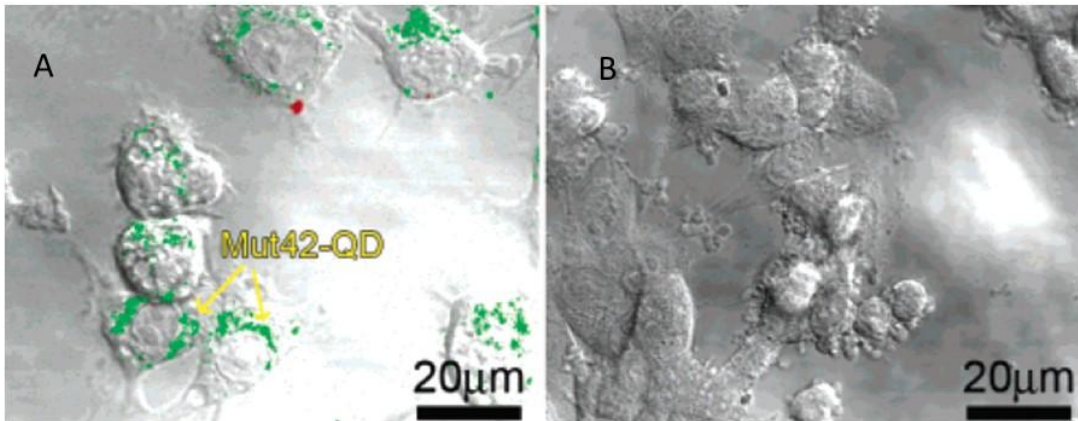


**Figure 5.1.** Binding assay of the Pep42 phage with recombinant proteins. Pep42 phage demonstrates high binding affinity and specificity for GRP78. Figure adapted from reference 3.

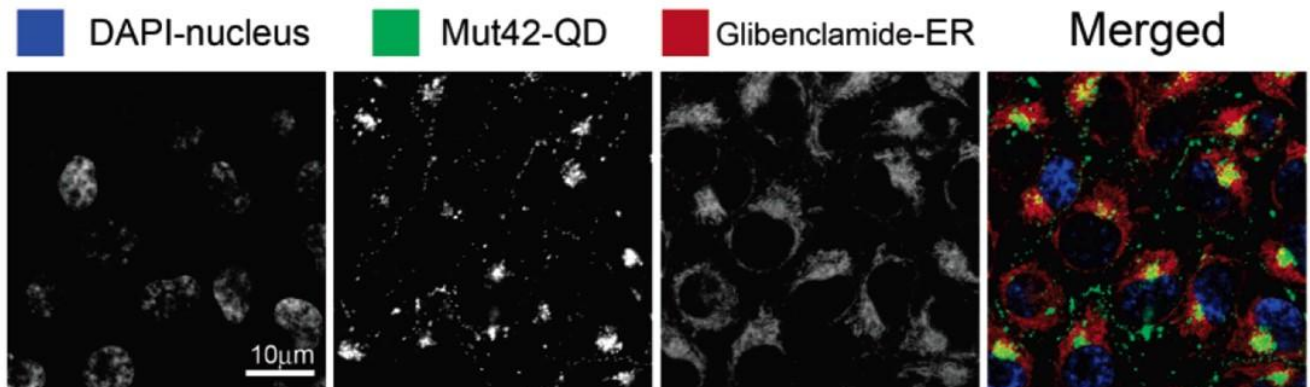
The cell surface Pep42:GRP78 binding selectivity was also explored on human cancer cell lines, including the highly metastatic melanoma cells (Me6652/4), lung adenocarcinoma cells (A549), osteocarcinoma cells (A549) and HepG2 hepatoblastoma cells relative to two normal human fibroblast cell lines (HDFa and CCD-11Lu).<sup>3</sup> Significantly, FITC-labeled Pep42 was found to bind to the human cancer cells but not the normal cell line controls according to flow cytometry. The same observation was also noticed with the FITC-labeled monoclonal antibody specific for GRP78, suggesting that the Pep42:GRP78 interaction may be responsible for tumor binding selectivity. In order to validate this hypothesis, a polyclonal antibody was used to block GRP78 on the surface of HepG2 cells, followed by treatment with FITC-labeled Pep42. This resulted in a decrease in the fluorescence signaling from the FITC-Pep42 probe. A similar decrease in fluorescence signaling from the FITC-Pep42 conjugate was observed following a GRP78-silencing siRNA treatment, illustrating the importance of the GRP78 cell surface receptor for Pep42 binding.

Confocal laser scanning fluorescence microscopy was used to support the Pep42:GRP78 binding interaction on the surface of tumors and examine whether the peptide exhibited cell permeability.<sup>1,3</sup> In this study, a derivative of Pep42, Mut42, which replaced the valine at position 10 with a lysine to facilitate the incorporation of the FITC label was used to ascertain cell translocation activity. It is imperative to note that this site specific substitution in Pep42 was not found to alter its GRP78 binding activity. Thus, treatment of FITC-labeled Mut42 with metastatic melanoma cells (Me6652/4) and the low metastatic control (Me6652/56) resulted in greater uptake within the tumorigenic melanoma cells (**Figure 5.2, i**).<sup>1</sup> Similarly, Mut42-quantum dots (Mut42-QD) were prepared and applied for detecting cellular localization with greater sensitivity relative to their fluorescent counterpart. In this case, the Mut42-QD probes were found to translocate and localize within the cytosol of highly metastatic melanoma cells without entering their nucleus. Further investigation revealed that the Mut42-QD co-localized in the endoplasmic reticulum with the co-administration of Glibenclamide, a biomarker that stains the ER (**Figure 5.2, ii**).

i.



ii.



**Figure 5.2.** Cell uptake (i.) and localization (ii.) of Mut42. i. Comparison of the cell uptake of Mut42-FITC in (a) highly metastatic melanoma cells (Me6652/4) and (b) low metastatic melanoma cells (Me6652/56). Mut42-FITC green signal apparent in (a) but not in (b). ii. Cellular co-localization of Mut42-QD in the ER of highly metastatic melanoma cells (Me6652/4) with Glibenclamide. Figure adapted from reference 1.

Confocal microscopy was also employed to elucidate the mechanism of Pep42 cell translocation.<sup>3</sup> A Pep42-QD was prepared and applied to discern the mechanism of internalization in A549 osteocarcinoma cells. In this assay, Pep42 was found to partially co-localize with known markers of endocytosis such as transferrin and cholera toxin subunit B.

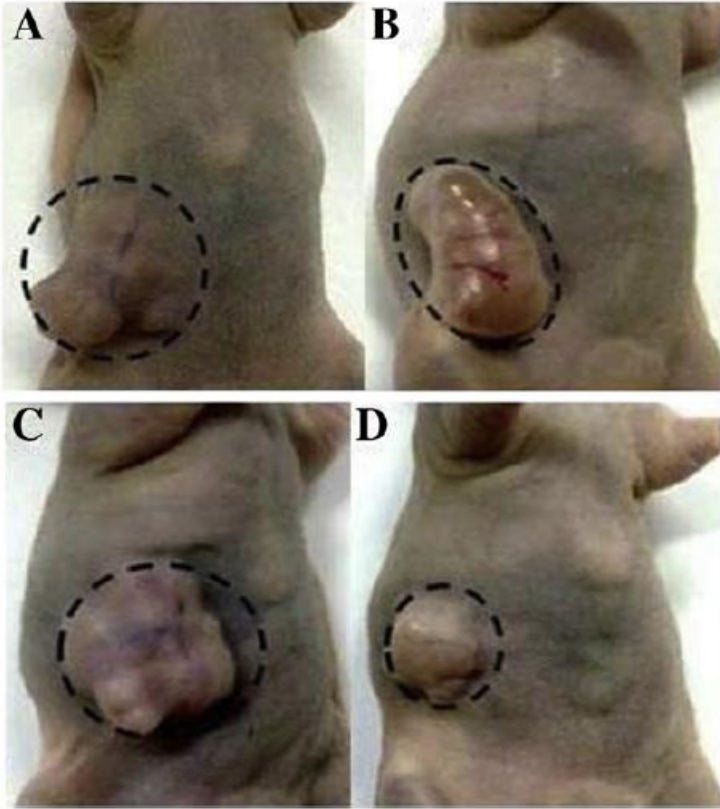
Transferrin glycoproteins have been found to internalize within cells by an endocytosis pathway which involves the formation of clathrin-coated vesicles at the cell surface.<sup>4</sup> Whereas, the cholera toxin subunit B internalizes within cells by caveolae-mediated endocytosis.<sup>5</sup> In order to delineate the endocytosis pathway of Pep42, several inhibitors of endocytosis were examined, including chlorpromazine, a known inhibitor of clathrin mediated endocytosis.<sup>6</sup> In its presence, Pep42 and transferrin did not internalize within A549 osteocarcinoma cells; whereas chlorpromazine had no effect on cholera toxin subunit B.<sup>3</sup> These results suggests that Pep42, in similar fashion to transferrin, internalizes within A549 osteocarcinoma cells by a clathrin-coated endocytosis pathway.

In light of Pep42's GRP78 targeting and internalization within cancer cell types but not in healthy ones, Pep42 was tested as a targeting drug delivery agent for anti-cancer applications.<sup>1,3,7</sup> Towards this goal, Pep42 has been effectively conjugated with cytotoxic anti-cancer drugs such as Taxol and Doxorubicin, photosensitizers such as a functionalized hematoporphyrin for applications in photodynamic therapy and the pro-apoptotic D-(KLAKLAK)<sub>2</sub> sequence triggering programmed cell death specifically in human cancer cells and in xenograft mouse models.<sup>1,3,7</sup> Thus, the highly specific Pep42:GRP78 ligand-receptor interaction may form the basis for new and improved drug delivery methods in cancer treatment.

### **5.2.2 POLY(ARGININE) PEPTIDES AS siRNA CELL DELIVERY AGENTS**

Poly(arginine) peptides encompass a special class of cell-penetrating peptides (CPPs) that have the ability to participate in ionic binding interactions with negatively charged biomolecules and cell-membrane translocation activity.<sup>8</sup> Moreover, the number of arginine residues within the CPPs have been found to influence membrane permeability, with poly(arginine) sequences

containing in between 6-12 arginine residues eliciting optimal permeability and localization within the cytosol or nucleus of the cell.<sup>8,9</sup> Their translocation mechanism is still widely debated, from which the nature of the arginine-rich sequence, its secondary structure and cell types have each been found to influence its membrane permeability and cellular localization.<sup>8-10</sup> Moreover, poly(arginine) peptides have typically shown minimal cellular cytotoxicities<sup>9</sup>, facilitating their applications in the delivery of biomolecules across the plasma membrane. Specifically, poly(arginine) peptides have been employed in siRNA transfections due to their favorable ionic binding interactions with the negatively charged phosphodiester backbone of the oligonucleotide sequences. For example, human epidermal growth factor receptor 2 (HER-2) silencing siRNA has been effectively transfected within Cos-7 cells and in subcutaneous tumor transplants in mice with an arginine peptide (R15) leading to potent down-regulation of HER-2 mRNA and marked decrease in tumor size over a 17 day treatment regimen (**Figure 5.3**).<sup>11</sup> Although arginine-rich peptides are highly efficient in mediating siRNA cellular uptake for RNAi activity *in vitro* and *in vivo*, their translation from pre-clinical to clinical use has been hindered by poor specificity and widespread toxicity, as these peptides and their cargo are dispersed in almost all tissues.<sup>12</sup> In order to address this limitation, cancer-targeting peptides have been associated with poly(arginine) sequences to effect targeted cell delivery of siRNA *in vitro* and *in vivo*.<sup>13</sup>



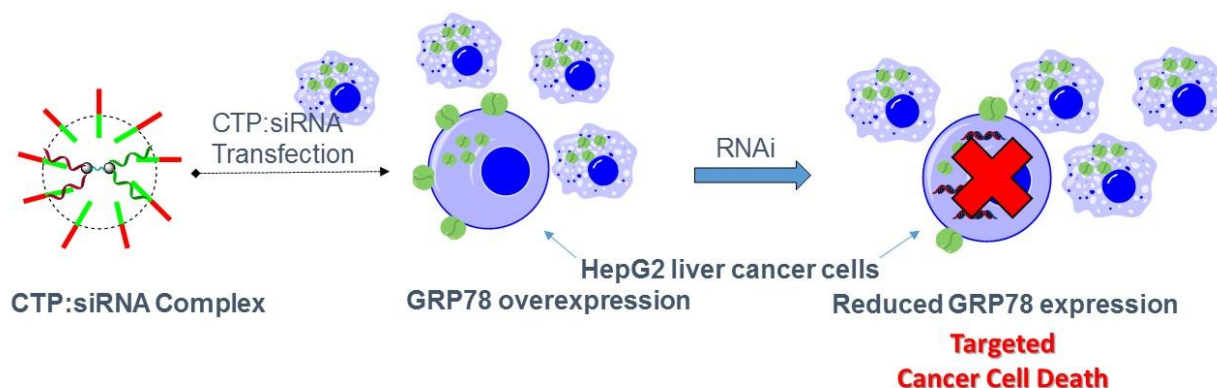
**Figure 5.3.** Tumor growth in xenograft mouse with (A) no treatment, (B) siRNA, (C) R15:mismatch HER-2 siRNA and (D) R15:HER-2 siRNA following a 17 day treatment regimen. Transfection of R15:HER-2 siRNA shrunk the tumor size by more than 7 times relative to the un-treated control. Figure adapted from reference 11.

### 5.3 CHAPTER OBJECTIVES

This chapter sets the stage for the development and application of a cancer-targeting gene therapy approach (**Figure 5.4**). Towards this ultimate goal, preliminary results are highlighted in this chapter that demonstrates the effective formation of GRP78-targeting CTP:siRNA complexes and their application in RNAi. This endeavor was partially accomplished in collaboration with Stesha Joseph (Dr. Sabatino's group) who synthesized and characterized the CTPs used in this study and assisted in their complex formation/ characterization studies. TEM and dynamic light scattering (DLS) measurements were obtained at Queens College with the

assistance of Reeta Yadav, a graduate student in Dr. Samuni's research group. Additionally, Brittany Blackman, Christopher Parronchi, Megan Kelly (Dr. Blake's group) and Mariana Phillips (Dr. Sabatino's group) have conducted the preliminary biological studies reported in this chapter and continue to investigate the bio-activity of the CTP:siRNA constructs. More specifically, complex formation between the CTP:siRNA ionic particles was validated by native PAGE, thermal denaturation, CD spectroscopy, DLS and TEM experiments. These methods served to elucidate the optimal stoichiometric ratios of the CTPs and siRNAs necessary for complex formation, thermal stabilities, particle size distributions and the structures of the higher-ordered assemblies. Prior to RNAi application, the serum stability of the CTP:siRNA complexes relative to their individual components was examined in 10% fetal bovine serum (FBS) to determine their resistance towards degradation in biological media. With stable CTP:siRNA complexes in hand, their potential in RNAi application is discussed en route towards the development of an effective cancer-targeting approach.

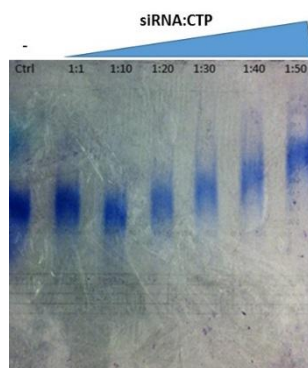
**Figure 5.4.** Proposed cancer-targeting gene therapy strategy



## 5.4 RESULTS AND DISCUSSION

### 5.4.1 PREPARATION AND CHARACTERIZATION OF CTP:siRNA COMPLEXES

With pure samples of linear, V-shape, Y-branch and  $\lambda$  hyperbranch siRNAs (**Table 2.1**, **sequence no. 1-7**) and CTPs containing the GRP78-targeting Pep42 with varying poly(arginine) sequences<sup>14</sup>, the optimal stoichiometric ratio for CTP:siRNA complex formation was established by native PAGE. Stoichiometric ratios of 1-50:1, CTP:siRNA were combined in an annealing 30% sucrose (Tris-Acetate-EDTA) TAE buffer pH 8.3, incubated for 30 min at 37 °C and loaded on a native PAGE absent of urea. Samples were resolved on the native gel and detected by staining with a Stains All™ dye (Aldrich) which forms a dark blue colored complex with the oligonucleotides.<sup>15</sup> From this gel shift assay, increasing mole ratios of a CTP (1.0-50  $\mu$ mol, 1-50 bearing a nona-arginine sequence (R9) relative to a single-stranded siRNA control (1.0  $\mu$ mol, **Table 2.1**, sequence 3) produced shifts in the electrophoretic mobilities of the forming CTP:siRNA complexes (**Figure 5.5**). Specifically, at a stoichiometric ratio of 50:1 CTP:siRNA formed a slower moving band indicative of a higher-ordered complex relative to the single strand siRNA control.

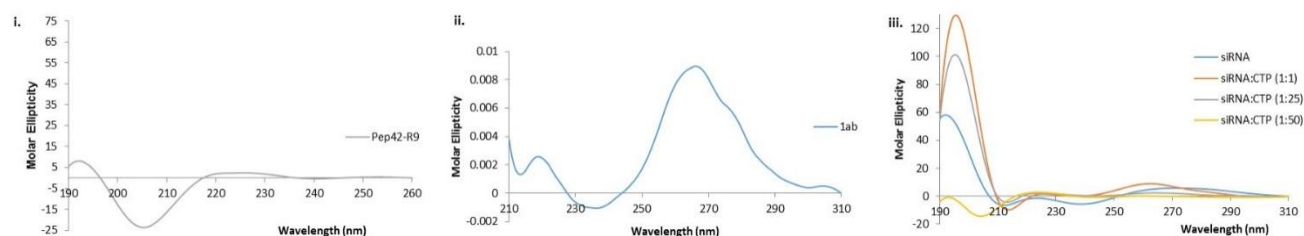


**Figure 5.5.** Native PAGE gel shift assay. Linear single strand siRNA (1.0  $\mu$ mol, Table 2.1, sequence 3) and increasing (1-50:1) stoichiometric ratios of CTP (1.0 – 50  $\mu$ mol, Pep42-R9).

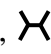


Similarly, this CTP sequence was found to effectively produce higher-ordered complexes at a mole ratio of 50:1 with double-stranded, Y-shape and  $\times$  hyperbranch siRNAs (**Table 2.1, sequence nos. 2, 5 and 7**) by native PAGE (**Appendix C**).

CD spectroscopy was then used to assess the changes in CTP and siRNA structures in their free form and bound state (**Figure 5.6**). The cyclic Pep42-R9 sequence demonstrated a CD spectrum that contained an ordered turn conformation with minimal random coil observed. Some types of peptide turn geometries have been characterized by a minimum band at around 210 nm and maximum molar ellipticities centered around 220 and 190 nm (**Figure 5.6, i**).<sup>16</sup> Conversely, disordered peptide structures or random coils have strong negative bands centered around 190 nm.<sup>17</sup> The linear siRNA control (**Table 2.1, sequence 1**) demonstrated a typical CD profile for the canonical double-stranded A-form RNA helix (Chapter 3), displaying a minimum peak at around 240 nm and a broad maximum in between 255-290 nm (**Figure 5.6, ii**).<sup>18</sup> In combination, the CTP:siRNA complexes exhibited profound changes on their respective secondary structures (**Figure, 5.6, iii**) and produced higher-ordered structures that were atypical of the putative CTP turn conformation or siRNA A-type helix. Similar trends were observed for the remaining CTP:siRNA complexes (**Appendix D**).



**Figure 5.6.** CD spectra of i. CTP: Pep42-R9 (0.1 mg/mL), ii. siRNA (0.26  $\mu$ mol, Table 2.1, sequence 1) and iii. CTP:siRNA complexes (13  $\mu$ M, 1-50:1 mol/mol) in PBS (137 mM NaCl, 2.7 mM KCl, 10 mM Na<sub>2</sub>HPO<sub>4</sub>, 2 mM KH<sub>2</sub>PO<sub>4</sub> adjusted to pH 7.4) at 25 °C.

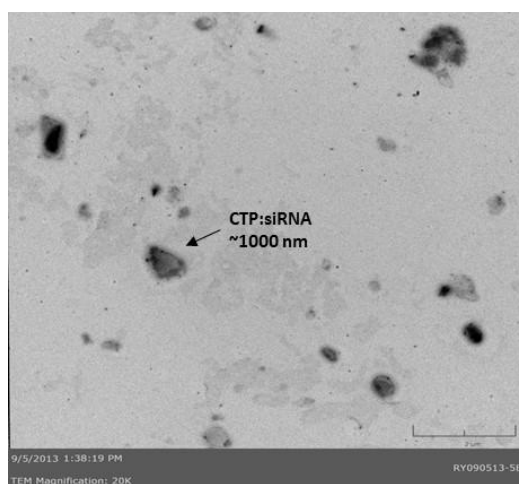
In order to determine the sizes, shapes and structures of the CTP:siRNA complexes, DLS and transmission electron microscopy (TEM) experiments were conducted. DLS was initially employed to investigate the size distributions of the particles formed between the CTP:siRNA relative to their individual components (**Table 5.1**). DLS measurements of the effective diameters (nm) observed from the nanoparticles indicated a uniform size distribution for the CTP, Pep42-R9 (~ 40 nm) and aggregates for the linear siRNA (**Table 2.1, sequence no. 2**, 600-1000 nm, and a monomer size of 20 nm). Comparatively, the CTP:siRNA complex (13  $\mu$ M, 50:1 CTP:siRNA) displayed a bimodal size distribution according to the DLS measurements, with one distribution occurring at around 210 nm and a much larger one at about 1400 nm. The latter results in more than a 50-fold increase in CTP:siRNA particle size relative to the unbound components, validating the formation of higher-ordered complexes. Similar trends were observed from the DLS measurements obtained for the CTP:siRNA complexes formed in between the Pep42-R9 sequence and the Y-shape (**Table 2.1, sequence no. 5**),  hyperbranch (**Table 2.1, sequence no. 7**) siRNAs (**Appendix E**).

**Table 5.1** DLS measurements of the effective diameters (nm) observed.<sup>a</sup>

Samples	Effective Diameters (nm)
CTP, Pep42-R9	40 $\pm$ 4
Linear siRNA, 2 (monomers)	~ 20
CTP:siRNA	210 $\pm$ 14
	1400 $\pm$ 80

<sup>a</sup>Samples (0.05-0.15  $\mu$ M) were prepared in pre-filtered (0.2  $\mu$ m filter) pH 7.0 phosphate buffer (140 mM KCl, 1 mM MgCl<sub>2</sub>, 5 mM NaHPO<sub>4</sub>) and sonicated for 30 minutes before taking measurements. The reported diameter is the average of 5 runs for each sample reported with standard deviations about the mean.

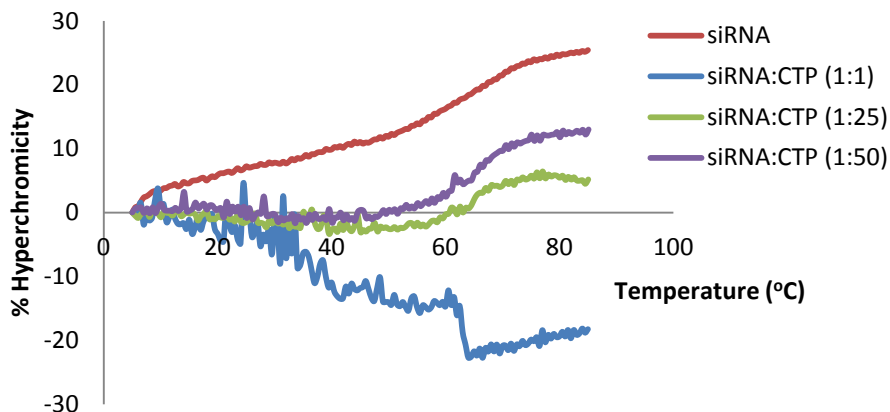
The TEM images provided an illustration of the shapes and structures formed from the CTP:siRNA complexes (**Figure 5.7**). In the case of the complex formed between a CTP, Pep42-R9 and a linear siRNA sequence (**Table 2.1, sequence no. 2**) the particles appeared as spherical shaped aggregates with approximate diameters of 1000 nm, that were in agreement with those observed from the DLS measurements. Moreover, similar results were also obtained for the remaining CTP:siRNA complexes (**Appendix F**), highlighting the efficiency of the Pep42-R9 sequence in condensing siRNAs of varying lengths, sequences and morphologies. These results were also in agreement with the TEM images reported for a myristoylated cell-penetrating peptide with a transferrin receptor-targeting sequence bound to siRNA for RNAi application.<sup>19</sup> Thus, the ability for the CTP sequence to effectively condense siRNA into stable nanoparticle formulations is an important requirement for their biological applications.



**Figure 5.7.** TEM image of the complex formed between Pep42-R9 and linear siRNA (Table 2.1, sequence no. 2). Samples (0.13  $\mu\text{M}$ ) were mixed with 1% uranyl acetate in ethanol (1:1 v/v), sonicated for 10 minutes, and added to a carbon film coated copper grid, 300 mesh (Electron Microscopy Sciences, PA) and dried overnight prior to viewing under the transmission electron microscope (JEOL, model JEM-1200 EX). Images were taken with a SIA-L3C CCD camera

(Scientific Instruments and Applications, Inc., GA) using the software Maxim DL5 (Diffraction Limited, Ottawa, Canada).

Thermal denaturation experiments were next conducted to determine the thermal stability of the CTP:siRNA complex. In the absence of peptide, the double-stranded siRNA (**Table 2.1, sequence no. 2**) exhibited a helix-to-coil transition<sup>18</sup> with increasing temperatures (5-90 °C) that produced a noticeable change in hyperchromicity (%H: 5-30%) and thermal denaturation temperature ( $T_m$ : 72 °C). This data is consistent with that reported for the linear, V-shape, Y-branch and  $\chi$  hyperbranch siRNAs described in this study (Chapter 3). Titration of CTP (0.26 – 13  $\mu$ mol) to siRNA (0.26  $\mu$ mol) produced striking changes in the thermal denaturation curves (**Figure 5.8**). These changes were associated with a sharp decrease in hyperchromicities (30% to  $\leq$ 10%) which abolished the single phase transition observed in the control (free-form) siRNA. Presumably, at optimal CTP:siRNA (15  $\mu$ M, 50:1 mol/mol) concentrations the siRNA no longer exhibits the characteristic biophysical traits of a double-stranded RNA hybrid. Similar trends were observed in the thermal denaturation curves of the remaining CTP:siRNA complexes (**Appendix G**).

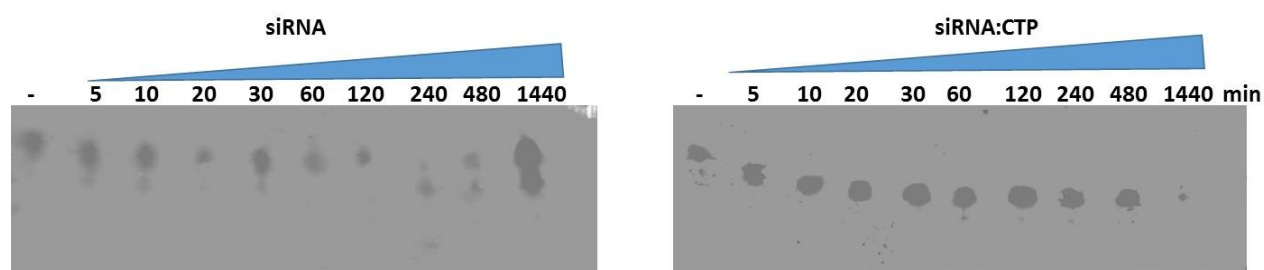


**Figure 5.8.** Thermal denaturation studies of the CTP:siRNA complex. Samples were prepared by mixing CTP:siRNA (15  $\mu$ M, 1-50:1 mol/mol) in phosphate buffer (140 mM KCl, 1 mM MgCl<sub>2</sub>, 5 mM NaHPO<sub>4</sub>) and placing on a heat block incubator set at 37 °C for 1 hour. Samples were cooled to room temperature and placed in the fridge overnight for use the next day.

#### 5.4.2 BIOLOGICAL STUDIES OF THE CTP:siRNA COMPLEXES

The ability for the CTP:siRNA complexes to retain metabolic stability is an important requirement for their fruitful RNAi applications. This is because the native siRNA sequences are typically prone to nuclease digestion in biological media, limiting their therapeutic potential.<sup>20</sup> Samples were subjected to a 10% fetal bovine serum (FBS) in Dulbecco's Modified Eagle Medium (DMEM) treatment in order to test the metabolic stability of the CTP:siRNA complex relative to the free-form siRNA. Aliquots were taken at measured time point intervals and run on a denaturing (urea) PAGE to resolve the samples. Stains-All™ (Aldrich) detection produced the desired siRNA bands with and without the CTP (**Figure 5.9**). Excitingly, the CTP:siRNA complexes remained intact up to 8 hours, (**Figure 5.9, B**) while in the naked siRNA produced short degradation products that were visible as lower migrating bands on the gel even after 5 minute FBS treatment (**Figure 5.9 A**). The ability of peptides to confer nuclease resistance to

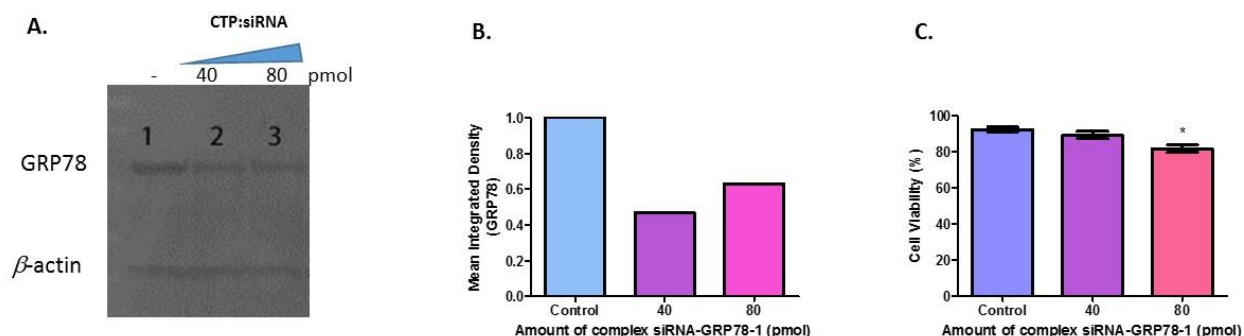
siRNA is not unexpected, peptide:siRNA complexes remained stable (> 8 hours) while the free-form siRNA was completely degraded within 4 hours in 50% FBS.<sup>19</sup>



**Figure 5.9.** 18% native (no urea) PAGE of (A) siRNA (20  $\mu$ M) and (B) CTP:siRNA (20  $\mu$ M) in 10% FBS in DMEM. Samples were incubated (0.15 mL, 10% FBS/DMEM) at 37 °C and at measured time points, aliquots (10  $\mu$ L) were treated with gel loading buffer (10  $\mu$ L of 80 % formamide in TBE), heated at 95 °C and resolved on denaturing PAGE. The gels were stained with Stains-All™ (Aldrich) to view the siRNA decomposition patterns.

With stable constructs in hand, the RNAi activity of the CTP:siRNA complex was next evaluated in HepG2 cells (**Figure 5.10**). A CTP:siRNA complex (50:1 mole ratio, 20  $\mu$ M) was prepared in a suitable binding buffer (50 mM Tris-HCl, pH 8.0, 100 mM NaCl, 5 mM EDTA) for transfection within the HepG2 monolayers. The cells were incubated and cultured (48 h, 37 °C, 5% CO<sub>2</sub>) prior to analysis. Following incubation, cell lysates were prepared (RIPA lysis buffer, Invitrogen) and resolved by SDS PAGE, transferred to a PVDF membrane and immunoblotted with an anti-GRP78 primary antibody and a secondary antibody coupled to horseradish peroxidase (HRP). GRP78 expression levels were detected by autoradiography which produced reduced GRP78 (~50%) at quantities that were comparable to the benchmark Lipofectamine:siRNA transfections reported in Chapter 4. This experiment thus validates the utility of the CTP as an siRNA transfection agent for RNAi activity in HepG2 cells (**Figure 5.10**,

**A, B**). Finally, a Trypan blue cell staining assay was used to track the number of dead HepG2 cells (~15%) following GRP78 silencing (**Figure 5.10, C**).



**Figure 5.10.** RNAi activity of CTP:siRNA complex. (A) Western blot and (B) data analysis by autoradiography of GRP78 expression (n=1) following CTP:siRNA transfection (0, 40 and 80 pmol siRNA, 50:1 mole ratio CTP:siRNA, in Tris buffer pH 8). (C) Cell viability data (0, 40 and 80 pmol siRNA, 50:1 mole ratio CTP:siRNA, 20  $\mu$ M in 50  $\mu$ L of OPTIMEM) determined by Trypan blue exclusion (mean  $\pm$  S.E.M.; n=3, \*P< 0.05).

## 5.5 CONCLUSIONS

An entry point into a cancer-targeting gene therapy approach has been realized. In this chapter, a representative CTP:siRNA complex has been formulated and characterized by electrophoresis, spectroscopy and microscopy. Moreover, the CTP:siRNA complex was entirely stable (up to 8 hours) to a 10% FBS in DMEM treatment, highlighting the shielding effects of the CTP in protecting the siRNA from nuclease degradation in biological media. This feature is an imperative requirement for increasing the therapeutic index of the siRNA in the RNAi application.<sup>20</sup> Towards this effect, the GRP78-targeting CTP:siRNA complex effectively down-regulated GRP78 expression (~50%) in HepG2 hepatoblastoma cells while triggering noticeable apoptosis (~15%). Thus, the CTP:siRNA complexes formulate an effective transfection strategy. Future work is geared towards validating the remaining siRNAs (Chapter 2, **Table 2.1**) for RNAi

application, while exploring the influence of the poly(arginine) sequences on Pep42 targeted delivery of the siRNAs in GRP78 overexpressing tumors. The latter forms the basis of our cancer-targeting gene therapy approach, which has been partially realized by the notable contributions highlighted in this thesis.



## 5.6 REFERENCES

1. Kim, Y.; Lillo, A. M.; Steiniger, S. C.; Liu, Y.; Ballatore, C.; Anichini, A.; Mortarini, R.; Kaufmann, G. F.; Zhou, B.; Felding-Habermann, B.; Janda, K. D., Targeting Heat Shock Proteins on Cancer Cells: Selection, Characterization, and Cell-Penetrating Properties of a Peptidic GRP78 Ligand. *Biochemistry* **2006**, *45*, 9434-9444.
2. (a) Arap, M.A. Phage display technology. *Gen. Mol. Biol.* **2005**, *1*, 1-9, (b) Kay, B.K.; Kasanov, J.; Yamabhai, M. Screening phage-displayed combinatorial peptide libraries. *Methods* **2001**, *24*, 240-246.
3. Liu, Y.; Steiniger, S. C.; Kim, Y.; Kaufmann, G. F.; Felding-Habermann, B.; Janda, K. D., Mechanistic Studies of a Peptidic GRP78 Ligand for Cancer Cell-Specific Drug Delivery. *Mol. Pharm.* **2007**, *4*, 435-447.
4. Le Roy, C.; Wrana, J.L. Clathrin and non-clathrin mediated endocytic regulation of cell signaling. *Nature Rev.* **2005**, *6*, 112-126.
5. Fittipaldi, A.; Ferrari, A.; Zoppe, M.; Arcangeli, C.; Pellegrini, V.; Beltram, F.; Giacca, M. Cell membrane lipid rafts mediate caveolar endocytosis of HIV-1 Tat Fusion proteins. *J. Biol. Chem.* **2003**, *278*, 34141-34149.
6. Vercauteren, D.; Vandenbroucke, R.E.; Jones, A.T.; Rejman, J.; Demeester, J.; De Smedt, S.C.; Sanders, N.N.; Braeckmans, K. The use of inhibitors to study endocytic pathways of gene carriers: optimization and pitfalls. *Mol. Ther.* **2010**, *18*, 561-569.
7. Yoneda, Y.; Steiniger, S. C.; Čapková, K.; Mee, J. M.; Liu, Y.; Kaufmann, G. F.; Janda, K. D., A cell-penetrating peptidic GRP78 ligand for tumor cell-specific prodrug therapy. *Bioorg. Med. Chem. Lett.* **2008**, *18*, 1632-1636.
8. Futaki, S. Membrane-permeable arginine-rich peptides and the translocation mechanisms. *Adv. Drug Del. Rev.* **2005**, *57*, 547-558.
9. Futaki, S.; Suzuki, T.; Ohashi, W.; Yagami, T.; Tanaka, S.; Ueda, K.; Sugiura, Y. Arginine-rich peptides. An abundant source of membrane-permeable peptides having potential as carriers for intracellular protein delivery. *J. Biol. Chem.* **2001**, *276*, 5836-5840.
10. Mitchell, D.J.; Kim, D.T.; Steinman, L.; Fathman, C.G.; Rothbard, J.B. Polyarginine enters cells more efficiently than other polycationic homopolymers. *J. Pept. Res.* **2000**, *56*, 318-325.

11. Kim, S.W.; Kim, N.Y.; Choi, Y.B.; Park, S.H.; Yang, J.M.; Shin, S. RNA interference in vitro and in vivo using an arginine peptide/siRNA complex system. *J. Control. Release* **2010**, *143*, 335-343.
12. Vives, E. Present and future of cell-penetrating peptide mediated delivery systems: "is the Trojan horse too wild to go only to Troy?" *J. Control. Release*. **2005**, *109*, 77-85.
13. Kumar, P.; Wu, H.; McBride, J.L.; Jung, K-E.; Kim, M.H.; Davidson, B.L.; Lee, S.K.; Shankar, P.; Manjunath, N. Transvascular delivery of small interfering RNA to the central nervous system. *Nature* **2007**, *448*, 39-43.
14. Joseph, S.C.; Martinez, I.; Phillips, M.; Blackman, B.A.; Parronchi, C.J.; Kelly, M.; Blake, A.D.; Sabatino, D. Synthesis, characterization and biological activity of poly(arginine) derived cancer-targeting peptides. *J. Pept. Sci.* **2014**, manuscript in revision.
15. Wade, M.F.; O'Conner, J.L. Using a cationic carbocyanine dye to assess RNA loading in Northern gel analysis. *BioTechniques* **1992**, *12*, 794-796.
16. (a) Ladokhin, A.S.; Selsted, M.E.; White, S.H. CD spectra of indolicidin antimicrobial peptides suggest turns, not polyproline helix. *Biochemistry* **1999**, *38*, 12313-12319, (b) Sabatino, D.; Proulx, C.; Pohankova, P.; Ong, H.; Lubell, W.D. Structure-activity relationships of GHRP-6 azapeptide ligands of the CD36 scavenger receptor by solid-phase submonomer azapeptide synthesis. *J. Am. Chem. Soc.* **2011**, *133*, 12493-12506.
17. Kelly, S.M.; Jess, T.J.; Price, N.C. How to study proteins by circular dichroism. *Biochim. Biophys. Acta* **2005**, *1751*, 119-139.
18. Gray, D.M.; Hung, S.H.; Johnson, K.H. Absorption and Circular Dichroism Spectroscopy of Nucleic Acids Duplexes and Triplexes. *Methods Enzymol.* **1995**, *246*, 19.
19. Youn, P.; Chen, Y.; Furgeson, D. Y. A Myristoylated Cell-Penetrating Peptide Bearing a Transferrin Receptor-Targeting Sequence for Neuro-Targeted siRNA Delivery. *Mol. Pharm.* **2014**, *11*, 486-495.
20. Bumcrot, D.; Manoharan, M.; Koteliansky, V.; Sah, D.W.Y. RNAi therapeutics: a potential new class of pharmaceutical drugs. *Nat. Chem. Biol.* **2006**, *2*, 711-719.

## **5.7 EXPERIMENTAL SECTION**

### **5.7.1 CTP:siRNA COMPLEX FORMATION**

Pep42-R9 was added in increasing stoichiometric quantities (0.50 – 25  $\mu\text{mol}$ ) relative to the siRNA (0.50  $\mu\text{mol}$ ) in annealing buffer (50 mM Tris-HCl, pH 8.0, 100 mM NaCl, 5 mM EDTA). The samples were incubated at 37 °C for 1 hour and left to cool down to room temperature and stored in the fridge (4 °C) overnight prior to use the next day.

### **5.7.2 CTP:siRNA STABILITY IN 10% FBS/DMEM**

CTP:siRNA complexes and native siRNAs were incubated in 10% FBS/DMEM (150  $\mu\text{L}$ ) at 37 °C. Aliquots (10  $\mu\text{L}$ ) were removed at set time intervals (0-24 h), treated with gel loading buffer (10  $\mu\text{L}$  of 80 % formamide in TBE loading buffer) and heated at 95 °C to quench the reactions. Samples were loaded and resolved on an 18% denaturing PAGE (7M urea) and visualized with Stains-All™ (Aldrich) to determine the siRNA integrity.

### **5.7.3 GEL SHIFT ASSAY**

CTP:siRNA complexes (15  $\mu\text{M}$ , 1-50:1 mol/mol) were analyzed by native (no urea) PAGE. Samples were prepared by adding stoichiometric ratios (1-50:1) of CTP:siRNA in 30% sucrose in 1X TAE loading buffer (10  $\mu\text{L}$ ). Samples were incubated at 37 °C for 1 hour, cooled to room temperature and stored at 4 °C overnight. A 18% native PAGE was prepared using 5 mL of 10X TBE buffer, 22.5 mL (acrylamide and *N,N*-methylene bisacrylamide) and 22.5 mL of autoclaved water. The gel was run at 500 V for 2.5 h and stained with Stains-All™ (Aldrich) to visualize the CTP:siRNA bands.

#### **5.7.4 DYNAMIC LIGHT SCATTERING (DLS)**

DLS measurements were performed on a 90 plus particle size analyzer (Brookhaven Instruments Corporation, NY) employing a 90° scattering angle and a 35 mW incident laser (658 nm). Samples were diluted in a pH 7 buffer consisting of 140 mM KCl, 1 mM MgCl<sub>2</sub>, 5 mM NaHPO<sub>4</sub> and sonicated for 30 minutes before taking measurements. The reported diameter is the average of 5 runs for each sample with the corresponding standard deviation.

#### **5.7.5 TRANSMISSION ELECTRON MICROSCOPY (TEM)**

The diluted samples from the DLS measurements were mixed in a 1:1 (v/v) ratio with 1% uranyl acetate in ethanol and sonicated for 10 minutes. An aliquot (5 μL) was transferred to a carbon film coated copper grid, 300 mesh (Electron Microscopy Sciences, PA) and the excess solution was removed immediately using an absorbent paper. The grids were dried overnight and viewed under the transmission electron microscope (JEOL, model JEM-1200 EX). Images were taken with a SIA-L3C CCD camera (Scientific Instruments and Applications, Inc., GA) using the software Maxim DL5 (Diffraction Limited, Ottawa, Canada).

#### **5.7.6 HepG2 CELL CULTURE**

The human hepatoblastoma, HepG2 cells (American Type Culture Collection, VA) were cultured in T25 cm<sup>2</sup> and T75 cm<sup>2</sup> flasks (Grenior Bio-one Cell star, FL) in Dulbecco's Modified Eagle Medium (DMEM) with GlutaMAX and heat-inactivated 10% Fetal Bovine Serum (Gibco, CA), containing 1% penicillin/streptomycin (Gibco, CA), in an incubator set at 37 °C with a humidified atmosphere of 5% CO<sub>2</sub>. Cells were routinely passaged at 75% confluence using Dulbecco's PBS (Gibco, CA) and 0.05% Trypsin-EDTA (1X), Phenol Red (Gibco, CA) and then

split into a 1:10 dish ratio. Cells used in the transfection experiments were cultured in 6- 96-well culture plates and allowed to recover for 24 hours before treatment.

### **5.7.7 CTP:siRNA TRANSFECTION IN HepG2 CELLS**

HepG2 cells were transfected with the appropriate siRNA, **1**, (40-80 pmol) and CTP (4.0 nmol) in binding buffer (50 mM Tris-HCl, pH 8.0, 100 mM NaCl, 5 mM EDTA). The cell monolayers were plated and incubated at 37 °C with 5% CO<sub>2</sub>. After 24 h, the serum free basal medium was removed and replaced with growth medium. Transfected cells were harvested (48 h) after transfection for analysis.

### **5.7.8 SDS-PAGE AND WESTERN BLOTTING**

Cell lysates were prepared with RIPA lysis buffer, heated to 70 °C for 10 min., resolved on NuPAGE 10% Bis-Tris gels and electroblotted onto polyvinylidene difluoride (PVDF) membranes. Membranes were treated for 90 min in a blocking buffer containing 5% (w/v) of non-fat dehydrated milk to minimize non-specific binding. Total HepG2 cells' GRP78 expression was immunodetected with a 1:200 dilution of anti-GRP78 N-20 antibodies. The membrane associated immunoreactivity was then detected using a 1:5000 dilution of a horseradish peroxidase-conjugated anti-goat secondary antibody and detected using ECL Plus chemiluminescence. The resulting autoradiograph was scanned, quantified with NIH ImageJ and expressed as integrated pixel density.

### **5.7.9 CELL VIABILITY**

Cell viability was determined in 24-well plates with HepG2 cells cultured in serum-free basal medium for 24 h and then incubated in the presence or absence of varying concentrations

of CTP:siRNA (20  $\mu$ M) for 48 h at 37 °C. The samples were removed with Enzyme Free Dissociation Buffer for 3 minutes at 37 °C. Samples were pelleted and re-suspended in Dulbecco's PBS (1 mL) and Trypan blue 0.4% stain (100  $\mu$ L) was added. Samples were quantified using a Countess automated cell counter. The resulting data was analyzed with GraphPad Prism 4.0 and statistical significance was determined by ANOVA ( $p < 0.05$ ).

## CHAPTER 6. CONCLUSION AND CONTRIBUTIONS TO KNOWLEDGE

### 6.1 CONCLUSIONS AND CONTRIBUTIONS TO KNOWLEDGE MADE IN THIS THESIS

#### 6.1.1 SYNTHESIS AND CHARACTERIZATION OF BRANCH AND HYPERBRANCH siRNAs

The solid phase synthesis and characterization of a new brand of siRNAs (**Figure 2.9**) has been disclosed in Chapter 2 of this thesis. The siRNA sequences were derived from multiple sites of GRP78 mRNA, an oncogene known to trigger cancer proliferation and resistance in a wide range of tumors. Therefore, potent silencing of GRP78 mRNA has been shown to compromise cancer cell activity leading to the development of potent anti-cancer approaches. Towards this unified goal, novel V-shape, **2.8**, Y-branch, **2.9**, and  $\times$  hyperbranch, **2.10-2.11**, siRNAs were synthesized by an efficient semi-automated solid phase synthesis method, producing a library (17) of GRP78-silencing siRNAs for exploring structure-activity relationships in cancer. Notably, the synthesis procedure featured the use of either 5'-OLv 2'-or 3'-OMMT ribouridine phosphoramidite branchpoint nucleotides (**Scheme 2.2, 2.16 and 2.24**), to procure the branch and hyperbranch siRNAs in good yields (17-83%) and purities ( $\geq 90\%$ ) following ion pairing reverse-phase HPLC analysis and purification. The sequence identities of the siRNAs were confirmed by molecular weight analyses using ESI-MS (Novatia Inc, Newton PA), whereas denaturing and native PAGE were used to respectively confirm siRNA purity and hybridization for bio-physical and structural studies.

The biophysical traits and structural characteristics of the newly formed branch and hyperbranch siRNAs were also evaluated for the first time in Chapter 3 of this thesis. Namely, CD spectroscopy was used to investigate siRNA secondary structure to ascertain the A-type

helix in the newly formed siRNAs. This helical trajectory is a requirement for RISC recognition of the siRNA substrates for mRNA silencing activity. Moreover, thermal denaturation experiments using UV-Vis spectrophotometry were used to evaluate hybrid thermal stability. Interestingly, branch and hyperbranch siRNAs displayed stable hybrid structures ( $T_m$ : 68 - >90 °C) relative to the linear controls ( $T_m$ : 67 - 76 °C), and in some cases were found to contain multiple hybrid-to-single-strand transitions due to the multiple siRNA motifs embedded within these types of higher-ordered structures. From these spectroscopic studies, branch and hyperbranch siRNAs were found to display the pre-requisite hybrid structures for stimulating RNAi activity in cancer.

### **6.1.2 GRP78 SILENCING AND CELL DEATH ACTIVITY OF BRANCH AND HYPERBRANCH siRNAs IN HepG2 CANCER CELLS**

In this study, the RNAi activity of the GRP78-silencing branch and hyperbranch siRNAs (**Table 2.1, sequence no. 4-7**) has been validated for the first time in HepG2 hepatoblastomas. HepG2 cells have been shown to overexpress and cell surface localize GRP78, thereby forming a valid tumor cell line model for validating the proposed GRP78-silencing strategy and a clinically relevant form of pediatric liver cancer for exploring new and improved forms of therapy. In chapter 4, the novel V-shape, Y-branch, and  $\times$  hyperbranch siRNA motifs (**Table 2.1, sequence no. 4-7**) were found to trigger potent GRP78 silencing (50% – 60%) while eliciting noticeable apoptosis (~5 - 15%) in HepG2 cells. Significantly, hyperbranch siRNA, **7**, targeting GRP78 mRNA expression at distinct sites was found to trigger more potent GRP78 silencing (60% vs. 40%) and HepG2 cell death (15% vs. 5%) activity relative to the linear siRNAs, **1** and **2**, highlighting its synergistic effects. This finding is important for the development of new siRNA



constructs that may target multiple genes in a combination approach for improving the RNAi effect. Moreover, confocal laser scanning microscopy also supported the western blot data, by illustrating significant cell surface GRP78 silencing (~70%) with hyperbranch siRNA, 7. Interestingly, FITC-labeling of cell surface GRP78 on HepG2 cells also suggests the possibility of developing tumor-targeting strategies (Chapter 5).

In Chapter 5, the first steps towards the development of a cancer-targeting gene therapy approach are highlighted, by the combination of GRP78-targeting siRNAs and peptides (*i.e.* cancer-targeting peptides, CTPs). In this approach, GRP78-silencing siRNAs are combined with poly(arginine) derived CTPs for the selective delivery of siRNAs into GRP78 HepG2 cells for RNAi and cell death activity. The CTP:siRNA complexes were effectively characterized by native PAGE, CD spectroscopy, thermal denaturation, DLS and TEM experiments. Moreover, the transfection of GRP78 silencing siRNA (**Table 2.1, sequence no. 1**) with a CTP derived from the Pep42-R9 sequence demonstrated significant GRP78 silencing (50-60%) and modest cell death (5-15%) in HepG2 cells which were in agreement with the Lipofectamine:siRNA transfection studies (Chapter 4). These results highlights the utility of the Pep42-R9 sequence as a useful transfection reagent that may be applicable in a wide range of tumors that display the cell surface GRP78 antigen. This discovery is also important for the development of an effective cancer-targeting gene therapy approach, which aims to kill cancer cells selectively, while leaving the healthy ones unmarked.

## 6.2 PUBLICATIONS, INVENTION DISCLOSURES AND CONFERENCE PRESENTATIONS

- *Manuscripts accepted for publication*

1. Anthony Maina, Brittany Blackman, Christopher Parronchi, Eva Morozko, Maria Bender, Allan D. Blake, David Sabatino. **Solid-Phase Synthesis, Characterization and RNAi Activity of Branch and Hyperbranch siRNAs**, *Bioorganic & Medicinal Chemistry Letters*, **2013**; 23, 5270-5274.

- *Manuscripts in preparation*

1. Stesha C. Joseph, Anthony Maina, Brittany A. Blackman, Christopher J. Parronchi, Reeta Yadav, Mariana Phillips, Uri Sumuni, Allan D. Blake and David Sabatino. **GRP78 targeting and silencing in HepG2 hepatocellular carcinoma with cancer-targeting peptide siRNA complexes** *manuscript in preparation*.
2. Anthony Maina, Eva Morozko, Maria E. Bender, Brittany Blackman, Allan D. Blake and David Sabatino, **Synthesis and Characterization of GRP78 siRNAs for Silencing Gene Expression in HepG2 Liver Carcinoma Cells** *NJAS Bulletin manuscript in review*.

- ***Patent Disclosures***

1. David Sabatino, Allan D. Blake, Anthony Maina, Brittany Blackman. **Silencing gene expression with Branch and Hyperbranch Oligonucleotides**. *U.S. Provisional Patent Application, # 61/810, 067 Provisional Patent* filed April 9, **2013**.

- ***Poster Presentations***

1. Anthony Maina and David Sabatino, **Design, Synthesis and Gene Silencing Activity of Branch and Hyperbranch siRNAs**, NYAS, Chemical Biology Discussion Group Year-End Symposium, New York, NY, June 2013
2. Anthony Maina and David Sabatino, **Design, Synthesis and Gene Silencing Activity of Branch and Hyperbranch siRNAs**, IBC's 15<sup>th</sup> annual TIDES Conference, Boston, MA, May 13, 2013.
3. Anthony Maina and David Sabatino, **Design, synthesis and characterization of a branchpoint phosphoramidite and its use in the assembly of branch and hyperbranch oligonucleotides**, NJAS, 58<sup>th</sup> Annual Meeting, Kean University, Union, NJ April 2013.
  - Awarded NJAS Best Graduate Student Poster Award

4. Anthony Maina and David Sabatino, **Cancer Targeting Peptides as anti-cancer drugs**, Petersheim Academic Expositions, Seton Hall University, South Orange, NJ, April 2013.
  
5. Anthony Maina and David Sabatino, **Synthesis and Characterization of siRNAs for GRP78 gene-silencing**, NJAS, 57<sup>th</sup> Annual Meeting, Seton Hall University, South Orange, NJ, April 2012.
  - Awarded NJAS Best Graduate Student Poster Award
  
6. Anthony Maina and David Sabatino, **Synthesis and Characterization of GRP78-siRNAs for potential anti-cancer applications**, Petersheim Academic Expositions, Seton Hall University, South Orange, NJ, April 2012.
  
7. Anthony Maina and David Sabatino, **DNA Synthesis, Then, Now and at Seton Hall University**, Petersheim Academic Expositions, Seton Hall University, South Orange, NJ, April 2011.

# Appendix

## TABLE OF CONTENTS

### A. Supplemental NMR spectra

<b>Figure A1.</b>	<sup>1</sup> H NMR spectrum of 5'- <i>O</i> -levulinyl ribouridine, <b>2.21</b>	A3
<b>Figure A2.</b>	<sup>13</sup> C NMR spectrum of 5'- <i>O</i> -levulinyl ribouridine, <b>2.21</b>	A3
<b>Figure A3.</b>	<sup>1</sup> H NMR spectrum of 5'- <i>O</i> -levulinyl 2'- <i>O</i> -monomethoxytrityl ribouridine, <b>2.22</b>	A4
<b>Figure A4.</b>	<sup>13</sup> C NMR spectrum of 5'- <i>O</i> -levulinyl 2'- <i>O</i> -monomethoxytrityl ribouridine, <b>2.22</b>	A4
<b>Figure A5.</b>	<sup>1</sup> H NMR spectra of 5'- <i>O</i> -levulinyl 3'- <i>O</i> -monomethoxytrityl ribouridine, <b>2.23</b>	A5
<b>Figure A6.</b>	<sup>13</sup> C NMR spectra of 5'- <i>O</i> -levulinyl 3'- <i>O</i> -monomethoxytrityl ribouridine, <b>2.23</b>	A5
<b>Figure A7.</b>	<sup>31</sup> P NMR spectra of 5'- <i>O</i> -levulinyl 2'- <i>O</i> -monomethoxytrityl 3'- <i>O</i> -phosphoramidous ribouridine, <b>2.16</b>	A6
<b>Figure A8.</b>	<sup>31</sup> P NMR spectra of 5'- <i>O</i> -levulinyl 2'- <i>O</i> -monomethoxytrityl 3'- <i>O</i> -phosphoramidous ribouridine, <b>2.24</b>	A6

### B. Supplemental IP RP HPLC chromatograms and MS spectra

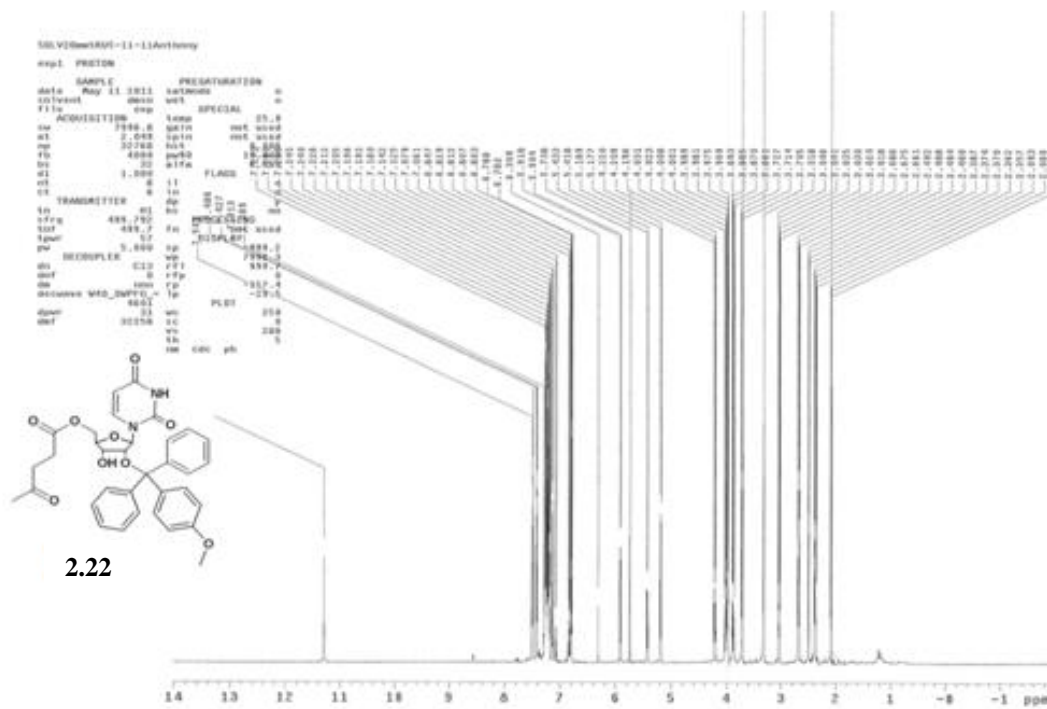
<b>Figure A9.</b>	IP RP LC/MS Analysis of ( <b>Table 2.1, sequence 1a</b> )	A7
<b>Figure A10.</b>	IP RP LC/MS Analysis of ( <b>Table 2.1, sequence 1b</b> )	A8
<b>Figure A11.</b>	IP RP LC/MS Analysis of ( <b>Table 2.1, sequence 2a</b> )	A9
<b>Figure A12.</b>	IP RP LC/MS Analysis of ( <b>Table 2.1, sequence 2b</b> )	A10
<b>Figure A13.</b>	IP RP LC/MS Analysis of ( <b>Table 2.1, sequence 4</b> )	A11
<b>Figure A14.</b>	IP RP LC/MS Analysis of ( <b>Table 2.1, sequence 5</b> )	A12
<b>Figure A15.</b>	IP RP LC/MS Analysis of ( <b>Table 2.1, sequence 6</b> )	A13
<b>Figure A16.</b>	IP RP LC/MS Analysis of ( <b>Table 2.1, sequence 8</b> )	A14
<b>Figure A17.</b>	IP RP LC/MS Analysis of ( <b>Table 2.1, sequence 9</b> )	A15
<b>Figure A18.</b>	IP RP LC/MS Analysis of ( <b>Table 2.1, sequence 10</b> )	A16
<b>Figure A19.</b>	IP RP LC/MS Analysis of ( <b>Table 2.1, sequence 11</b> )	A17

<b>Figure A20.</b>	IP RP LC/MS Analysis of ( <b>Table 2.1, sequence 12a</b> )	A18
<b>Figure A21.</b>	IP RP LC/MS Analysis of ( <b>Table 2.1, sequence 12b</b> )	A19
<b>Figure A22.</b>	IP RP LC/MS Analysis of ( <b>Table 2.1, sequence 14</b> )	A20
<b>Figure A23.</b>	IP RP LC/MS Analysis of ( <b>Table 2.1, sequence 15</b> )	A21
<b>Figure A24.</b>	IP RP LC/MS Analysis of ( <b>Table 2.1, sequence 16</b> )	A22
<b>Figure A25.</b>	IP RP LC/MS Analysis of ( <b>Table 2.1, sequence 17</b> )	A23
<b>C. CTP:siRNA PAGE</b>		
<b>Figure A26.</b>	Native gel analysis of Pep42-R9:siRNA	A24
<b>D. CTP:siRNA analysis by CD Spectroscopy</b>		
<b>Figure A27.</b>	CTP:siRNA analyses by CD Spectroscopy	A25
<b>E. DLS studies of the CTP:siRNA complexes</b>		
<b>Table A1.</b>	Summary table of CTP:siRNA studies by DLS and TEM	A26
<b>F. TEM images of the CTP:siRNA complexes</b>		
<b>Figure A28.</b>	TEM images of Pep42:siRNA	A27
<b>G. Thermal melts analysis of CTP: siRNA complex</b>		
<b>Figure A29.</b>	Thermal melts analyses of CTP:siRNA	A28

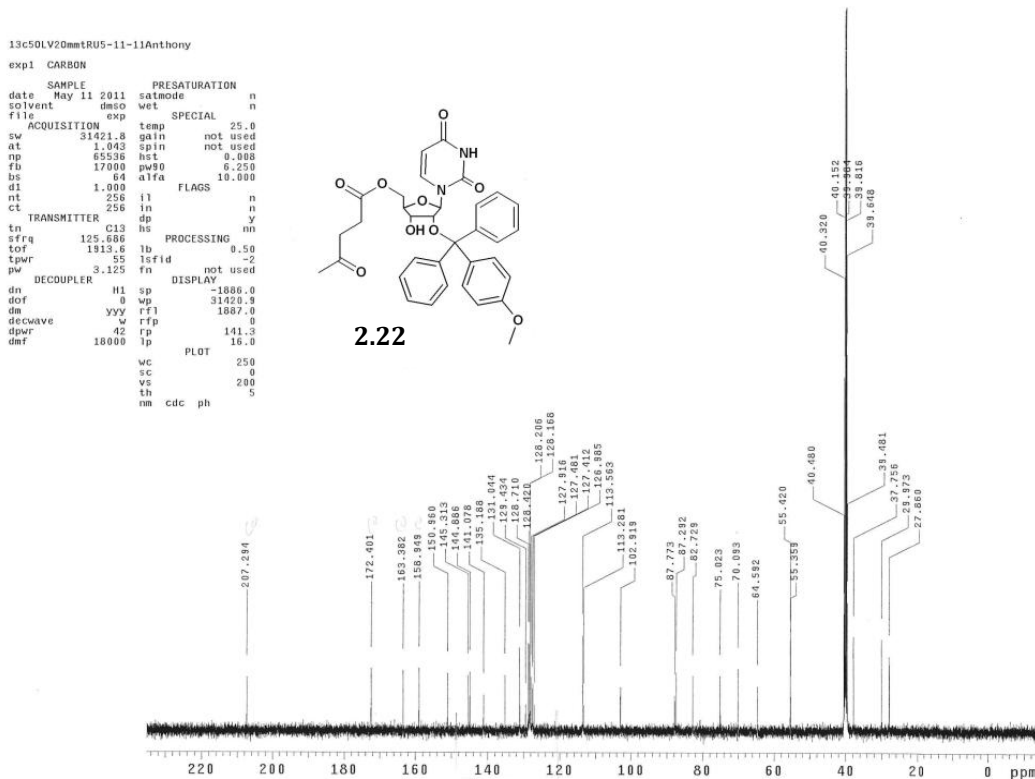




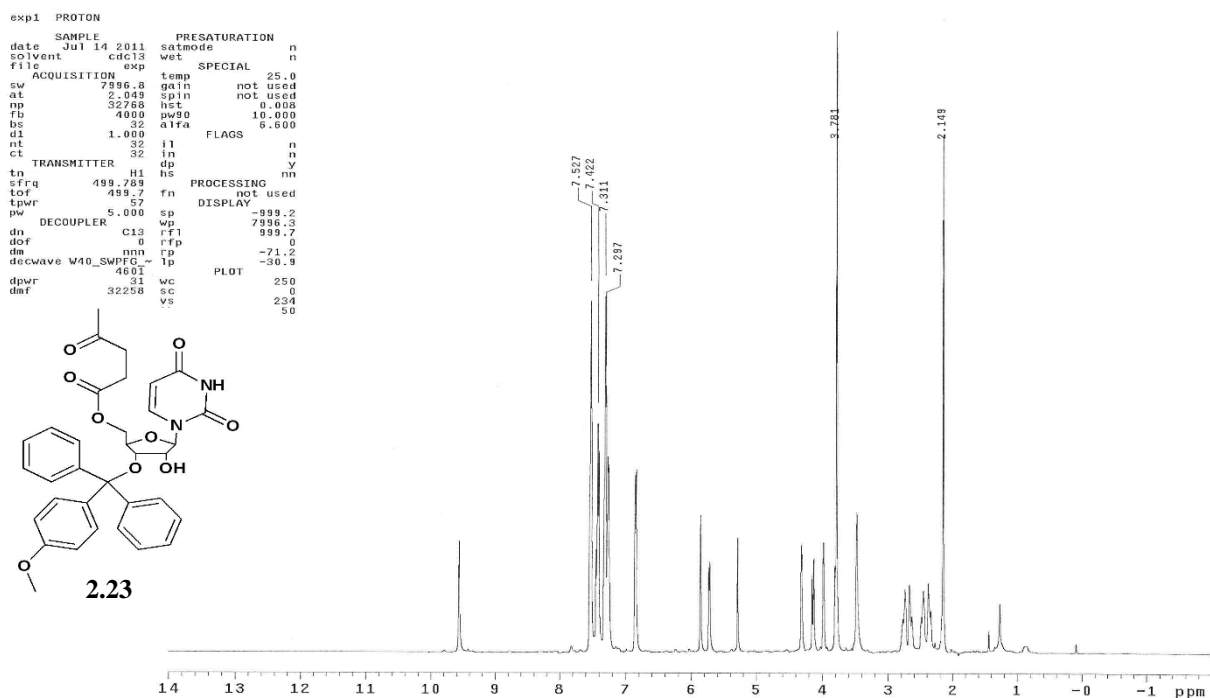
**Figure A3.**  $^1\text{H}$  NMR spectrum of 5'-*O*-levulinyl 2'-*O*-monomethoxytrityl ribouridine, **2.22**



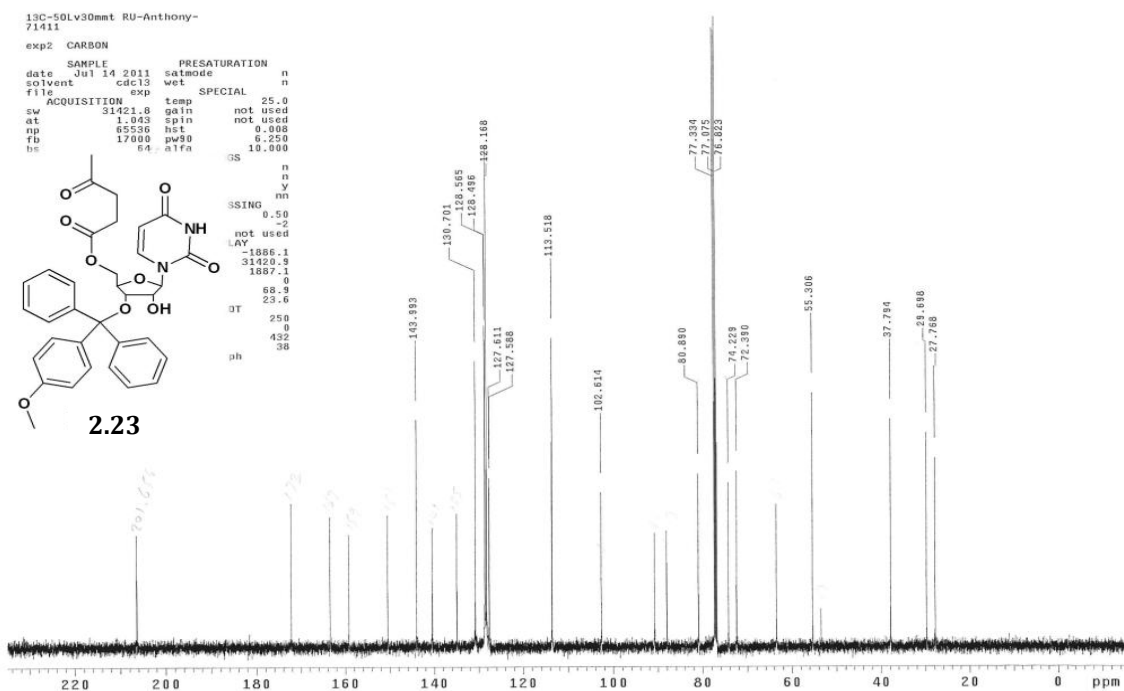
**Figure A4.**  $^{13}\text{C}$  NMR spectrum of 5'-*O*-Levulinyl 2'-*O*-monomethoxytrityl ribouridine, **2.22**



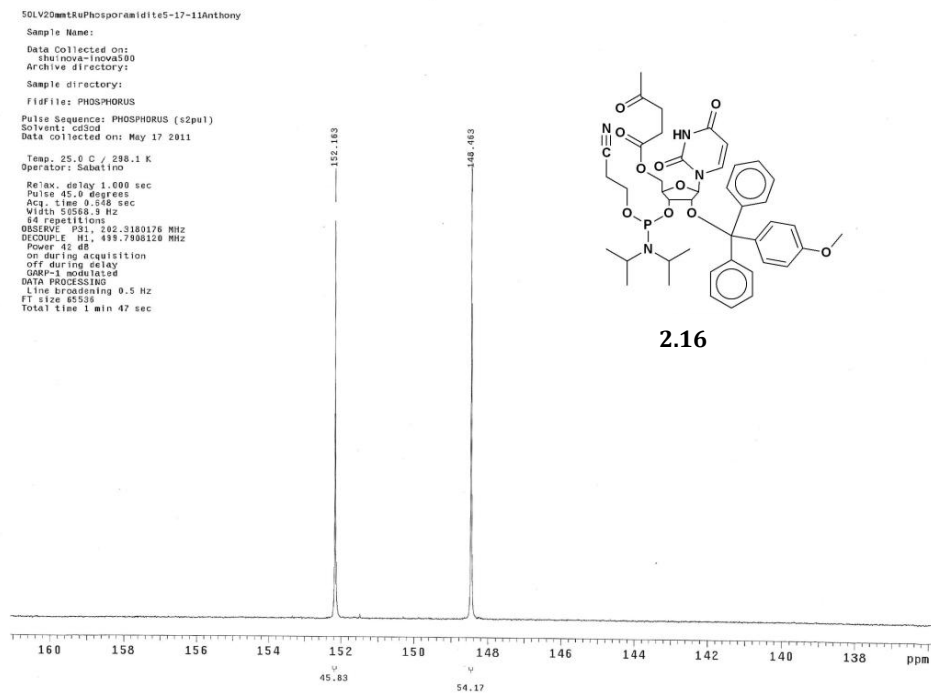
**Figure A5.**  $^1\text{H}$  NMR spectra of 5'-*O*-levulinyl 3'-*O*-monomethoxytrityl ribouridine, **2.23**



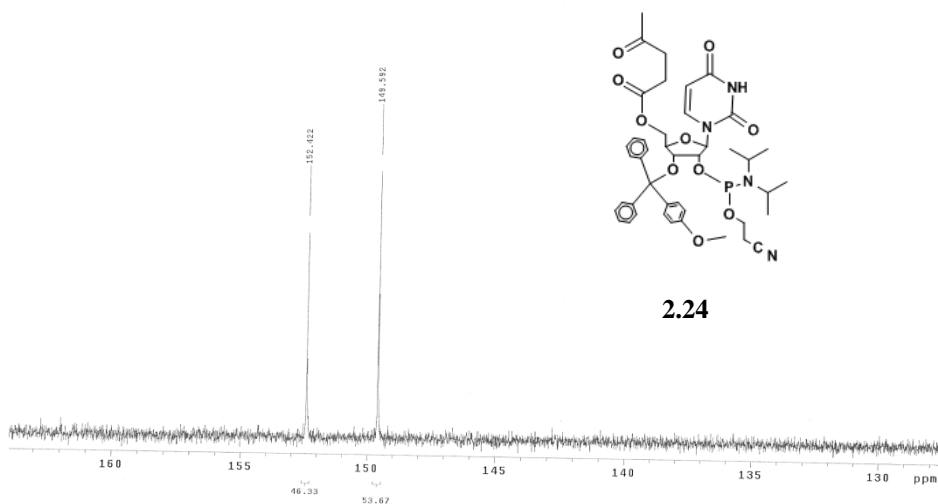
**Figure A6.**  $^{13}\text{C}$  NMR spectra of 5'-*O*-levulinyl 3'-*O*-monomethoxytrityl ribouridine, **2.23**



**Figure A7.**  $^{31}\text{P}$  NMR spectra of 5'-*O*-levulinyl 2'-*O*-monomethoxytrityl 3'-*O*-phosphoramidous ribouridine, **2.16**



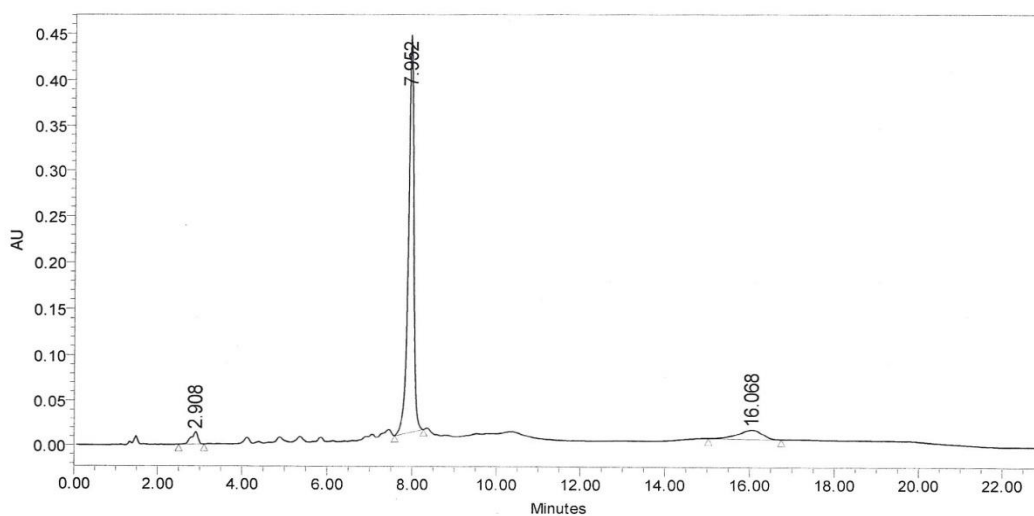
**Figure A8.**  $^{31}\text{P}$  NMR spectra of 5'-*O*-levulinyl 2'-*O*-monomethoxytrityl 2'-*O*-phosphoramidous ribouridine, **2.24**



## APPENDIX B. Supplemental IP RP HPLC Chromatograms and MS spectra

**Figure A9.** IP RP LC/MS Analysis of (Table 2.1, sequence 1a)

SAMPLE INFORMATION			
Sample Name:	grp78-1ss	Acquired By:	System
Sample Type:	Unknown	Sample Set Name:	GRP78_SSLN820
Vial:	20	Acq. Method Set:	RNA_AMV2489_MS
Injection #:	1	Processing Method:	oligoprocessing
Injection Volume:	100.00 ul	Channel Name:	W2489 ChA
Run Time:	23.0 Minutes	Proc. Chnl. Descr.:	W2489 ChA 260nm
Date Acquired:	8/20/2012 1:31:07 PM EDT		
Date Processed:	2/13/2013 12:10:40 PM EST		



	RT	Area	% Area	Height
1	2.908	154036	3.42	14047
2	7.952	3932727	87.35	432518
3	16.068	415707	9.23	10313

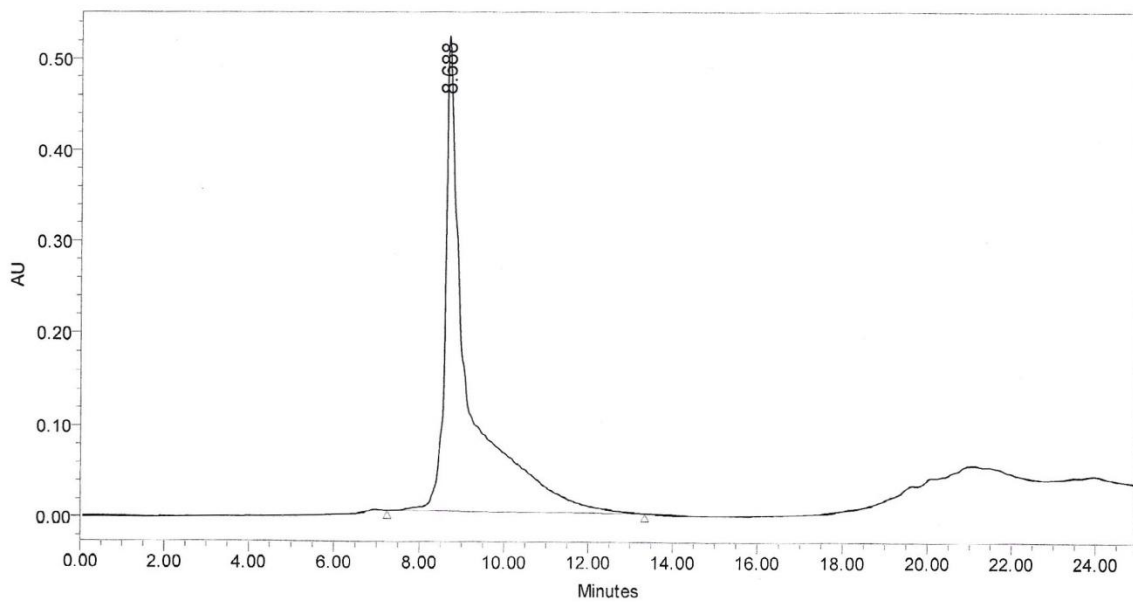
### Sequence 1a.

5'-A GUG UUG GAA GAU UCU GAU-3'

MS. Calc. 6103.7 g/mol Found 6103.7 g/mol

**Figure A10. IP RP LC/MS Analysis of (Table 2.1, sequence 1b)**

SAMPLE INFORMATION			
Sample Name:	grp78-1as	Acquired By:	System
Sample Type:	Unknown	Sample Set Name:	RNA_AM50212_2489SS
Vial:	24	Acq. Method Set:	RNA_AM032612_2489_MS
Injection #:	1	Processing Method:	oligoprocessing
Injection Volume:	50.00 ul	Channel Name:	W2489 ChA
Run Time:	25.0 Minutes	Proc. Chnl. Descr.:	W2489 ChA 260nm
Date Acquired:	5/2/2012 2:57:09 PM EDT		
Date Processed:	2/13/2013 11:56:52 AM EST		



	RT	Area	% Area	Height
1	8.688	19427612	100.00	519025

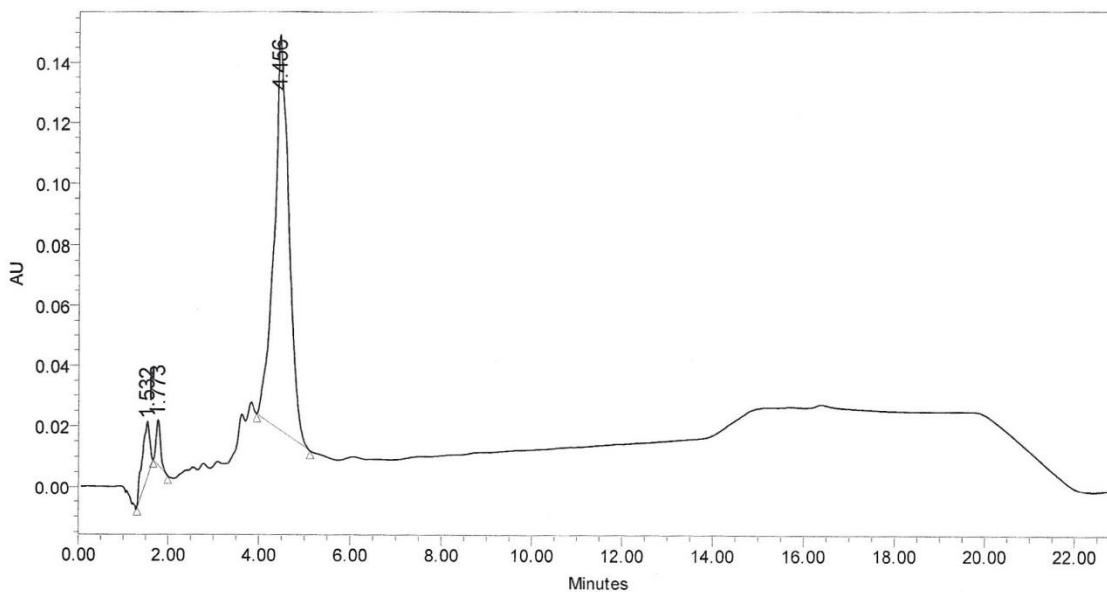
**Sequence 1b.**

5'- A UCA GAA UCU UCC AAC ACU -3'

MS. Calc. 5947.4 g/mol Found 5949.4 g/mol

**Figure A11. IP RP LC/MS Analysis of (Table 2.1, sequence 2a)**

SAMPLE INFORMATION			
Sample Name:	GRP78-2 SS	Acquired By:	System
Sample Type:	Unknown	Sample Set Name:	GRP78_RNA_21312_SS
Vial:	88	Acq. Method Set:	RNA_AM120111_MS
Injection #:	1	Processing Method:	oligoprocessing
Injection Volume:	100.00 ul	Channel Name:	2998 Ch3 260nm@1.2nm
Run Time:	23.0 Minutes	Proc. Chnl. Descr.:	2998 Ch3 260nm@1.2nm
Date Acquired:	2/13/2012 11:58:06 AM EST		
Date Processed:	2/13/2013 1:09:30 PM EST		



	RT	Area	% Area	Height
1	1.532	214605	6.63	17958
2	1.773	97420	3.01	14611
3	4.456	2926071	90.36	130342

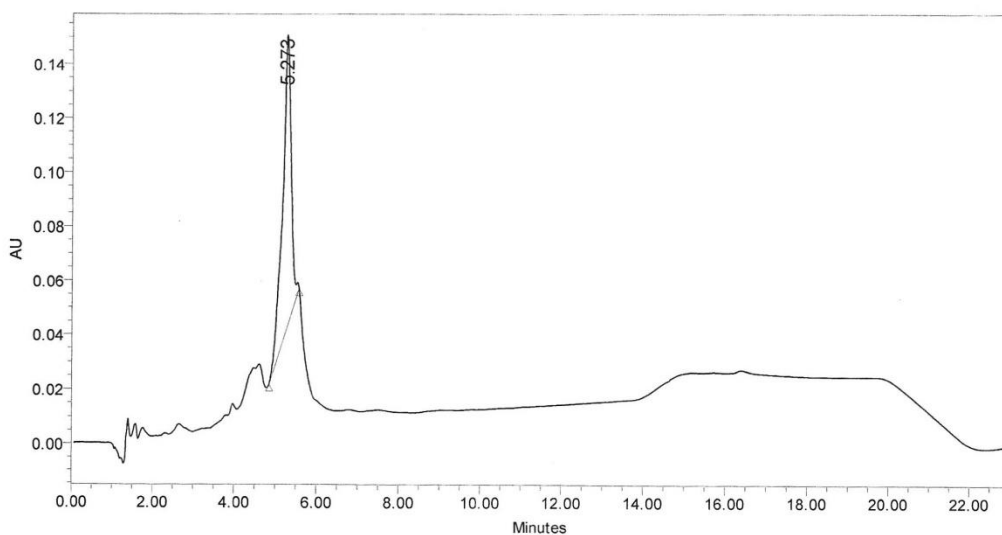
**Sequence 2a.**

5'-G GAG CGC AUU GAU ACU AGA-3'

MS. Calc. 6124.5 g/mol Found 6124.7 g/mol

**Figure A12. IP RP LC/MS Analysis of (Table 2.1, sequence 2b)**

SAMPLE INFORMATION			
Sample Name:	GRP78-2 AS	Acquired By:	System
Sample Type:	Unknown	Sample Set Name:	GRP78_RNA_21312_SS
Vial:	87	Acq. Method Set:	RNA_AM120111_MS
Injection #:	1	Processing Method:	oligoprocessing
Injection Volume:	100.00 ul	Channel Name:	2998 Ch3 260nm@1.2nm
Run Time:	23.0 Minutes	Proc. Chnl. Descr.:	2998 Ch3 260nm@1.2nm
Date Acquired:	2/13/2012 11:33:29 AM EST		
Date Processed:	2/13/2013 1:08:28 PM EST		



	RT	Area	% Area	Height
1	5.273	1528414	100.00	108039

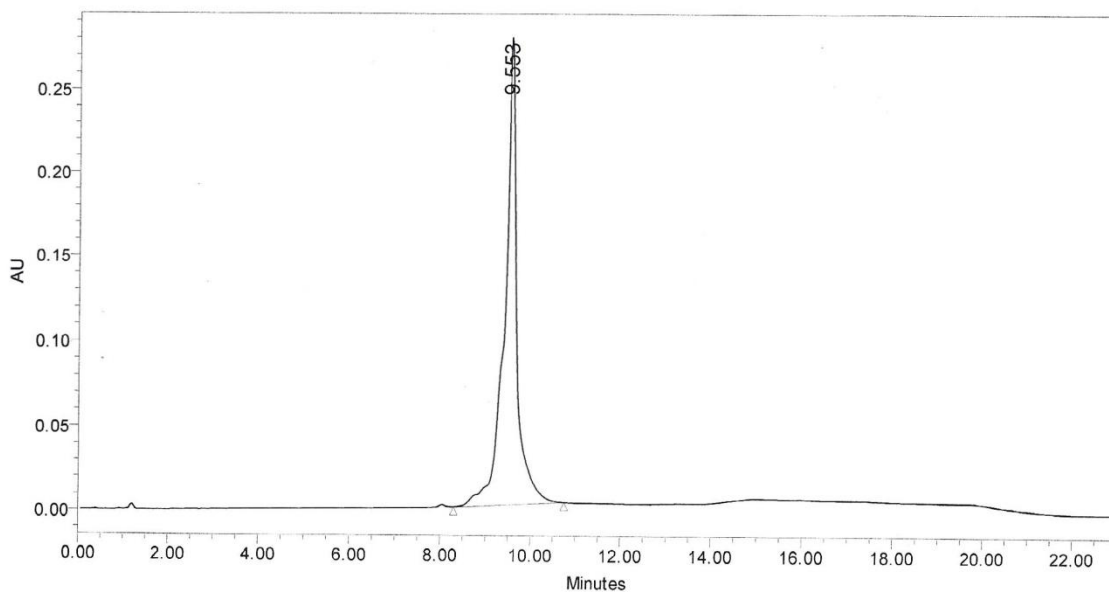
**Sequence 2b.**

5'-UCU AGU AUC AAU GCG CUC C-3'

MS. Calc. 5955.3 g/mol Found 5958.6 g/mol

**Figure A13.** IP RP LC/MS Analysis of (Table 2.1, sequence 4).

SAMPLE INFORMATION			
Sample Name:	avrna	Acquired By:	System
Sample Type:	Unknown n	Sample Set Name:	vrna_hplcpure820
Vial:	16	Acq. Method Set:	RNA_AMW2489_MS
Injection #:	1	Processing Method:	oligoprocessing
Injection Volume:	50.00 ul	Channel Name:	W2489 ChA
Run Time:	23.0 Minutes	Proc. Chnl. Descr.:	W2489 ChA 260nm
Date Acquired:	8/20/2012 11:23:30 AM EDT		
Date Processed:	2/13/2013 12:09:17 PM EST		



	RT	Area	% Area	Height
1	9.553	5291733	100.00	276406

**Sequence 4.**

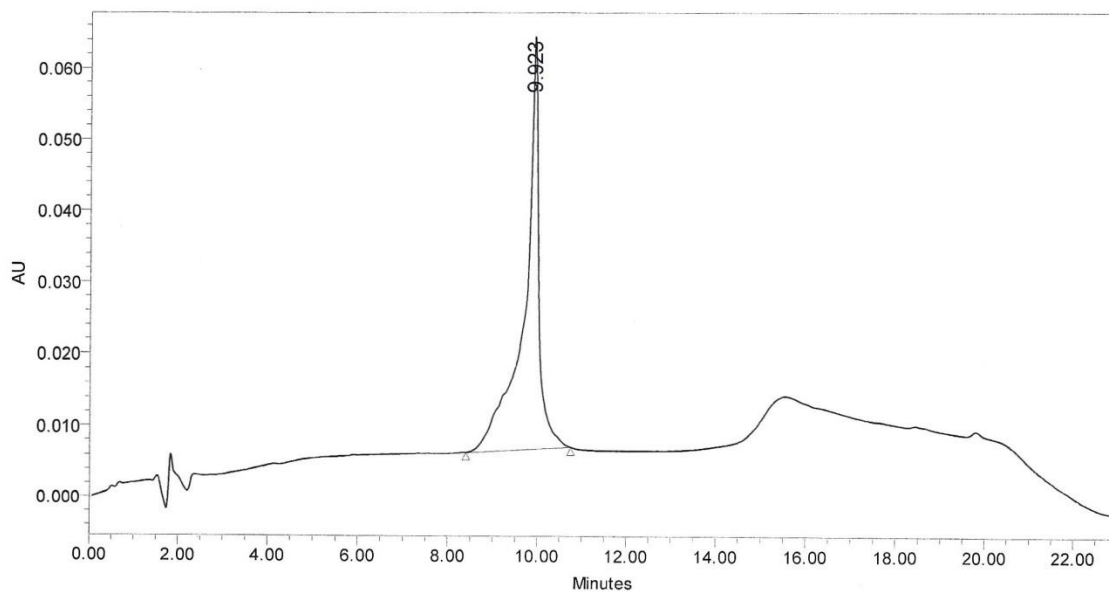
2'3' UCA CAA CCU UCU AAG ACU A-5'  
 5'-rU  
 3'5' AGU GUU GGA AGA UUG UGA U-3'

MS. Calc. 12412.5 g/mol Found 12420.5 g/mol



**Figure A14.** IP RP LC/MS Analysis of (Table 2.1, sequence 5).

SAMPLE INFORMATION			
Sample Name:	A Y 84	Acquired By:	System
Sample Type:	Unknown	Sample Set Name:	GRP78_A_121412_SS
Vial:	52	Acq. Method Set:	RNA_AMW2489_MS
Injection #:	1	Processing Method:	oligoprocessing
Injection Volume:	100.00 ul	Channel Name:	W2489 ChA
Run Time:	23.0 Minutes	Proc. Chnl. Descr.:	W2489 ChA 260nm
Date Acquired:	12/14/2012 3:06:48 PM EST		
Date Processed:	2/13/2013 12:29:05 PM EST		



	RT	Area	% Area	Height
1	9.923	1290974	100.00	57685

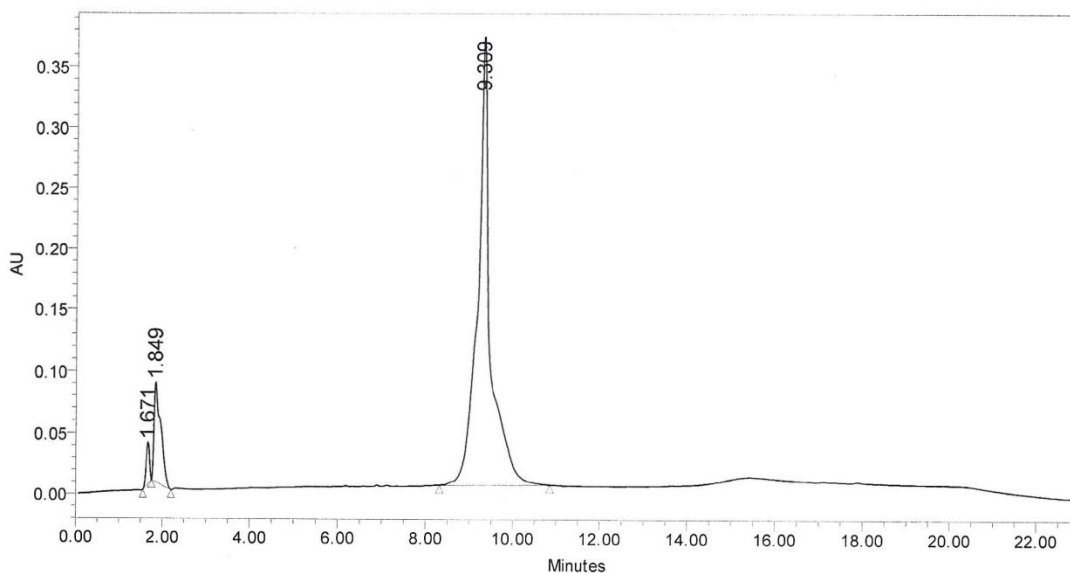
**Sequence 5.**



MS. Calc. 14936.0 g/mol Found 14934.9 g/mol

**Figure A15.** IP RP LC/MS Analysis of (Table 2.1, sequence 6).

SAMPLE INFORMATION			
Sample Name:	GRPA1-1	Acquired By:	System
Sample Type:	Unknown	Sample Set Name:	1_1 NAP 10 PURE11813
Vial:	62	Acq. Method Set:	RNA_AMW2489_MS
Injection #:	1	Processing Method:	oligoprocessing
Injection Volume:	100.00 ul	Channel Name:	V2489 ChA
Run Time:	23.0 Minutes	Proc. Chnl. Descr.:	W2489 ChA 260nm
Date Acquired:	1/18/2013 2:50:29 PM EST		
Date Processed:	2/13/2013 12:31:56 PM EST		



	RT	Area	% Area	Height
1	1.671	186553	2.21	34028
2	1.849	874028	10.33	80609
3	9.309	7399435	87.46	368831

**Sequence 6.**

3'-U AGU CUU AGA GGA UUG UGA-5'2'

2'3' UCA CAA CCU UCU AAG ACU A-5'

rU3'5'-UCA CAA CC - 3'5'-rU

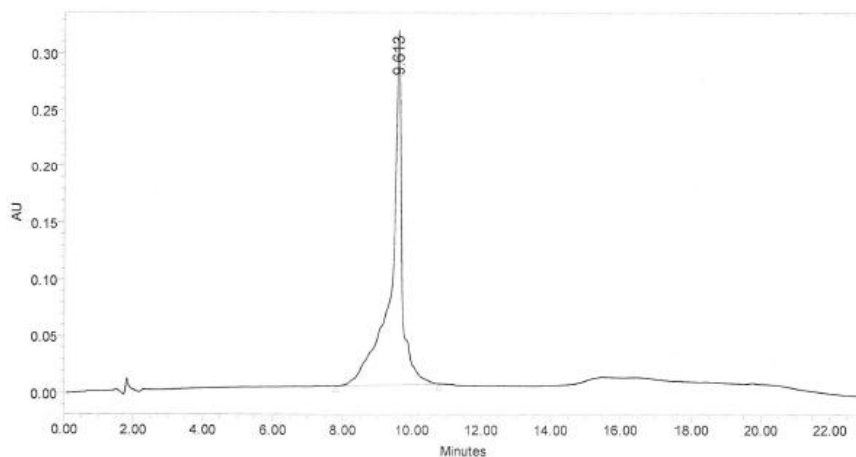
5'-A UCA GAA UCU CCU AAC ACU-3'5'

3'5' AGU GUU GGA AGA UUG UGA U-3'

MS. Calc. 27419.5 g/mol Found 27450.0 g/mol

**Figure A16.** IP RP LC/MS Analysis of (Table 2.1, sequence 8).

SAMPLE INFORMATION			
Sample Name:	B V	Acquired By:	System
Sample Type:	Unknown	Sample Set Name:	GRP78_B_121412_SS
Vial:	53	Acq. Method Set:	RNA_AMM2489_MS
Injection #:	1	Processing Method:	oligoprocessing
Injection Volume:	100.00 ul	Channel Name:	W2489 ChA
Run Time:	23.0 Minutes	Proc. Chnl. Descr.:	W2489 ChA 260nm
Date Acquired:	12/14/2012 12:02:27 PM EST		
Date Processed:	1/13/2014 10:40:45 AM EST		



	RT	Area	% Area	Height
1	9.613	6710996	100.00	312625

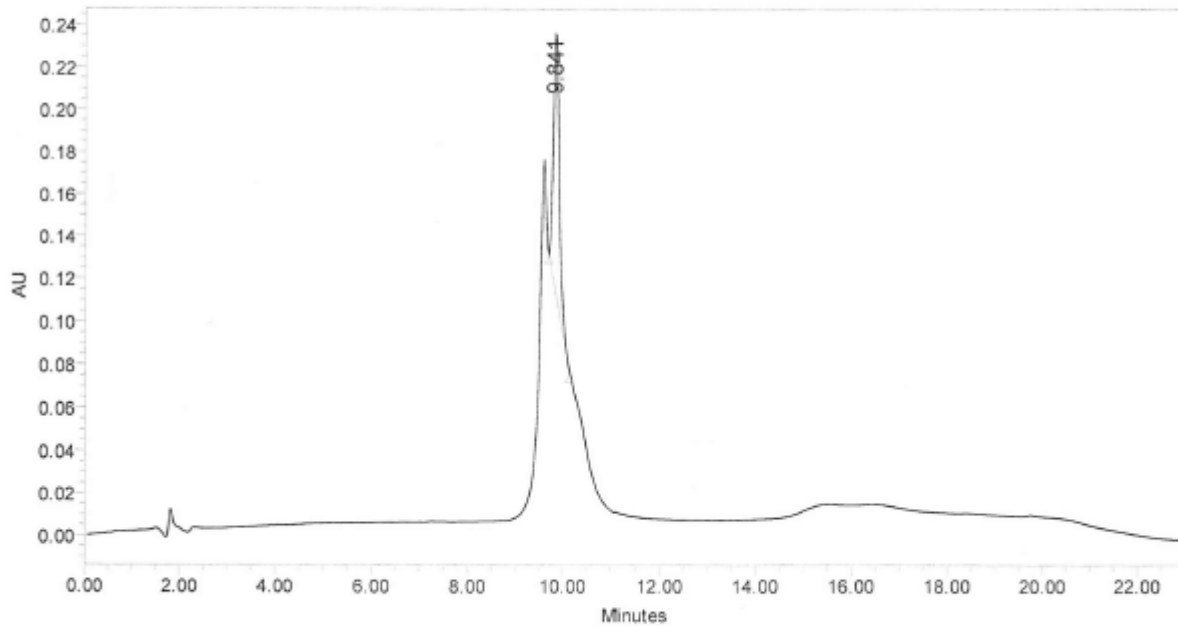
**Sequence 8.**

2'5' AGU GUU GGA AGA UUG UGA U-3'  
 5'-rU  
 3'3' UCA CAA CCU UCU AAG ACU A-5'

MS. Calc. 12420.5 g/mol Found 12428.0 g/mol

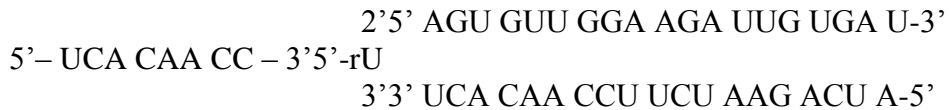
**Figure A17.** IP RP LC/MS Analysis of (Table 2.1, sequence 9).

SAMPLE INFORMATION			
Sample Name:	BY	Acquired By:	System
Sample Type:	Unknown	Sample Set Name:	GRP78_B_121412_SS
Vial:	54	Acq. Method Set:	RNA_AMM2489_MS
Injection #:	1	Processing Method:	oligoprocessing
Injection Volume:	100.00 ul	Channel Name:	W2489 ChA
Run Time:	23.0 Minutes	Proc. Chnl. Descr.:	W2489 ChA 260nm
Date Acquired:	12/14/2012 12:27:00 PM EST		
Date Processed:	1/13/2014 10:40:46 AM EST		



	RT	Area	% Area	Height
1	9.841	1039615	100.00	122369

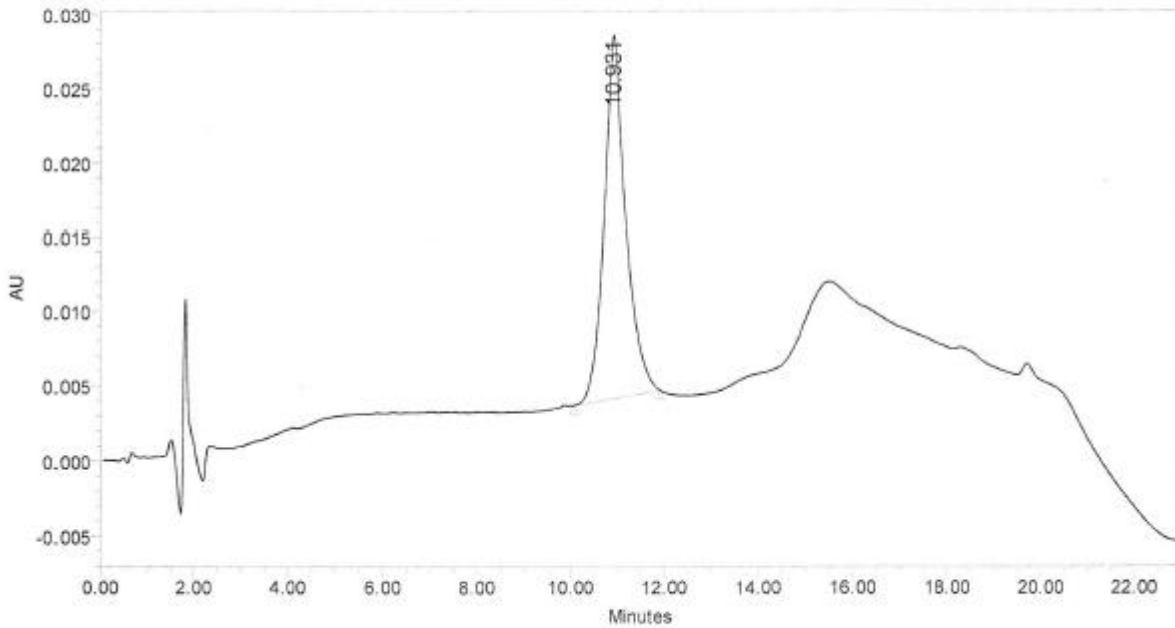
**Sequence 9.**



MS. Calc. 14934.9 g/mol Found 14941.6 g/mol

**Figure A18.** IP RP LC/MS Analysis of (Table 2.1, sequence 10)

SAMPLE INFORMATION			
Sample Name:	B1-1	Acquired By:	System
Sample Type:	Unknown	Sample Set Name:	GRP78_B_121412_SS
Vial:	51	Acq. Method Set:	RNA_AMW2489_MS
Injection #:	1	Processing Method:	oligoprocessing
Injection Volume:	100.00 ul	Channel Name:	W2489 ChA
Run Time:	23.0 Minutes	Proc. Chnl. Descr.:	W2489 ChA 260nm
Date Acquired:	12/14/2012 11:13:25 AM EST		
Date Processed:	1/13/2014 10:40:44 AM EST		



	RT	Area	% Area	Height
1	10.931	776590	100.00	24386

**Sequence 10.**

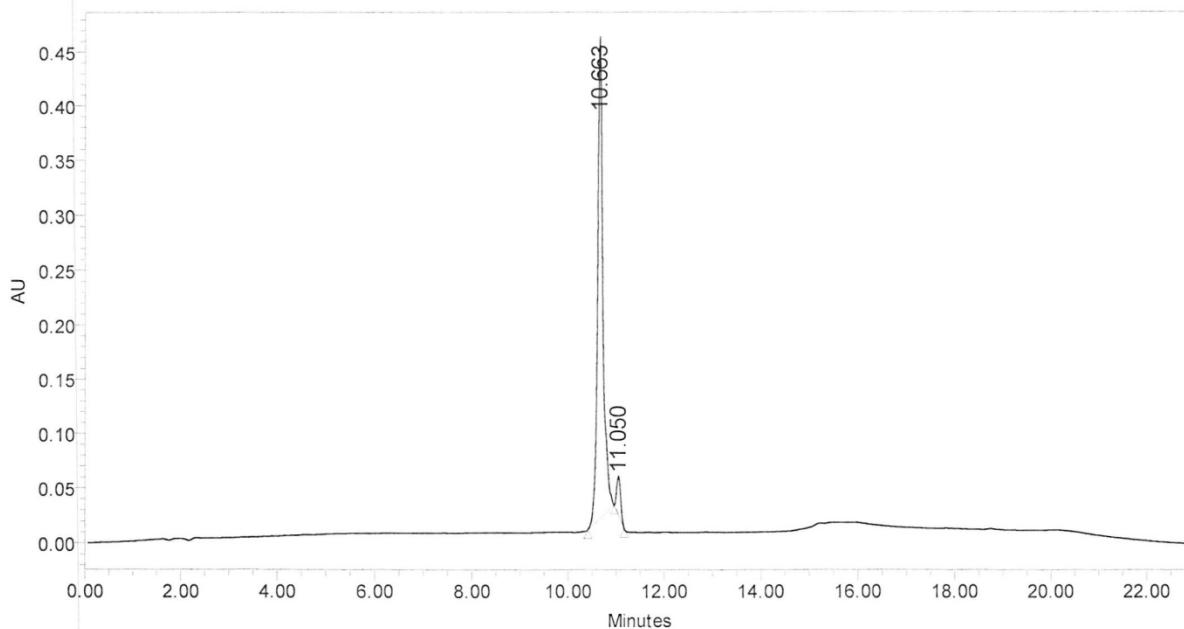


MS. Calc. 27419.5 g/mol Found 27668.8 g/mol



**Figure A20. IP RP LC/MS Analysis of (Table 2.1, sequence 12a)**

SAMPLE INFORMATION			
Sample Name:	1as_ome	Acquired By:	System
Sample Type:	Unknown	Sample Set Name:	1_OME_hplc_pure_12413
Vial:	56	Acq. Method Set:	RNA_AMM2489_MS
Injection #:	1	Processing Method:	oligoprocessing
Injection Volume:	50.00 ul	Channel Name:	W2489_ChA
Run Time:	23.0 Minutes	Proc. Chnl. Descr.:	W2489_ChA_260nm
Date Acquired:	1/24/2013 11:01:47 AM EST		
Date Processed:	1/24/2013 11:24:59 AM EST		



	RT	Area	% Area	Height
1	10.663	3410728	94.46	440724
2	11.050	200026	5.54	34994

**Sequence 12a.**

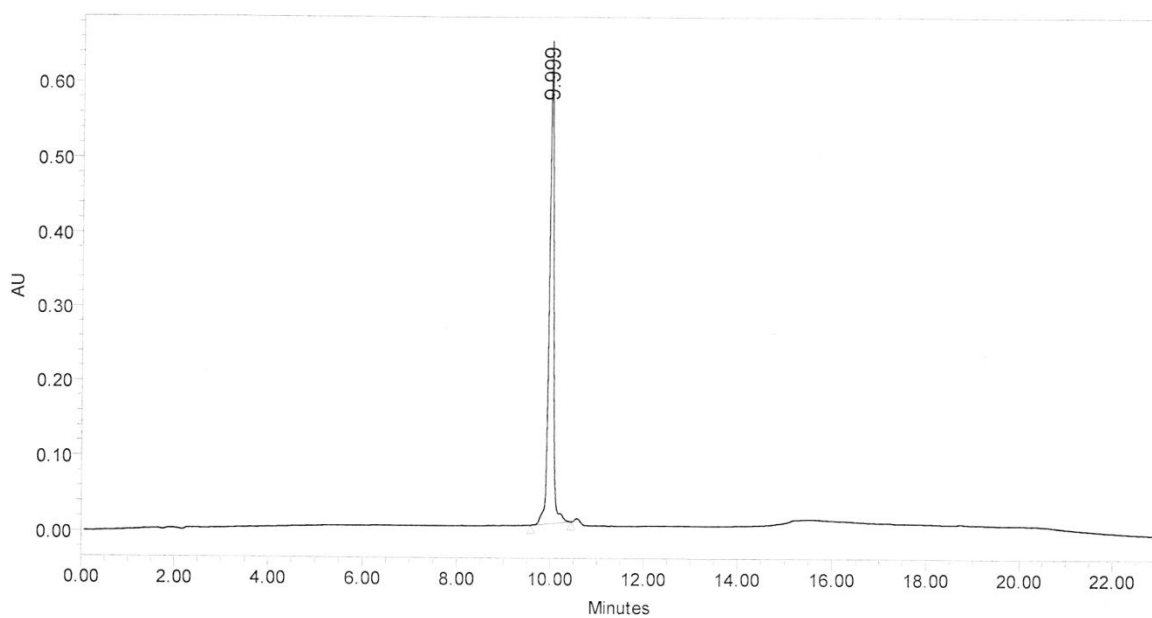
5'- A UCA GAA UCU UCC AAC ACU -3'

MS. Calc. 6075.0 g/mol Found 6076.0 g/mol

Note: Underlined residues refers to 2'-OMe RNA

**Figure A21. IP RP LC/MS Analysis of (Table 2.1, sequence 12b)**

SAMPLE INFORMATION			
Sample Name:	1ss_ome	Acquired By:	System
Sample Type:	Unknown	Sample Set Name:	1_OME_hplc_pure_12413
Vial:	55	Acq. Method Set:	RNA_AMM2489_MS
Injection #:	1	Processing Method:	oligoprocessing
Injection Volume:	50.00 ul	Channel Name:	W2489_ChA
Run Time:	23.0 Minutes	Proc. Chnl. Descr.:	W2489_ChA_260nm
Date Acquired:	1/24/2013 10:37:37 AM EST		
Date Processed:	1/24/2013 11:00:49 AM EST		



	RT	Area	% Area	Height
1	9.999	4244447	100.00	638415

**Sequence 12b.**

5'-A GUG UUG GAA GAU UCU GAU-3'

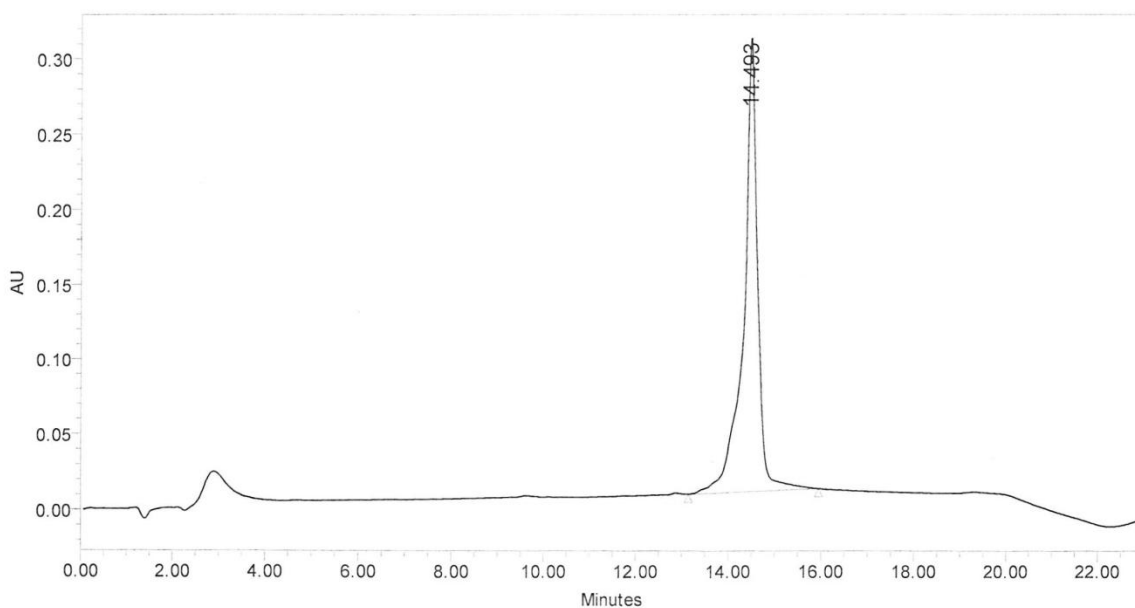
MS. Calc. 6214.9 g/mol Found 6215.9 g/mol

Note: Underlined residues refers to 2'-OMe RNA



**Figure A22. IP RP LC/MS Analysis of (Table 2.1, sequence 14)**

SAMPLE INFORMATION			
Sample Name:	V-ome	Acquired By:	System
Sample Type:	Unknown	Sample Set Name:	31714_retest1
Vial:	27	Acq. Method Set:	RNA_AMW2489_MS
Injection #:	1	Processing Method:	oligoprocessing
Injection Volume:	100.00 ul	Channel Name:	W2489 ChA
Run Time:	23.0 Minutes	Proc. Chnl. Descr.:	W2489 ChA 260nm
Date Acquired:	3/17/2014 11:03:23 AM EDT		
Date Processed:	3/17/2014 11:55:00 AM EDT		



	RT	% Area	Area ( $\mu\text{V}\cdot\text{sec}$ )
1	14.49	100.00	6306319

**Sequence 14.**

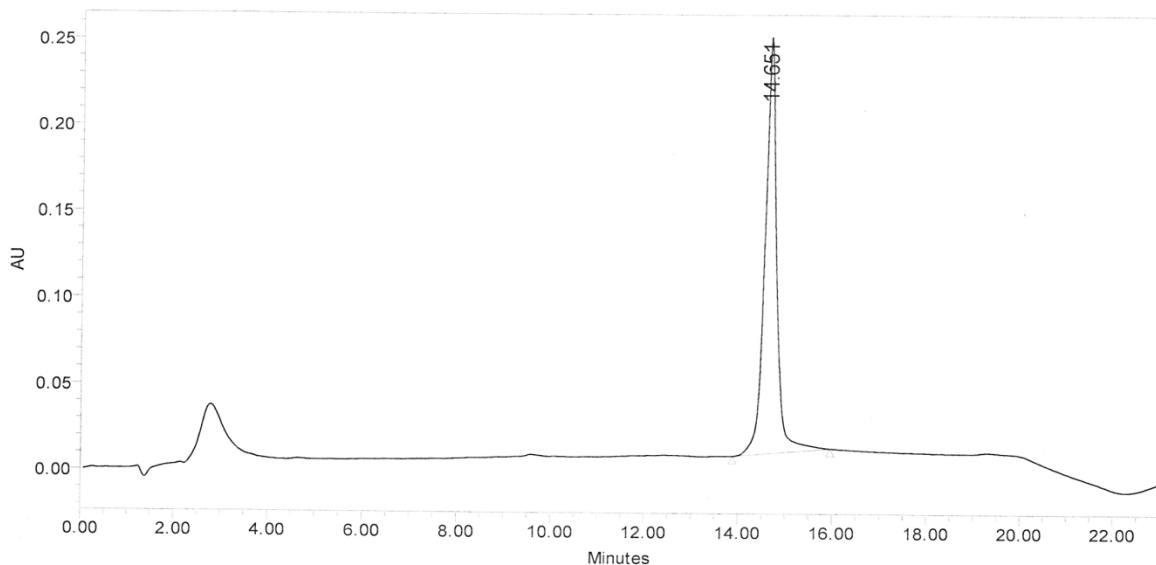
2'3' UCA CAA CCU UCU AAG ACU A-5'  
 5'-rU  
 3'5'-A GUG UUG GAA GAU UCU GAU-3'

MS. Calc. 12658.8 g/mol Found 12659.9 g/mol

Note: Underlined residues refers to 2'-OMe RNA

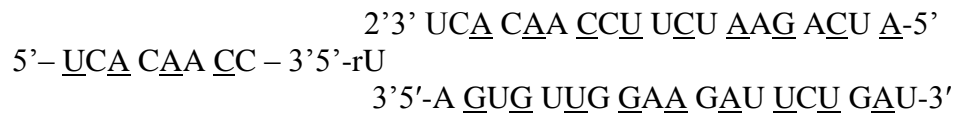
**Figure A23. IP RP LC/MS Analysis of (Table 2.1, sequence 15)**

SAMPLE INFORMATION			
Sample Name:	Y-ome	Acquired By:	System
Sample Type:	Unknown	Sample Set Name:	31714_retest1
Vial:	28	Acq. Method Set:	RNA_AMW2489_MS
Injection #:	1	Processing Method:	oligoprocessing
Injection Volume:	100.00 ul	Channel Name:	W2489 ChA
Run Time:	23.0 Minutes	Proc. Chnl. Descr.:	W2489 ChA 260nm
Date Acquired:	3/17/2014 11:28:05 AM EDT		
Date Processed:	3/17/2014 11:55:01 AM EDT		



	RT	% Area	Area ( $\mu\text{V}\cdot\text{sec}$ )
1	14.65	100.00	4178812

**Sequence 15.**



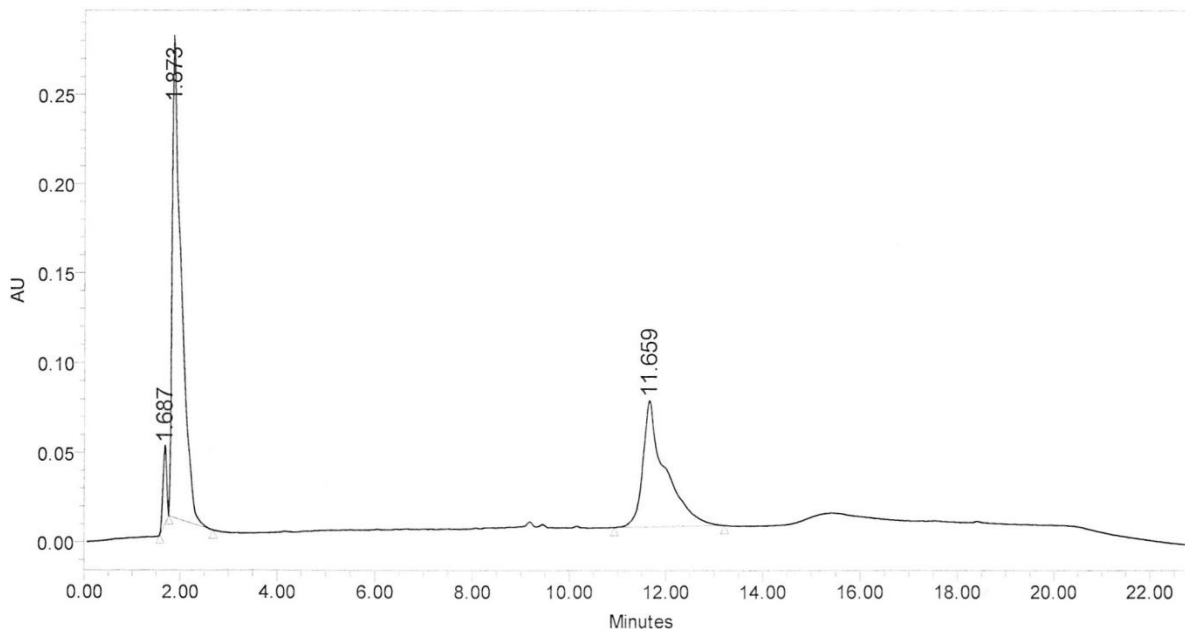
MS. Calc. 15229.5 g/mol Found 15230.5 g/mol

Note: Underlined residues refers to 2'-OMe RNA



## SAMPLE INFORMATION

Sample Name: 1-2 OME TP NP10	Acquired By: System
Sample Type: Unknown	Sample Set Name: OME BR NAP 10 PURE12313
Vial: 61	Acq. Method Set: RNA_AMW2489_MS
Injection #: 1	Processing Method: oligoprocessing
Injection Volume: 100.00 ul	Channel Name: W2489 ChA
Run Time: 23.0 Minutes	Proc. Chnl. Descr.: W2489 ChA 260nm
Date Acquired: 1/23/2013 2:14:24 PM EST	
Date Processed: 1/23/2013 2:37:36 PM EST	



	RT	Area	% Area	Height
1	1.687	229158	3.83	43678
2	1.873	3489452	58.26	269858
3	11.659	2270564	37.91	70647

### Sequence 17.

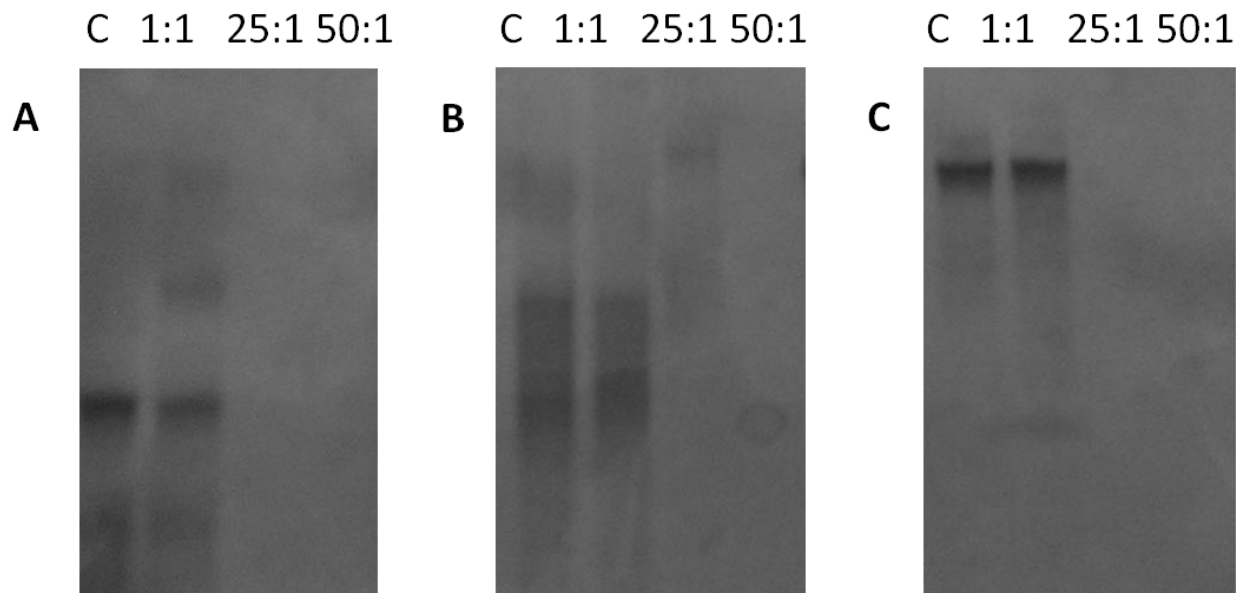
3'-A GAU CAU AGU UAC GCG AGG -5'  
 rU3'5'-UCA CAA CC -3'5'-rU  
 5'-U CUA GUA UCA AUG CGC UCC-3'5'  
 2'3'-UCA CAA CCU UCU AAG ACU -5'  
 3'5'-A GUG UUG GAA GAU UCU GAU-3'

MS. Calc. 27870.2 g/mol Found 27766.3 g/mol

Note: Underlined residues refers to 2'-OMe RNA

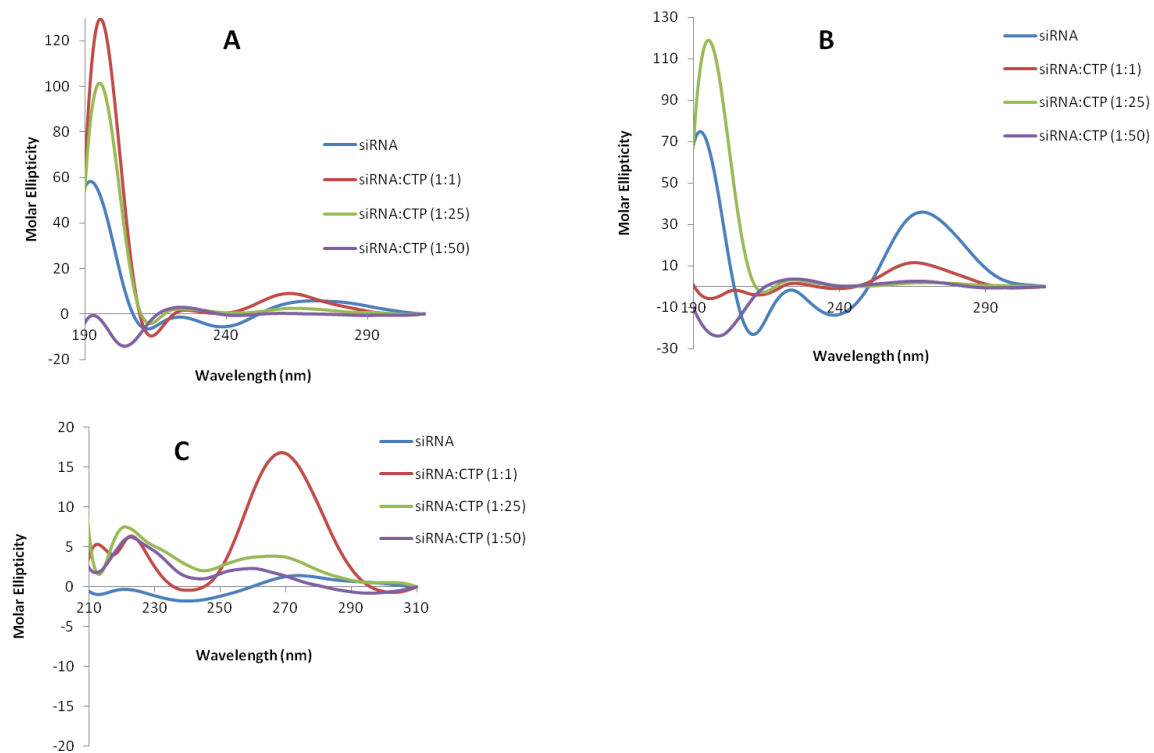
## APPENDIX C. CTP:siRNA PAGE

**Figure A26.** Native gel analysis of Pep42-R9 and (A) **Table 2.1 sequence 2**; (B) **Table 2.1 sequence 5** and (C) **Table 2.1 sequence 7**.



## APPENDIX D. CTP:siRNA analysis by CD Spectroscopy

**Figure A27.** CTP:siRNA analysis by CD Spectroscopy. (A) Table 2.1 Sequence 2, (B) Table 2.1 Sequence 5, (C) Table 2.1 Sequence 7.



## APPENDIX E: DLS studies of CTP:siRNA

**Table A1.** Summary table showing CTP:siRNA studies by DLS and TEM

Sample	Effective Diameter from DLS (nm)	Comments
<b>Sequence 2 (Duplex siRNA)</b>	~ 20 600-1000	monomers mostly aggregates
<b>Pep42-r9: seq. 2 (50:1)</b>	210 ± 14 1400 ± 80	Bimodal complex
<b>Sequence 5 (Y siRNA)</b>	20 ± 5 700 -2000	monomers aggregates
<b>Pep42-r9: seq. 5 (50:1)</b>	900 ± 50 170 ± 9	Bimodal complex
<b>Sequence 7 (Hyperbranch siRNA)</b>	~ 20 20-2000	monomers mostly aggregates
<b>Pep42-r9: seq. 7 (50:1)</b>	340 ± 2	

### CTP:siRNA (Pep42-R9:siRNA, **Sequence no. 2**)

The DLS and TEM both show complex formation with approximately similar sizes around 1000 nm. However **sequence 2** alone is highly aggregated with unstable DLS readings and high aggregation seen on TEM grids. This supports the conclusion that complexes are formed because the complex duplex is uniform and looks different on TEM grids.

### CTP:siRNA (Pep42-R9:siRNA, **Sequence no. 5**)

The TEM and DLS results show the population of 170 nm as well as 900 nm population on DLS. Complex formation is supported by the observation of uniform complexes seen on grids which are not seen in the controls. **Sequence 5** alone has a DLS population 5 nm, while on TEM

uniform particles of approx. 20-25 nm were observed. In both cases the **sequence 5** sizes alone are smaller than the sizes seen in complexed samples.

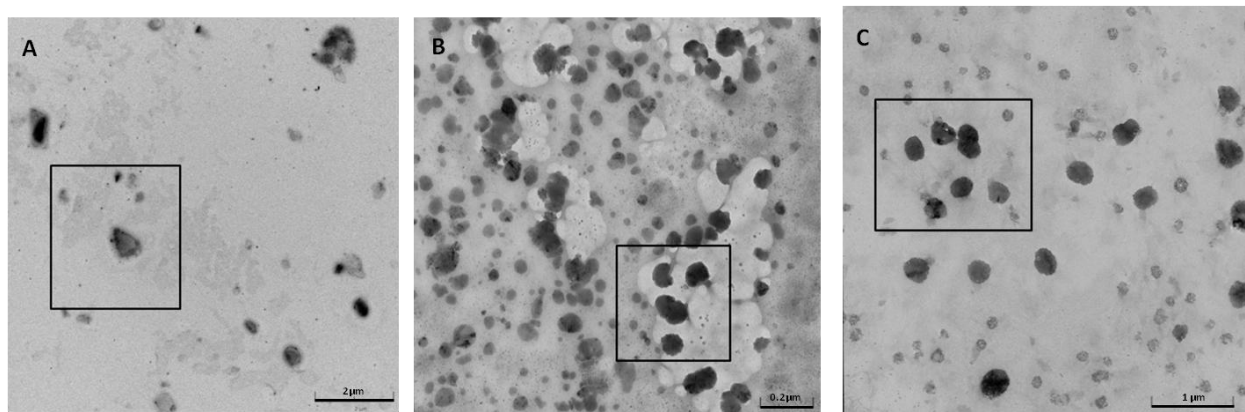
#### CTP:siRNA (Pep42-R9:siRNA, **Sequence no. 7**)

About 340 nm complex size is observed in both DLS and TEM (300 – 500nm) . Also seen are smaller sized particles (approx. 100-300 nm) which could be smaller complexes. **Sequence 7** alone is multimodal with different populations and high aggregation suggested by DLS and TEM. The monomeric form is approximately 25 nm, some particles of size 100 nm are seen and a few aggregates ranging from 700 -2000 nm are seen.

In all three cases there seems to be complex formation, as deduced from TEM images. DLS data does not always correlate with the TEM sizes especially as seen in the siRNA sequences alone, mostly due to instability or multimodal populations showing aggregation. Sample preparation for TEM could also be a contributing factor to slight changes observed when comparing DLS and TEM.

#### APPENDIX F. TEM images of CTP:siRNA

**Figure A28.** TEM images of Pep42-R9 and (A) **Table 2.1 sequence 2**; (B) **Table 2.1 sequence 5** and (C) **Table 2.1 sequence 7**. Data explanation provided in Appendix E.





## APPENDIX G. Thermal melts of CTP: siRNA

**Figure A29.** Thermal melts of CTP:siRNA between Pep42-R9 and (A) **Table 2.1 sequence 2**, (B) **Table 2.1 sequence 5** and (C) **Table 2.1 sequence 7**.

